UNIVERSITY OF OKLAHOMA

GRADUATE COLLEGE

INFLUENCES OF THE AEROSOL INVIGORATION EFFECT ON RADAR SIGNATURES OF DEEP CONVECTION NEAR HOUSTON TX USING A BULK STATISTICAL FRAMEWORK

A THESIS

SUBMITTED TO THE GRADUATE FACULTY

in partial fulfillment of the requirements for the

Degree of

MASTER OF SCIENCE

By

JONAH CHRISTOPHER PEHL
Norman, Oklahoma
2023

INFLUENCES OF THE AEROSOL INVIGORATION EFFECT ON RADAR SIGNATURES OF DEEP CONVECTION NEAR HOUSTON TX USING A BULK STATISTICAL FRAMEWORK

A THESIS APPROVED FOR THE
SCHOOL OF METEOROLOGY

BY THE COMMITTEE CONSISTING OF

Dr. Greg M. McFarquhar (Chair)

Dr. Jeffrey C. Snyder

Dr. Jason C. Furtado

Acknowledgments

First and foremost, I would like to thank my dear mother for raising me the way that she did in a single-parent home where life was constantly a struggle. You nurtured the will within me to pursue a life that invested in my future and one day, it will be all worth it. Also, my dearest Grandpa Jess and Grandma Kathy, thank you for being my second and third parents and giving me everything you could out of the kindness in your heart. I know you would give me the moon if you could.

A huge thank you goes out to my two advisors, Greg and Jeff. Jeff, thank you very much for all of the technical help in basically creating this project out of nothing. This project has been the hardest thing I've ever done, but you made it a lot easier by helping calm my own critiques of my work. Greg, thank you for working hard on the MANY edits that I needed to make the thesis as good as I could, even in the midst of your extremely busy Spring schedule. I am very grateful for your expertise, advice, and help to make me a better scientist and writer. Also, Dr. Furtado, thank you very much for your expertise, especially within your Advanced Statistical Meteorology course that I took back in the Spring of 2022. Your course was taught in a superb manner that allowed for immediate practical use of the concepts in students' research.

Thank you to my wonderful group of friends that I've met since I enrolled here at OU in Fall of 2020. Of course Emily, my girlfriend, thank you for being my best friend since I've been here and sharing so many awesome memories and difficult struggles with me. You help keep my head on straight when code and life get frustrating. Emily, Jason, Angela, Laura, Brandon, and Alec, thank you for being my good friends throughout our time here and making the weeks tolerable during the tough semesters through our really loud and funny game nights.

Dr. Lerach, Dr. Flynn, and Dr. Shellito, my undergraduate professors, thank you for making me the atmospheric scientist that I am. I miss you three dearly, along with all the great times we had at UNC. I could not have asked for a better undergraduate

experience. While life changes and chapters turn, I never want to forget you three and given that this is an interconnected field, I know it won't be long until I can see (or even work) with you again.

Thank you to Dr. Jiaxi Hu whose work provided a guide for this project. Thank you to John Krause in the National Severe Storms Laboratory for help with the MCIT algorithm as well as Horst Severini and Brad Spitzbart from the University of Oklahoma's Supercomputing Center for Education and Research, who helped with the super-computing side of the project on Schooner. Finally, I would like to thank the National Science Foundation for providing the funding for this project via grant AGS-2019968 and CIWRO for giving me this amazing opportunity.

Table of Contents

List Of Tables

List Of Figures

Abstract

Aerosol-deep convective cloud (DCC) interactions remain a frontier in the study of water cycles, energy budgets, climate models, and air quality, partly because it can be difficult to disentangle aerosol impacts from the impacts of variations in the temperature, moisture, and wind fields that strongly affect the structure and evolution of DCCs. Theoretical and observational studies have shown that increased aerosol concentration ingestion by DCC updrafts can promote their invigoration by delaying the warm rain process and increasing latent heat release at the freezing level through a narrowing of the drop size distribution. This mechanism, known as the aerosol invigoration effect (AIE), increases a convective precipitating updraft's strength and alters microphysical structures throughout its lifetime. However, other recent studies refute claims that the AIE increases updraft strength and instead claim that increased aerosol loading can weaken updrafts and/or reduce precipitation intensity. This study seeks to examine the impact of the AIE on DCCs by using a bulk statistical framework with a sample size of 2500 DCCs observed by ground-based radar observed in the vicinity of Houston, TX in the months of June, July, and August between 2013 – 2021. The vicinity of Houston was chosen for this investigation as regular summertime sea-breeze triggered DCCs occur in low-shear environments and weak synoptic-forcing conditions, with large aerosol concentration differences on varying days. Data are obtained from the Houston-Galveston WSR-88D (KHGX), ECMWF Reanalysis v5 (ERA5), Modern-Era Retrospective analysis for Research and Applications, version 2 (MERRA-2), and Texas Commission for Environmental Quality (TCEQ). DCC tracking was completed using the Multi-Cell Identification and Tracking (MCIT) algorithm using radar data from KHGX. Results from a spatial analysis of DCC locations using 2D kernel density estimates show that their locations, initiation times, and aerosol regime are largely governed by the direction and strength of the sea-breeze. Composite difference contoured frequency by altitude diagrams (CFADs) are used to uncover differences in the

vertical structure of dual-polarization radar signatures and show that under certain meteorological conditions, differences in radar data consistent with the AIE are present across many DCCs within specific meteorological regimes. These regimes have been shown to promote the AIE by previous work, such as environments with moderate to high instability, low shear, and high free tropospheric relative humidity. Additionally, some meteorological regimes promote inhibition of updraft and precipitation intensity for DCCs under high aerosol mass loading, mainly within an anthropogenic aerosol regime.

Chapter 1

Introduction

Aerosols emitted into Earth's atmosphere provide the necessary particles that allow for condensation of water vapor to occur at relative humidities just above saturation. Without them, liquid clouds would not be able to form under the conditions they currently do. Given aerosol prevalence across the globe and their effects on the climate system, and the modification of these effects due to human activities, the importance of understanding their impacts on radiative forcing through cloud interactions is increasing. Due to the difficulty in separating meteorological influences from aerosol influences, aerosols' exact physical influence on all types of clouds and the precipitation they produce remains poorly known. To measure the interactions between aerosols and clouds, detailed in-situ data collected via aircraft across many different types of meteorological environments, aerosol regimes, and cloud types can aid in a process-oriented understanding of how aerosol impact clouds, which compliments understanding gained from satellite remote sensing and modeling studies.

Throughout the 20th and early 21st centuries, technological advancements in remote sensing instruments such as weather radars have allowed new methodologies for studying microphysical interactions between aerosols and clouds. This has occurred because of the capability of retrieving microphysical properties of clouds and the large spatio-temporal scales at which radar data exist compared to in-situ data. Weather

radars measure the backscattered signal from the interaction of the transmitted electromagnetic field with hydrometeors, which can be used to estimate hydrometeor concentrations and diameters within a sampling volume, typically assuming liquid composition and Rayleigh scattering. One of the most commonly used products derived from the returned signal is the radar reflectivity factor (Z) and is typically determined using horizontal polarization and displayed in decibel units or dBZ. For spherical hydrometeors for which the Rayleigh approximation is appropriate, Z is proportional to the 6th-moment of the drop size distribution (DSD) within a sampling volume of the radar and given by

$$Z = \int_0^\infty N(D) D^6 dD, \tag{1.1}$$

where $N(D)$ is the number distribution function, which is dependent on drop diameter D.

The advancement of dual-polarization radar technology for use in weather radar applications has opened new frontiers for retrieving the microphysical properties of clouds. In particular, differential reflectivity (Z_{DR}) (Seliga and Bringi, 1976) and co-polar correlation coefficient (ρ_{HV}) (Balakrishnan and Zrnic, 1990) are two heavily used dual-polarization radar variables. Z_{DR} is defined as the logarithmic ratio of the Z measured at the horizontal polarization (Z_h) and the Z measured at the vertical polarization (Z_v), given by

$$Z_{DR} = 10 \log Z_h / Z_v, \tag{1.2}$$

where Z_h and Z_v are in linear units ($\mathrm{mm}^6/\mathrm{m}^3$). The ρ_{HV} at lag-0 can be defined as

$$\rho_{HV}(0) = \frac{< S_H^i S_V^{i*} >}{[< |S_H^i|^2 >< |S_V^i|^2 >]^{0.5}}, \tag{1.3}$$

where <> indicates time-average quantities and * is the complex conjugate operator. S_H^i (S_V^i) is the scattering coefficient of the ith hydrometeor within the sampling volume at the horizontal (vertical) polarization and is given by

$$S_{H,V} = \pi^3 K_w D^3 / 2\lambda^2, \tag{1.4}$$

where K_w describes the refractive index of water and λ is the wavelength of the radar. Z_{DR} provides information on the typical shape of hydrometeors within the sampling volume, with higher Z_{DR} meaning more oblate or horizontally oriented particles. Additionally, Z_{DR} is Z-weighted, meaning that particles that produce higher Z will dominate the Z_{DR} returns. ρ_{HV} is typically used to identify if the scatterers within a sampling volume are uniform in composition and thus can be a good indicator of meteorological targets versus other scatterers such as bugs and debris (Balakrishnan and Zrnic, 1990). Additionally, it can provide information about mixed-phase regions of clouds such as melting layers.

Many studies have taken advantage of dual-polarization technology to study cloud-aerosol interactions, and these are thoroughly discussed in Chapter 2. This study seeks to add to knowledge gained from these previous works by using dual-polarization radar observations of convective clouds within a large bulk statistical framework to study aerosol-cloud interactions. Specifically, this study seeks to uncover aerosol impacts on mixed-phase deep convective clouds (DCCs) within the Houston, Texas region using the operational S-band WSR-88D NEXRAD radar KHGX to answer the following:

1. What is the spatial distribution of convection around Houston under differing aerosol regimes?

2. Can aerosol effects on deep convection be seen using an operational NEXRAD radar considering the vertical resolution and coverage of operational scanning strategies may be sub-optimal and incomplete for such a task?

3. If aerosol effects are observed, what are these effects on the vertical radar profiles of DCCs? Are the effects of aerosols consistent with invigoration or inhibition of convection? Do meteorological influences mediate the aerosol effects?

The remainder of this thesis consists of chapters as follows. Chapter 2 presents background information on important convective cloud microphysical processes that aerosols might impact; past studies on aerosol effects on convective clouds are also summarized. Chapter 3 presents the methodology behind the construction of the bulk statistical framework used to investigate aerosol impacts on convective cloud properties. Chapter 4 presents results found from the statistical analysis and interprets those results. Chapter 5 presents important conclusions regarding aerosol effects on convective clouds, limitations of those results, and offers suggestions for future research.

Chapter 2

Background

2.1 Aerosols & CCN

2.1.1 Origin and effects of CCN

Aerosols consist of substances that are in a solid or liquid state, and typically microscopic. They can range in diameters from less than 20 nm up to millimeters. This wide range of diameters warrants specific delineations of size ranges to categorize how different sizes behave in Earth's atmosphere. The nucleation mode is defined as aerosols with diameters less than 20 nm, Aitken mode with diameters between 20 nm and 100 nm, accumulation mode with diameters between 100 nm and 1 μm, and coarse mode with diameters above 1 μm.

Sources of aerosols include particles scavenged by the wind from the ground, condensation of gases in the atmosphere, and anthropogenic emissions (Seinfeld, 1986). These three broad mechanisms can lead to two distinct formation processes for aerosols, primary and secondary. A primary aerosol is defined as an aerosol that has been directly emitted from its source. For example, sea salt that is ejected into the atmosphere by sea spray at the ocean surface, lofting of dust particles by wind, or ash from a volcano. A secondary aerosol is a product of condensing gases in our atmosphere and is typically organic in nature or contains sulphates and nitrates, with large production regimes

originating from anthropogenic sources (Lewis, 2018). With the arrival of the Industrial Revolution in the late 19th century, proportions of these types of aerosols have increased (Yang et al., 2022) and cause concern for adverse health effects across many large urban areas (e.g., Nel, 2005). Additionally, these secondary processes are difficult to infer information about and model due to their complex and heterogeneous nature. Consequently, many resources from governments and private entities from across the globe have been utilized to understand how these aerosols affect the atmosphere and determine their atmospheric lifetime (e.g., Miskell et al., 2017; Morawska et al., 2018; Olalekan et al., 2018). In addition to health concerns, aerosol emissions have long been established as a notable driver to climate change from both direct radiative and indirect microphysical effects (e.g., Boer et al., 2000; Charlson et al., 1992; IPCC, 2007; Kondratyev et al., 2006; Rotstayn and Penner, 2001; Schwartz, 1996). For large temporal scales, net cooling through the direct effects of aerosols from absorption of short wave radiation in the atmosphere can have a profound impact on long-term climate both regionally and globally (Andreae, 2001; Andreae et al., 2005; Menon et al., 2002). Additionally the semi-direct effect, from the absorption of solar radiation by carbonaceous aerosols, can impact cloud formation and depends on the vertical distribution of aerosols (e.g., McFarquhar and Wang, 2006) as well as their concentrations and compositions.

A largely unresolved consequence of aerosols on climate is their effects on cloud microphysical properties. Not all aerosols within the atmosphere serve as embryos for cloud drops but the subset that does covers a wide range of sizes and chemical compositions (Twomey, 1959) and are referred to as cloud condensation nuclei (CCN). The size and chemical composition of an aerosol along with ambient supersaturation determine the ability of an aerosol to activate as nucleation embryos for water vapor to condense onto and hence to be defined as CCN (Köhler, 1921). Common CCN originate from

biomass burning, sea salt, dust, fossil fuel emissions, and volcanic activity (Andreae and Rosenfeld, 2008, among others) and typically have sizes in the accumulation mode with diameters between 0.1 and 5 μm. Giant CCN (GCCN) are a subset of CCN that have diameters of about 5 μm or larger and can activate at lower supersaturations according to Köhler theory. GCCN are mainly formed from sea spray across ocean surfaces (Feingold et al., 1999) and mineral dust (Levin et al., 1996; Wurzler et al., 2000), but can also be produced by biomass burning (Adler et al., 2011). Other CCN that cover a wider range of sizes are composed of primary biogenic and secondary organic aerosols (SOAs). Primary biogenic aerosols include organic debris, viruses, fungi, and bacteria and are thus a difficult type to identify sources for in a reliable manner (Bauer et al., 2003; Diehl et al., 2001; Franc and DeMott, 1998; Levin and Yankofsky, 1983; Möhler et al., 2007; Sattler et al., 2001; Schnell and Vali, 1976). These types can act as GCCN given the correct environmental conditions but also can serve as ice nucleating particles (INPs) if their surface properties are adequate (Bauer et al., 2003; Sharma and Rao, 2002). SOAs are formed through secondary aerosol formation processes that are both biogenic and anthropogenic. SOA precursors are typically biogenic but can be catalyzed by anthropogenic emissions due to increased oxidation products in the condensed phase and rate of oxidation (Kanakidou et al., 2000).

2.1.2 Effects of CCN on mixed-phase clouds

The impact of variations in the number concentrations of CCN on DCCs is the ultimate focus of this study given that these clouds have sufficiently large drops to be detectable by operational S-band NEXRAD radars. Below these clouds, updraft parcels initialize in or slightly above the boundary layer and extend several kilometers above the environmental freezing level (Hall, 1980), thus ingestion of boundary layer aerosols into updrafts is assumed. A majority of the CCN population is activated at or immediately

above cloud base where the maximum supersaturation with respect to water is typically reached (Rogers and Yau, 1989), with larger maximum supersaturations leading to activation of CCN with smaller diameters. Fan et al. (2018) explored the possibility of higher supersaturations being attained higher in the updrafts which would lead to the activation of smaller ultra-fine aerosol particles, and subsequent invigoration of convection. After activation the drops continue to grow by condensation, however the drop size distributions (DSDs) narrow as the radial vapor diffusion growth rate decreases with drop size. Once these DSDs broaden by a poorly understood process, the collision-coalescence process will produce larger drops and the onset of precipitation (e.g., McFarquhar, 2022, and references therein).

Increases in CCN number concentration lead to an increased number concentration of cloud droplets. An increase in cloud droplet concentration given a fixed liquid water path leads to increased cloud optical thickness (Twomey, 1977). This is simply due to the increased surface area of the smaller cloud droplets, allowing for more scattering of shortwave radiation and is known as the first aerosol indirect effect on clouds.

The second indirect effect or the Albrecht effect (Albrecht, 1989) describes how increased number concentrations of CCN leads to precipitation suppression and hence clouds with longer lifetimes, higher cloud fractions, and thus more net scattering of shortwave radiation. Increases in CCN concentrations mean that more numerous cloud drops form at the lifting condensation level (LCL) and above within the DCC's updraft, and hence reach smaller sizes due to the competition for condensate. The less broad DSD and small drop sizes decreases the probability for precipitation development through the collision-coalescence process (Gunn and Phillips, 1957; Squires, 1958).

However, it has been hypothesized and modeled that the presence of hygroscopic GCCN, which are frequent near coastal locations due to sea spray or where mineral dust particles are abundant (Kuba and Murakami, 2010), can overcome the inhibition of the

warm rain process from increased CCN concentrations and instead produce broader DSDs (Saleeby and Cotton, 2004). More broad DSDs can then initiate the collision-coalescence process. This raises complexities when interpreting increased CCN number concentration effects on DCCs if size distributions of the CCN are not known.

How aerosols impact DCCs, through the Albrecht effect, is what this study investigates and specifically if increased CCN number concentrations lead to stronger and longer lasting DCCs with more intense precipitation. This process is deemed the aerosol invigoration effect (AIE) and is hypothesized to act in DCCs that precipitate and whose updrafts reach above the freezing level. The AIE is defined as a thermodynamic invigoration of a DCC's updraft through the microphysical mechanisms discussed above (Rosenfeld et al., 2008). When there is a narrower DSD and smaller drop sizes, more condensate reaches the EFL and consequently more freezing takes place at and above the EFL, increasing the updraft buoyancy. Interestingly, competing effects can take place at the EFL when CCN concentrations are perturbed within a DCC. At first instance, more freezing and associated latent heat is released because condensate is available since there has been less precipitation. Alternatively, freezing is delayed because the cloud drops are smaller. Thus, an initially stronger updraft may be necessary to take advantage of the dormant latent heat that could be released by the more numerous but smaller supercooled droplets for perturbed CCN conditions (Khain et al., 2005; Rosenfeld et al., 2008). Ice nucleation events can also complicate the impact of varying CCN concentrations. For example, if there are sufficient INP number concentrations within updraft parcels then heterogeneous freezing mechanisms such as immersion, contact, or deposition can be more efficient to produce ice at temperatures closer to 0°C than at about -40°C where homogeneous freezing takes place.

A second mechanism of the AIE can increase cloud fraction through the thermodynamic enhancement of cold pools (Koren et al., 2010; Rosenfeld et al., 2008). Here,

increased number concentrations of ice crystals that are small with slower fall speeds than raindrops have more time to sublimate below cloud, especially if shear is present, and thus increase net latent cooling. Stronger downdrafts from increased latent cooling can then lead to increased chances of triggering more DCCs along stronger surface cold pool boundaries (Rosenfeld et al., 2008).

Much work has quantified the AIE in different meteorological environments. The capability of the AIE to invigorate DCCs can be drastically affected by three main meteorological variables: relative humidity throughout the depth of the troposphere, bulk shear, and convective available potential energy (CAPE) (Dagan et al., 2015; Fan et al., 2009; Khain et al., 2008; Koren et al., 2010). In brief, humid environments with weak wind shear and moderate instability are ideal in fostering aerosol invigoration for mixed phase convection because these clouds are better able to withstand entrainment at the cloud periphery (Dagan et al., 2015) and have higher precipitation efficiency due to the lack of strong shear and instability available to loft condensate mass to the freezing level (Khain et al., 2008).

Although the AIE plays a major role in the climate feedback system of Earth, it is poorly understood and represented in global climate models (Ghan and Schwartz, 2007) because aerosol-cloud interactions occur on microscopic scales but their effects cascade up to the larger spatial and temporal scales simulated by climate models. In general, the AIE directly affects the hydrologic cycle and redistributes precipitation and energy throughout the troposphere (e.g., Ramanathan et al., 2001). For example, Nishant et al. (2019)'s modeling study found that there could be a 4 ± 3.8 % decrease in the ratio of rain to cloud water when CCN number concentration is doubled, leading to enhanced cloud top cooling. Further, an increase in CCN loading can weaken the hydrologic cycle if cold pool-triggered convection occurs less frequently increasing the residence time of water vapor (Ramanathan et al., 2001). The weakened hydrologic cycle from warm

rain suppression by the AIE may be most prominent in the northern hemisphere where anthropogenic and continental aerosols are numerous over land (Ramanathan et al., 2001). The climate system response to a weakening hydrologic cycle varies on global to regional scales. Globally it seems that climate response is negligible from disruption of the water cycle (Hansen et al., 2000; Ramanathan et al., 2001), but regionally it impacts surface precipitation trends significantly. For example, a shift in precipitation towards low latitudes partly due to aerosol impacts has been noted (Allen et al., 2015) and other studies point to long term impacts of precipitation suppression in areas such as the Pearl River Delta, Houston, TX, and the Amazon rain forest (Guo et al., 2018; Martin et al., 2017; Shepherd and Burian, 2003). In summary, aerosol perturbations and the AIE change the global and regional climate in a complex manner necessitating the need for more detailed modeling and observational studies to further quantify the anthropogenic and natural impacts on water resources. This study uses observations to examine these impacts of aerosols on DCCs in the vicinity of Houston, TX.

2.1.3 Applications to Houston, TX

Sections 2.1.1 and 2.1.2 present a general overview of the AIE and interactions with DCCs. In this section, the objectives of this study to examine the impact of the AIE on DCCs in the Houston, TX region are introduced along with background information regarding the sources of CCN in the Houston area.

The Houston metropolitan area sits upon many marshes, forested lands, swamps, and prairies within the Gulf Coastal Plain biome (Blair, 1950). Some of the major geographic characteristics of the city are the Trinity and Galveston Bays which sit just to the southwest of the main urban area. These bays support a multitude of shipping and fishing routes near the metropolitan area which makes them major ports for intercontinental trade and commerce and supports the ever-growing population of

Houston. Schadewald (1999) found that throughout the 20th century Houston had a population growth rate of 4,000%, number one in the country during that period. This population growth was coincident with the vast economic development of the energy and oil industries in Houston (Cash, 2013). Houston has two of the top four largest U.S. oil refineries and exports feedstocks, fuel and chemical products, plants, and animals at one of the highest levels in the country (Sectors, 2022). Houston's increase of urbanization and industrialization in the recent century has undoubtedly increased the aerosol burden in the regions around southeast Texas (Dzubay et al., 1982). In fact, Houston now regularly exceeds the Environmental Protection Agency's National Ambient Air Quality Standards (Daum et al., 2004; Lei et al., 2004) and frequently a threat due to high tropospheric ozone is posed (Levy et al., 2013). The net impact of the emitted aerosols, whether meteorological or health related, varies greatly depending on their types, sizes, concentrations, and current air mass conditions. To quantify aerosol impacts, a multitude of studies and field projects have been conducted on the climate, meteorology, and human health around southeast Texas (Carrió et al., 2011; Hu et al., 2019a; Jin et al., 2005; Lance et al., 2009; Shakya et al., 2011; Shepherd and Burian, 2003). This study seeks to quantify the impact of the AIE on Houston DCCs using $PM_{2.5}$ mass concentrations as a proxy measure of CCN number concentrations. $PM_{2.5}$ is defined as particulate matter with diameters of 2.5 μm or smaller and is typically produced by incomplete combustion of fossil fuels, biomass burning, fine dust or sea salt particles, and SOA processes (Sullivan et al., 2013).

Yoon et al. (2020) recently reviewed carbonaceous aerosol data from the Deriving Information on Surface conditions from Column and Vertically Resolved Observations Relevant to Air Quality (DISCOVER-AQ) field experiment conducted in September of 2013 in the Houston area. They found that there was a significant diurnal cycle of elemental and organic carbon mass concentrations. In the morning with a low-altitude

boundary layer and increases in motor vehicle usage, black, elemental, and organic carbonaceous aerosols increased in mass concentration. Thus, primary aerosol sources dominated within the morning hours and more active SOA formation occurred in the afternoon from photochemical reactions. Second, they concluded that most of the carbon found was emitted from present anthropogenic sources as opposed to fossils using ^{14}C analysis, especially when isolating $PM_{2.5}$. Dai et al. (2019) also highlighted the importance of the diurnal cycle on the types and concentrations of aerosols within Houston and found a stark contrast of diurnal aerosol mass loading between summer and winter. For the summer, low-oxidized oxygenated aerosols exhibited about 54% of organic aerosol mass and contributed heavily to SOA formation in the summer when compared to winter. This mechanism along with the efficiency of photochemical reactions was found to be influenced mainly by relative humidity. Specifically at night, increasing relative humidity led to enhanced aqueous-phase production of SOAs and contributed to increased organic aerosol mass concentrations. SOA formation is another mechanism that promotes $PM_{2.5}$ concentrations and is frequently observed in Houston (Levin et al., 1996). Al-Naiema et al. (2018) found that SOA $PM_{2.5}$ typically forms from primary fossil sources with biomass burning contributing little and sulfates from vehicle emissions contributing significantly to the overall $PM_{2.5}$ mass concentrations. They also found a large difference in anthropogenic and biogenic sources of these SOA precursors, with anthropogenic SOA vastly outweighing biogenic volatile organic compounds (VOCs) and biomass burning particles. Sea salt aerosol mass concentrations around the Houston area are largely constant on the seasonal/monthly scale (Song et al., 2021) and dust $PM_{2.5}$ mass concentrations can become elevated during Saharan dust transport episodes (Bozlaker et al., 2013). In general however, the typical number concentration of these aerosols are highly variable which adds difficulty in using $PM_{2.5}$ mass concentration to approximate aerosol number concentration.

Over the Houston region, there is a lack of observations of explicit CCN size distributions near DCCs for the time and spatial scales this study uses. Thus, in this study the mass concentration of $PM_{2.5}$ is used as a proxy to quantify the loading of common-sized CCN particles. Although in general increased air pollution leads to increased CCN number concentrations (e.g., Duan et al., 2018; Lance et al., 2009), this relationship is not linear because the number of CCN that can activate under a given supersaturation can be highly variable since not all particles, even within the $PM_{2.5}$ category, are equally effective at activating. Duan et al. (2018) reported in the Guangzhou region that a general elevation of CCN number concentration occurred with increased $PM_{2.5}$ mass concentration, but was not easily predicted. To reduce the complexity of these interactions it is usually assumed that the most important factor for determining if a particle can act as CCN is its size (Saxena and Hildemann, 1996) even though particle composition can also have an impact. This assumption follows from the Kelvin-Köhler-Junge equation (Köhler, 1921), given by

$$s(r) = [1 + \frac{2\sigma}{\rho_l R_v T r}][1 - \frac{3 i m_o M_w}{4 \rho_l M_o r^3}], \tag{2.1}$$

where $s(r)$ is the supersaturation along the droplets surface, σ is the surface tension of the droplet, ρ_l is the density of water, R_v is the specific gas constant for water vapor, T is the temperature of the air, r is the radius of the droplet, i is the Van't-Hoff disassociation factor, m_o is the dry mass of the dissolved aerosol, M_w is the molecular weight of water, and M_o is the molecular weight of the dissolved aerosol. The resulting Köhler curves typically show that if the diameter of a solution droplet is below about 1 μm, depending on chemical composition, Raoult's Law (Guggenheim, 1937) dominates because the r^3 located in the second term's denominator has a bigger effect than the r located in the first term's denominator, meaning $s(r) < 1$, so that

saturation over a plain surface of water has not been achieved and the droplet has not been nucleated. This means the solution droplet is a haze droplet whose size is controlled by the humidity, but unimpeded growth via condensation does not occur because the supersaturation needed to overcome the increase in energy to form the droplet surface is not available. For aerosol particles large enough to act as CCN at the LCL the ambient supersaturation within the cloud is greater than the critical supersaturation, which is the maximum value of $s(r)$ in Eq. (4.1) which occurs at the critical radius of the droplet. Further increases in r lead to reductions in the Gibbs free energy of the droplet as the reduction in energy from the condensation of liquid is greater than the increase in energy associated with the larger surface. However, Lance et al. (2009) found the organic carbon present in Houston impacts the ability of aerosol particles to activate as CCN in Houston, regardless of size. This means that while the size of an aerosol is typically the dominant characteristic for CCN criteria there are some instances where it is important to account for composition and its effects on CCN activation through the solute term.

It is recognized that $PM_{2.5}$ mass concentration is not an ideal proxy for CCN number concentration and is incapable of accounting for the complex processes of CCN activation. However, other studies which use imperfect aerosol proxies such as $PM_{2.5}$ mass concentration to deduce AIE impacts (e.g., Chen et al., 2021; Fuchs et al., 2015) show that these data are viable for estimating periods of high and low CCN number concentrations. Further, the availability of these data for the large time period of this study is crucial for constructing a large dataset and performing the statistical analysis, since direct measurements or retrievals of CCN concentration are not available.

2.2 Previous studies of the AIE

2.2.1 Observations of the microphysical effects of the AIE

In general, in-situ observational studies that have found evidence of the AIE in DCCs point to a narrowing of DSDs (Rosenfeld and Lensky, 1998) and a reduction of cloud droplet effective radius in the presence of high aerosol loading at temperatures above 0°C (e.g., Andreae et al., 2004; Koren et al., 2005; Matsui et al., 2004; Rosenfeld and Woodley, 2000) impacting the evolution of DCCs. For example, due to narrower DSDs within the warm region, Lindsey and Fromm (2008), Sherwood (2002), and Sherwood et al. (2006) all showed smaller ice particles above the freezing level with the increased aerosol loading. Increased number concentrations of supercooled drops have also been observed in continental aerosol regimes (higher aerosol number concentrations) compared to maritime regimes (lower aerosol number concentrations) by Rosenfeld and Woodley (2000). Further, the narrower DSD can reduce the precipitation efficiency and delay precipitation formation to higher altitudes within DCCs, sometimes well above the freezing level (Rosenfeld and Woodley, 2000; Williams et al., 1999). However, the impacts of aerosol loading on the total amount of precipitation observed at the surface is less clear. Huang et al. (2009) found that aerosols reduced the amount of total precipitation in agreement with other studies conducted by Jirak and Cotton (2006) and Givati and Rosenfeld (2004). But, other studies such as Bell et al. (2008), Koren et al. (2012), and Li et al. (2011) show larger accumulations of precipitation in mixed phase clouds under high aerosol loading. The uncertainty in the impact of high aerosol loading on precipitation accumulation can be attributed to the complex nature of thermodynamic and microphysical feedbacks that occur in deep mixed-phase convection, and the ability of further convection to be triggered along outflow boundaries. Freezing processes occurring within the mixed-phase region of DCCs are highly

sensitive not only to the number of cloud droplets being transported above the freezing level, but also to the number concentrations of INPs, humidity, instability, and wind shear. Outflow boundary strength is also susceptible to meteorological influences affecting the viability of cold pools to support further DCC initiation in cloud systems and thus increases in total precipitation amount. These effects however are hard to disentangle in observational studies alone.

2.2.2 Modeling of the AIE

Modeling studies that examine the influences of aerosols on DCCs can better attribute causality of aerosol impacts rather than the correlations noted in observations due to the ability to examine impacts from a single variable or process. However, it is important that simulations be evaluated against observational data to determine if they are representative of natural clouds and can hence evaluate hypotheses on the role of different processes. For example, Khain et al. (2005) conducted aerosol/DCC interaction experiments using the spectral bin Hebrew University Cloud Model (HUCM) and found that the effects of aerosol loading within the boundary layer were non-linear and dependent upon a maritime or continental aerosol regime. Continental aerosol regimes (higher CCN number concentrations) typically had decreased precipitation efficiency compared to the maritime regimes (lower CCN number concentration), but there were cases when rain-rates were larger in continental regimes. In fact, they found that larger rain rates could occur within continental DCCs given sufficient instability, high free tropospheric relative humidity, and moderate wind shear. Further, Fan et al. (2009), using the System for Atmospheric Modeling (SAM) cloud resolving model, found that aerosol loading can affect isolated DCCs differently depending on the wind shear and relative humidity profiles. Similar to Khain et al. (2005), they showed increased shear

could allow for stronger downdrafts and thus could increase the probability of outflow boundaries triggering convection/squall line development even though the initial invigoration could be limited in high shear environments.

Carrió et al. (2010) ran multiple simulations using the Regional Atmospheric Modeling System (RAMS) non-hydrostatic model to simulate a case of urban pollution around the Houston area to understand sensitivities of convection to urban aerosol intensities. They concluded that CCN concentration significantly affected the total volumetric precipitation in storms that were in polluted air near the Houston urban area, with the precipitation at the ground increasing up to some threshold of CCN loading (2000 cm^{-3}). But, they found a non-monotonic behavior of CCN loading on surface precipitation, which they attributed to changes in the size distributions of supercooled drops and ice crystals that affected riming efficiencies and cold rain processes. Carrió et al. (2011) conducted additional simulations with varying CAPE, finding that although the peak value of CCN concentration that yielded the maximum precipitation and supercooled mass changed, there was no change in the non-monotonic variation of precipitation intensity with CCN concentration. They thus concluded that the supercooled water mass resulting from differing aerosol regimes was the main precursor of how much precipitation was occurring at the ground. Ilotoviz et al. (2018) explored the consequences of increased CCN ingestion into updrafts on the microphysics and dynamics of a DCC using the HUCM with typical mid-latitude environmental characteristics. When they increased the CCN concentrations from 100 cm^{-3} to 3000 cm^{-3}, they found increases in the concentration and sizes of supercooled droplets in the first few kilometers above the freezing level which enhanced the wet growth of hail allowing it to reach very large sizes. In the low CCN concentration case the accretion of supercooled droplets onto hail and freezing drops was extremely inefficient. It was also found that higher vertical velocities occurred in the higher CCN case from the

increased latent release associated with the diffusional growth of drops from the higher supersaturations achieved and increased riming of super cooled droplets onto hail and other frozen particles.

Within these modeling studies, common themes arise which include increased supercooled liquid mass above the freezing level in more polluted environments and the modulation of this mechanism to invigorate DCCs by meteorological factors such as instability, shear, and humidity. In fact, this is largely consistent with the "ideal" scenario where aerosol invigoration takes place which is summarized by Altaratz et al. (2014). Namely, that there should be a deep warm region of the DCC occurring in a relatively unstable environment with humid conditions and weak shear. These types of environments are frequent in the summertime over southeast Texas, where conditions are analyzed for the current study allowing for appropriate selection of cases as discussed in chapter 3. Additionally, the use of the dual-polarization Houston-Galveston NEXRAD WSR-88D radar (KHGX) permits detection of increased amounts of liquid above the freezing level through analysis of contoured frequency by altitude diagrams (CFADs) (Yuter and Houze Jr, 1995) of Z and Z_{DR}. The ability of an operational NEXRAD radar to detect AIE impacts can then be compared to what has been reported by some of the previous modeling and in-situ observational studies. .

2.2.3 Uncertainties in the AIE

Many studies have claimed that the impact of the AIE on DCCs is observable (e.g., Altaratz et al., 2014; Andreae et al., 2004; Chen et al., 2021; Fuchs et al., 2015; Guo et al., 2018; Hu et al., 2019a; Ilotoviz et al., 2018; Khain et al., 2005, 2008; Li et al., 2011; Mansell and Ziegler, 2013; Rosenfeld et al., 2008, 2014; Tao et al., 2007, 2012; van den Heever et al., 2006, 2011; Wang et al., 2011; Yuan et al., 2011). Some of the observational studies that claim to uncover influences of the AIE on DCCs have

used remote sensing data from satellites (e.g., Koren et al., 2005, 2010; Lin et al., 2006). Such studies were constrained to examining cloud properties such as cloud top temperature and cloud fraction, which only allow for limited conclusions about the microphysical structure to be made. In general, these studies found that increased aerosol optical depth (AOD) leads to increased cloud fraction and lower cloud top temperatures, even when meteorological influences are accounted for. They hypothesized that this is occurring due to the increased aerosol loading leading to invigoration of DCCs through the AIE (causing colder cloud tops) with subsequent convection triggered from stronger cold pools and outflow boundaries (higher cloud fractions). However, there is some ambiguity about the conclusions due to the potential contamination of satellite retrieved AOD from atmospheric moisture and high-altitude cirrus clouds that lead to strong meteorological/AOD correlations that are impossible to separate (Altaratz et al., 2013; Chand et al., 2012; Chew et al., 2011; Gryspeerdt et al., 2014; Mauger and Norris, 2007; Omar et al., 2013; Zhang et al., 2005).

Additional studies examining the AIE include modeling simulations (e.g., Ilotoviz et al., 2018; Khain et al., 2005; Lebo and Seinfeld, 2011; Storer and Van den Heever, 2013) and analysis of retrievals from ground-based radar remote sensing (Fuchs et al., 2015; Hu et al., 2019a), all of whom have found evidence of aerosol invigoration. However some studies have found conflicting evidence through modeling (e.g., Boucher and Quaas, 2013; Grabowski, 2015; Grabowski and Morrison, 2016; Morrison and Grabowski, 2011; Morrison, 2012; White et al., 2017) and these discrepancies show inherent limitations of modeling with potential biases depending on the microphysical schemes, initialized data, boundary conditions, resolution, and other parameterizations, such as those of the boundary layer, used (White et al., 2017).

Ground-based radar retrievals provide more information about the vertical profile of microphysical properties than can be obtained by satellite, but can be limited

by vertical resolution, update times, attenuation, uncertain retrievals, and radar signal sensitivity that complicate observations of small-scale microphysical properties in DCCs. Additionally, some ground-based radar studies have found conflicting results of aerosol invigoration (Altaratz et al., 2013; Chand et al., 2012; Chew et al., 2011; Gryspeerdt et al., 2014; Omar et al., 2013; Wall et al., 2014; Yuter et al., 2013; Zhang et al., 2005), pointing to the importance of carefully disentangling meteorological impacts from aerosol impacts on DCCs.

Veals et al. (2022) presented a large statistical framework using data from the Cloud, Aerosol, and Complex Terrain Interactions (CACTI) field campaign to determine aerosol effects on DCCs. They showed that univariate statistics were not a viable method to determine aerosol effects on DCCs, but bivariate methods found that aerosol number concentrations were negatively correlated with DCC intensity when accounting for meteorological influences. Through multiple linear regression and a machine learning random forest model, positive correlations between aerosol and condensation nuclei number concentrations with cloud top temperatures were found. However, the study did not consider the life cycle of the observed cells nor their convective mode and relied on data from a small area in the Andes mountains. Another study by Varble (2018) used data from an Atmospheric Radiation Measurement (ARM) site located in Oklahoma to compare to the findings of Li et al. (2011), who found evidence of the AIE. Varble (2018) found conflicting results due to the improper treatment of correlations between aerosol measurements and meteorological influences such as instability by Li et al. (2011). Studies such as Varble (2018) and Veals et al. (2022) both point out the obvious and difficult problem when studying the AIE using observations: aerosols produce second order effects on DCCs and thus can be extremely difficult to separate from meteorological effects.

The project presented here using data collected over the Houston area seeks to overcome some of the main problems put forth by Varble (2018), Veals et al. (2022), and others mainly by increasing statistical significance and separating meteorological influences from aerosol effects. For example, sample sizes from studies similar in methodology to this one, where individual DCCs are tracked or analyzed (e.g., Fuchs et al., 2015; Hu et al., 2019a; Varble, 2018; Veals et al., 2022), range between 140 to 2300 individual DCCs. While some of these sample sizes were shown to yield statistically significant results, the current study uses a total sample size above this range of upwards of 2400 DCCs which aids in the ability to sort into stricter meteorological conditions while maintaining significant sample sizes in subsetted data. This reduces the first-order effects of meteorological variability more than some previous studies, and allows for second-order aerosol effects to be uncovered more robustly. To quantify the presence of aerosols, AOD is not used but rather model-derived $PM_{2.5}$ mass concentration is used as a proxy for CCN number concentration. Additionally, simple correlation analysis is used to explore the relationship between $PM_{2.5}$ mass concentration and DCCs because they can be cataloged according to meteorology, with a distinction between the sea-breeze circulation over land and the Gulf of Mexico. The Houston area also provides an ideal environment consisting of low wind shear, high tropospheric humidity, and instability, as well as the presence of isolated cumulus cells, for investigating the AIE.

Chapter 3

Data & Methods

3.1 Case selection

While a plethora of convective environments occur within the southeast Texas region in the summer season, warm-season mesoscale sea-breeze circulations are the focus of this study. Other synoptic-scale phenomena such as cold fronts, extra-tropical cyclones, and hurricanes, or mesoscale boundaries such as outflows, often provide stronger forcing on the DCCs and increase the difficulty in disentangling any aerosol impacts because they can cause differing modes of convection that can dominate vertical microphysical structure and impact aerosol/CCN transport within the boundary layer (e.g., Varble, 2018).

Sea-breeze circulations form from the differential heating of land and water (Haurwitz, 1947) and cause a baroclinic circulation to occur that is thermally directed. When synoptic forcing is lacking, these sea-breezes can form regularly within the morning to afternoon periods and trigger DCC formation if sufficient moisture, instability, and low-level convergence is available. In Houston, sea-breeze circulations generally exhibit a consistent wind direction from the southwest or southeast within the boundary layer due to the orientation of the coastline. This regular on-shore flow can help keep aerosol transport trends relatively constant reducing the probability of largely different aerosol and meteorological regimes. For example, Levy et al. (2013) found that after a cold-front passage with low humidity, species such as black carbon increase in

mass concentration compared to southerly on-shore flow with high humidity. DCCs in sea-breeze environments are typically ordinary and single cell in nature and lack updrafts strong enough for large hail production due to lack of vertical shear. Given these characteristics of the regular sea-breeze over Houston, these environments were chosen to investigate the AIE.

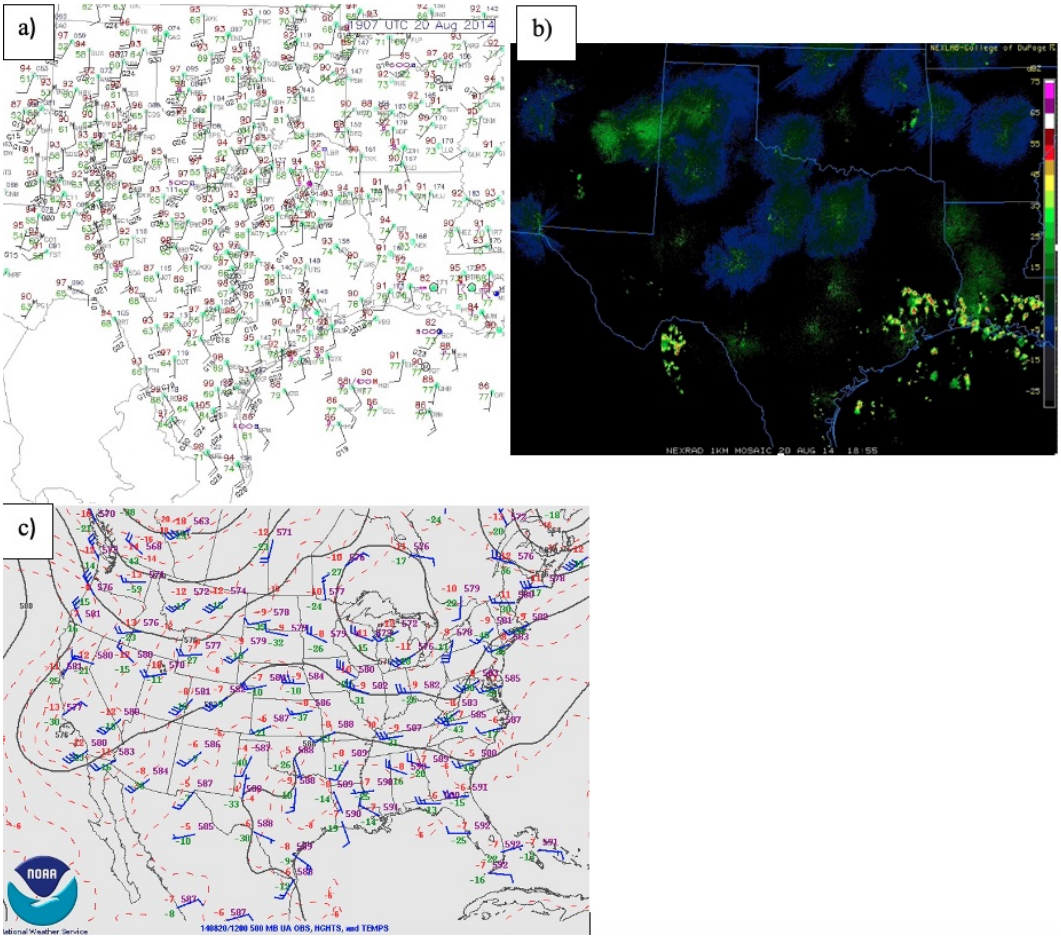

Figure 3.1: Observed (a) surface METAR stations at 19:07 UTC, (b) composite radar reflectivity at 18:55 UTC, and (c) 12 UTC 500 mb analysis from Aug. 20, 2014 over southeast Texas.

Manual case selection was completed by observing the meteorological environments from the observed upper-air charts, radar reflectivity evolution from KHGX, and surface METAR evolution. Figure 3.1 shows an example of a typical meteorological environment chosen for this study using these types of data. The case day shown exhibits a clear onshore surface flow throughout the morning and afternoon hours that triggers isolated DCCs near KHGX in an environment with weak or negligible synoptic forcing. Each day in the months of June, July, and August from the years 2013 – 2021 was analyzed, and a day was chosen for subsequent analysis based on whether ordinary convective cells formed within the scanning volume of KHGX in a sea-breeze environment. Additionally, if any synoptic-scale cold fronts, tropical cyclones, or outflow boundaries passed over the Houston area the day before, that day was not selected for further analysis to ensure that wind influences on aerosol transport would remain as similar as possible. A total of 256 case days were selected for this study with Table 3.1 listing all of them along with number of DCCs sampled during each day (for description of both datasets, refer to section 3.2.3), and period of hours when DCCs were occurring.

Case day	radar DCCs	spatial DCCs	Start Time	End Time	Case day	radar DCCs	spatial DCCs	Start Time	End Time	Case day	radar DCCs	spatial DCCs	Start Time	End Time
20130608	13	24	17:00	23:59	20150709	2	10	19:00	23:59	20180614	8	21	14:00	23:00
20130610	4	8	17:00	23:59	20150710	0	6	16:00	23:59	20180615	6	14	9:00	23:59
20130611	9	25	13:00	23:59	20150711	1	8	17:00	23:59	20180616	1	10	14:00	23:59
20130620	7	10	17:00	23:00	20150717	4	10	8:00	23:00	20180628	0	1	16:00	22:00
20130622	0	8	15:00	23:00	20150721	1	9	12:00	23:59	20180710	1	5	18:00	23:00
20130623	3	11	11:00	23:59	20150722	1	1	16:00	22:00	20180712	7	10	19:00	23:59
20130624	2	11	6:00	23:59	20150727	0	4	19:00	23:59	20180713	6	12	10:00	23:59
20130703	1	3	17:00	23:59	20150804	4	10	12:00	23:59	20180714	7	11	10:00	23:00
20130707	9	33	7:00	23:59	20150805	0	2	17:00	22:00	20180715	0	6	16:00	23:59
20130708	21	39	12:00	23:59	20150815	6	11	16:00	22:00	20180730	2	7	17:00	23:59
20130709	1	3	18:00	23:59	20150817	2	7	16:00	21:00	20180804	39	76	10:00	23:59
20130719	18	47	13:00	23:59	20150818	12	50	10:00	23:59	20180805	2	15	17:00	23:59
20130720	18	57	13:00	23:59	20150822	15	32	9:00	21:00	20180806	17	43	7:00	23:59
20130721	33	96	6:00	23:59	20160610	8	29	7:00	23:59	20180807	18	44	8:00	22:00
20130722	1	2	16:00	23:59	20160611	9	28	6:00	23:59	20180808	9	17	16:00	23:59
20130804	4	7	14:00	23:59	20160620	18	40	13:00	23:59	20180809	18	48	8:00	23:59
20130810	21	51	10:00	23:59	20160621	17	46	12:00	23:59	20180810	21	45	13:00	23:59
20130811	26	63	13:00	23:59	20160622	4	5	9:00	20:00	20180815	3	8	12:00	23:59
20130812	4	4	17:00	23:59	20160624	3	6	14:00	23:00	20180816	4	5	15:00	23:59
20130820	25	45	11:00	23:59	20160625	10	28	9:00	23:59	20180820	7	13	17:00	23:00
20130821	7	20	16:00	23:59	20160626	9	12	12:00	23:59	20180826	11	19	7:00	23:00
20130822	2	11	8:00	23:59	20160627	6	11	18:00	23:59	20180827	15	24	6:00	23:59
20130823	3	9	18:00	23:59	20160701	3	18	14:00	22:00	20180828	16	39	7:00	23:59
20130825	9	22	15:00	23:59	20160702	1	8	8:00	19:00	20180830	12	32	12:00	20:00
20130826	32	77	6:00	23:59	20160708	0	1	15:00	19:00	20180831	0	14	10:00	23:00
20140601	9	29	11:00	23:59	20160709	2	3	17:00	23:59	20190615	0	0	13:00	23:00
20140616	4	13	13:00	23:00	20160717	11	31	12:00	23:59	20190616	20	6	11:00	23:59
20140619	0	5	15:00	23:59	20160718	21	54	8:00	23:59	20190622	0	0	17:00	23:59
20140620	7	15	13:00	23:00	20160719	29	57	9:00	22:00	20190623	0	0	16:00	23:59
20140621	5	23	12:00	23:59	20160720	9	18	14:00	23:59	20190626	8	1	16:00	23:59
20140624	28	57	15:00	23:59	20160723	1	2	18:00	23:00	20190627	9	2	16:00	23:59
20140626	22	48	12:00	23:59	20160724	3	6	11:00	23:59	20190628	10	6	18:00	23:59
20140627	11	37	11:00	23:59	20160729	8	11	15:00	23:59	20190701	0	0	19:00	23:59
20140702	4	12	18:00	23:59	20160730	5	13	19:00	23:59	20190702	28	70	9:00	23:59
20140704	5	20	19:00	23:59	20160731	6	16	14:00	23:00	20190703	12	37	14:00	23:59
20140705	23	47	8:00	23:59	20160805	3	10	16:00	23:59	20190708	1	4	17:00	23:59
20140706	11	24	11:00	23:59	20160819	21	54	13:00	23:59	20190717	6	11	16:00	23:59
20140707	8	17	10:00	23:59	20160823	3	12	16:00	23:59	20190720	2	4	12:00	23:59
20140708	5	6	12:00	23:59	20160824	5	9	17:00	23:59	20190722	17	38	10:00	23:59
20140710	10	27	13:00	23:59	20160825	14	33	17:00	23:59	20190727	3	16	9:00	23:59
20140711	2	6	19:00	23:59	20170602	25	54	8:00	23:59	20190728	25	53	10:00	23:00
20140712	2	7	14:00	23:59	20170603	11	20	13:00	23:59	20190729	8	23	17:00	23:59
20140713	4	15	14:00	22:00	20170611	1	6	15:00	23:59	20190802	3	10	18:00	23:59
20140714	12	17	15:00	23:59	20170612	6	37	7:00	23:59	20190803	2	6	18:00	23:59
20140720	1	4	19:00	23:59	20170613	4	12	15:00	23:00	20190804	12	22	12:00	23:59
20140726	1	1	16:00	23:59	20170705	1	6	14:00	23:59	20190805	10	40	8:00	23:59
20140804	4	10	17:00	23:59	20170706	6	18	15:00	23:59	20190806	13	31	9:00	23:00
20140805	7	11	16:00	23:59	20170707	10	24	9:00	23:59	20190807	0	5	8:00	20:00
20140806	6	15	7:00	23:59	20170708	7	22	10:00	23:59	20190808	4	6	20:00	23:59
20140809	9	21	16:00	23:59	20170711	6	23	14:00	23:59	20190816	15	42	8:00	23:59
20140810	16	37	13:00	23:59	20170712	23	52	5:00	23:59	20190817	9	17	4:00	23:59
20140815	13	30	6:00	23:59	20170713	6	15	8:00	23:59	20190818	10	19	12:00	23:59
20140816	6	13	16:00	23:59	20170714	4	22	16:00	23:59	20190819	12	25	14:00	23:59
20140818	8	22	13:00	23:59	20170719	7	22	9:00	23:59	20190820	31	51	7:00	23:00
20140820	13	28	16:00	23:00	20170720	5	10	18:00	23:59	20190821	11	19	14:00	23:59
20150611	1	9	9:00	23:59	20170721	9	14	10:00	23:59	20190822	11	35	9:00	23:59
20150612	13	61	6:00	23:59	20170726	3	12	16:00	23:59	20190823	25	65	6:00	23:00
20150619	7	18	15:00	23:59	20170801	3	8	10:00	23:00	20190826	0	1	8:00	14:00
20150620	9	16	14:00	23:59	20170805	29	73	10:00	21:00	20190827	9	19	17:00	23:59
20150625	7	19	14:00	23:59	20170810	13	31	14:00	23:59	20190829	11	27	8:00	23:59
20150626	13	36	7:00	23:59	20170811	8	18	15:00	23:59	20190830	7	27	10:00	23:59
20150627	4	19	16:00	23:59	20170815	4	19	12:00	22:00	20190831	11	26	8:00	23:59
20150629	10	17	12:00	23:59	20170820	6	13	17:00	22:00	20200601	4	4	19:00	23:59
20150701	18	32	14:00	20:00	20170821	4	20	9:00	23:59	20200603	11	32	15:00	23:59
20150703	2	6	18:00	23:59	20170822	2	8	16:00	23:59	20200604	3	5	17:00	23:59
20150704	16	47	7:00	23:59	20180609	13	35	16:00	23:59	20200605	0	0	17:00	23:59

Case day	radar DCCs	spatial DCCs	Start Time	End Time	Case day	radar DCCs	spatial DCCs	Start Time	End Time	Case day	radar DCCs	spatial DCCs	Start Time	End Time
20200614	1	3	20:00	23:59	20200829	1	3	20:00	23:59	20210727	2	5	20:00	23:59
20200615	2	2	8:00	23:59	20200830	8	18	11:00	23:59	20210730	6	12	18:00	23:59
20200616	2	2	17:00	23:00	20200831	0	4	14:00	23:59	20210731	13	25	15:00	23:59
20200619	9	13	12:00	23:59	20210602	7	13	16:00	23:59	20210801	18	33	7:00	23:59
20200621	29	54	12:00	23:59	20210620	20	39	11:00	23:59	20210806	18	35	11:00	23:59
20200628	1	3	12:00	18:00	20210621	9	25	12:00	23:59	20210807	4	12	12:00	23:59
20200707	8	22	9:00	23:59	20210623	5	8	13:00	23:59	20210808	4	9	7:00	23:59
20200718	9	31	10:00	23:59	20210624	12	21	12:00	23:59	20210810	4	16	13:00	23:59
20200719	11	22	12:00	23:59	20210625	8	23	14:00	23:59	20210811	3	9	17:00	23:59
20200722	13	38	0:00	23:59	20210626	6	11	16:00	23:59	20210812	8	23	8:00	23:59
20200723	0	2	12:00	23:59	20210627	26	62	13:00	23:59	20210813	26	52	5:00	23:59
20200728	30	48	12:00	23:59	20210629	46	101	0:00	23:59	20210815	10	29	13:00	23:59
20200729	15	28	14:00	23:59	20210630	18	35	5:00	23:59	20210817	6	26	7:00	23:59
20200807	1	1	14:00	23:59	20210705	27	65	5:00	23:59	20210818	31	58	9:00	23:59
20200808	3	16	12:00	23:59	20210710	4	21	8:00	23:59	20210819	9	26	8:00	23:59
20200809	13	35	8:00	23:59	20210714	16	37	8:00	23:59	20210825	6	14	15:00	23:59
20200812	0	2	12:00	23:59	20210715	15	31	6:00	23:59	20210826	21	49	10:00	23:59
20200821	15	28	6:00	23:59	20210716	7	21	13:00	23:59	20210827	1	6	2:00	23:59
20200822	10	18	14:00	23:59	20210718	6	16	16:00	23:59	20210828	23	68	0:00	23:59
20200823	4	12	15:00	23:59	20210719	17	39	8:00	23:59	20210829	7	14	0:00	15:00
20200828	19	45	8:00	23:59	20210722	12	37	12:00	23:59	20210831	2	12	18:00	23:59

Table 3.1: Table of case days (in YYYYMMDD) with number of identified DCCs for both the radar and spatial datasets and start/end times of MCIT in UTC.

3.2 Radar data

3.2.1 KHGX WSR-88D

KHGX is the remote-sensing radar that was used in this study to sample the DCCs. The microphysical structure and temporal evolution was determined using Z, Z_{DR}, and ρ_{HV}. KHGX was upgraded to dual-polarization in early 2013, which hence marks the earliest period for which the data can be used. The radar is located in Galveston County, TX with an elevation of 35 m and provides radar coverage of the entire south-east Texas region and north-western regions of the Gulf Coast. The WSR-88D volume coverage patterns (VCPs) utilized in this study are from various precipitation modes (VCP 11, 21, 211, 121, 212, & 12) and clear air modes (VCP 32 & 35) (Council et al., 2002). KHGX operates using the typical NEXRAD wavelength, scanning strategies, transmit power, pulse-repetition frequencies, and dual-polarization calibration (Council et al., 2002).

Utilization of a WSR-88D to measure impacts of the AIE on DCCs provides advantages and disadvantages. Advantages include a large sample size of individual DCCs

as the radar is always scanning and covers a large spatial area. Further, KHGX's dual-polarization capability is a necessity when retrieving microphysical measurements. The S-band frequency also provides essentially attenuation-free measurements whereas attenuation through rain is more significant at higher frequencies. However, as the radar wavelength increases, the sensitivity to smaller hydrometeors is decreased due to the Rayleigh scattering regime at which weather radars operate (White et al., 2000), which can then affect the quality of the microphysical retrievals. The largest disadvantage of an operational WSR-88D compared to the smaller mobile radars or other research-focused radars that are typically used in field campaigns is the inability to use range-height-indicator (RHI) scans that offer much better vertical coverage and resolution. Instead, the VCPs used only perform planned-position-indicator (PPI) scans that increasingly under-sample the atmosphere at higher elevation angles and, in turn, provide quite poor vertical resolution/coverage (e.g., Figure 3.2a). Additionally, these PPIs yield volumetric update times of $4 - 7$ minutes which does not always provide enough temporal resolution to observe the quick evolution of DCCs that may occur due to the AIE (Oue et al., 2022). Volumetric update times when using PPI scans can also cause problems with constructing vertical profiles as DCCs can move significantly between adjacent elevation angles, inhibiting the ability to coherently document features such as Z_{DR}-columns (Snyder et al., 2015). The sub-optimal resolution of reconstructed vertical profiles from KHGX is the main reason why the maximum domain for DCC tracking was set at 80 km for the radar data analysis so that DCCs could be sampled by least 7 elevation angles in the vertical, depending on the VCP (Figure 3.2b).

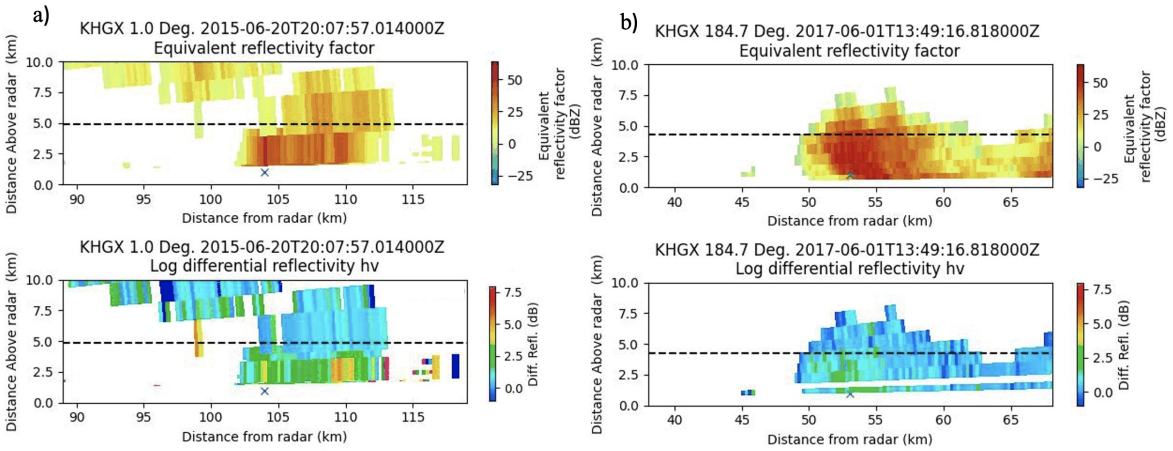

Figure 3.2: Reconstructed RHIs of Z (top panels) and Z_{DR} (bottom panels) using VCP 212 from (a) 105 km away and (b) 53 km away from KHGX on June 20, 2015 and June 1, 2017, respectively.

3.2.2 The MCIT algorithm

The Multi-Cell Identification and Tracking algorithm (MCIT) was originally described in Hu et al. (2019b) and has been further developed at the National Severe Storms Laboratory (NSSL) and Cooperative Institute for Severe and High-Impact Weather Research and Operations (CIWRO); it has also been implemented in the private sector (Cao et al., 2021). This algorithm has been shown to improve tracking capabilities compared to centroid or cross-correlation strategies and is able to handle merging and splitting of convective cells more accurately (Cao et al., 2021).

MCIT uses three main steps to output an objective dataset of identified individual DCCs tracked in time and space as summarized here and discussed in more detail by Hu et al. (2019b). The first step involves data input and pre-processing of raw level two radar data. Then, for each volumetric scan of the radar, reflectivity is interpolated to a 3D Cartesian field, from which vertically integrated liquid (VIL) is calculated in each horizontal grid space. Additional smoothing techniques are used to calculate locations of watershed-lines from a watershed algorithm (Meyer, 1994) which will provide the

basis for step two. Step two consists of using the VIL to calculate watershed imaging and boundaries. Multiple cell tracking and identification is done in step three by merging watershed segments into clusters depending on neighbor and saddle criteria. Neighbor criteria decides whether or not to merge identified DCCs based on their proximity to other DCCs. Saddle criteria defines the minimum threshold of VIL valleys in which neighboring DCCs are merged into one. The neighbor and saddle criteria are set by adjusting parameters such as the minimum valley depth of VIL, minimum cell size, and minimum cell strength. Merging and splitting processes are handled based on these thresholds, so that the time and space location of individual cells is output on the per volume update time of the radar. Due to the large computational time required by the algorithm, sensitivity tests for changing the neighbor criteria, saddle criteria, and grid spacing were not conducted. While uncertainties due to this are difficult to quantify, this omission may only have a minimal impact on overall conclusions since most ordinary single-cell DCCs investigated here are not merging or connected together like mesoscale convective or multi-cell systems are where the choice of these criteria has a greater impact on results. The neighbor and saddle criteria used were as follows: minimum valley depth = 2 kg/m^2, minimum cell size = 50 km^2, and minimum cell strength = 5 kg/m^2 while grid spacing was 1 km in both the zonal and meridional directions. Figure 3.3 shows an example of MCIT output from July 4, 2017 along with the domains of the radar and spatial datasets around KHGX. MCIT provides an objective way of tracking the many DCCs observed near Houston and allows for the creation of a large database containing the individual DCCs along with their centroid locations, timeseries, and areal boundaries.

Further processing was conducted to ensure spurious identification of cells was minimized. Requirements for a DCC to be used in the analysis are that it exists for at

least 6 MCIT timesteps (about 30 minutes) and that it is within ranges described by section 3.2.3 (Figure 3.3) for its entire lifetime.

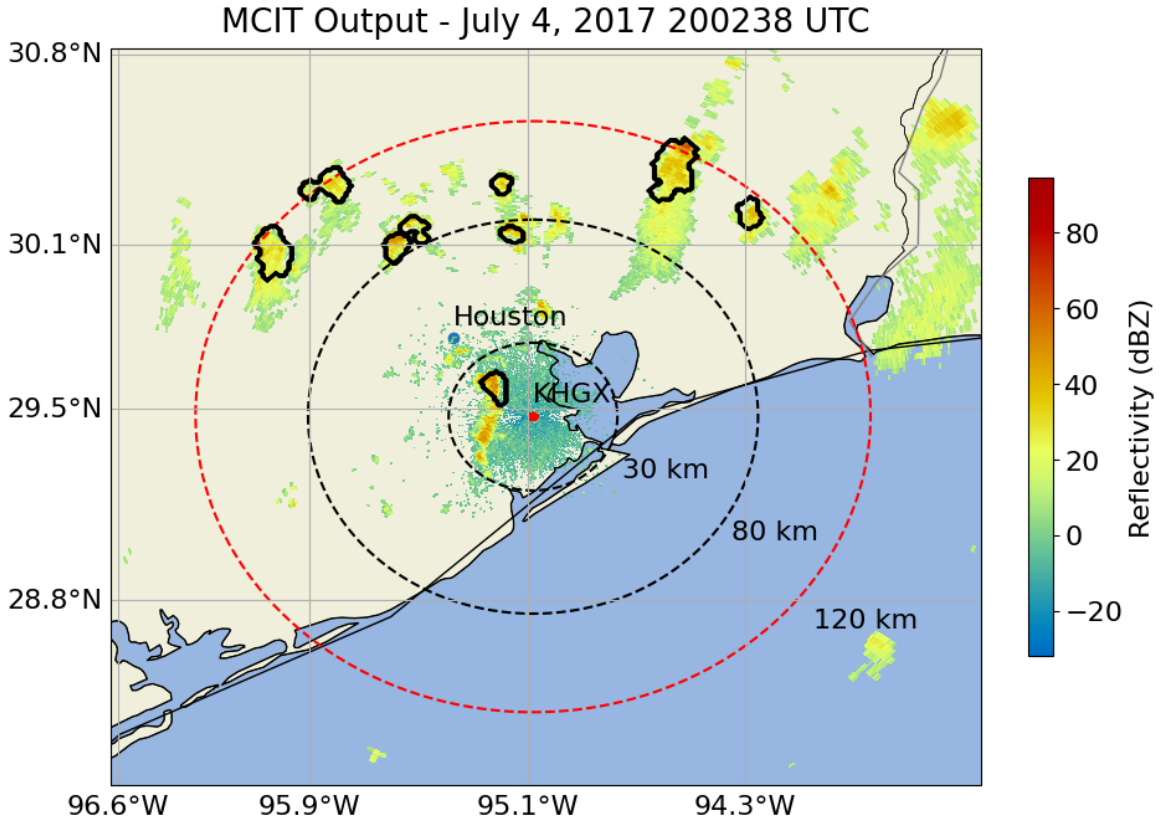

Figure 3.3: Map of the Houston area showing MCIT cell boundaries (black solid lines) with overlaid reflectivity (colored pixels) from the 6.4 degree elevation angle on July 4, 2017 at 200238 UTC. The black dotted circles indicate the upper and lower bounds for the domain of the radar dataset while the red dotted circle indicates the upper bound for the domain of the spatial dataset.

3.2.3 Treatment of radar data

Two separate datasets were created to analyze different properties of DCCs under differing $PM_{2.5}$ mass concentrations, radar and spatial. Instead of constraining the identified DCCs by the MCIT to be between 30 – 80 km of KHGX as done for the radar dataset, the spatial dataset includes all DCCs up to the 120 km range ring of KHGX.

This yields a substantially larger number of cells, 5830 compared to 2412 for the radar dataset. However, only the MCIT output, meteorological data, and aerosol data are used for the 5830 DCCs because the radar data at different altitudes are not available in sufficient vertical resolution past 80 km (Figure 3.2) or the entire vertical profile of DCCs is not always attainable at distances < 30 km from KHGX, depending on the VCP. Therefore, the spatial dataset is used to understand other properties of DCCs around Houston such as their lifetime, diurnal variability, and geospatial distribution, which are presented in section 4.1. Figure 3.3 illustrates the two domains respective to KHGX.

Appropriate analysis of the radar data is essential, with the details of the methodology discussed in the remainder of this section. Only radar gates with $\rho_{HV} \geq 0.8$ and $Z \geq -10$ dBZ were analyzed to ensure that they likely represented a weather echo, and MCIT provided the horizontal boundaries for each DCC.

CFADs are used to visualize the vertical variability of normalized histograms of radar returns but do not provide information on horizontal variability or distribution (Yuter and Houze Jr, 1995). Herein, "aggregate" CFADs are presented where radar data from all DCCs in each subset (e.g., all DCCs over land) are used to calculate the normalized histogram at each altitude, an example of which is shown in Figure 3.4a. The y-axis is the altitude relative to the freezing level, which is determined by the ERA5 reanalysis (Hersbach et al., 2020), in order to isolate aerosol invigoration that typically occurs at and above the freezing level. Bins of 0.5 km are used in the vertical. For CFADs of Z, the x-axis is binned every 2 dBZ; for CFADs of Z_{DR}, the x-axis is binned every 0.25 dB. One inherent problem to note of CFADs is that the normalized frequencies can become inflated at high altitudes where there may be fewer observations. Lastly, the composite difference of two aggregate CFADs allows for a direct comparison of the probability of specific radar values occurring at given

altitudes. In this study, the CFAD composite difference will typically be between the aggregate CFADs of DCCs with high (or an anthropogenic aerosol regime) and low $PM_{2.5}$ mass concentration (or a natural aerosol regime) (discussion regarding definition of high and low $PM_{2.5}$ and anthropogenic vs. natural aerosol regime is in section 3.4.3), unless otherwise stated.

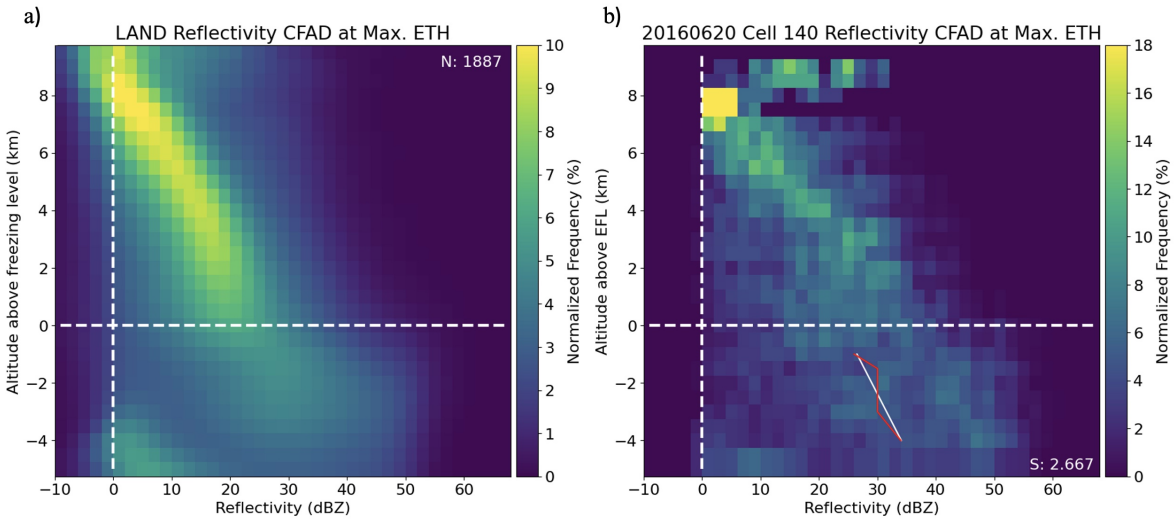

Figure 3.4: Reflectivity CFADs for (a) all cells over land (N = 1887) and (b) Cell 140 on June 20, 2016 at the time of maximum ETH achieved by the DCCs. In (b), the red line refers to the median values of reflectivity at each altitude bin between -1 and -4 km and the white line is the best fit for those points, yielding a ΔZ of 2.667 dBZ/km. The same calculation for ΔZ_{DR} can be done using a Z_{DR} CFAD.

Kumjian et al. (2022) describe the meaning of the parameter space given by the vertical gradients of Z and Z_{DR} below the freezing level (ΔZ & ΔZ_{DR}, respectively) and associates regions of the parameter space with important microphysical processes that occur with liquid precipitation (Figure 3.5). The ΔZ and ΔZ_{DR} for this study were calculated for each individual DCC by first determining the median of the normalized histogram at each altitude bin for -1 km $\leq z \leq$ -4 km. This altitude range is used to ensure only data from liquid precipitation are used, that changes due to melting precipitation are not included, and to reduce unrealistic values from sparse datasets

at altitudes below -4 km. A linear best fit is applied to the median values of radar data at each altitude bin which yields a slope of km/dBZ (or km/dB) which is shown in Figure 3.4b. The reciprocal of this slope gives a slope of dBZ/km (or dB/km) and is then multiplied by -1 so that a positive gradient indicates an increase towards the ground, as defined by Kumjian et al. (2022).

The top left quadrant in Figure 3.5 is known as the size sorting quadrant and is associated with $\Delta Z < 0$ and $\Delta Z_{DR} > 0$. Size sorting often occurs when updrafts are able to keep drops with smaller sizes from falling as fast as larger ones, so larger drops are typically found closer to the ground in smaller concentrations where smaller ones are lofted higher in altitude in larger concentrations. This necessitates that $\Delta Z_{DR} > 0$ because the mean drop diameter increases toward the ground and that $\Delta Z < 0$ because concentrations of drops become smaller. The evaporation regime also exists in the top left quadrant, as it can produce the same fingerprint as size sorting because the smallest drops will evaporate first, which increases the mean-mass diameter and leaves only the largest ones to fall closer to the ground. Kumjian et al. (2022) explain however that typically this regime does not produce as large of a magnitude of ΔZ and ΔZ_{DR} as size sorting, hence why evaporation occurs closer to the origin. The top right and bottom left quadrants are both types of warm rain processes that can sometimes occur simultaneously, producing the balance regime seen in purple text in Figure 3.5. Collision-coalescence produces $\Delta Z > 0$ and $\Delta Z_{DR} > 0$ because smaller drops collide and produce larger drops as they fall, which keeps the amount of liquid mass in the sampling volume constant while increasing mean drop diameter, increasing Z_{DR}. This also increases Z toward the ground since the concentrations of large drops increase toward the ground, which, given that $Z \sim D^6$ (for spheres in the Rayleigh regime), means $\Delta Z > 0$. Drop breakup produces the opposite of this signature because, as drops break apart during fallout, the mean drop diameter will decrease, yielding both

a decrease in Z and Z_{DR} toward the ground. In this study, the 2D space given by ΔZ and ΔZ_{DR} is used in conjunction with the CFADs to supplement information regarding microphysical signatures of the DCCs.

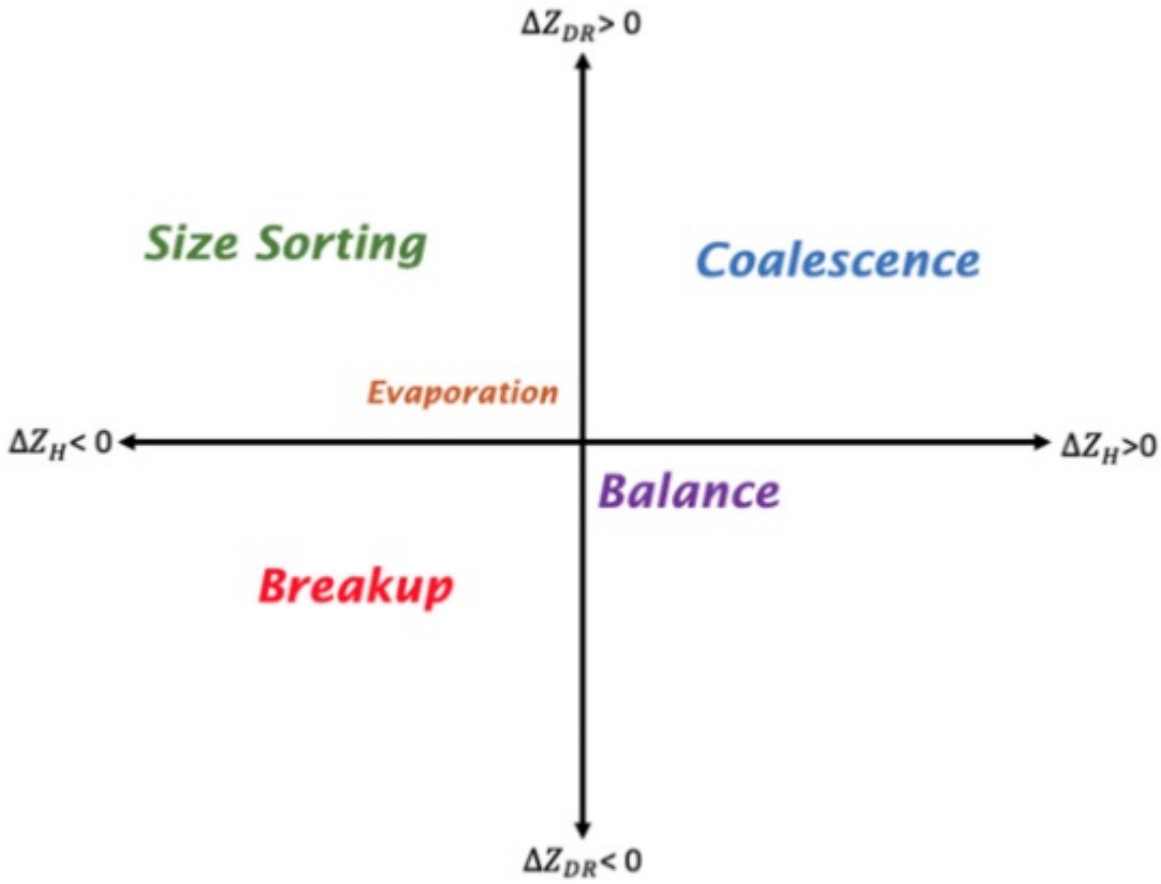

Figure 3.5: The parameter space of ΔZ and ΔZ_{DR} with important microphysical processes in liquid precipitation inferred from signs of ΔZ and ΔZ_{DR} (colored text). Taken from Kumjian et al. (2022).

Due to the potential impact that the AIE has on the temporal evolution of DCCs and to ensure consistent analysis, the life cycle of each DCC is assessed. As discussed by Kumjian (2013), Kumjian et al. (2014), and Snyder et al. (2015), Z_{DR}-columns can be used to approximate updraft intensity and thus stages of cell life cycle. In brief, Z_{DR}-columns are columnar fields of enhanced Z_{DR} (e.g., $Z_{DR} > 1$ dB) that extend above

the freezing level within DCC updrafts. Values above 1 dB usually indicate presence of liquid within the first few kilometers above the freezing level and are attributed to the presence of supercooled drops, wet hail, and wet graupel (Conway and Zrnić, 1993; Hall et al., 1984; Ryzhkov et al., 1994; Shupyatsky et al., 1990). Z_{DR}-column depth calculations are ideally used to approximate updraft intensity because their formation, width, and depth have been shown to be affected by important microphysical processes such as size sorting (Bringi et al., 1997) and warm rain onset (Tuttle et al., 1989), both of which are affected by the AIE (Ilotoviz et al., 2018). Unfortunately, due to time constraints and the inability to use a Z_{DR}-column calculation algorithm provided by NSSL on the University of Oklahoma's Supercomputing Center for Education and Research (OSCER) supercomputer, Z_{DR}-columns are not used to approximate updraft strength.

Instead, a less microphysically-sensitive approximation known as the echo top height (ETH) is used for quantifying updraft intensity. ETHs have been used ever since weather radars were deployed (e.g., Evans et al., 2004; Held, 1978, among others) and are used frequently today in operational settings such as in the NEXRAD network. Typically, ETH is computed by retrieving the highest elevation scan in which at least an 18 dBZ echo is returned (Donaldson Jr, 1964). The height of each range gate within that elevation is then calculated using a 4/3 earth model to account for standard atmospheric refraction of the radar beam (Doviak et al., 1994), and the half-power beamwidth above the nominal elevation angle is used to account for the vertical extent of the beam. However, Lakshmanan et al. (2013) proposed a slight change in methodology for calculating ETH since the standard method can produce over- and underestimates. This change was simply to interpolate the ETH based upon the elevation scans that bracket the threshold of 18 dBZ and is the technique used in this study.

3.3 Meteorological dataset

The meteorological fields were supplied by the ECMWF Reanalysis v5 (ERA5) reanalysis model which uses a 30 km x 30 km grid, 137 vertical pressure levels, and hourly temporal output (Hersbach et al., 2020). Variables were chosen based on relevance to DCC initiation, dynamics, and microphysics and are shown in Table 3.2. These variables are collected to separate meteorological effects from aerosol effects and to test the hypotheses that the strength of AIE is dependent on free-tropospheric humidity, instability, and shear. Figure 3.6 shows the grid of the ERA5 within the domain of this study to illustrate the spatial resolution of the model in this context.

The ERA5 reliability in representing relevant atmospheric conditions for DCCs was investigated by Rodríguez and Bech (2021), who analyzed the viability of using ERA5 for retrieving MUCAPE values compared to observational soundings. They found a lack of statistically significant differences between vertical profiles of the nearest spatio-temporal grid points of the model to a DCC compared to a proximity-inflow method where observed soundings were taken at slightly further ranges and several hours earlier. This supports the use of the nearest spatio-temporal grid point to each DCC for retrieving the meteorological variables used here. In addition, Hersbach et al. (2020) notes the possibility of unrealistically large values of MUCAPE that can occur, but this was not seen in the current study based on Figure 3.7, which shows that the highest mean MUCAPE values for DCCs were near 5500 J/kg and are not unrealistically large for this region and time period.

Correlation analysis is used to understand how the strength of updrafts (i.e., ETHs) are correlated with the many meteorological variables used from the ERA5. However, the ERA5 grid boxes are very large in area compared to the spatial scale of individual

Variable	**Pressure Levels (mb)**
Relative humidity (rh)	1000,975,950,925,900,875,850,825,800,775,750,700,650,600,550,500,450,400
Dew point (DEW)	Surface
Precipitable water (PW)	Column
Geopotential height (GH)	1000,975,950,925,900,875,850,825,800,775,750,700,650,600,550,500,450,400
Temperature (T)	Surface
Divergence (D)	1000,975,950,925,900,875,850,825,800,775,750,700,650,600,550,500,450,400
U-wind (u), V-wind (v)	1000,975,950,925,900,875,850,825,800,775,750,700,650,600,550,500,450,400
Omega (ω)	1000,975,950,925,900,875,850,825,800,775,750,700,650,600,550,500,450,400
Relative vorticity (ζ)	1000,975,950,925,900,875,850,825,800,775,750,700,650,600,550,500,450,400
Magnitude of shear (sh)	1000,975,950,925,900,875,850,825,800,775,750,700,650,600,550,500,450,400
Surface pressure (SP)	Surface
Boundary layer height (BLH)	Column
Most-unstable CAPE (MUCAPE)	Column
Surface-based CIN (CIN)	Column
Freezing level height (EFL)	Column

Table 3.2: Table of ERA5 meteorological variables sampled near DCCs and associated pressure levels.

DCCs, and further the temporal output of ERA5 is every hour whereas the DCCs are tracked every 4 – 7 minutes. Large discrepancies in both the time and space scales increase the probability of low correlations between ETHs and the meteorological variables, which is evident throughout the correlation analyses presented in Figure 3.8. To reduce some of the impact of the spatio-temporal scale differences, daily means were calculated for both ETHs and the meteorological profiles of the individual DCCs for correlation analysis. This allowed for a more consistent correlation analysis between the meteorological variables and the ETHs as discussed in chapter 4. However, this method is complicated by the diurnal variability that exists in DCCs. Thus, if a given case day is dominated by morning convection, the ETHs may very well be lower than a day dominated by afternoon convection where diurnally driven instability may

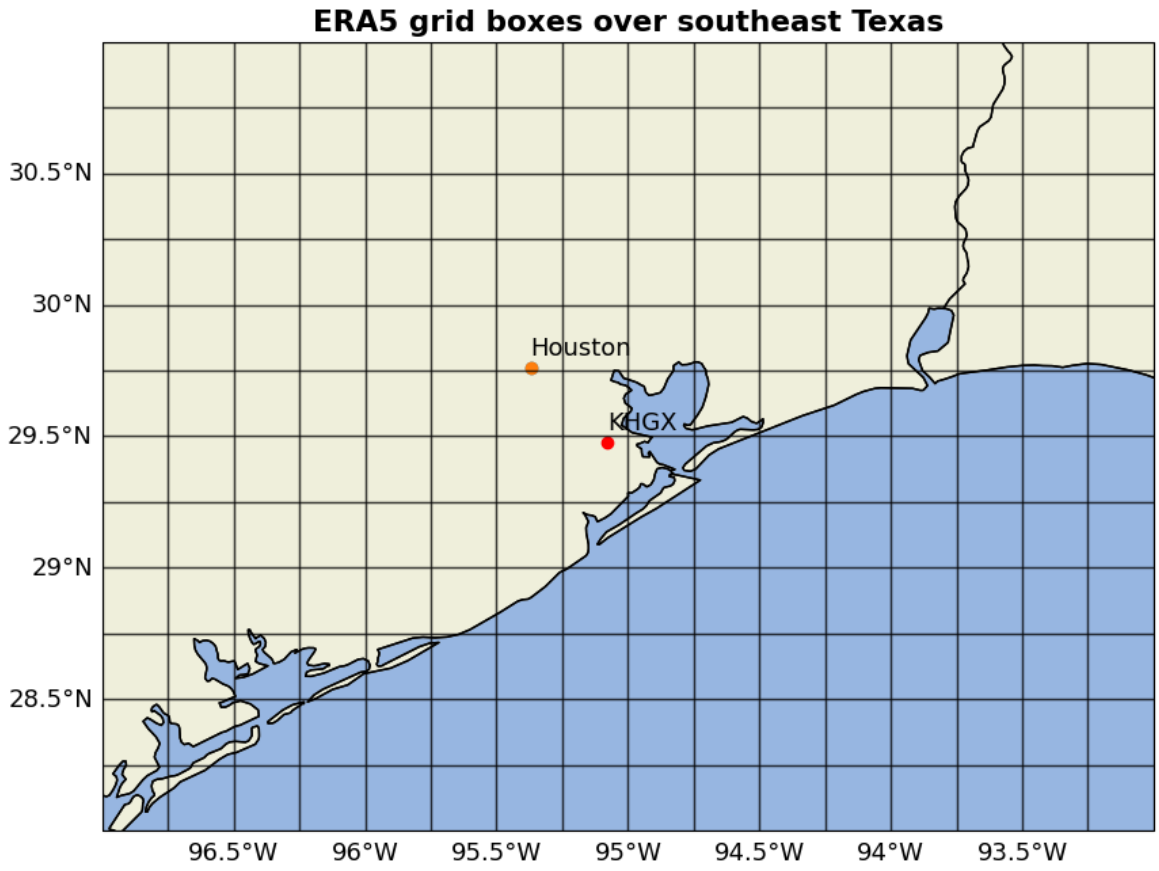

Figure 3.6: Map of southeastern Texas with ERA5 grid boxes (solid black squares) overlaid.

promote stronger updrafts. It is important to consider these caveats when interpreting the calculated correlations.

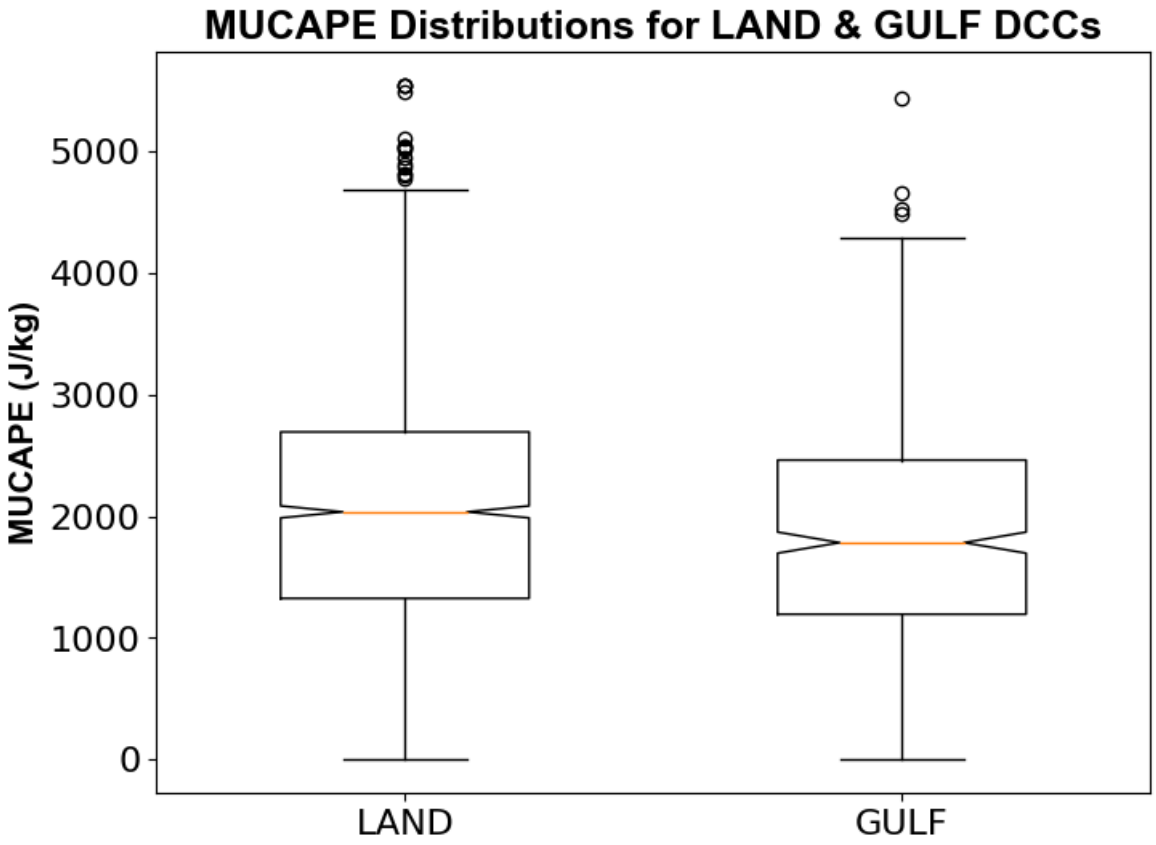

Figure 3.7: Box and whisker plots of every DCC's median MUCAPE (J/kg) value for LAND and GULF locations sampled using the nearest spatio-temporal grid point from the ERA5 reanalysis.

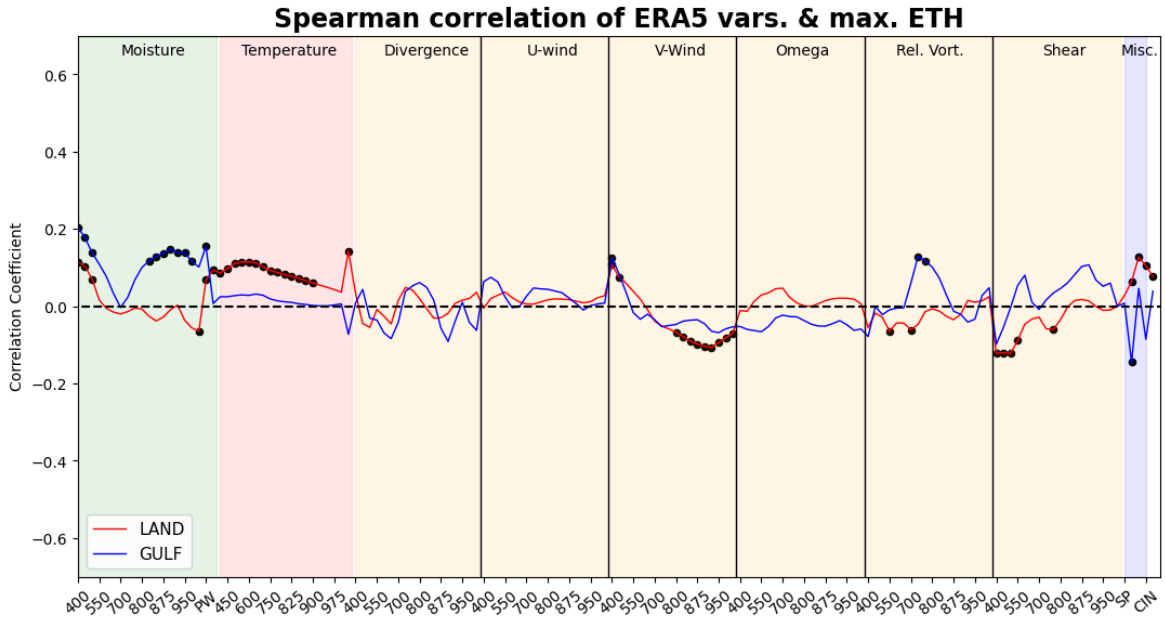

Figure 3.8: Spearman correlation values for every ERA5 meteorological variable and maximum DCC ETH for cells over LAND (N = 1887) and GULF (N = 525). Black dots indicate the 95% confidence level using the t-statistic. Correlations are calculated by taking the mean of the meteorological variable time series before time of maximum ETH and correlating it with the maximum ETH for each DCC. The x-axis is labeled left to right with ERA5 pressure levels of the respective variable in ascending pressure order except where stated. Colored regions represent different categories of meteorological data. The Misc. (blue) section includes: surface pressure (SP), boundary layer height (BLH), MUCAPE, CIN, and freezing level height in order from left to right. This correlation diagram used the radar DCC dataset.

3.4 Aerosol dataset

3.4.1 MERRA-2

The Modern-Era Retrospective analysis for Research and Applications, Version-2 (MERRA-2) reanalysis model is used for sampling the $PM_{2.5}$ mass concentration in the vicinity of the DCCs. The MERRA-2 uses a resolution of $0.625^{\circ}\times0.5^{\circ}$ and includes hourly data. Randles et al. (2017) discusses MERRA-2 aerosol assimilation techniques used to calculate mass concentrations of certain aerosol species and describes the calculation of the $PM_{2.5}$ mass concentration as:

$$PM_{2.5} = DU25 + OC + BC + SS25 + SO4(132.14/96.06), \tag{3.1}$$

where DU25 is dust, OC is organic carbon, BC is black carbon, SS25 is sea salt, and SO4 is sulfate. Dust and sea salt size distributions are explicitly resolved using five size bins that do not allow for growth or shrinking of particles and there is consideration of wind driven emissions. Emissions of dust are based on a map of potential dust sources such as deserts, and particles are sorted into size bins using methods from Marticorena and Bergametti (1995). Sea salt is parameterized from a size dependent number flux (Gong, 2003) with additional wind and sea-surface temperature correction terms. Other aerosols, such as sulfate and organic carbon, are also emitted by volcanic events, secondary processes such as terpene (Chin et al., 2002) and di-methyl sulfide reactions, and biomass burning. Anthropogenic emissions of sulfate, black carbon, and sulfur dioxide are all based on patterns from the Emissions Database for Global Atmospheric Research (EDGAR) and AeroCom Phase II (Diehl et al., 2012) datasets from 2006 and 2008, respectively. It is worth noting that MERRA-2 tends to overestimate sea-salt mass concentrations in coastal regions because of data assimilation bias if there

is an initial underestimation of AOD in polluted episodes. However, this is not a large concern for this study as discussed further in section 3.4.3.

3.4.2 TCEQ sites

The Texas Center for Environmental Quality (TCEQ) air quality sites provide observed hourly mean $PM_{2.5}$ mass concentration observations across the state of Texas. Air quality sites that were recording $PM_{2.5}$ mass concentration at any time in the months of June, July, and August in the years 2013-2021 in the southeast Texas region were used to compare against the MERRA-2 analysis, not just for case days used for the MCIT. Figure 3.9 shows the location of these sites around southeast Texas with the MERRA-2 grid boxes overlaid, illustrating the spatial heterogeneity of the sites compared to the model grid boxes. This inhibits the ability to use techniques involving objective analysis of TCEQ site observations. Instead, this study uses the TCEQ dataset to statistically compare the MERRA-2 predictions against observations over the southeast Texas region.

3.4.3 Treatment of aerosol data

For this study that relies on model derived $PM_{2.5}$ mass concentration, it is pivotal that the MERRA-2 $PM_{2.5}$ dataset be understood in terms of its ability to capture the general evolution of the $PM_{2.5}$ mass concentration in the southeast Texas region. This section presents findings from differing correlation analysis techniques to evaluate the validity of the MERRA-2 reanalysis. Data from all TCEQ sites are used for the analysis with the closest spatio-temporal grid point of the MERRA-2 compared to each site's observation (Figure 3.9).

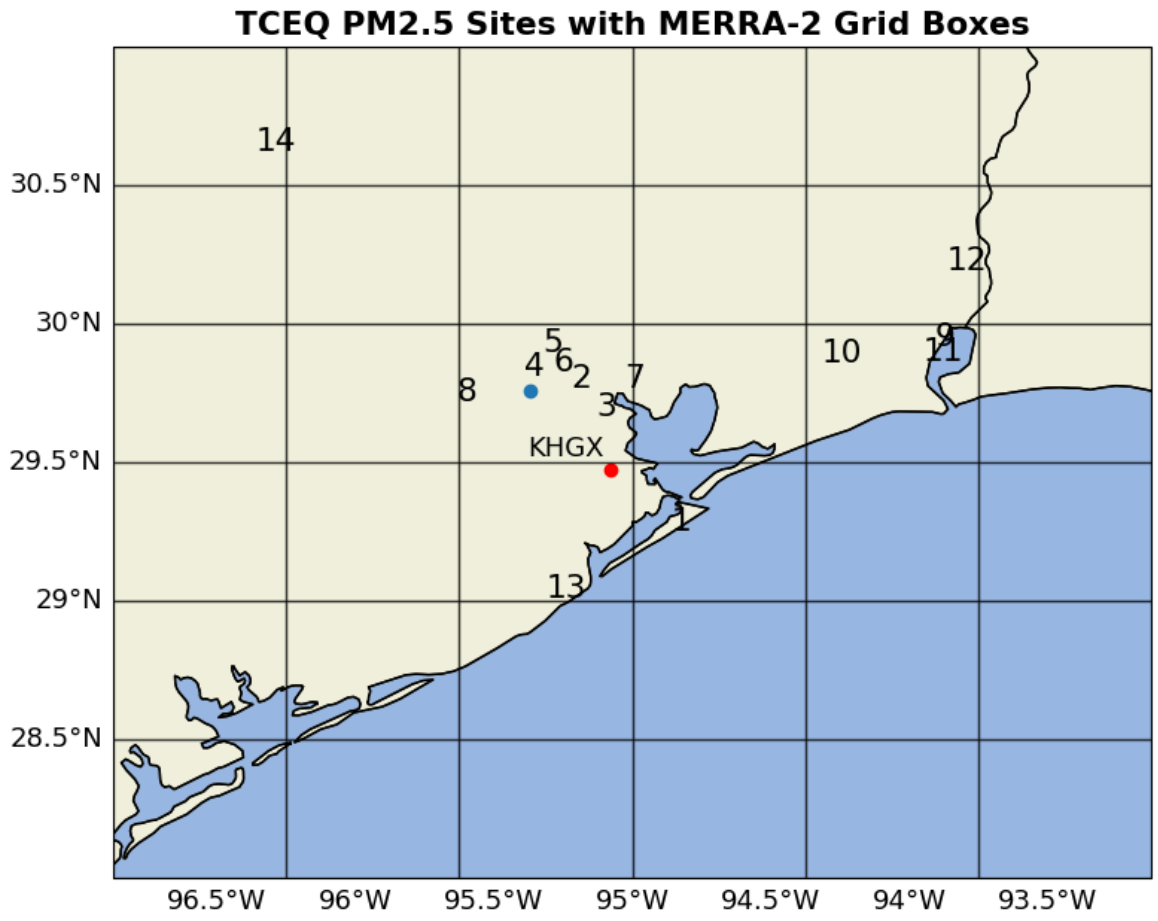

Figure 3.9: Map showing MERRA-2 grid boxes (solid black squares) over southeast Texas with locations of TCEQ sites, numbered 1 - 14. Blue dot shows location of Houston.

Mean daily autocorrelations were calculated for both datasets so that the hourly variability can be quantified and compared. Figure 3.10a shows the mean of all TCEQ sites' lag-1 autocorrelation across all days. These autocorrelations (and correlation techniques hereafter) are calculated by using the lag-1 of the 24-hour time series from 12 AM to 11:59 PM local time each day the respective TCEQ site was recording for. Other than for Site 11 with an autocorrelation of about 0.8, mean lag-1 autocorrelations are generally around $0.4 - 0.5$. This shows that the hour-to-hour variability can be large for the observations of $PM_{2.5}$ which is consistent with the findings of Lance et al. (2009).

Figure 3.10b shows the daily mean lag-1 autocorrelation calculated in the same manner for MERRA-2 predictions, except shown on a contour map. Spatially, the contour plot seems to capture the land/ocean contrast as higher autocorrelations occur over the Gulf of Mexico where more pristine, less variable marine air is prominent. Further, a region of higher autocorrelations onto land can be seen just to the southwest of and extending east of Houston. As discussed in chapter 4, this region of enhanced autocorrelations is co-located with an enhanced probability of DCCs occurring and could be a result of the preferred sea-breeze location. Compared to the TCEQ autocorrelations, the magnitudes of these autocorrelations are larger by about 0.3, quantifying the degree to which MERRA-2 does not capture the hourly variability of the observations. The inability of MERRA-2 to capture the hourly variability well suggests the use of the daily means of MERRA-2 to define high and low aerosol mass concentrations on a daily basis, similar to methodology used by Guo et al. (2016). However, this would remove the ability to quantify differing aerosol loadings diurnally which is an objective of this study. Thus, results must be interpreted in the context of the poorly resolved hourly variability by MERRA-2.

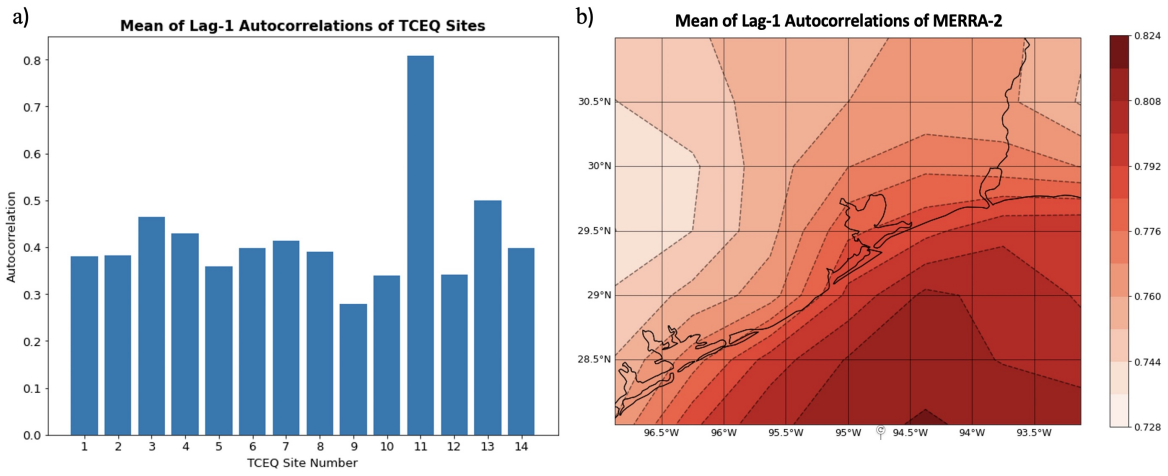

Figure 3.10: Mean of (a) each TCEQ site's and (b) MERRA-2's lag-1 autocorrelation. Autocorrelation was calculated by taking the 24 hour timeseries from 12 AM - 11:59 PM local time for each day and shifting forward by one hour.

The locations of the TCEQ sites (Figure 3.9) are not evenly distributed, but rather many of sites are closest to the same MERRA-2 grid point because they are located in more populated areas such as in Houston and Beaumont. Thus, data from the individual sites may not be completely independent and this may skew the TCEQ $PM_{2.5}$ mass concentration distribution. The TCEQ site correlation matrix shown in Figure 3.11 shows two main groups with elevated values of correlation, sites 2 – 8 and sites 9 – 12. Sites 2 – 8 are located within the Houston metropolitan area and sites 9 – 12 are located in the Beaumont region. This suggests a possibility to resample the TCEQ dataset by taking a mean of each hourly observation of $PM_{2.5}$ mass concentration for the sites in Houston (sites 2-8) and Beaumont (sites 9 - 11). Implementing resampling did not change the shape of the TCEQ $PM_{2.5}$ mass concentration probability density function (PDF) as seen in Figure 3.12, which shows the two PDFs of the original and resampled TCEQ distributions. In general, the MERRA-2 PDFs of $PM_{2.5}$ mass concentration show higher probabilities of larger values occurring compared to TCEQ which is a result of large estimations of dust $PM_{2.5}$ mass concentration by MERRA-2.

This is evident in the summer timeseries by year presented in Figure 3.13 where some of the very large peaks in the MERRA-2 $PM_{2.5}$ mass concentration are coincident with large peaks in the dust $PM_{2.5}$ mass concentration estimated by MERRA-2, meaning that MERRA-2 struggled to appropriately represent the dust constituent. This shows then that the data assimilation bias mentioned earlier regarding sea salt is not a concern for this study. Figure 3.13 shows that the dates of June 11, 2013, June 16, 2014, June 24, 2014, and July 16, 2021 had MERRA-2 overestimating $PM_{2.5}$ mass concentration by 30 $\mu g/m^3$ compared to TCEQ and thus these days were removed from subsequent analysis of radar and spatial datasets.

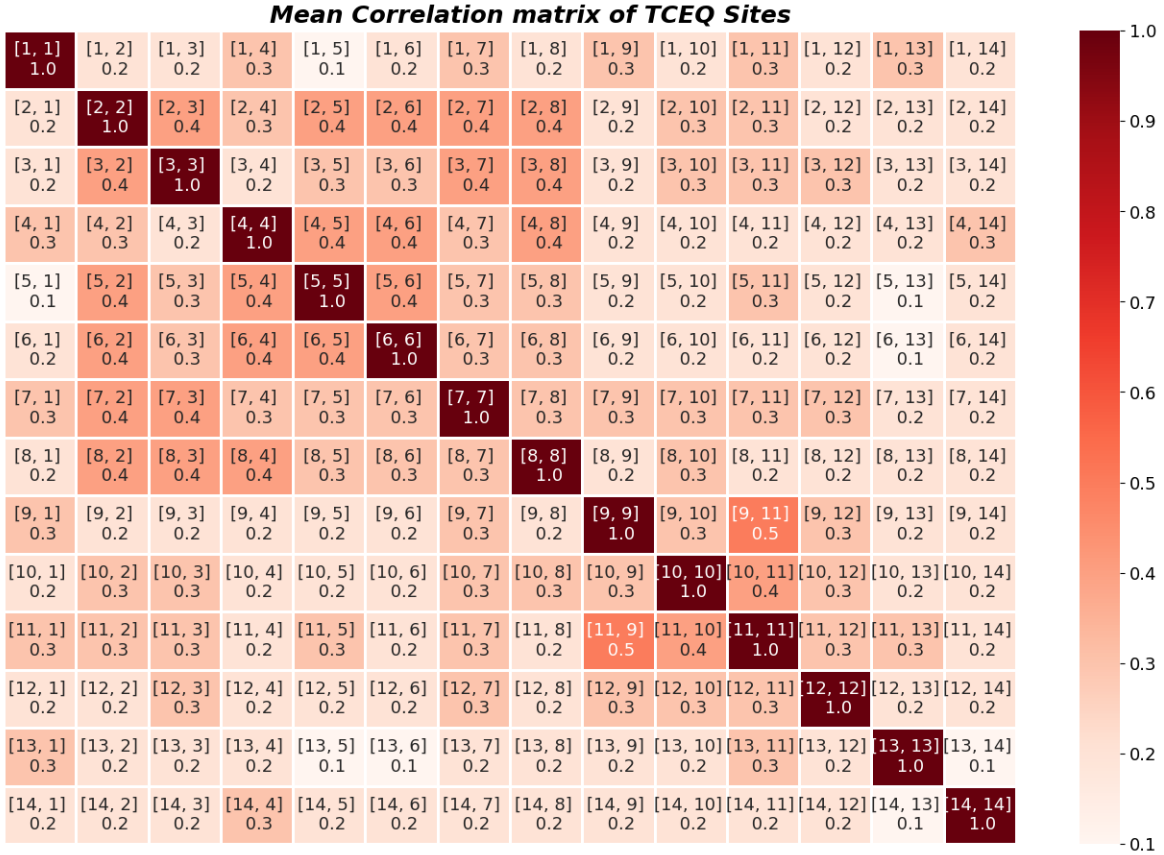

Figure 3.11: Matrix for each TCEQ site's mean correlation calculated using the 24 hour timeseries for each day the respective site was recording for. Number pairs in brackets on the top of each grid box refer to the two sites used for the calculation. Shading refers to value of correlation from the colorbar.

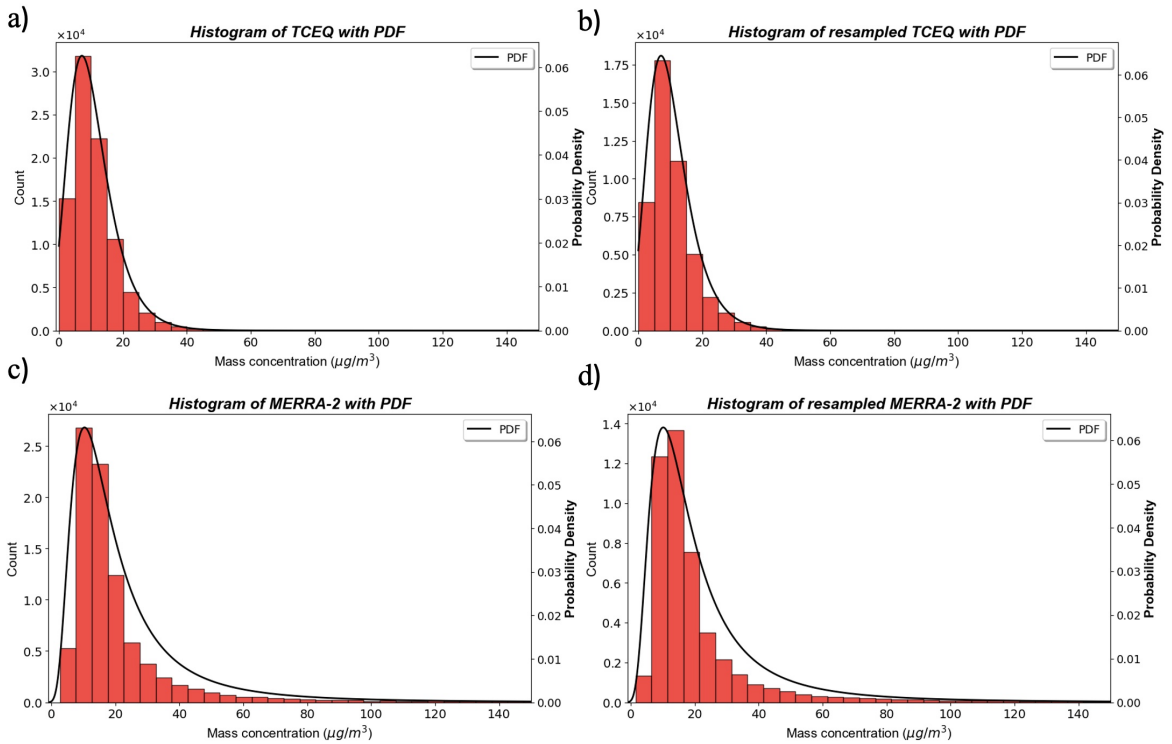

Figure 3.12: Histograms with fitted PDFs (black curves) for (a) TCEQ dataset, (b) resampled TCEQ dataset, where a mean was taken for each hour for sites 2-8 and sites 9-11, (c) MERRA-2 dataset corresponding to nearest spatio-temporal grid point for each observation in the TCEQ dataset, and (d) resampled MERRA-2 dataset corresponding to the resampled TCEQ dataset.

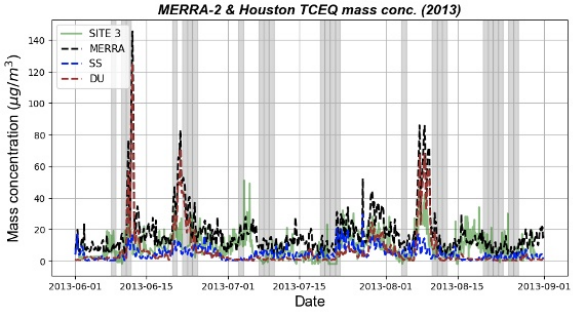
MERRA-2 & Houston TCEQ mass conc. (2013)
SITE 3
MERRA
SS
DU
Mass concentration (μg/m³)
Date

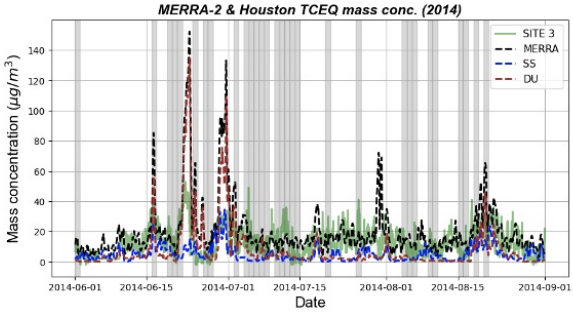
MERRA-2 & Houston TCEQ mass conc. (2014)
SITE 3
MERRA
SS
DU
Mass concentration (μg/m³)
Date

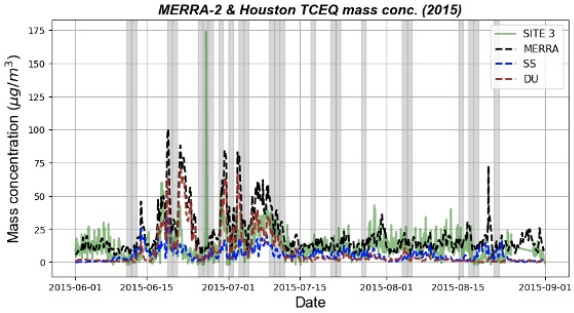
MERRA-2 & Houston TCEQ mass conc. (2015)
SITE 3
MERRA
SS
DU
Mass concentration (μg/m³)
Date

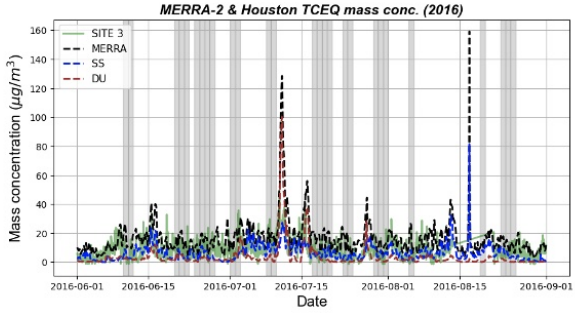
MERRA-2 & Houston TCEQ mass conc. (2016)
SITE 3
MERRA
SS
DU
Mass concentration (μg/m³)
Date

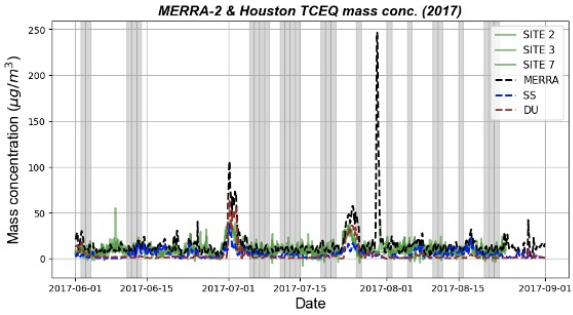
MERRA-2 & Houston TCEQ mass conc. (2017)
SITE 2
SITE 3
SITE 7
MERRA
SS
DU
Mass concentration (μg/m³)
Date

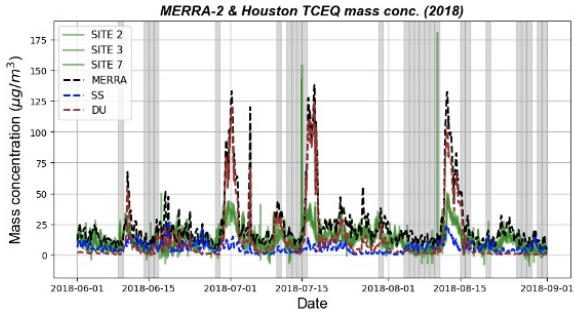
MERRA-2 & Houston TCEQ mass conc. (2018)
SITE 2
SITE 3
SITE 7
MERRA
SS
DU
Mass concentration (μg/m³)
Date

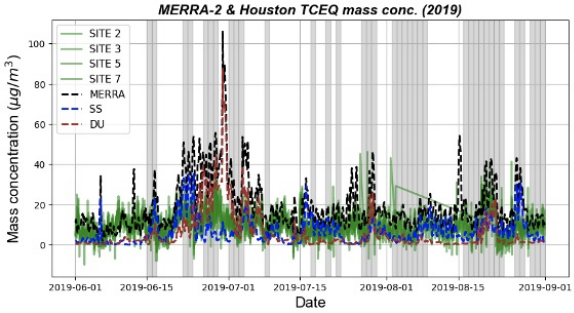
MERRA-2 & Houston TCEQ mass conc. (2019)
SITE 2
SITE 3
SITE 5
SITE 7
MERRA
SS
DU
Mass concentration (μg/m³)
Date

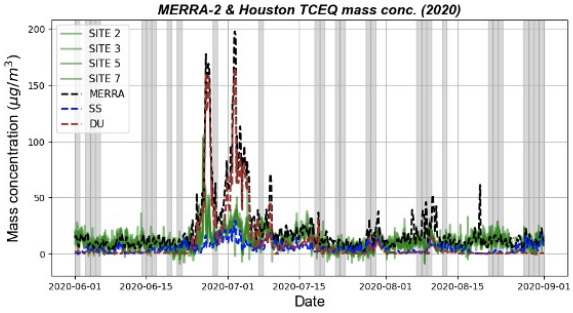
MERRA-2 & Houston TCEQ mass conc. (2020)
SITE 2
SITE 3
SITE 5
SITE 7
MERRA
SS
DU
Mass concentration (μg/m³)
Date

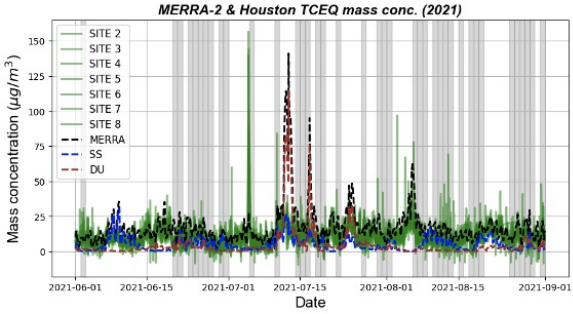
MERRA-2 & Houston TCEQ mass conc. (2021)
SITE 2
SITE 3
SITE 4
SITE 5
SITE 6
SITE 7
SITE 8
MERRA
SS
DU
Mass concentration (μg/m³)
Date

Figure 3.13: Hourly timeseries for each year used in the study showing $PM_{2.5}$ mass concentration from MERRA-2 (black dotted line), sea salt $PM_{2.5}$ mass concentration from MERRA-2 (blue dotted line), dust $PM_{2.5}$ mass concentration from MERRA-2 (brown dotted line), and TCEQ sites observations of $PM_{2.5}$ (green lines). Grey vertical bars shows periods of MCIT runs. It should be noted that TCEQ sites can record $PM_{2.5} < 0$ and these times are not used in aerosol calculations.

Correlations and percentage of variance explained by MERRA-2 (R^2) are presented here to quantify how well MERRA-2 represents the variance of the observed TCEQ dataset across different lags. Figures 3.14 *a* and *b* summarize results from applying techniques used in calculating the maximum R^2 across different lags and Figure 3.14c shows the mean of the daily maximum variance explained by MERRA-2. Site 11 is anomalous with a high fraction of the TCEQ $PM_{2.5}$ variance explained by MERRA-2 due to the low hourly variability that site 11 exhibits, whereas sites 4, 6, and 8 exhibit mean $R^2 < 0.1$. This is attributed to sites 4, 6, and 8 having a very short period of records from only select days in 2021, and thus a meaningful mean of R^2 was not established. MERRA-2 overall does not explain the hourly $PM_{2.5}$ well with most R^2 below 50% for the remainder of the sites. This is not surprising as MERRA-2 does not have high spatial resolution, so it may not capture the spatial heterogeneous nature of $PM_{2.5}$ sources and transport like the observed TCEQ sites show. Lag analysis was added to this investigation because observations between the TCEQ sites and MERRA-2 estimations differ by 30 minutes so a decision to shift estimations forward or backward 30 minutes was needed. For clarification, since MERRA-2 outputs at the bottom of every hour and TCEQ sites validate observations at the top of every hour, MERRA-2 estimations are initially shifted forward by 30 minutes to be coincident with TCEQ. This is then defined as lag-0 since neither timeseries is technically lagged relative to the other. Figure 3.14c shows that on average a lag of 0 is adequate and the initial

shift of MERRA-2 forward by 30 minutes is thus kept. This analysis has shown that MERRA-2's ability to capture the variability of the TCEQ sites is somewhat limited but the spatial homogeneity is useful for sampling environments across the many years of this study.

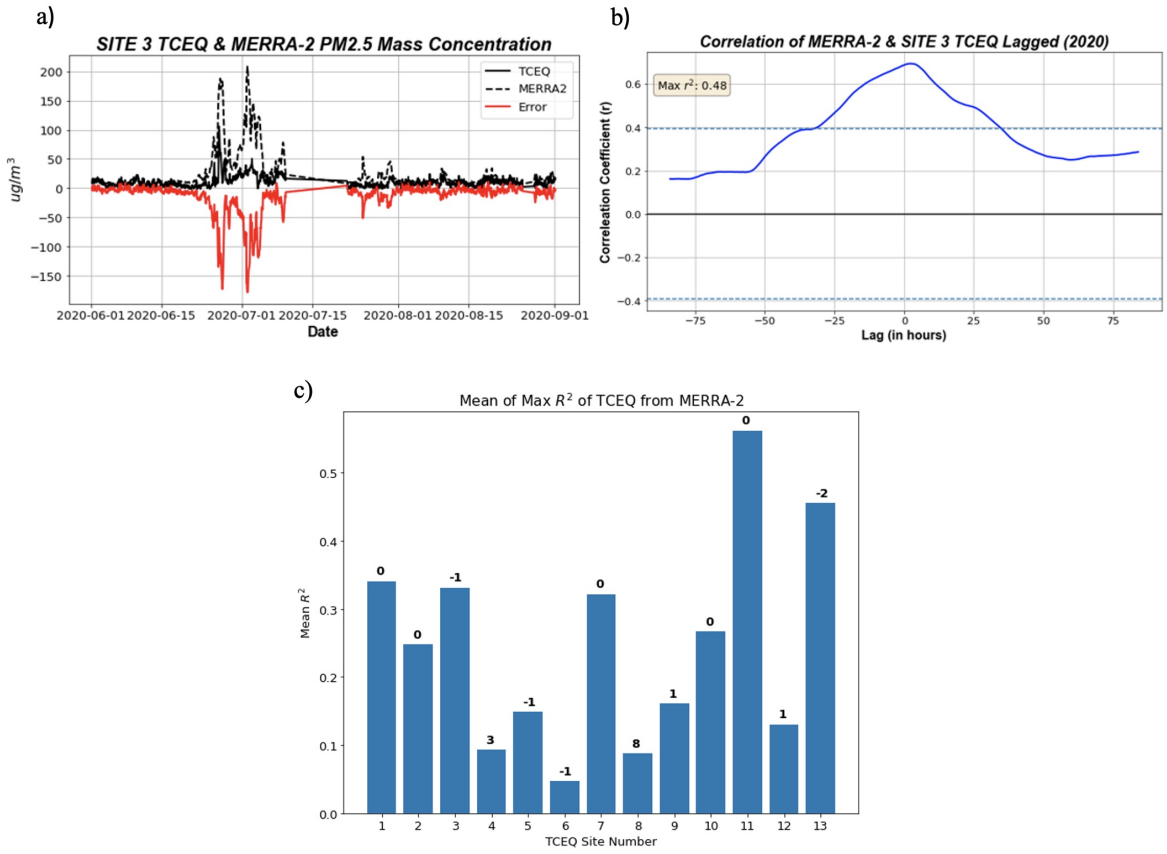

Figure 3.14: (a) Summer time series showing an example of the MERRA-2 and TCEQ site 3 datasets and error by the MERRA-2. (b) Example lag-correlation analysis (blue line) across 85 hours in positive and negative lag for the summer of 2020. Blue dotted lines denote 95% confidence interval using a t-test. (c) Results from the analysis done in (a) & (b) for all sites over all years. The y-axis is the mean R^2 across all years and the numbers above each bar are the mean lag that showed the largest variance explained by MERRA-2. Negative lags equate to TCEQ leading MERRA-2 in time.

When sampling DCCs, the MERRA-2 $PM_{2.5}$ mass concentration is split into either a natural (sea salt and dust) or anthropogenic (organic carbon, black carbon, and sulfate) regime defined by which constituents make up greater than 75% of the total

$PM_{2.5}$ mass concentration across all timesteps of a DCC's existence. This accounts for different types of aerosol loading on the DCCs that could play a role in how the AIE evolves. For example, an anthropogenic regime typically equates to smaller aerosol particles and larger number concentrations (IPCC, 2007), which could promote the AIE, whereas natural regimes may exhibit more frequent GCCN that end up promoting warm rain instead of delaying it, inhibiting the AIE. This is represented within the MERRA-2 scheme as all anthropogenic species are assigned a radius of 0.35 μm and the natural species a radius sometimes larger than 2 μm within the model. For analysis of DCCs in chapter 4, the $PM_{2.5}$ mass concentration is determined as the mean over the DCC lifetime. Classification of DCCs with high and low $PM_{2.5}$ mass concentration is done on a per-subset basis depending on the subsetting techniques. For example, given a distribution of $PM_{2.5}$ mass concentration for all DCCs over the Gulf with MUCAPE $>$ 1000 J/kg in the natural aerosol regime, classification of DCCs with high and low $PM_{2.5}$ is done by using the top and bottom quartiles (Figure 3.15), except where stated. This means that the classification of high and low $PM_{2.5}$ mass concentration is not fixed across all datasets but instead allows for a similar number of DCCs to be in the high and low $PM_{2.5}$ mass concentration classifications when subsetting, which leads to a similar significance across high and low regimes. This is able to be done because typically the DCC's mean $PM_{2.5}$ mass concentration is approximately distributed as a generalized extreme value distribution, which allows for comparison of DCCs with $PM_{2.5}$ mass concentration typically < 10 $\mu g/m^3$ against ones with typically > 30 $\mu g/m^3$ (see Figure 4.39c in section 4.2.2.1.1 for a distribution of $PM_{2.5}$ for all DCCs). However, because of some DCCs with extremely large $PM_{2.5}$ mass concentration evident in Figure 4.39c (i.e. > 60 $\mu g/m^3$), a limit for all high vs. low $PM_{2.5}$ analyses is set such that no DCCs with > 60 $\mu g/m^3$ will be used in the high $PM_{2.5}$ subsets.

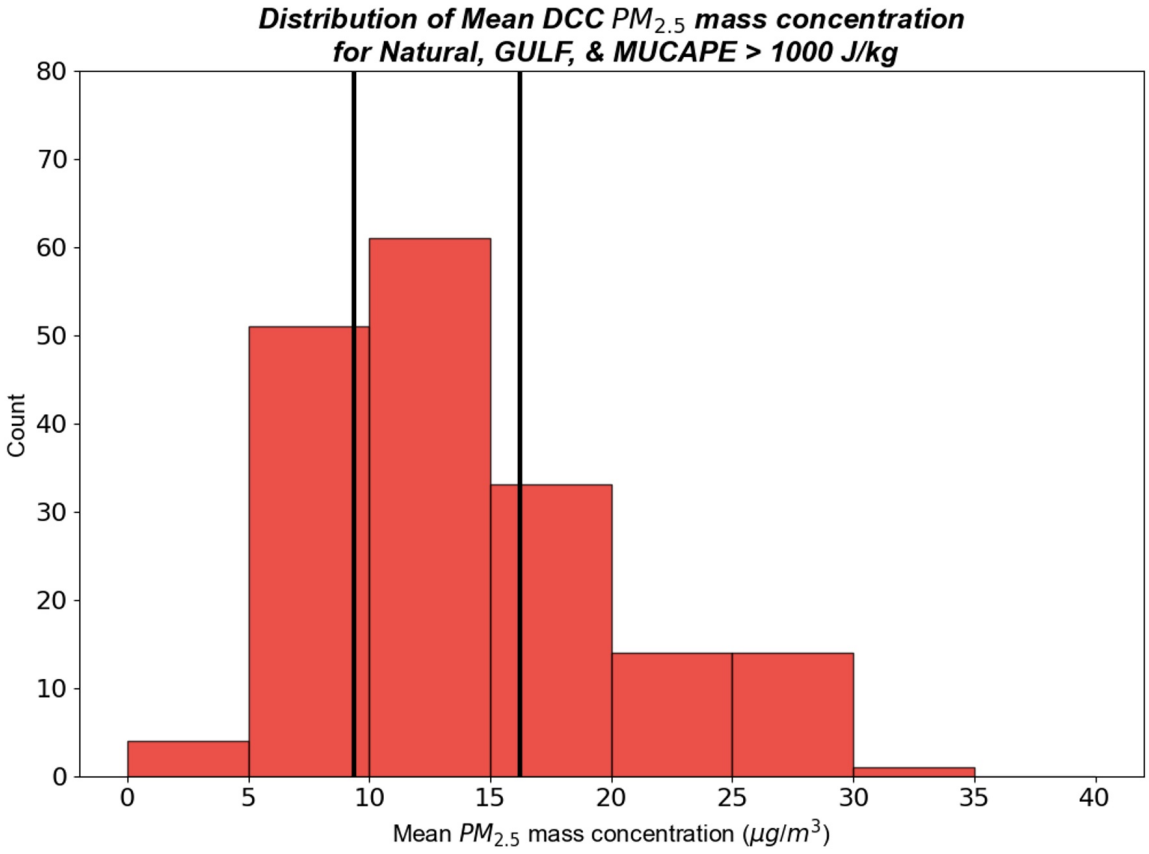

Figure 3.15: Example histogram of mean $PM_{2.5}$ mass concentration for all DCC's over the Gulf of Mexico within the natural aerosol regime and mean MUCAPE $>$ 1000 J/kg. Black bars denote the 25^{th} and 75^{th} percentiles of the distribution and thus the DCC's with high and low $PM_{2.5}$ mass concentration for this subset.

Chapter 4

Results & Discussion

4.1 Spatio-temporal DCC distributions & lifetime

Before analyzing vertical radar profiles, it is important to characterize where in space and time in the vicinity of Houston, TX DCCs occur, what aerosol regimes occur in this area, and the aerosol loading encountered by DCCs. DCC initiation and aerosol transport was largely driven by the sea-breeze circulation in the Houston area, but differences in the strength and direction of this circulation occur, which must be assessed. These differences can lead to the presence of high and low $PM_{2.5}$ mass concentrations within anthropogenic (A) and natural (NA) aerosol regimes in which DCCs occur. This impacts the evolution and lifetime of the DCCs, as well as the development of precipitation, which affects the water resources of southeast Texas.

4.1.1 Spatial distribution of DCCs

The analysis of DCCs presented in this section uses the spatial dataset described in section 3.2.3. The main technique used for analyzing DCCs spatially is the composite difference kernel density estimate (KDE) on the two-dimensional MCIT x-y grid. Figure 4.1 demonstrates this grid in southeast Texas along with the KDE of all DCC tracks within the spatial dataset. This KDE (and others hereafter) are calculated by using the python package scipy.gaussian_kde with the "Scott" bandwidth calculation

method (Virtanen et al., 2020). This method returns a 2D probability density estimate in bins that are 10 km^2 in area. For composite differencing, the KDE of all DCCs with low (or *NA*) $PM_{2.5}$ mass concentration is subtracted from the KDE of DCCs with high (or *A*) $PM_{2.5}$ mass concentration. The values shown in the composite difference KDEs are thus the difference in the relative likelihood of DCC occurrence and thus it does not show absolute probability. In other words, positive values show that high (or *A*) DCCs occur in that grid box more frequently compared to the low (or *NA*) DCCs normalized by the number of total DCCs in each subset. The normalization is important as *NA* DCCs are very frequent, with a total of 3318 *NA* DCCs compared to only 287 *A* DCCs, so results should be interpreted with these sample sizes in mind. In essence, these composite difference KDEs show relative dominance of respective DCCs subsets at specific locations given certain meteorological and aerosol regimes.

Figure 4.1 shows that high likelihoods ($> 0.35/10$ km^2) of DCC occurrence exist on the east side of Houston extending toward Beaumont. Near Houston, these probabilities are oriented along a line mostly parallel to the coastline and then transition to a large circular area of high probabilities near Beaumont. The $0.2/10$ km^2 contour is mostly oriented just along the coastline and marks the effects of DCC initiation due to the sea breeze circulation moving in-land. Over the Gulf, DCC occurrence is low relative to over land consistent with sinking motion from the sea-breeze circulations and lack of frictional effects from the sea-land transition. An interesting pattern can also be seen near Galveston Bay where there is a minimum of DCC probability density, which is consistent with a bay-breeze circulation influence with sinking motion occurring over Galveston Bay. This mechanism of bay-breeze influence on DCCs has been noted in several studies such as those of Byers and Rodebush (1948), Mazzuca et al. (2019),

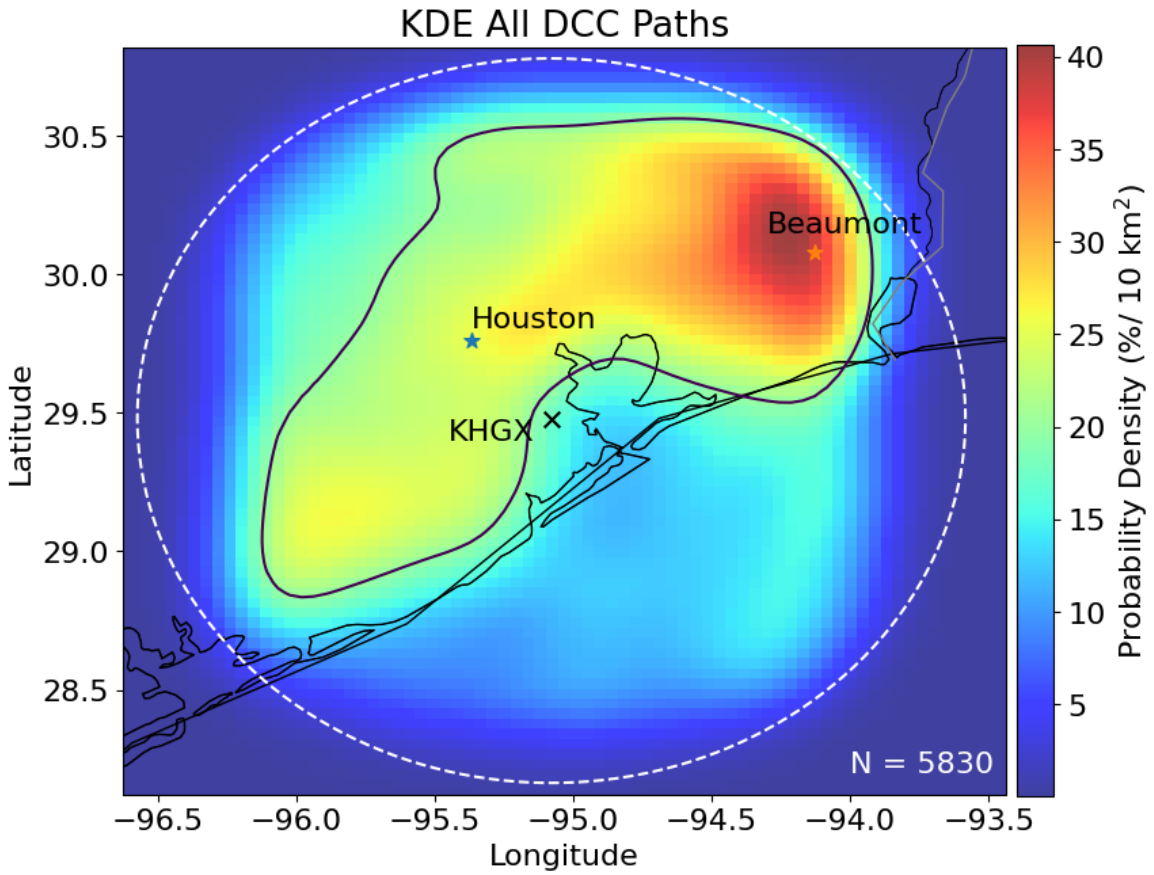

Figure 4.1: A KDE for DCC paths in the spatial dataset (colored pixels). Black curve represents the 20% probability density contour and the white dotted circle is the 120 km range ring. Each pixel is 10 km^2 in area.

and others in other bay locations. Overall, this pattern of DCC occurrence captures the expected sea-breeze circulation influence.

Figure 4.2a shows the relative spatial differences for all *NA* and *A* DCCs as a composite difference KDE. In general, the *NA* and *A* identification from MERRA-2 grasps the expected spatial differences between *NA* and *A* DCCs as *NA* DCCs dominate relative occurrence over the Gulf and *A* DCCs dominate relative occurrence to north of the Gulf and over Houston. Some heterogeneities exist in the relative dominance of *A* and *NA* DCCs near the coast, which highlights a need for further investigation of the factors that govern aerosol transport and areas of DCC initiation in this region.

Figure 4.2b shows windrose plots for all cells used in the composite difference KDE calculation. A key difference between *NA* and *A* DCCs is that *NA* DCCs are more likely to exhibit flow from a southerly direction with stronger speeds while easterly flow occurs more frequently for the *A* DCC regime. Given that the sea-breeze is the main influence of the spatial characteristics of DCCs and is a direct result of diurnal heating, the diurnal distribution of DCCs needs to be assessed to understand how the onset of the sea-breeze influences *NA* and *A* DCC occurrence.

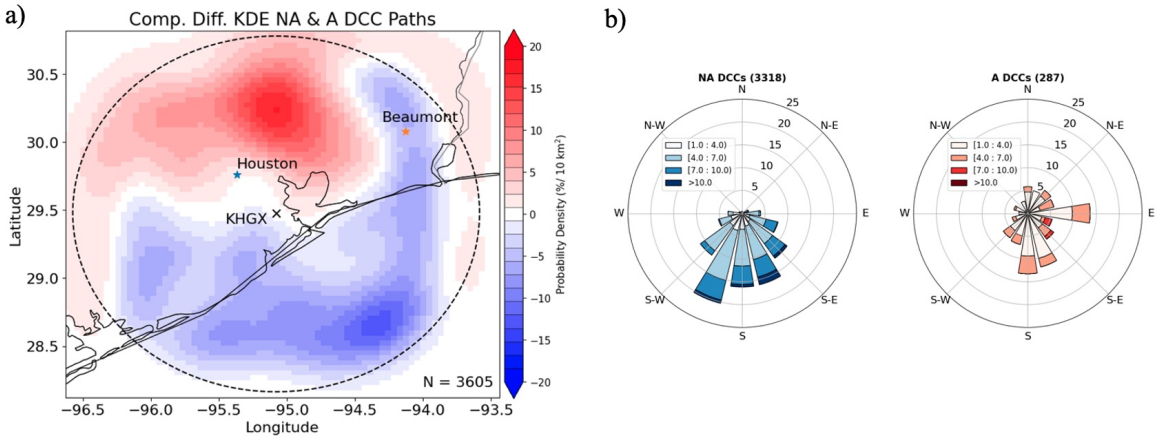

Figure 4.2: (a) Composite difference KDE for all *NA* and *A* DCC normalized occurrence frequencies. Positive (negative) values refer to higher probability densities for *A* (*NA*) DCC locations. (b) Windrose plots for all *A* and *NA* DCCs used in the calculation of (a). These are calculated as the 1000 - 900 mb mean wind for each DCC. Color shading refers to wind speed in m/s. Bars on windrose point towards where the wind is coming from.

4.1.1.1 Diurnally-driven differences in DCCs

Figure 4.3 shows the diurnal probability densities binned every hour for all DCCs and split between *NA* and *A* DCCs. An increase in the occurrence frequency of all DCCs begins at around 9 UTC with the peak of occurrence between 18 – 19 UTC (1 - 2 PM local time). However, the *NA* and *A* distributions show key differences, namely that the *A* DCCs are most likely to occur later in the day at around 20 – 21 UTC (3 - 4 PM)

where *NA* DCCs are most likely to occur between 17 – 18 UTC (12 - 1 PM), with a relative minimum of *A* DCC occurrence happening in the mid-morning hours (13 – 14 UTC, 8 - 9 AM local time). This period marks when the Sun begins to rise high enough to begin heating the surface and trigger the sea breeze, when sea-salt aerosols thus begin to advect inland and initially dominate the $PM_{2.5}$ mass concentrations. This is seen in Figure 4.4, where panel *a* shows that the second derivative of the latitude-mean v-wind with respect to hour of day (d^2v_{lat}/dh^2) is near 0 and becoming positive, especially for middle-higher latitudes within the domain. This means that the decreasing trend of v-wind from the overnight land-breeze influence is waning and the southerly flow is beginning to become stronger from the sea-breeze. This is accompanied in the hours of 12 - 14 UTC (7 - 9 AM) by a quick uptick in both the *NA* mass concentration and mass fraction ($NA/PM_{2.5}$) in DCCs over land, seen in Figure 4.4b. Hence, when DCCs occur during this period they are more likely to be in *NA* rather than *A* air masses. The trend of *NA* DCC occurrence throughout the afternoon continues to increase, until about 17 - 19 UTC (12 - 2 PM) when the occurrence begins to decrease substantially due to the sea-breeze front convergence zone waning in intensity (Bao et al., 2005).

The diurnal variability of the occurrence of *A* DCCs is consistent with the findings of Dai et al. (2019) and Yoon et al. (2020) who describe the diurnal variation of anthropogenic species in the Houston region due to transportation emissions of organic carbon, black carbon, and sulfate. They reported that emission rates of these constituents increase rapidly during morning rush-hour times and lead to increasing rates of SOA formation during the day into the afternoon hours. The MERRA-2 captures this trend, because beginning at 13 UTC (8 AM) in Figure 4.4b the *A* mass concentration of DCCs over land gradually increases throughout the day and maximizes at 1 UTC (8 PM). Thus, the combination of primary transportation emissions and SOA formation along with the sea-breeze convergence zone combine to cause an increase

in A DCC occurrence beginning at 14 UTC (9 AM) and waning at 23 UTC (6 PM) (Figures 4.3b and 4.4). The hours after the peak A DCC occurrence show a large decrease in the probability of both DCC regimes in Figure 4.3b as the sea-breeze ends, which is also marked in Figure 4.4a between 0 - 1 UTC (7 - 8 PM) where d^2v_{lat}/dh^2 is now near 0 again and becoming negative.

Due to the large changes in the probability of occurrence for both DCC regimes marked by the onset and termination of the sea-breeze discussed above, two daily periods will be used to separate DCCs so analysis of the pre- and post-sea breeze onset spatial differences and associated factors can be completed. These periods are during the sea breeze flow (9 AM - 7 PM local time) and after/before sea-breeze onset (7 PM - 9 AM).

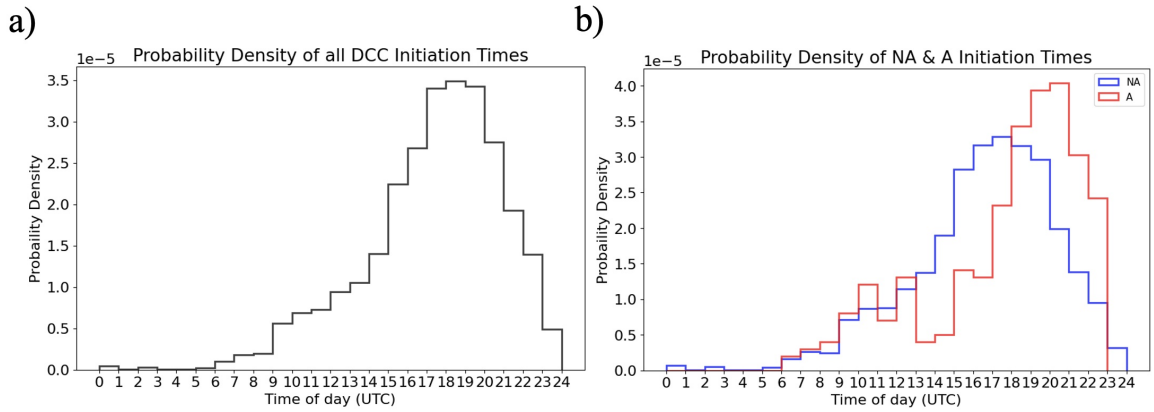

Figure 4.3: Probability densities (a) for all DCCs in the spatial dataset and (b) for all NA DCCs (blue) and A DCCs (red) binned every hour. X-axes are presented in UTC time.

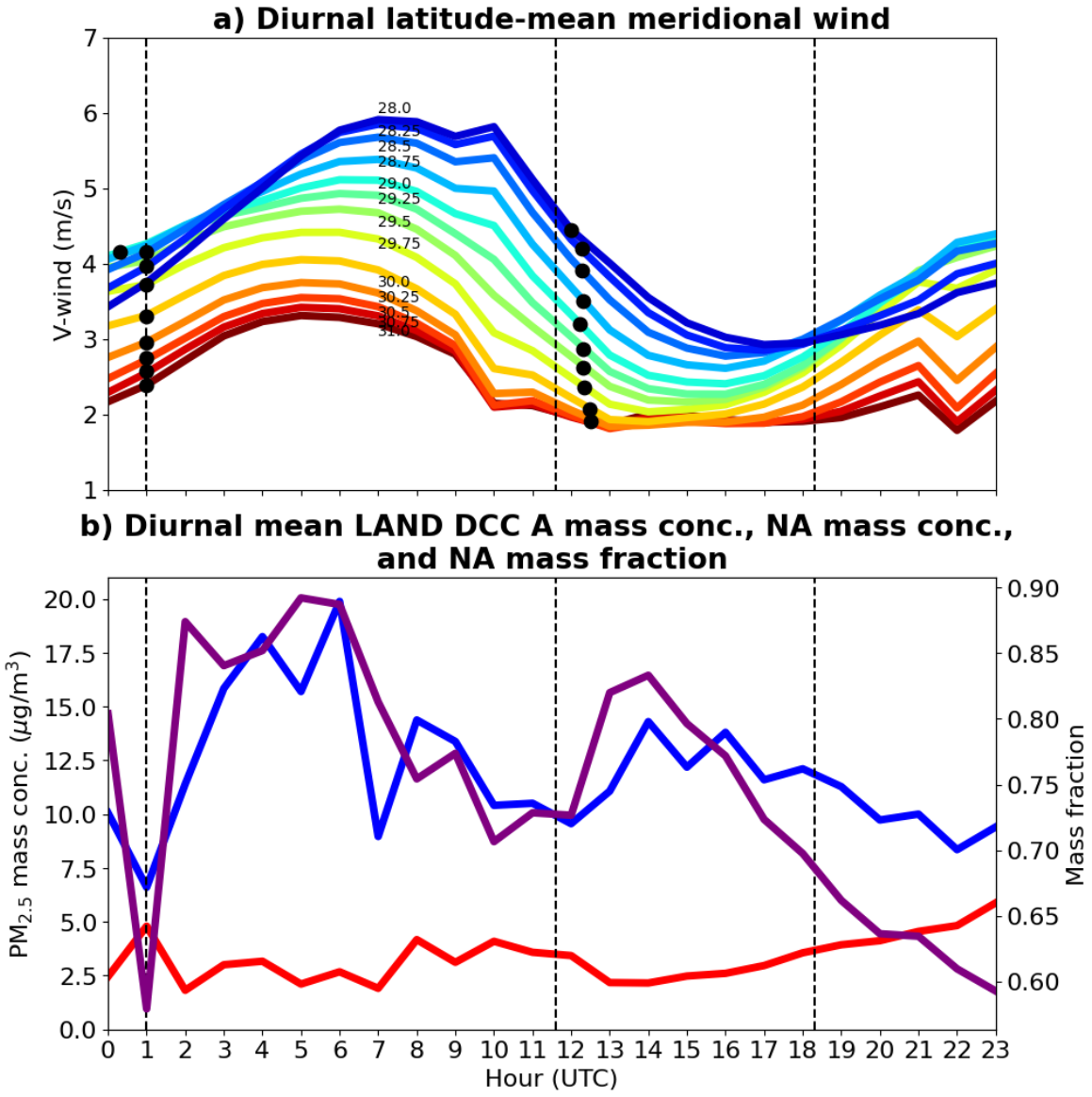

Figure 4.4: (a) Hourly means of latitude-mean meridional wind. Colors correspond to latitudes of the ERA5 within the domain with warmer colors indicating higher latitudes. Black dots illustrate important inflexion points (where $d^2v_{lat}/dh^2 = 0$) for all of the ERA5 latitudes. (b) Hourly means of *NA* and *A* LAND DCC mean $PM_{2.5}$ mass concentration (blue and red lines, respectively) and *NA* mean LAND DCC mass fraction (purple line, right y-axis). Vertical black dotted lines in both figures mark the average times of (from left to right) sunset, sunrise, and solar noon from June 1 to August 31 over Houston.

Figure 4.5a shows the composite difference KDE for *NA* and *A* DCCs that occur between 7 PM - 9 AM local time. There is a stark contrast in the orientation of the relative spatial dominance between *NA* and *A* DCCs in Figure 4.5a. Instead of the difference being oriented perpendicular to the coast as in Figure 4.2a, the difference is oriented zonally with the 95°W meridian approximating the separation boundary. *A* DCC relative dominance is mostly confined to the east of 95°W while *NA* DCC relative dominance is confined west of 95°W and south of KHGX. The windroses for each DCC regime show that *NA* DCCs are more likely to have stronger flow from the south than *A* DCCs (Figure 4.5b).

While both *A* and *NA* DCCs are dominated by flow from the south, there are about 20% of *A* DCCs that exhibit northerly flow (Figure 4.5b). Figure 4.6 shows locations of initiation for *A* DCCs before 9 AM under northerly and southerly flow, illustrating that *A* DCCs with both northerly and southerly flow occur inland, where the land-breeze would not be as prominent. Further, all 9 northerly *A* DCCs occurred on two days, August 31, 2019, and August 26, 2021, showing that this northerly flow regime before 9 AM is very rare on sea-breeze convective days. It seems unlikely then that the land-breeze is a mechanism for which to transport anthropogenic aerosols while also triggering DCC initiation.

Instead, it more likely seems that the emissions from shipping vessels traveling around Galveston Bay are responsible for the relative dominance of the *A* DCC regime over the eastern half of the domain. Schulze et al. (2018) presents the shipping emissions allocation factor (SEAF) (Wang et al., 2007) over the Gulf of Mexico that illustrates two main large-vessel routes are used in and out of Galveston Bay daily (Figure 4.7). These shipping routes are mainly from the south or east of the 95°W line and spatially agree well with the region of high *A* DCC relative occurrence over the Gulf in Figure

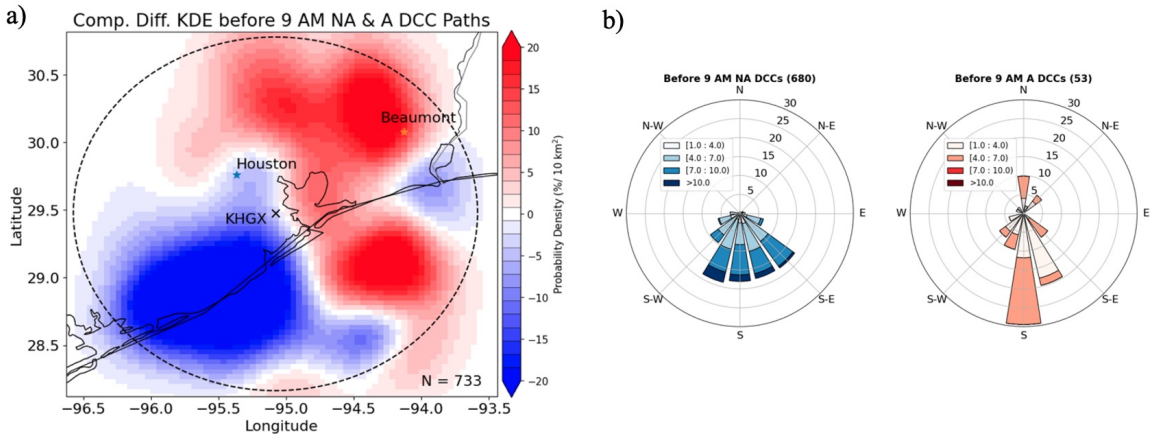

Figure 4.5: As in Figure 4.2 but for DCCs occurring before 9 AM local time.

4.5a. Because MERRA-2 takes into account international shipping emissions from across the globe (see section 3.4.1 for further details), these emissions are accounted for in the fields use to distinguish *A* and *NA* air masses. Further, the lack of boundary layer mixing from diabatic heating from the Sun in the early morning hours can trap these emissions within the boundary layer allowing for larger concentrations to remain present. Figure 4.8 shows that the CIN for *A* DCCs is typically larger than that for *NA* DCCs, illustrating the larger probability of trapping ship emitted aerosols over the Gulf when *A* air masses occur. In addition, advection northward of these ship emission aerosols occurs due to the preponderance of weak southerly winds shown in the *A* DCC windrose (Figure 4.5b), which shows a high likelihood of *A* air masses and hence *A* DCCs, extending further inland east of 95˚W.

Lastly, Figure 4.9 shows the two KDEs for the *NA* and *A* DCCs before 9 AM separately so that the spatial patterns of DCCs can be better visualized. Figure 4.9a shows that *NA* DCC occurrence is rare farther inland than the Houston and Beaumont cities consistent with the *NA* air masses not having been advected inland during the early morning hours so that *NA* DCC initiation and sea-salt advection further inland

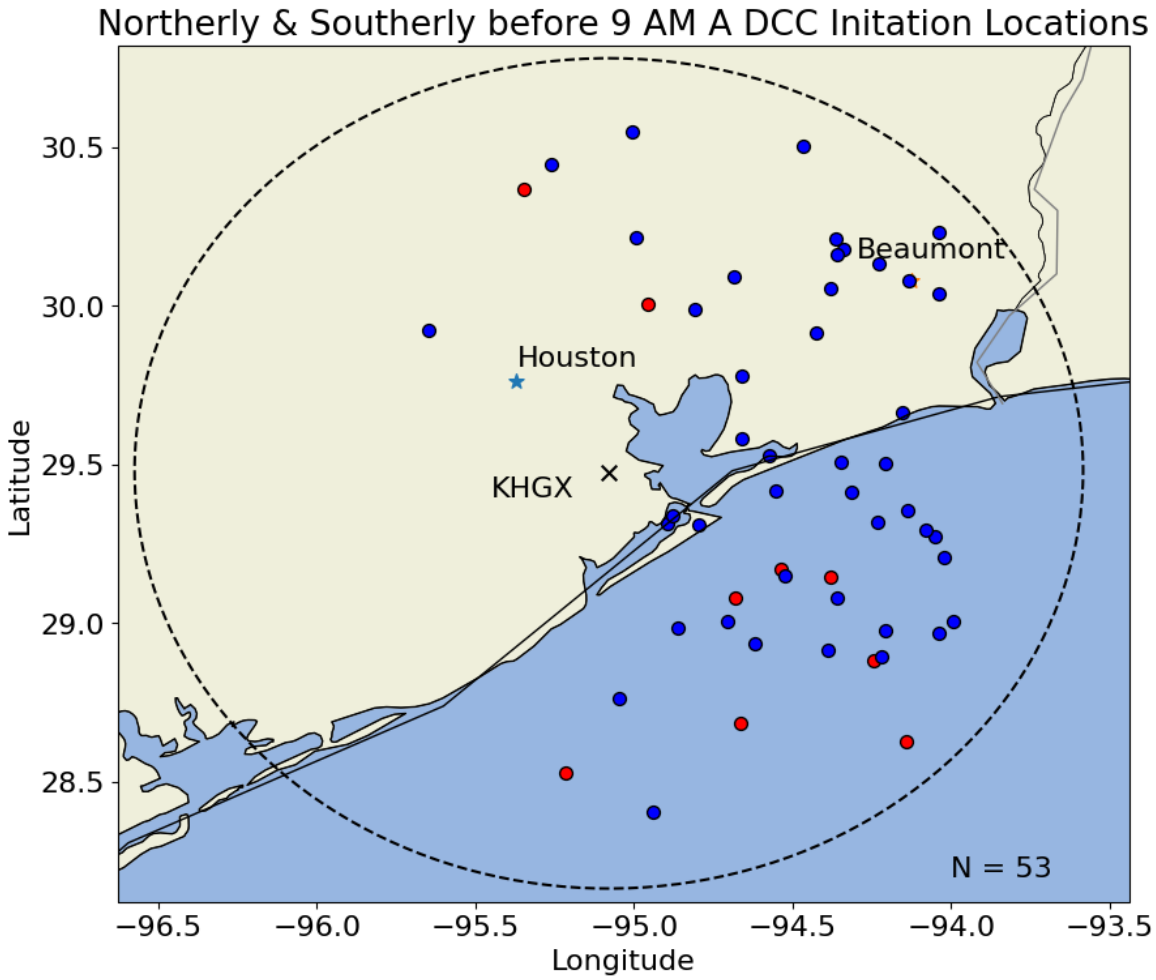

Figure 4.6: Initiation locations of A DCCs occurring before 9 AM under northerly (red dots) and southerly (blue dots) flow.

has not begun. For both regimes, DCCs occurring before 9 AM are likely to be impacted by southerly boundary layer flow, but the strength of this flow and boundary layer stability leads to either higher relative probability of NA DCCs just along the coast and over the Gulf, or leads to higher relative probability of A DCCs east of 95˚W.

The composite difference KDE for all DCCs occurring after 9 AM is shown in Figure 4.10a. The difference pattern shifts to be oriented more perpendicular to the coastline, much like that of Figure 4.2a. As expected, the Gulf is dominated by the NA DCCs because evaporation of sea water is more prevalent from diabatic heating and it is a

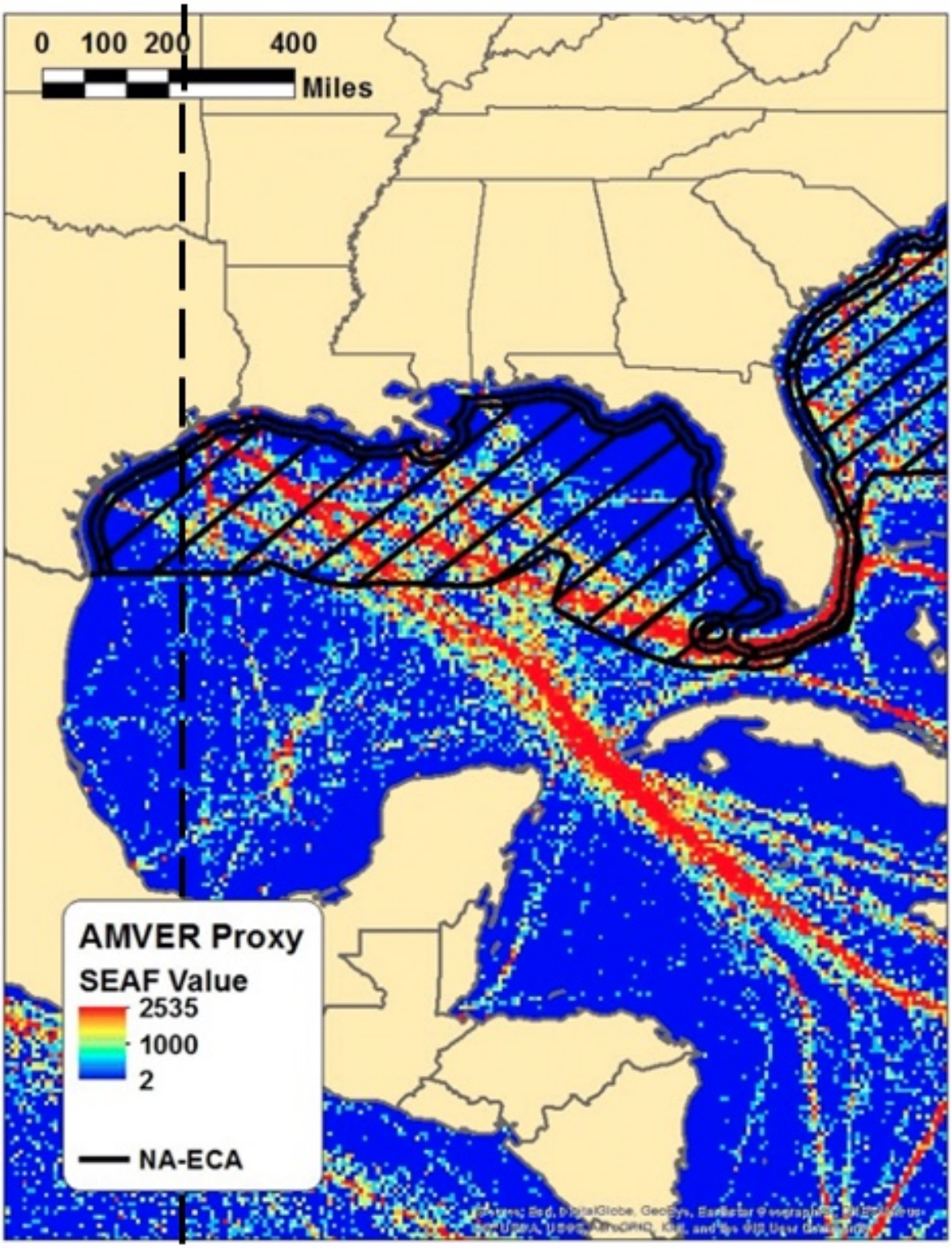

Figure 4.7: The Automated Mutual-Assistance Vessel Rescue (AMVER) proxy of Wang et al. (2007)'s SEAF value over the Gulf of Mexico. The vertical black dotted line is the 95°W meridian. Adapted from Schulze et al. (2018).

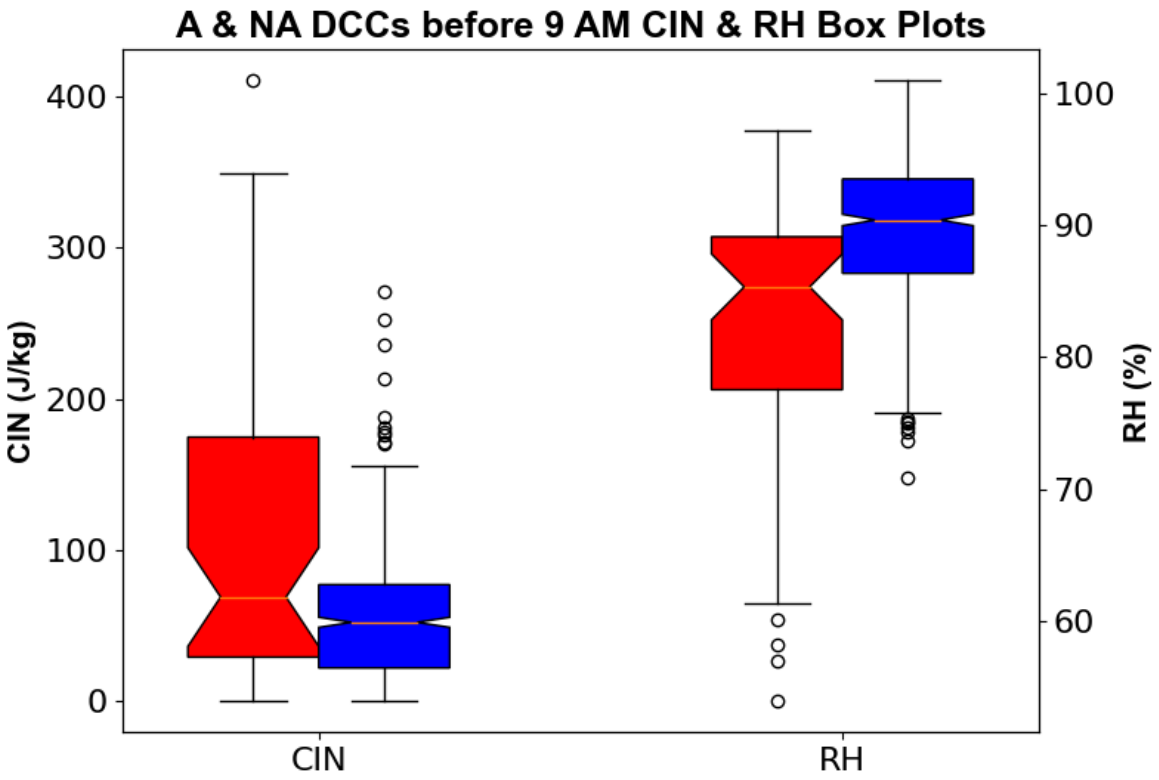

Figure 4.8: Box and whisker plots of before 9 AM *NA* (blue) and *A* (red) DCCs' mean CIN and 1000 - 900 mb mean relative humidity. These values are taken from the nearest spatio-temporal grid point for each DCC from the ERA5 reanalysis.

more pristine air mass. Additionally, strong southerly flow is present when *NA* DCCs occur just as before 9 AM, aiding in the advection of sea salt over the Gulf and onto land. Further, as expected, the regions north of Houston show relative dominance of *A* DCCs. Given the boundary layer wind profiles from the windroses (Figure 4.10b), flow can be variable in direction when these *A* DCCs occur but is most likely from the east, since 53% of the DCCs exhibit an easterly component. This flow regime diminishes the sea salt aerosol advection and allows for advection of anthropogenic emissions to dominate when DCCs occur north of Houston. Anthropogenic emissions coming from Houston increase after 9 AM due to transportation emissions, which promote photochemical reactions during afternoon hours, producing SOAs. The weak

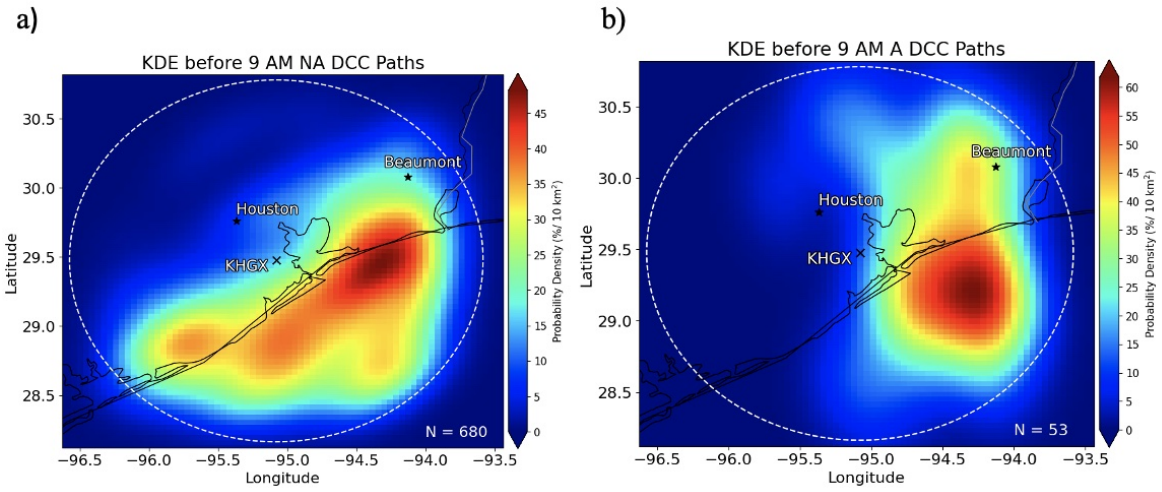

Figure 4.9: KDEs for before 9 AM (a) *NA* and (b) *A* DCC paths.

winds relative to the *NA* DCC speeds further promote this mechanism over Houston as advection of these anthropogenic aerosols is minimal (Figure 4.10b). However, spatial differences between *NA* and *A* DCCs in Figure 4.10a are more heterogeneous than those in Figure 4.5a with high *A* DCC relative occurrence near the coast, surrounded by areas of high *NA* DCC relative occurrence further inland which is not consistent with what is expected based on flow from a sea-breeze. The two black boxes encompassing these regions is shown in Figure 4.10a and mark the east and west regions that are further investigated to understand why these differences are seen.

Figures 4.11a and b show the eastern domain KDEs for both *NA* and *A* DCCs with boundary layer winds averaged from all hours between 9 AM and 7 PM calculated from the ERA5 on the respective days that have either *NA* or *A* DCCs overlaid. The maximum probability of *A* DCC occurrence is in the southern region of the domain close to Galveston Bay while for *NA* DCCs, the maximum probability is further north near Beaumont. Boundary layer mean wind patterns for days when *A* DCCs occurred are much more easterly than on days *NA* DCCs occurred and Figure 4.11c shows that the speeds are not likely to be greater than 7 m/s. This again shows that

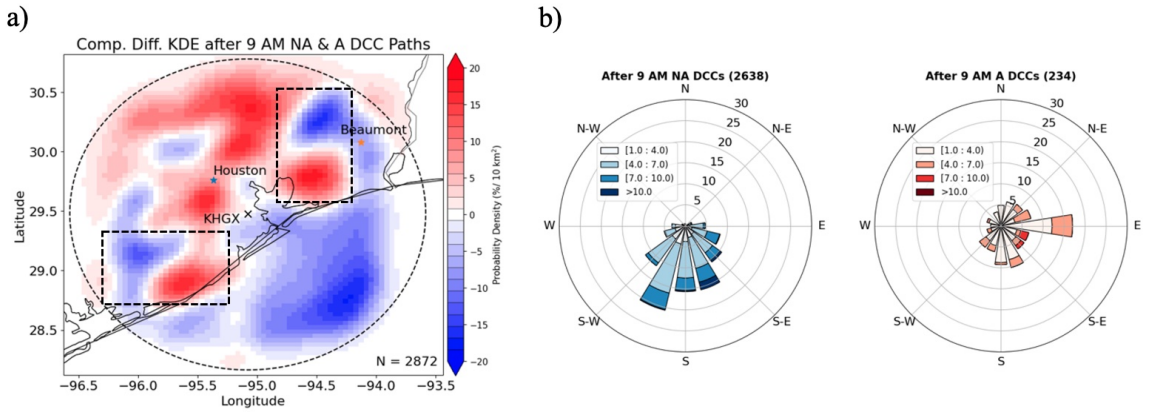

Figure 4.10: As in Figure 4.2 but for DCCs occurring after 9 AM local time. Black dotted boxes in (a) refer to the east and west domains.

the advection of sea salt aerosols is inhibited for *A* air masses due to weak flow that is more easterly. Advection of anthropogenic aerosols under these flow regimes can occur due to the eastern oil refineries and factories that populate the area east of Galveston Bay. Interestingly, the windrose for *A* DCCs also points to possible evidence of a bay-breeze from the Galveston Bay as the second most frequent wind direction is from the southwest. A bay-breeze can help promote *A* DCC occurrence through additional low-level convergence with the sea-breeze and upward motion from the baroclinic circulation. Anthropogenic aerosols from the bay-breeze would most likely originate from ship emissions and the Houston metropolitan area, with a lack of natural aerosols due to the relatively weak flow from the bay-breeze (Figure 4.11c). However, the ERA5 may struggle to resolve a small scale process such as the bay-breeze, and thus more investigation would be needed in studies utilizing field campaign data to quantify this process in terms of aerosol transport and DCC initiation. In summary, the mechanisms behind the observed dipole of *NA* and *A* DCCs occurrence in the eastern domain are similar to the rest of the study area with the possible addition of a bay-breeze influence. Most significantly, the location of *NA* and *A* DCCs in this region is governed by the direction and strength of the on-shore flow. If it is strong and southerly, *NA* DCCs are

likely to form in the northern part. If the flow is weaker and easterly, then *A* DCCs are more likely to form in the southern part close to Galveston Bay with influences from the weaker bay-breeze possible.

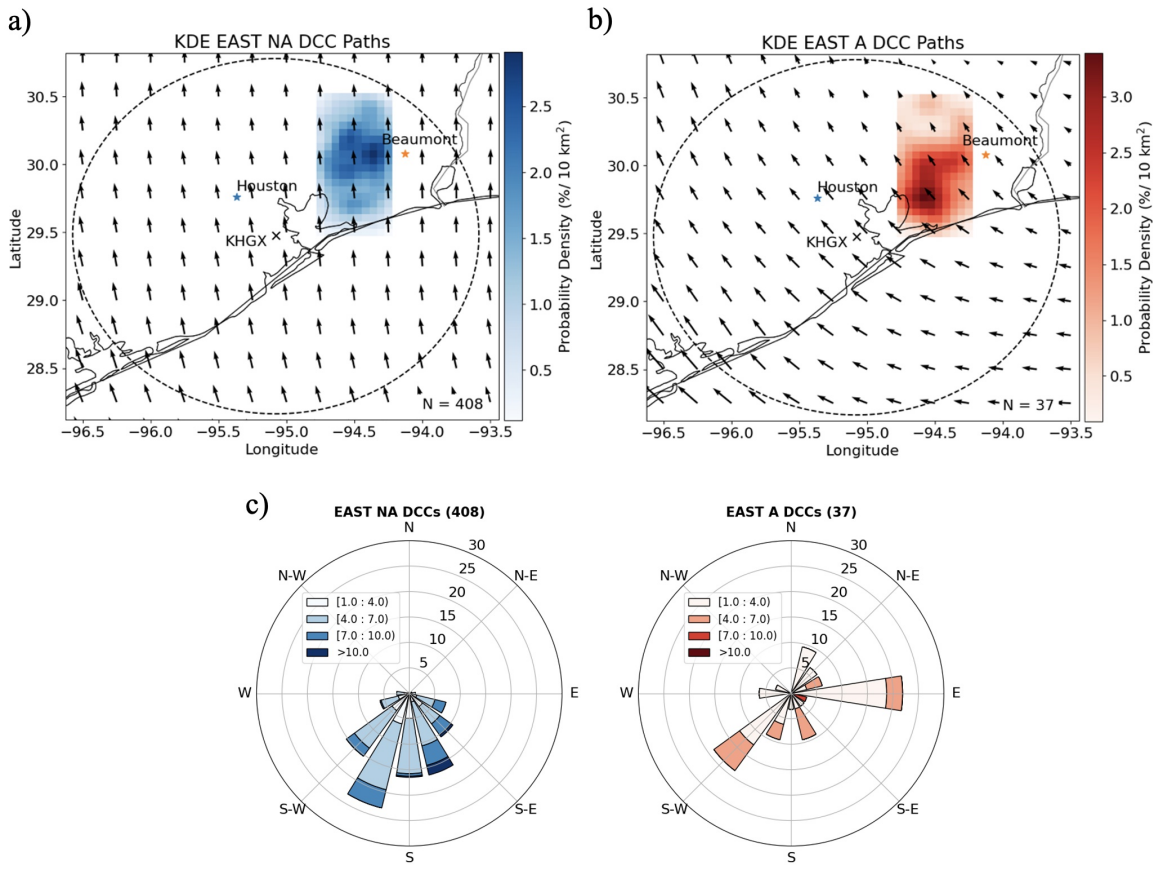

Figure 4.11: KDEs for (a) *NA* and (b) *A* DCCs occurring in the eastern domain. Black arrows show ERA5 1000 - 900 mb mean winds between 14 - 23 UTC for each day *NA* (or *A*) DCCs occurred in the eastern domain. Arrows are not representing speed across the two figures. (c) Windrose plots for all *NA* and *A* DCCs used in (a) and (b).

For the western domain, a similar pattern to Figure 4.11 is seen for the *A* and *NA* DCC probability densities in Figure 4.12. A large difference can be seen in the flow regime for days with *A* DCCs compared to days when *NA* DCCs occur. The windroses show that the strength and direction of the wind is most important in determining likelihood of *NA* or *A* DCC occurrence. *A* DCCs typically exhibit weak winds that are

usually easterly where *NA* DCCs occur when there is stronger flow from a southerly direction which activates sea-salt emissions and leads to dominance by sea-salt in $PM_{2.5}$ mass concentrations. Locations of the maximum probability of *NA* and *A* DCCs in this region are again dependent upon the flow regime as *NA* DCCs can occur frequently in the northern part of the domain if flow is strong and southerly (Figure 4.12a) and *A* DCCs can occur frequently closer to the coast if flow is weak and easterly (Figure 4.12b).

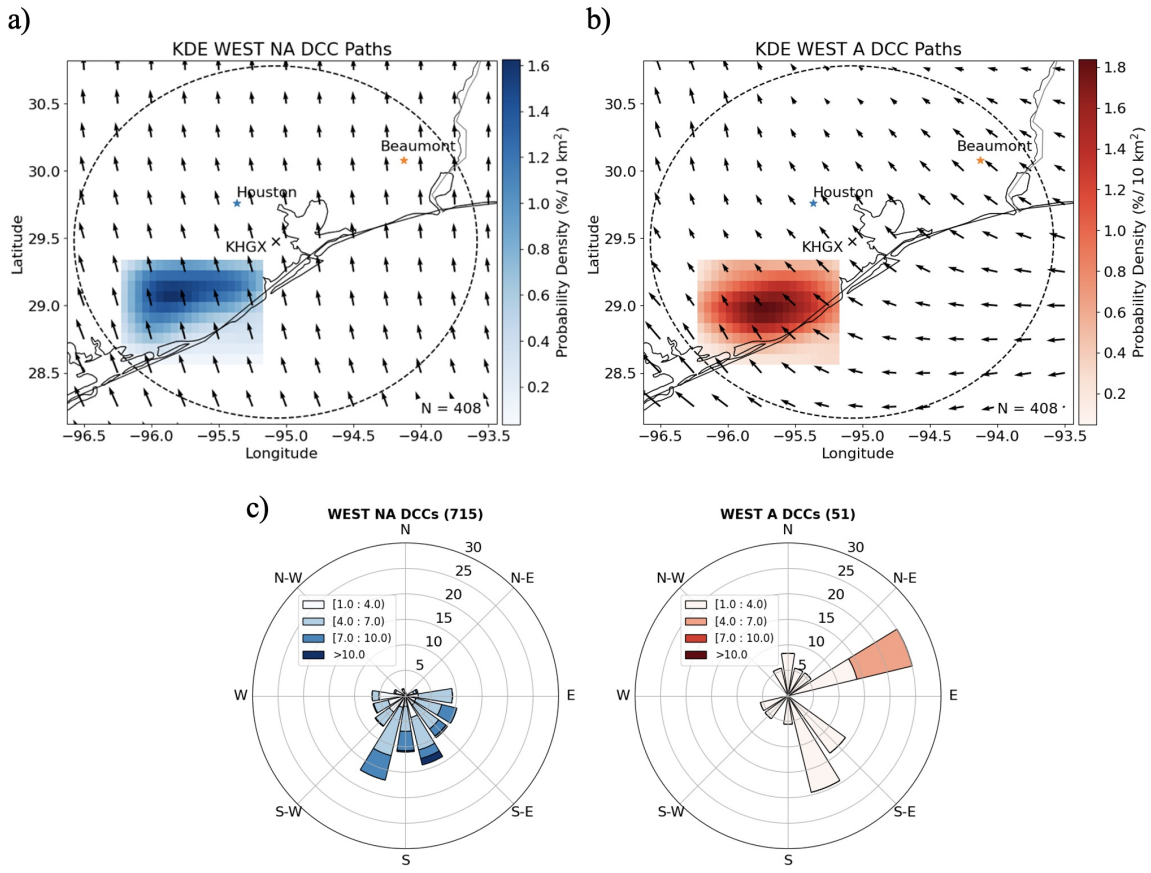

Figure 4.12: As in Figure 4.11 but for the western domain.

4.1.1.2 High & low $PM_{2.5}$ DCCs

The composite difference KDEs for high and low $PM_{2.5}$ mass concentrations for *NA* DCCs occurring before 9 AM are presented in Figure 4.13, along with their windroses showing wind speeds and direction for the environments in which DCCs occurred. High and low $PM_{2.5}$ DCCs are defined as the top and bottom quartiles of the $PM_{2.5}$ distribution for *NA* DCCs that occurred before 9 AM, which are 20 $\mu g/m^3$ and 9 $\mu g/m^3$, respectively. The windroses show that stronger southerly flow generally promotes higher *NA* $PM_{2.5}$ mass concentrations (Figure 4.13b). Additionally, the DCCs that occur within the higher $PM_{2.5}$ mass concentrations are generally further inland, which is consistent with the southerly flow initiating DCCs and advecting sea salt

aerosols further inland. Meanwhile, the *NA* DCCs with lower $PM_{2.5}$ mass concentrations occur more often near the coastline, likely due to the weaker southeasterly winds that are typically present when they occur. Thus, as in the previous analysis of *NA* DCCs, weaker southerly flow leads to lower natural aerosol mass loading when DCCs occur closer to the coast, and stronger southerly flow leads to higher natural aerosol mass loading when DCCs occur further inland. For the high (> 16 $\mu g/m^3$) and low (< 11 $\mu g/m^3$) *A* DCCs occurring before 9 AM, the sample size is very low with only 14 in each quartile (Figure 4.14). Therefore, the windroses in Figure 4.14b do not resolve a coherent pattern of wind direction and speed. However, the composite difference KDE (Figure 4.14a) does show a pattern that high *A* DCCs tend to occur near Beaumont while lower *A* DCCs occur more frequently over the Gulf. This pattern points to primary anthropogenic emissions of aerosols by oil refineries and factories east of Houston being present for DCCs east of Houston and to shipping emissions from vessel activity yielding lower anthropogenic mass concentrations when *A* DCCs occur over the Gulf.

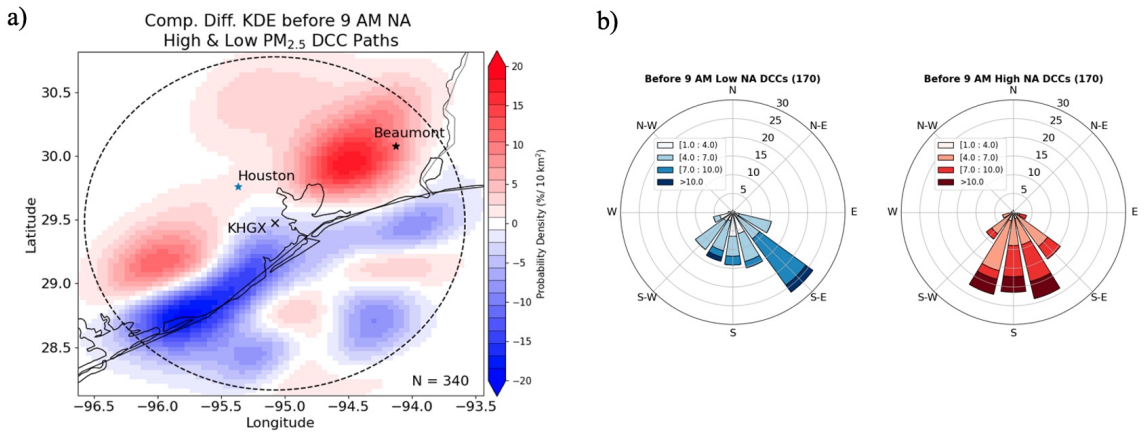

Figure 4.13: As in Figure 4.2 but for high and low $PM_{2.5}$ *NA* DCCs occurring before 9 AM local time.

The composite difference KDEs for high and low $PM_{2.5}$ mass concentrations for *NA* DCCs occurring after 9 AM are presented in Figure 4.15, along with their windroses

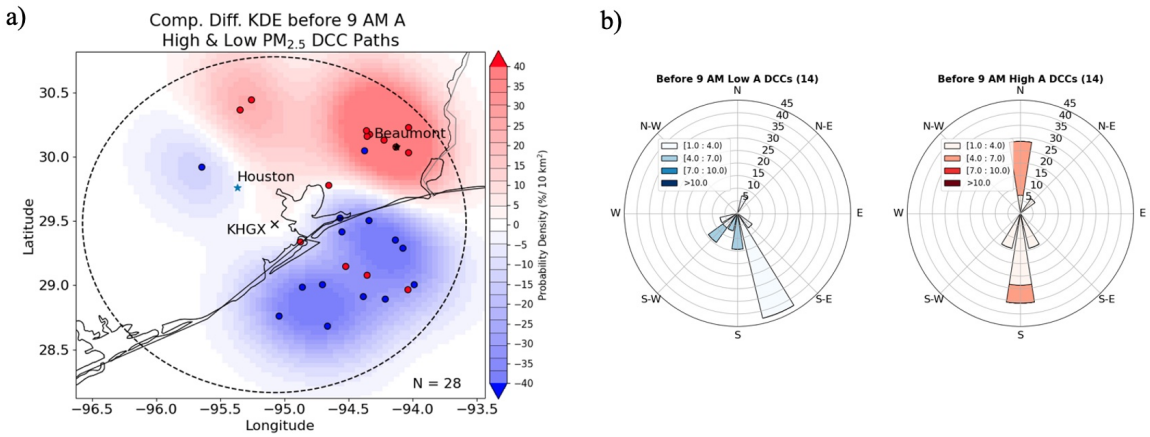

Figure 4.14: As in Figure 4.2 but for high and low $PM_{2.5}$ *A* DCCs occurring before 9 AM local time. (a) also shows the initiation locations of high (red dots) and low (blue dots) *A* DCCs.

showing wind speeds and direction for the environments in which DCCs occurred. The top and bottom quartiles for *NA* DCCs that occurred after 9 AM that define the high and low $PM_{2.5}$ thresholds are 21 $\mu g/m^3$ and 10 $\mu g/m^3$, respectively. Overall, Figure 4.15 shows that there is a stronger southerly flow, typically $>$ 7 m/s, that leads to higher natural $PM_{2.5}$ mass concentrations and *NA* DCC initiation further inland. For high ($>$ 15 $\mu g/m^3$) and low ($<$ 9 $\mu g/m^3$) *A* DCCs occurring after 9 AM, a unique spatial difference pattern can be seen in Figure 4.16. Two regions of more frequent high $PM_{2.5}$ when *A* DCCs occur can be seen near Houston and Beaumont, while low $PM_{2.5}$ is seen when *A* DCCs occur closer to the coastline and northwest of Houston. Figure 4.16b shows the main differences in wind speed and direction between the high and low *A* DCCs occurring under these conditions. Stronger southeasterly flow ($>$ 4 m/s) is present when high *A* DCCs occur downwind of Beaumont and Houston, which are the main sources for these aerosols. This means that the southeasterly sea-breeze flow regime promotes anthropogenic aerosol advection and DCC initiation in the red areas in Figure 4.16a. However, flow that is weak ($<$ 4 m/s) leads to a lack of both natural and anthropogenic aerosol advection and thus the DCCs in the blue

areas in Figure 4.16a do not occur when large amounts of sea-salt or anthropogenic mass concentrations are present. They instead occur with only aerosols emitted from sources near their initiation locations that are not over the Houston or Beaumont metropolitan areas.

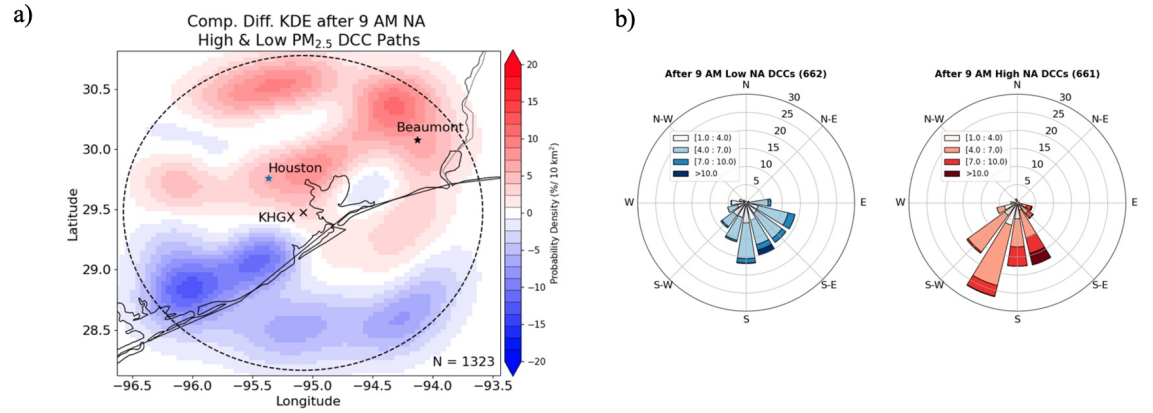

Figure 4.15: As in Figure 4.2 but for high and low $PM_{2.5}$ *NA* DCCs occurring after 9 AM local time.

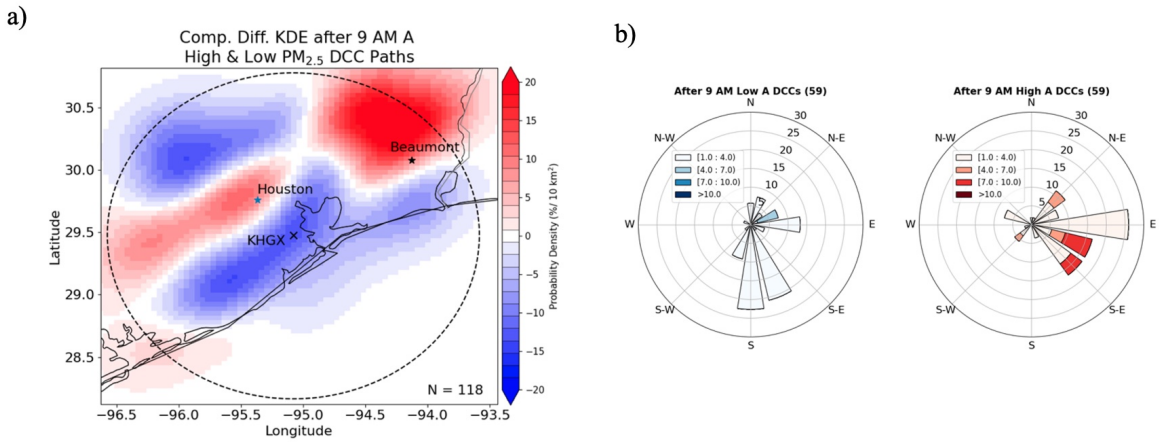

Figure 4.16: As in Figure 4.2 but for high and low $PM_{2.5}$ *A* DCCs occurring after 9 AM local time.

Throughout this analysis the dominant factor that dictates what type of aerosol regime under which DCCs occur has been the presence or lack of a strong southerly sea-breeze. In the morning hours before 9 AM, flow is typically from the south regardless of what aerosol regime is present, but the strength of the wind governs the fact that DCCs occur in *NA* conditions as the sea breeze begins. Smaller wind speeds and shipping emissions are present when *A* DCCs form east of Houston both in the Gulf and further inland, consistent with the weak flow limiting sea salt aerosol advection, so that the anthropogenic air mass dominates. After 9 AM when diurnal heating increases and the sea-breeze flow progresses inland, the *NA* regime is more likely present as the sea-salt aerosols are advected onto land. The peak likelihood of *A* DCCs occurs later in the day most likely due to both the waning influences of the initial sea-breeze surge with associated sea salt advection and peak emissions and impacts from human activities. Further, after the sea-breeze onset the spatial relative dominance flips to the more expected result with *NA* DCCs over the Gulf and *A* DCCs further inland over and northwest of Houston. However, two regions west and east of Houston exhibit differences with dipoles of high *NA* and *A* DCCs relative occurrence. Both regions were again governed by the strength of the on-shore flow. If the flow is strong ($>$ 4m/s) and southerly, the *NA* DCCs occur further inland in both regions. If the flow is weak and easterly, then the *A* DCCs occur closer to the coast. For both the east and west regions, the wind direction when *A* DCCs occur is more variable with the largest likelihood being from continental flow rather than from purely on-shore southerly flow. Figure 4.17 shows the two composite difference KDEs for the southerly and easterly sea-breeze regimes and summarizes the main differences in the spatial distribution between *NA* DCCs and *A* DCCs under the different regimes. Under southerly flow, the total number of *A* DCCs was only 37, of which all but 1 occurred over land, while the number of *NA* DCCs was 1825, which occurred throughout the domain. For

easterly flow, *A* DCCs occurred 129 times compared to 522 *NA* DCCs. The number and location differences of DCCs between *A* and *NA* regimes show the influence of the sea breeze on the likely location of and type of aerosol loading on the DCCs. Finally, whether *NA* or *A* DCCs experience high or low $PM_{2.5}$ loading is heavily driven by the strength of the sea-breeze flow regime combined with the primary sources of the anthropogenic (Houston and Beaumont) and natural (Gulf of Mexico) aerosols.

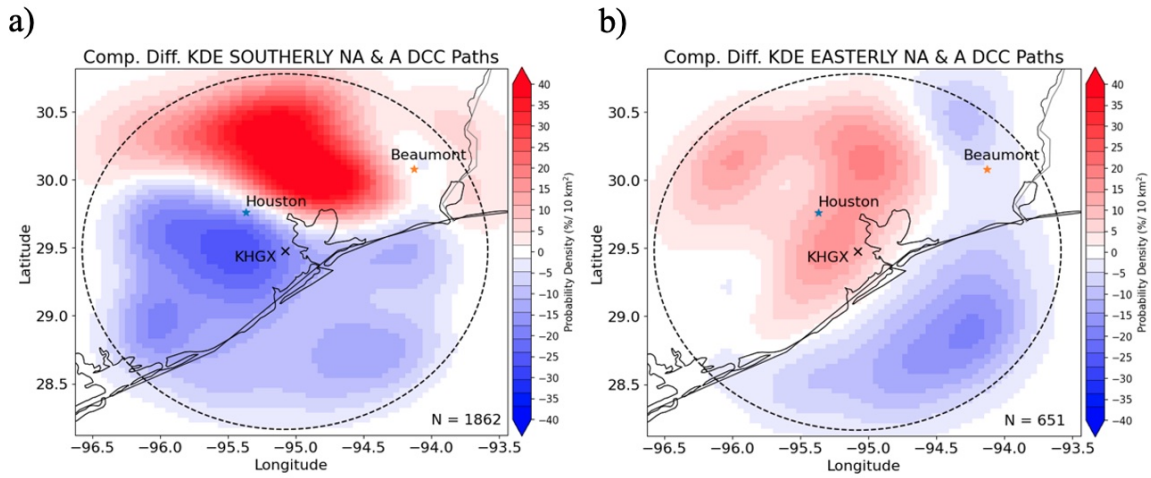

Figure 4.17: Composite difference KDEs of *NA* and *A* DCC paths for days with (a) southerly and (b) easterly flow. For (a), the number of *NA* DCCs is 1825 while for *A* DCCs the number is 37. For (b), the number of *NA* DCCs is 522 while for *A* DCCs the number is 129.

4.1.2 DCC lifetime

The first step described in the AIE is the delay of the warm rain process and thus an increase in cloud lifetime (Albrecht, 1989; Rosenfeld et al., 2008). If the AIE is important for DCCs around Houston, then DCC lifetime should increase with an increase in aerosol loading. To investigate this part of the AIE, correlations between $PM_{2.5}$ mass concentration and DCC lifetime are extracted. Distinction between DCCs occurring over land and over the Gulf is made because the meteorological and aerosol regimes can

be vastly different, making it easier to disentangle aerosol and meteorological effects on DCC lifetime. DCC lifetime is calculated by taking the difference between start and end times of DCCs identified within the MCIT algorithm.

A spearman correlation analysis of the ERA5 meteorological variables with both DCC lifetime and $PM_{2.5}$ mass concentration is shown in Figure 4.18, and was calculated using daily means of each variable as described in section 3.3. DCC lifetime over the Gulf is most correlated with low-level relative vorticity, mid-level shear magnitude, and 400 mb omega. $PM_{2.5}$ mass concentration is correlated significantly with u and v-wind and shear magnitude. Since shear magnitude is correlated significantly with $PM_{2.5}$ mass concentration and DCC lifetime, controlling for shear magnitude would lead to difficulties in separating correlations between meteorology and aerosols. Instead, the 400 mb omega is chosen to classify DCCs by over the Gulf. The low-level relative vorticity was not chosen to classify the DCCs as it and 400 mb omega have a pearson correlation coefficient of -0.26 across all DCCs over the Gulf, which is significant at the 95% confidence level. This means that weaker sinking motion (less positive omega) from the subsidence branch of the sea-breeze baroclinic circulation can correlate with less negative low-level relative vorticity over the Gulf, which would promote longer lasting DCCs from lack of strong subsidence. This thus suggests a coupling between omega and low-level vorticity regarding impact on DCC lifetime. Over land, DCC lifetimes only show a significant spearman correlation with 400 mb relative humidity and thus this is the variable used to control for meteorological influence on DCC lifetime for land DCCs. The lack of correlation with other meteorological variables is probably a result of the fact that many more DCCs occur over land where the ERA5 reanalysis is unable to capture the smaller scale meteorological environments in which these small-scale DCCs occur.

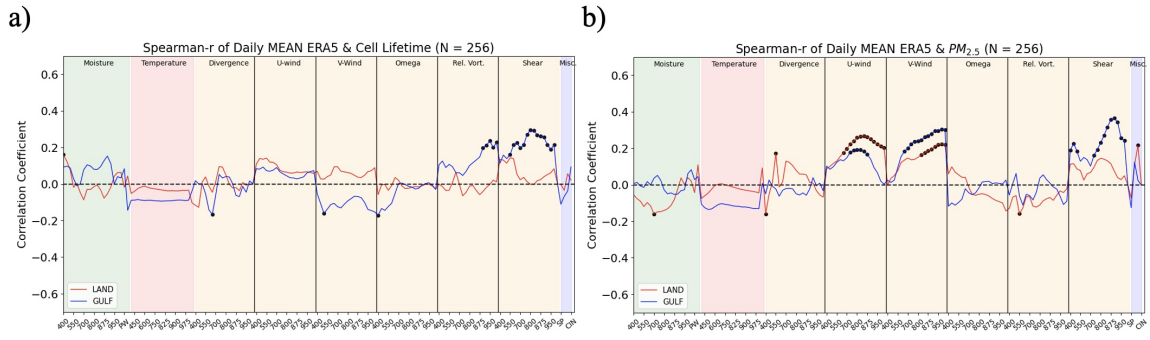

Figure 4.18: As in Figure 3.8 but for daily mean (a) DCC lifetime and (b) DCC $PM_{2.5}$ mass concentration. This diagram used the spatial DCC dataset.

Figures 4.19 a and b show scatter plots of DCC lifetime against $PM_{2.5}$ mass concentration for DCCs over land (Gulf) using the top and bottom quartiles of 400 mb relative humidity (omega). The distribution of points in both plots in Figure 4.19 are mostly parallel to the x axis showing near zero correlation between DCC lifetime and $PM_{2.5}$ mass concentration. Figure 4.20 shows similar analysis, but instead controls for MUCAPE as previous studies have shown the AIE on DCC lifetime can be strongly impacted by instability (e.g., Hu et al., 2019a; Khain et al., 2005, among others). No correlation in either MUCAPE environment is easily identifiable.

To further investigate correlations between DCC lifetime and $PM_{2.5}$ mass concentration, additional subsetting was completed by separating anthropogenic and natural aerosol regimes as done in section 4.1.1. First, correlation analysis was completed to identify correlations between meteorological variables and the two aerosol regime mass concentrations. Figure 4.21 shows that natural $PM_{2.5}$ mass concentration is strongly correlated with u and v-wind, consistent with analysis completed in section 4.1.1. Additionally, low-level relative humidity, surface dewpoint, and MUCAPE correlate significantly with natural $PM_{2.5}$ mass concentration over land. These correlations are consistent with physical understanding because if there are high natural $PM_{2.5}$ mass

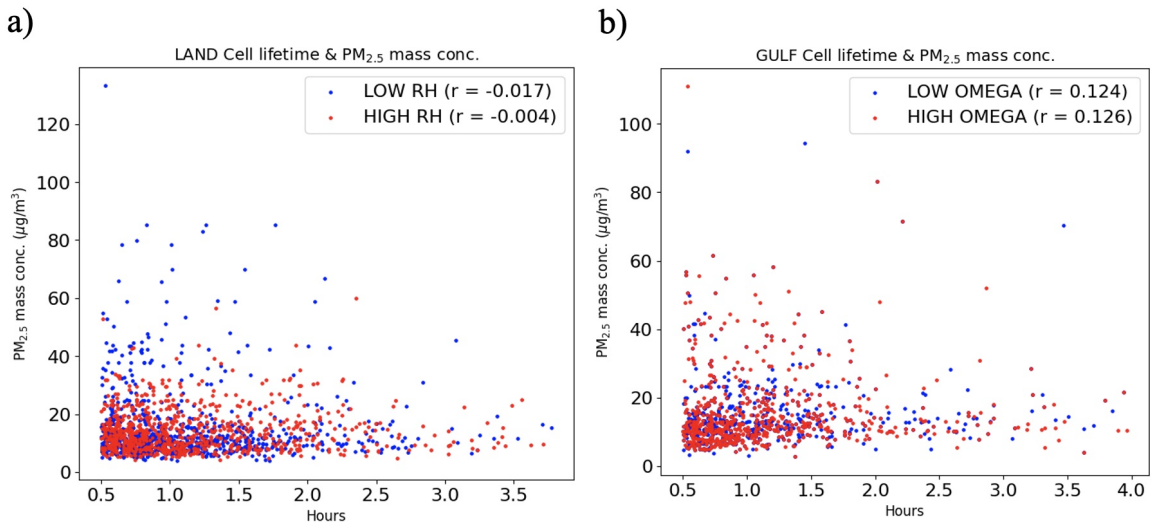

Figure 4.19: DCC lifetime vs. mean $PM_{2.5}$ mass concentration for DCCs in the top and bottom quartiles of (a) 400 mb mean relative humidity over land and (b) 400 mb mean omega over the Gulf of Mexico along with spearman correlation coefficients (r). None of the coefficients were significant at the 95% level.

concentrations inland from sea salt due to a strong southerly sea-breeze, then moisture and associated instability from these air masses should also be prevalent. Over the Gulf, natural $PM_{2.5}$ mass concentration correlates well with surface dew point and shear magnitude in the low-levels, consistent with increased evaporation of sea water and ejection of sea spray from strong flow regimes. For anthropogenic $PM_{2.5}$ mass concentration, correlations are very weak for DCCs over land and the Gulf with the only significant correlations occurring for land DCCs, namely with 600 mb relative humidity and 550 mb omega. Similar scatter plots as Figure 4.19 were constructed controlling for the meteorological variables discussed above to identify any dependence on lifetime and are shown in Figure 4.22. Regardless of how the data are stratified, no significant correlation with DCC lifetime can be seen for either the *NA* DCCs or *A* DCCs over land or over the Gulf.

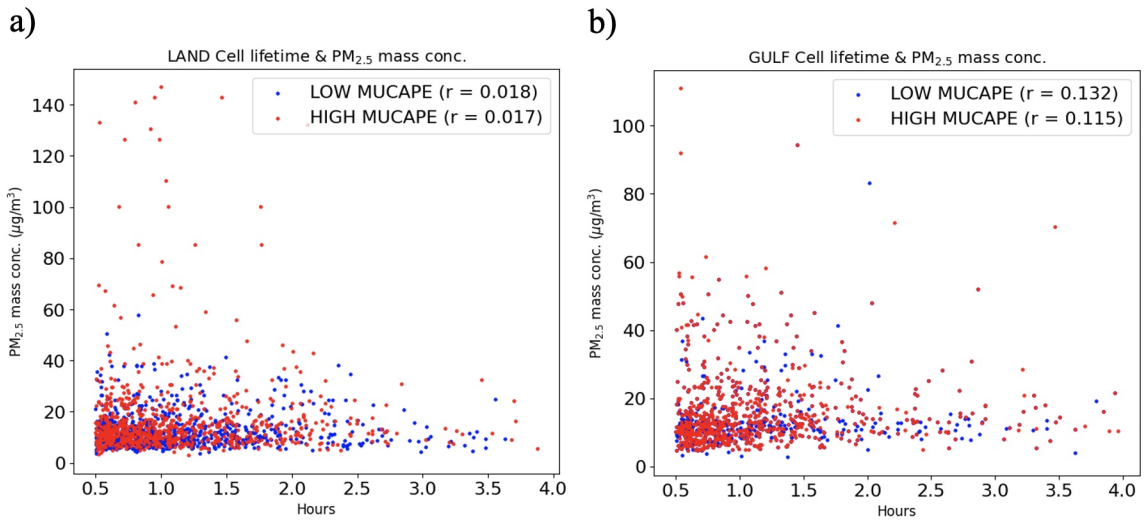

Figure 4.20: As in Figure 4.19 but DCCs were binned by the top and bottom quartiles of the MUCAPE distributions over land and the Gulf of Mexico.

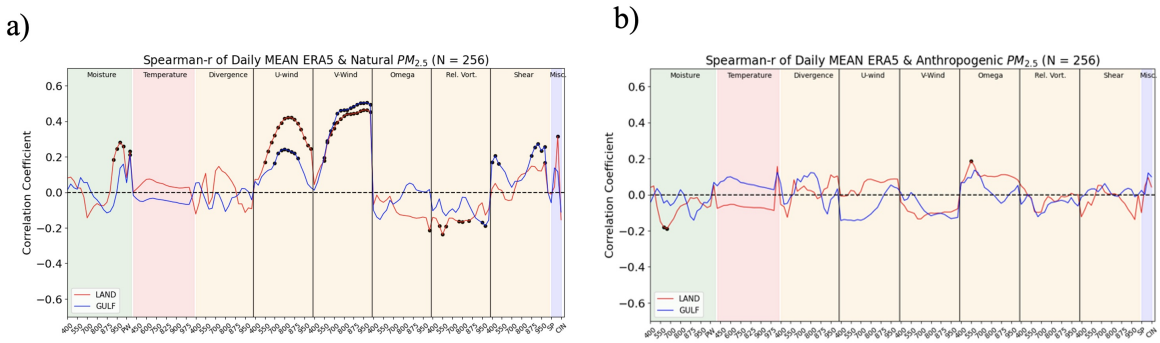

Figure 4.21: As in Figure 4.18 but for daily mean DCC (a) natural and (b) anthropogenic $PM_{2.5}$ mass concentration. This diagram used the spatial DCC dataset.

In summary, no correlation can be found between $PM_{2.5}$ mass concentration, whether natural or anthropogenic, and DCC lifetime. This indicates that DCC lifetime is heavily dependent upon many meteorological variables, and does not depend only on aerosol amount as noted by Varble (2018). This is compounded by the fact that the reanalysis data does not include all the meso- and smaller scale features that affect DCC evolution. There is a similar problem with the MERRA-2 aerosol representation as the grid spacing of the MERRA-2 is even larger than that of the ERA5. Lastly, the neighbor and saddle criteria used in the MCIT algorithm can influence the analyses as

the ability of the MCIT to detect DCCs when they are in the early or late stages of their life cycle directly affects the resulting calculation of DCC lifetime.

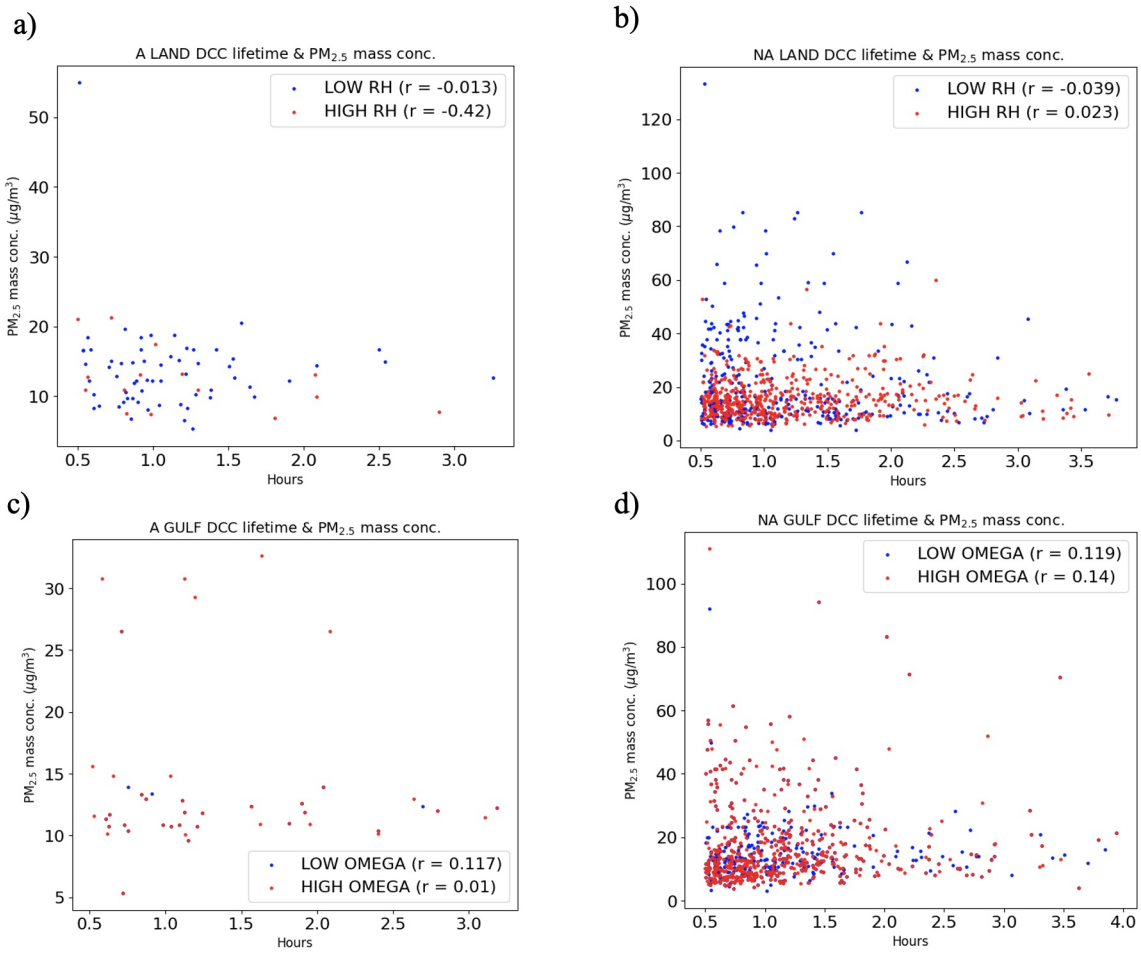

Figure 4.22: As in Figure 4.19 but subset for *NA* and *A* DCCs occurring over the land and Gulf of Mexico.

4.2 Vertical radar profiles

In this section, a comprehensive analysis of the distributions of Z and Z_{DR} across different altitudes in DCCs is presented. Similar to the analysis in section 4.1, DCCs are subset based upon their geographic location, aerosol regime, and meteorological

conditions. As discussed in section 3.2.3, composite difference CFADs are the primary method for determining differences in microphysical structure between DCCs supplemented by microphysical fingerprint parameter space (MPS) plots (Kumjian et al., 2022) that help interpret the physical meaning of the CFADs. CFADs are useful because they allow for a subset of DCCs to be quantitatively shown to have higher likelihoods of an inferred microphysical signature based on altitude relative to the freezing level, Z, and Z_{DR}.

4.2.1 Correlation analysis of ETH

Figure 4.23 shows daily mean correlations of maximum ETH achieved by DCCs and meteorological variables collected from the ERA5 reanalysis. MUCAPE and 550-400 mb relative humidity (RH) both show significant positive correlations with maximum ETH for DCCs over land and the Gulf. These variables are important for this study because they both have been shown to strongly mediate the AIE (e.g., Altaratz et al., 2014; Carrió et al., 2010, 2011; Hu et al., 2019a, among others) and thus should be controlled for to understand how different meteorological environments affect the AIE. Physically, a positive correlation between maximum ETH and RH indicates that there is less evaporation and sublimation of hydrometeors with increasing relative humidity, allowing for larger hydrometeors in higher concentrations in the DCCs that will reflect more signal power back to the radar, leading to a higher ETH. The opposite is also valid as lower relative humidity will cause higher evaporation and sublimation rates from entrainment and decrease the height to which an 18 dBZ echo reaches. A positive MUCAPE correlation is also physically consistent because higher instability equates to larger maximum vertical velocity and thus a larger acceleration of parcels, as represented by

$$w = \sqrt{\text{CAPE}} \tag{4.1}$$

and

$$\text{CAPE} = R_d \int_{p(z)}^{p_0} T_v^{'} d\ln p \ , \tag{4.2}$$

where p_0 and $p(z)$ define the lower and upper pressure levels of the layer, w is the maximum vertical velocity that can be attained by an updraft in that layer, R_d is the dry air gas constant, and $T_v^{'}$ is the layer mean virtual temperature (Moncrieff and Miller, 1976). Parcels with larger vertical velocities can loft larger hydrometeors further upward as well as create higher supersaturations within the updrafts that nucleate more particles, leading to higher altitudes of an 18 dBZ echo.

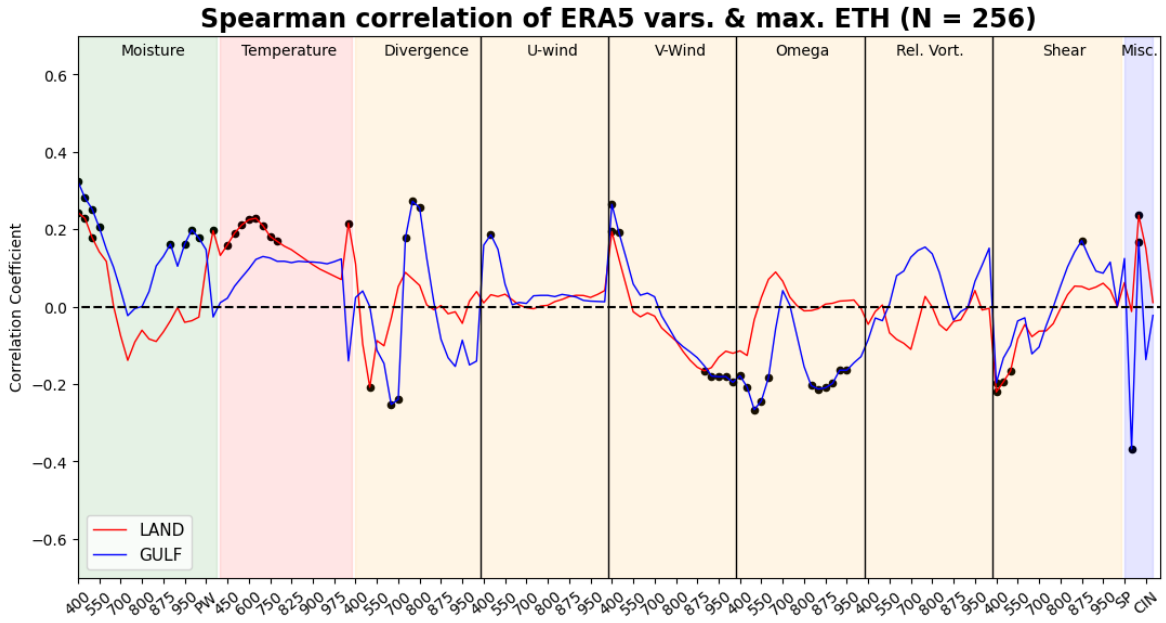

Figure 4.23: As in Figure 4.18 but for daily mean maximum ETH attained by the DCCs. This diagram used the radar dataset.

However, there are other significant correlations in Figure 4.23 in both geographic regimes that are important to understand and possibly account for. Including the

variables discussed above, the highest seven spearman correlation magnitudes for DCC maximum ETHs over the Gulf are with boundary layer height (BLH) (-0.37), RH (0.32), 650 mb divergence (D650) (-0.25), 500 mb omega (W) (-0.25), 400 mb v-wind (V) (0.25), 400 mb shear magnitude (SH) (-0.19), and MUCAPE (0.19). Over land, they are with RH (0.24), MUCAPE (0.23), 650 - 550 mb geopotential height (GH) (0.22), SH (-0.22), surface temperature (T) (0.21), 500 mb divergence (D500) (-0.21), and surface dewpoint (DEW) (0.19).

4.2.1.1 GULF DCCs

Figure 4.24a shows the mean spearman correlation matrix for all variables introduced above for Gulf DCCs. The spearman correlations in this figure are not calculated using a daily mean, but rather by taking the mean of each variable across the timeseries of each DCC. Figure 4.24a shows that D650 and W have a large spearman correlation of 0.7. Physically, this means that larger W (subsidence) occurs with larger divergence at lower levels, which is consistent with mass continuity. Since these two variables are highly correlated, only one needs to be chosen to classify DCCs. For this study, D650 is chosen instead of W for DCCs over the Gulf. Additionally, both of these variables present negative correlations with maximum ETH, which can be explained by the reasoning discussed in section 4.1.2, namely that less positive W, and thus less positive D650, from a weaker sinking branch of the sea breeze circulation allows updrafts to loft hydrometeors further upwards leading to higher ETHs.

The strongest correlation for maximum ETHs over the Gulf is BLH and is likely illustrating that higher surface temperatures over the Gulf cause stronger convective mixing, thus making the boundary layer taller (Stull, 1988). This is shown by the spearman correlation of 0.35 between T and BLH for DCCs over the Gulf and is

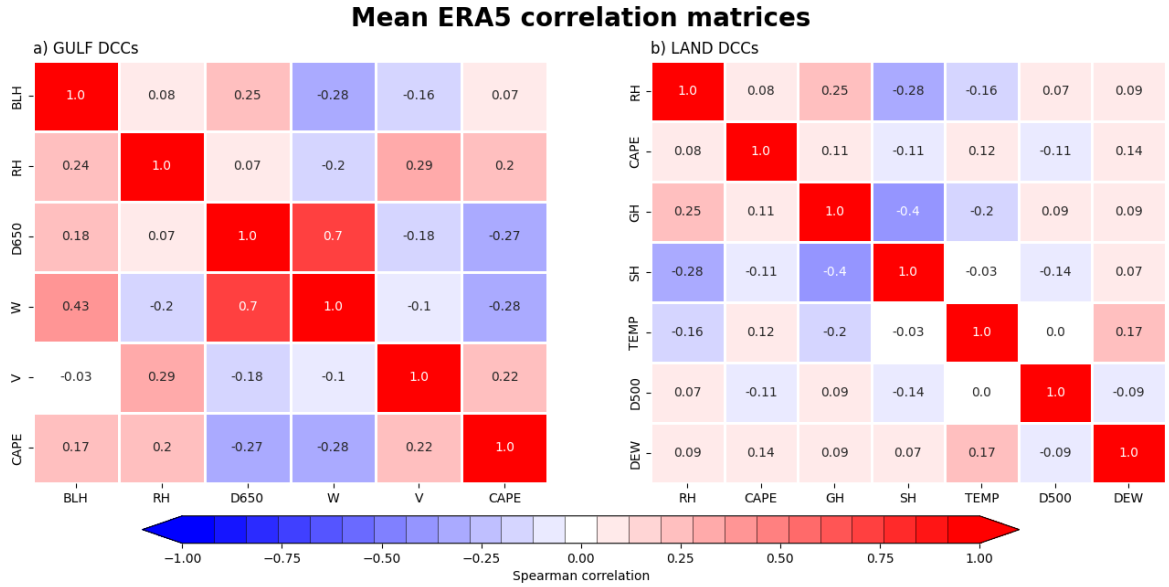

Figure 4.24: Correlation matrix for the meteorological variables that exhibit the top 6 (7) spearman correlation magnitudes from Figure 4.23 for GULF (LAND) DCCs for (a) ((b)). This figure excludes SH because SH correlates with $PM_{2.5}$ mass concentration from Figure 4.21 for Gulf DCCs. The correlations here are calculated by taking the mean of each DCC's timeseries for the respective meteorological variable to represent a single point and using those points to calculate correlation.

significant at the 95% level. A taller boundary layer over the Gulf exhibits more stability because the lapse rate is most likely near moist adiabatic, which limits surface instability and thus updraft buoyancy and associated ETH.

Finally, the last two correlated variables for Gulf DCC ETHs are SH and V. The negative correlations of SH and V with maximum ETH physically mean that the relatively narrow, ordinary, and isolated DCCs can be susceptible to entrainment effects caused by shear. The spearman correlation between these two variables is -0.42 and is significant at the 95% level. Physically, this means that a larger negative v-component of the wind at 400 mb can typically correlate with higher shear magnitude given that flow at the surface over the Gulf is typically southerly as discussed in section 4.1. Therefore, since SH and V are related and SH is significantly correlated with *NA* $PM_{2.5}$ mass concentration for DCCs over the Gulf (Figure 4.21), SH will be removed from subsequent analysis of DCCs over the Gulf and instead V will be used.

4.2.1.2 LAND DCCs

The strongest spearman correlation with DCC maximum ETHs over the land apart from RH and MUCAPE is GH. This is most likely due to stronger sea breeze frontogenesis that is established when synoptic-scale flow opposes on-shore flow (e.g. Arritt, 1993; Bechtold et al., 1991; Estoque, 1962; Noonan and Smith, 1987; Pielke, 1974). This opposing synoptic flow, which would be northerly or northwesterly to oppose the sea breeze front, is usually the result of a surface high pressure system near the study domain, meaning that GH is typically higher. The stronger frontogenesis can then lead to stronger DCCs over land that can loft hydrometeors further upwards. SH and D500 are both negatively correlated with DCC maximum ETHs because of similar reasoning as discussed in section 4.2.1.1. T and DEW for land DCCs are both positively correlated with maximum ETH because higher surface temperatures and dew points can

lead to larger surface instability. Figure 4.24b shows the mean correlation matrix for DCCs over land. The land correlation matrix does not show large values of correlation between the meteorological variables as did the gulf correlation matrix. Therefore, the highest seven meteorological variables are controlled for when analyzing LAND DCCs. However, MUCAPE and DEW are both correlated with *NA* $PM_{2.5}$ mass concentration for DCCs over the land (Figure 4.21) and thus are not used to classify DCCs in *NA* $PM_{2.5}$ regimes. A diagram depicting the breakdown of subsets for this analysis is presented in Figure 4.25, Table 4.1 illustrates all of the subsets with their sample sizes, and Figures 4.26 and 4.27 show the distributions for all meteorological variables sampled for DCCs discussed above across the two geographic regimes.

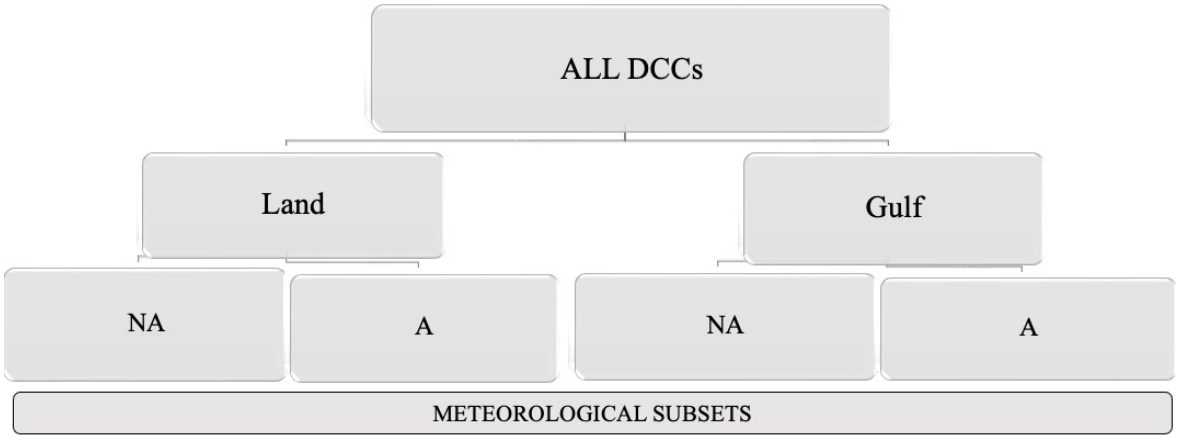

Figure 4.25: Breakdown of DCC subsets classification technique across geographic locations, aerosol regime, and meteorological conditions.

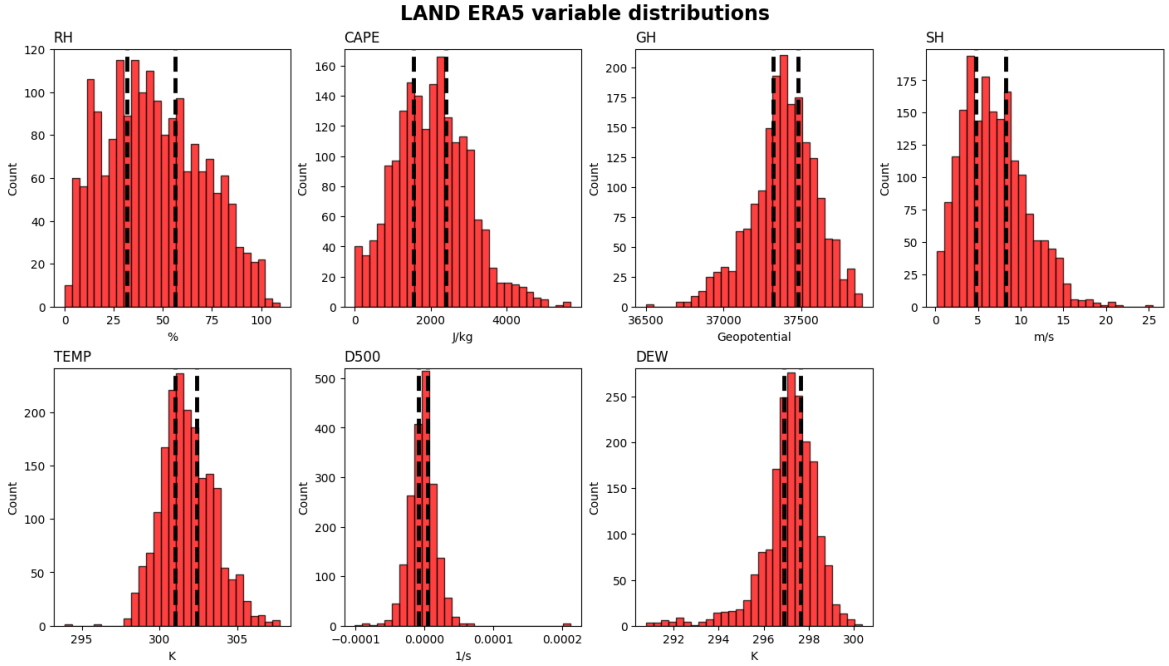

Figure 4.26: Distributions of the LAND DCC meteorological variables controlled for in the CFAD analysis. Vertical black dotted lines show the upper and lower terciles of the distributions.

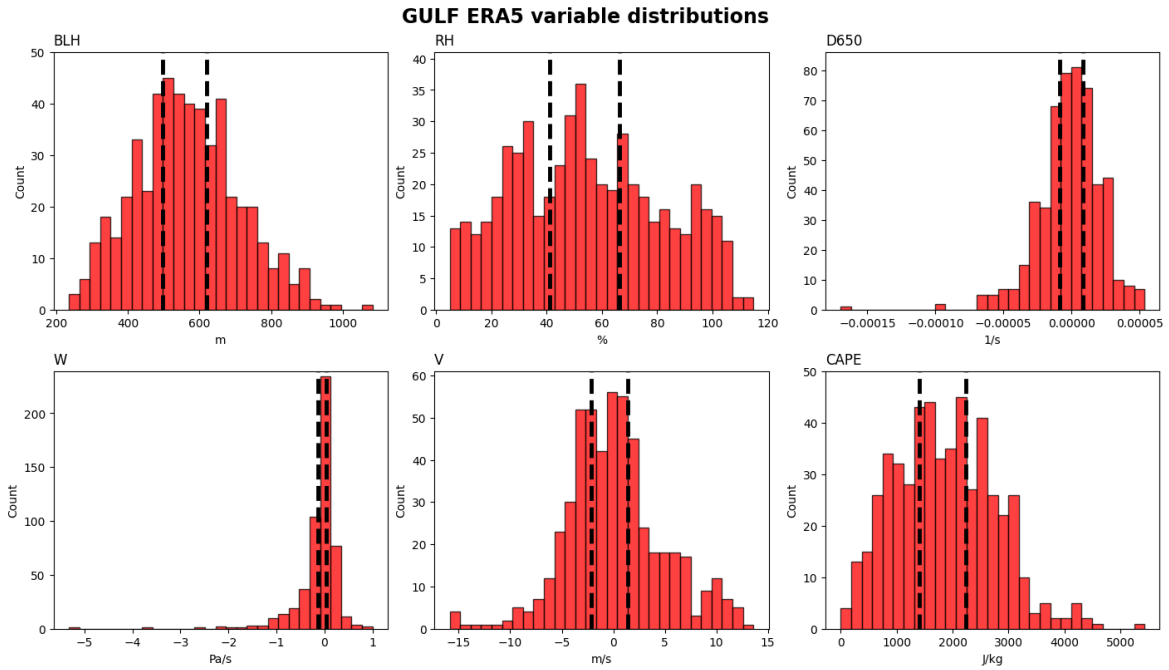

Figure 4.27: As in Figure 4.26 but for the GULF regime.

4.2.2 CFADs & microphysical fingerprints

Before showing analysis of DCCs under differing aerosol conditions, a comparison of stronger and weaker DCCs using the CFADs and MPS plots is presented so that correct interpretation of aerosol impacts can be made. Figures 4.28 and 4.29 show the CFADs and MPS plots for DCCs separated between geographic location and high and low MUCAPE since MUCAPE has been shown to positively correlate with stronger updrafts.

Below the freezing level, Figures 4.28a and 4.29a show that the difference in Z distributions of high and low MUCAPE DCCs is similar over land and over the Gulf. Low MUCAPE DCCs have a larger likelihood of exhibiting 25 dBZ $< Z <$ 40 dBZ whereas high MUCAPE DCCs are more likely to have Z in either the 0 – 25 dBZ or 40 – 55 dBZ range. Above the freezing level, Z is typically larger for high MUCAPE DCCs. The Z_{DR} profiles in Figures 4.28b and 4.29b show that the high MUCAPE DCCs are more likely to have larger Z_{DR} throughout the depth of the DCC, which includes dominance in the region bounded by 0 - 2 km and $Z_{DR} > 1$ dB, also known as the Z_{DR}-column region. The narrower distribution of Z and the larger likelihood of Z_{DR} less than 1 dB below the freezing level for low MUCAPE DCCs is consistent with a larger probability of smaller drops in higher concentrations. This is indicative of a larger probability of warm rain and is further corroborated by the KDE of the MPS plots (Figures 4.28d and 4.29d). This shows that low MUCAPE DCCs have a higher probability to occur in the upper-right quadrant, meaning that collision and coalescence is dominant since Z and Z_{DR} increase toward the ground. Meanwhile, the high MUCAPE DCCs have a larger likelihood of stronger size sorting in the CFADs because their Z_{DR} is more likely to be > 1 dB and $Z < 25$ dBZ, meaning sparse concentrations of large drops (Figures 4.28 and 4.29). The KDEs of the MPS plots

Invigoration	**# of DCCs**	**Inhibition**	**# of DCCs**	**Unclear**	**# of DCCs**
LAND-GULF	2412	A-NA GULF	413	NA LAND MED CAPE	356
A-NA LAND	1135	A LAND MED GH	44	NA LAND HIGH DEW	379
NA LAND	1034	A GULF	29	NA LAND MED DEW	373
NA GULF	384	A GULF LOW V	19	NA LAND MED GH	330
NA LAND HIGH CAPE	360	A GULF LOW CAPE	20	NA GULF HIGH BLH	38
NA LAND LOW CAPE	318	A LAND LOW RH	50	NA GULF LOW BLH	183
NA LAND HIGH RH	283			NA GULF MED W	109
NA LAND LOW DEW	282			NA GULF HIGH V	115
NA LAND HIGH RH	414			NA GULF MED V	109
NA LAND MED RH	329			NA GULF LOW V	160
NA LAND LOW RH	291			NA GULF HIGH D650	112
NA LAND HIGH SH	369			NA GULF MED D650	116
NA LAND MED SH	364			NA GULF LOW D650	156
NA LAND LOW SH	301			A LAND	101
NA LAND HIGH TEMP	275			A LAND HIGH D500	27
NA LAND MED TEMP	341			A LAND MED D500	32
NA LAND LOW TEMP	418			A LAND LOW D500	25
NA LAND HIGH GH	365			A LAND MED CAPE	22
NA LAND LOW GH	339			A LAND LOW CAPE	59
NA LAND HIGH D500	371			A LAND LOW GH	39
NA LAND MED D500	311				
NA LAND LOW D500	352				
NA GULF HIGH RH	188				
NA GULF MED RH	121				
NA GULF LOW CAPE	158				
NA GULF LOW W	172				
NA GULF MED BLH	163				
A LAND HIGH TEMP	51				

Table 4.1: Table listing all of the subsets generated from the techniques described in Figure 4.25 along with the sample sizes. Classifications are made based on if the subsets show invigoration, inhibition, or unclear impacts on DCCs from high $PM_{2.5}$, A, or LAND aerosol regimes. Some subsets generated have sample sizes < 10 DCCs and are not listed in this table.

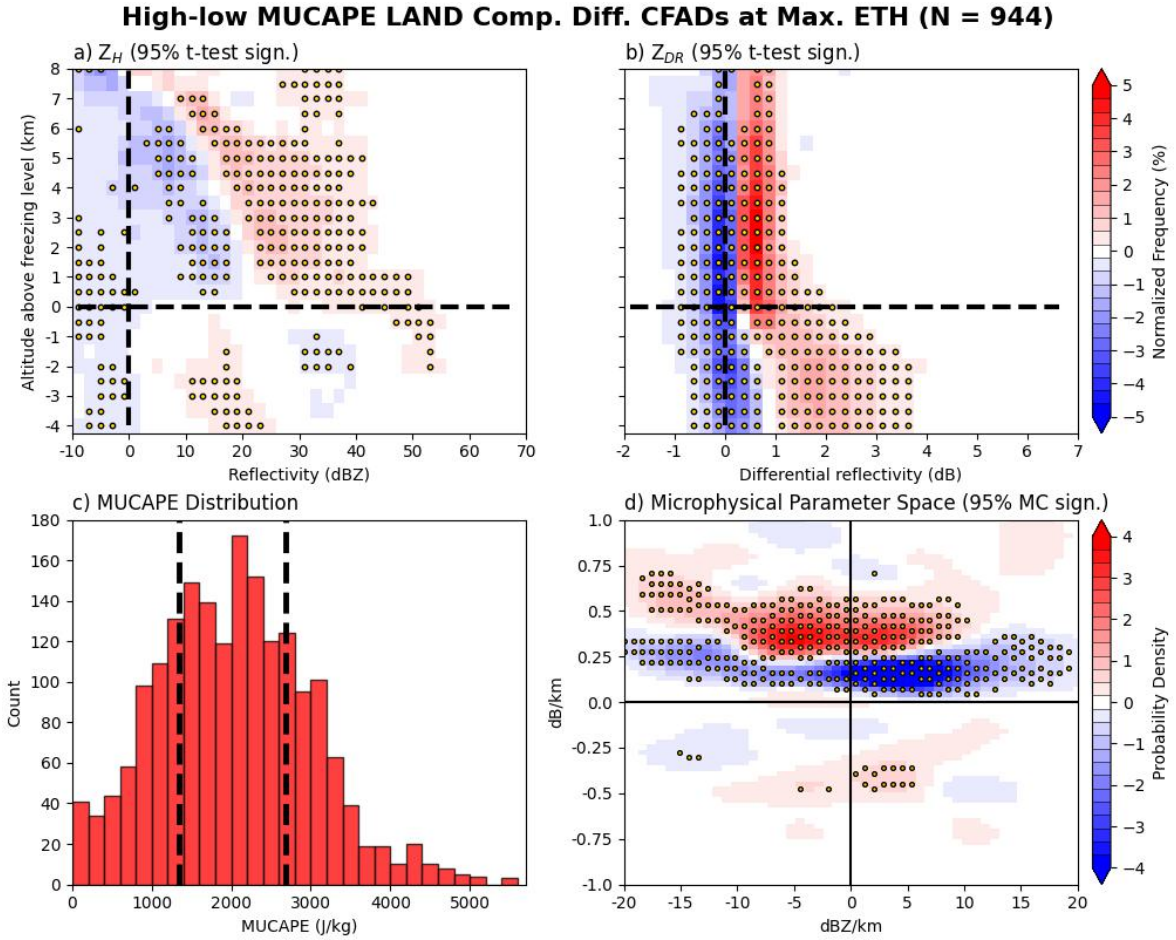

Figure 4.28: (a) Composite difference Z CFAD, (b) composite difference Z_{DR} CFAD, (c) distribution of LAND DCC's mean MUCAPE, and (d) composite difference KDE of the microphysical parameter space given by ΔZ and ΔZ_{DR} for DCCs used in the CFAD calculations. For (c), vertical black dotted lines indicate the upper and lower quartiles of the distribution and mark the DCCs which are used to calculate (a), (b), and (d). Color bar in first row corresponds to both CFADs. All DCCs are analyzed at the time of their maximum ETH. Stippling shows 95% significance using a t-test for (a) and (b) and using a 5000 iteration Monte-Carlo simulation for (d).

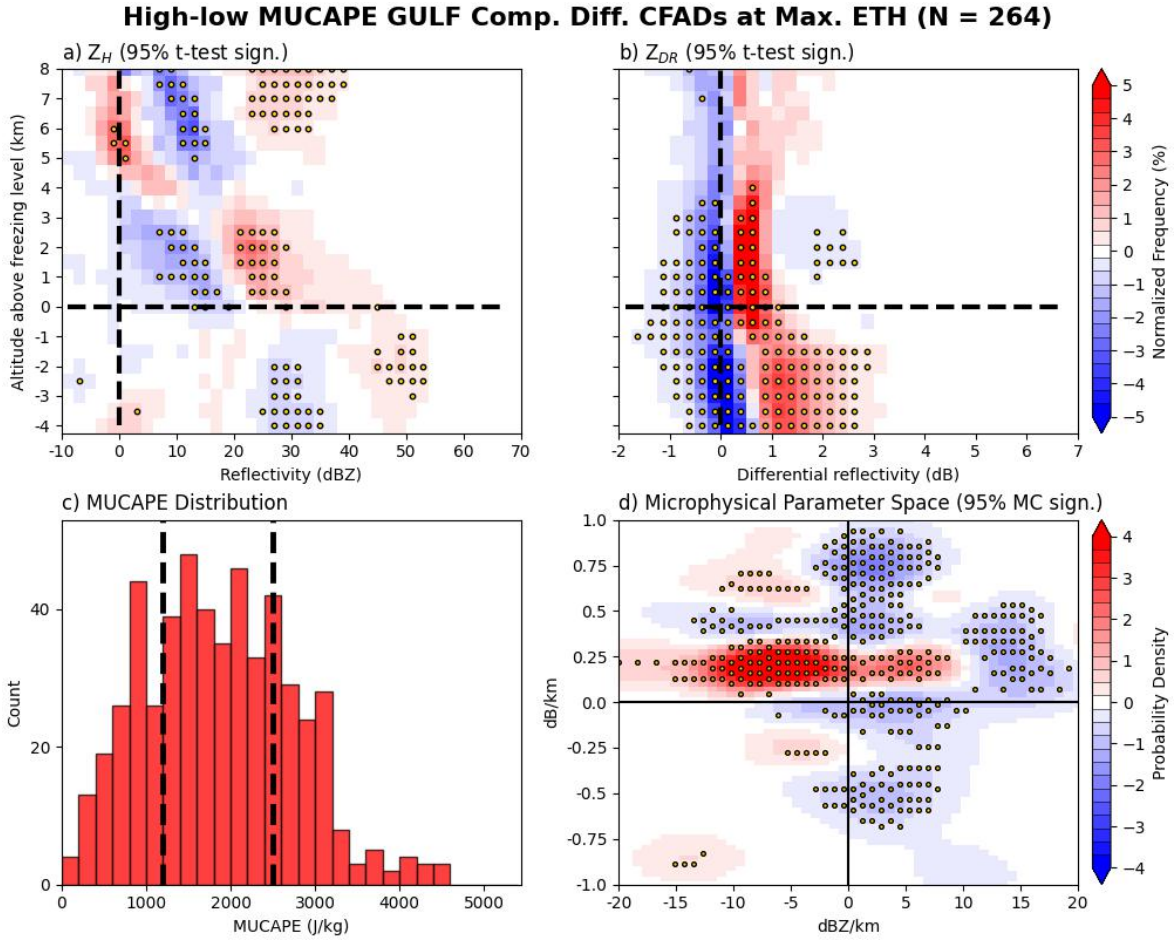

Figure 4.29: As in Figure 4.28 but for DCCs over the Gulf of Mexico.

also agree as they show higher likelihoods of high MUCAPE DCCs being in the upper-left quadrant (Figures 4.28d and 4.29d). A more probable size sorting signature means that the updrafts are likely to be stronger (Kumjian and Ryzhkov, 2012) and thus can loft more supercooled liquid further above the freezing level, creating more efficient riming and accretion processes on hail, graupel, and ice crystals, which produce higher Z_{DR} both above and below the freezing level. This is seen in the Z_{DR} CFADs which show the higher Z_{DR} for essentially all altitudes (Figures 4.28b and 4.29b). These more efficient mixed-phase processes then lead to heavier precipitation occurring below the freezing level as Z is also more likely to be $>$ 40 dBZ with $Z_{DR} > 1$ dB. Therefore,

DCCs with higher MUCAPE, regardless of geographic location, are more likely to be stronger in updraft strength and produce heavier precipitation.

As previously mentioned, the first step in the AIE is the inhibition of warm rain due to the increased concentration of CCN leading to smaller drops and a less efficient collision-coalescence processes. This means that DCCs with higher aerosol loading should exhibit less probability of warm rain compared to DCCs with lower aerosol loading under the same meteorological conditions. The AIE causes more liquid to be lofted above the freezing level and increase updraft strength via latent heat release from increased freezing rates. Therefore, to understand if there is an aerosol impact on DCCs within the Houston area, the differences in the dual-polarization distributions below the freezing level are examined. First, subsets from Table 4.1 that exhibit clear differences in the structure of radar data below the freezing level are discussed, followed by a discussion of the subsets that do not show a clear difference.

4.2.2.1 Clear microphysical impacts below the freezing level

4.2.2.1.1 Stronger size sorting for DCCs under high aerosol loading

The subsets that exhibit stronger size sorting for regimes with either high aerosol mass loading or an anthropogenic regime (i.e. DCCs over land or DCCs with the *A* distinction) are discussed first. High $PM_{2.5}$, LAND, or *A* DCCs within these subsets are assumed to have higher number concentrations of aerosols compared to the low $PM_{2.5}$ or *NA* DCCs. Results here are thus consistent with the first mechanism in the AIE theory, if it is the aerosol impacts that cause the stronger updrafts. The subsets that show the most coherent differences and that include large sample sizes are presented

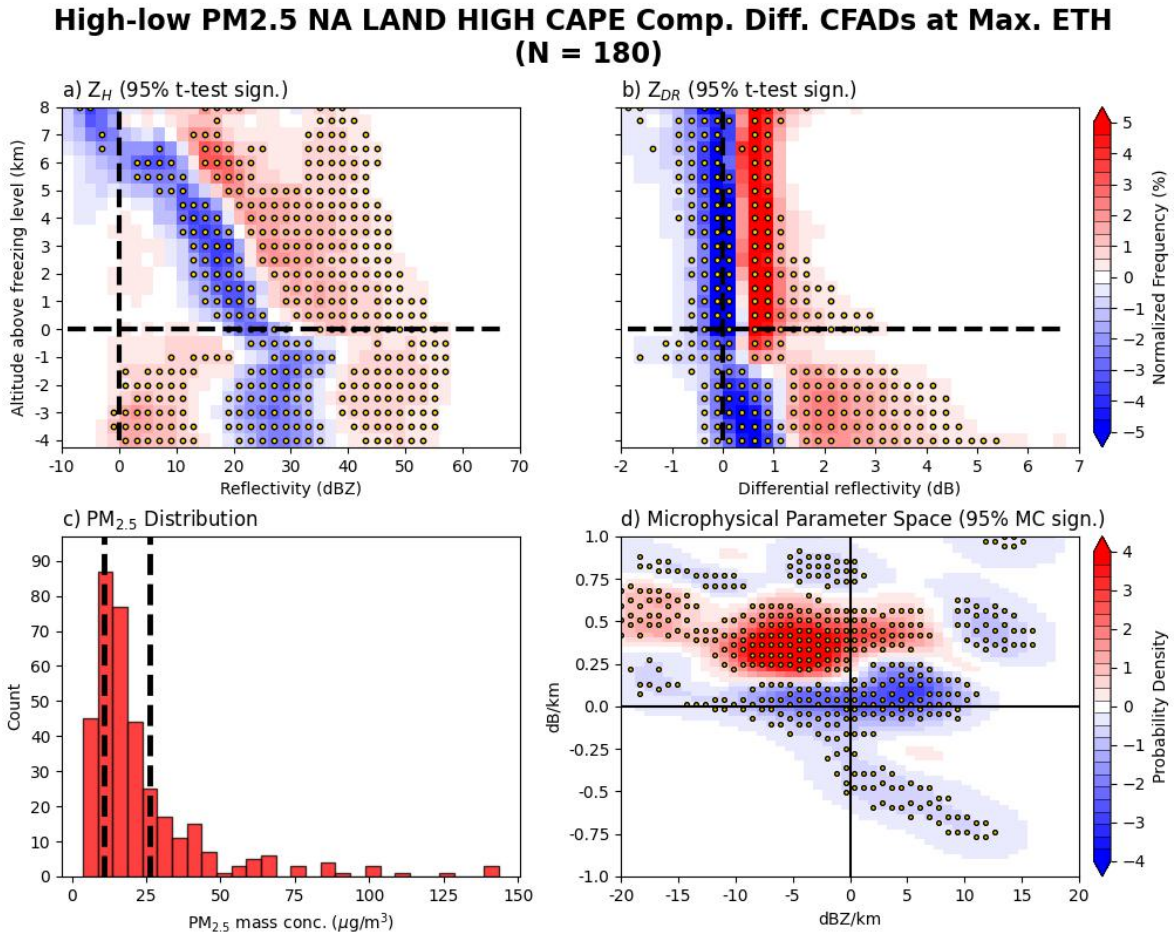

Figure 4.30: As in Figure 4.28 but for all *NA* LAND DCCs within the HIGH MUCAPE tercile. Also, distinction is made between high (red pixels) and low (blue pixels) $PM_{2.5}$ mass concentration, which are marked in (c) by the vertical black-dotted lines.

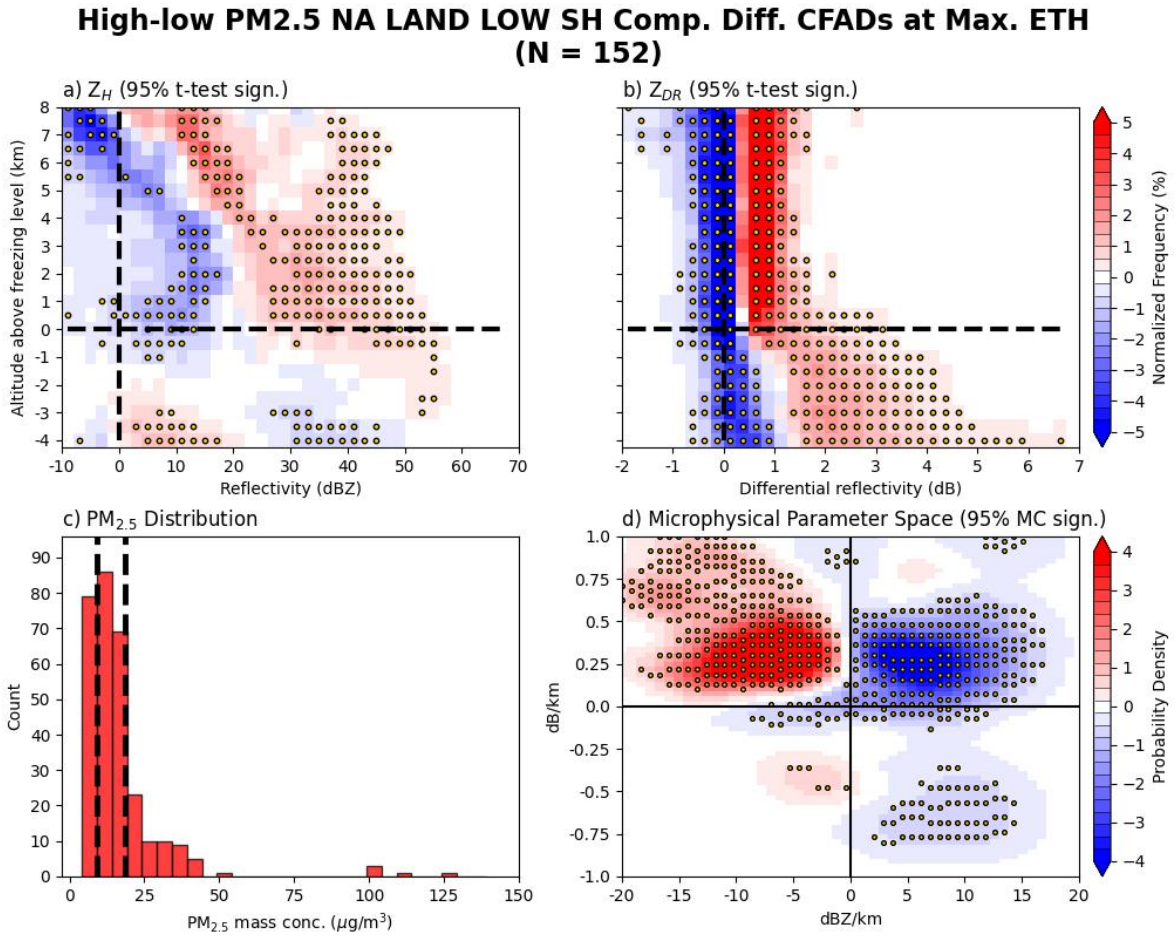

Figure 4.31: As in Figure 4.30 but for *NA* LAND DCCs within the LOW SH tercile.

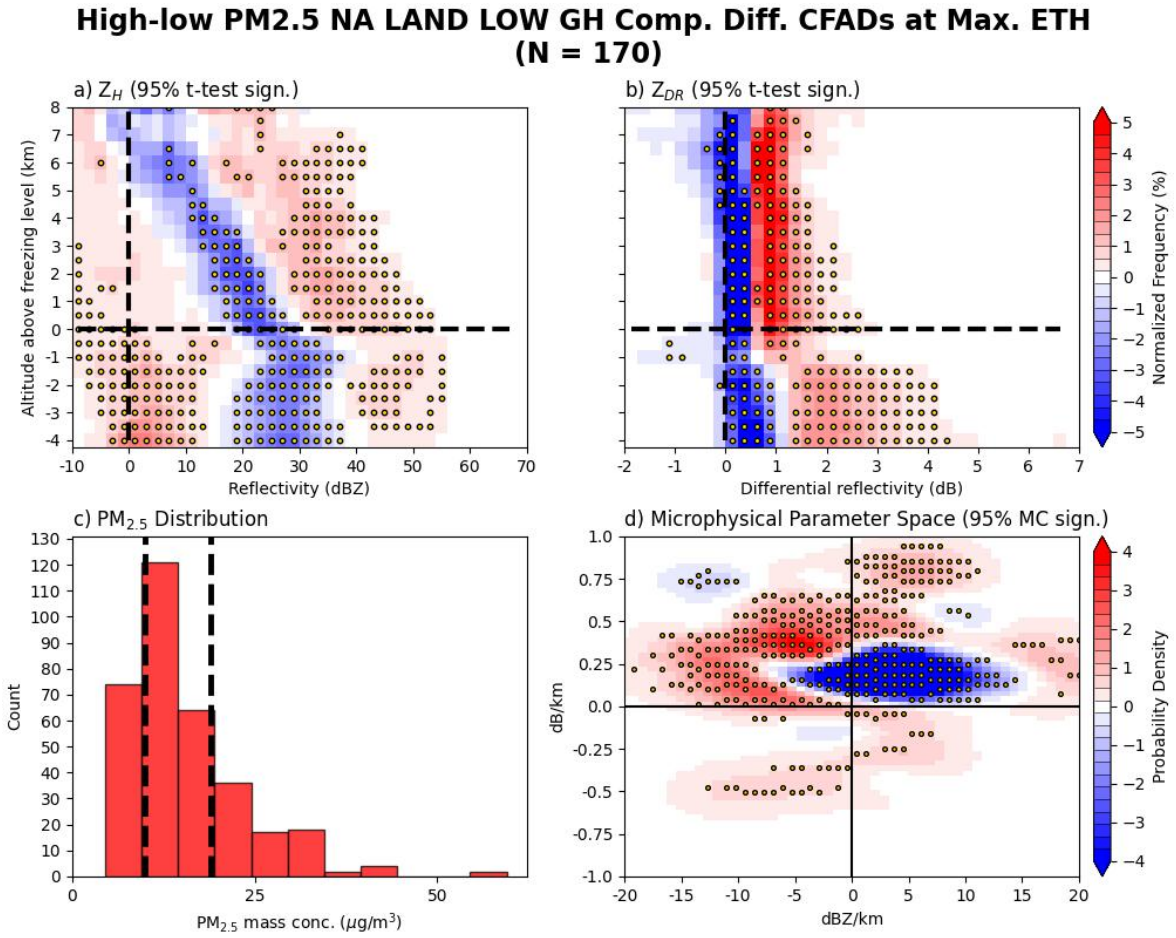

Figure 4.32: As in Figure 4.30 but for *NA* LAND DCCs within the LOW GH tercile.

and discussed thoroughly here (Figures 4.30 – 4.43). The numerous other subsets that are within this category are shown in Figures A.1 - A.12.

Figures 4.30, 4.31, 4.32, and 4.33 show the composite difference CFADs of Z and Z_{DR} below the freezing level for the *NA* LAND HIGH CAPE, LOW SH, LOW GH, and MED D500 subsets. They all show a narrow Z distribution that peaks around the 20 – 40 dBZ range coupled with Z_{DR} dominance < 1 dB for the low $PM_{2.5}$ DCCs (blue pixels). As discussed above with high and low MUCAPE DCCs, this signature represents an increased probability of warm rain because of the more probable moderate Z but small Z_{DR}. This is supported by the MPS plots where low $PM_{2.5}$ DCCs generally have their distribution of points in the coalescence quadrant. For high $PM_{2.5}$ DCCs, the CFADs show that the distribution of Z is wider with higher probability that Z_{DR} > 1 dB and is consistent with observations found by Martin et al. (2017). For these distributions of radar gates where $Z < 20$ dBZ and $Z_{DR} > 1$ dB, size sorting is more likely to occur for the high $PM_{2.5}$ DCCs. This is corroborated by the MPS plots which show higher probabilities for these DCCs in the size-sorting quadrant. In the larger side of the Z range, where radar gates from high $PM_{2.5}$ DCCs have a higher probability of $Z > 40 – 45$ dBZ, heavier precipitation is more likely to occur. The more intense precipitation may be caused by the increased buoyancy of the updrafts from an increased transport of liquid past the freezing level and associated increased latent heating from more efficient riming and accretion processes. This is consistent with the AIE and with processes that were noted in modeling studies such as Carrió et al. (2010), Carrió et al. (2011), Ilotoviz et al. (2018), and Khain et al. (2005) and through observations by Martin et al. (2017) in which increases in transport of liquid above the freezing level for high CCN DCCs led to higher Z_{DR} values due to more efficient riming

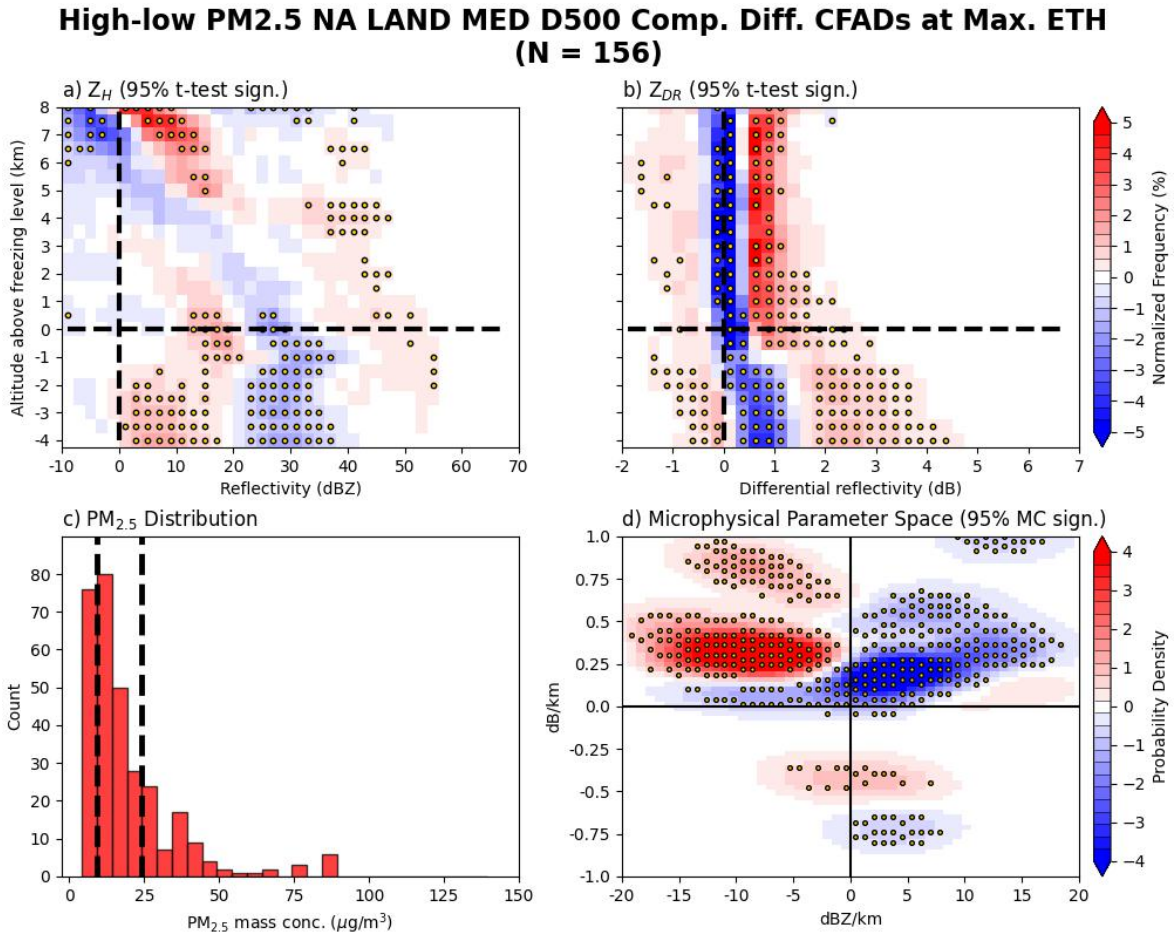

Figure 4.33: As in Figure 4.30 but for all *NA* LAND DCCs within the MED D500 tercile.

and accretion which can also produce higher Z. These stronger updrafts are then able to produce more intense precipitation, yielding larger Z below the freezing level.

Subsets *NA* LAND, *NA* LAND LOW CAPE, HIGH SH, MED SH, and LOW DEW in Figures 4.34, 4.35, 4.36, 4.37, and 4.38 all show a similar pattern in the Z_{DR} CFADs to the subsets discussed above in which higher Z_{DR} is more likely for the high $PM_{2.5}$ DCCs across all altitudes. However, above and below the freezing level the *NA* LAND, *NA* LAND LOW CAPE, HIGH SH, MED SH, and LOW DEW subsets do not exhibit the increased precipitation pattern illustrated for the high $PM_{2.5}$ DCCs. Instead, either there is not a statistically significant difference between high and low $PM_{2.5}$ DCCs for $Z > 40$ dBZ (Figures 4.34a, 4.36a, 4.37a, and 4.38a) or the low $PM_{2.5}$ DCCs exhibit higher likelihood of $Z > 40$ dBZ (Figure 4.35a) below the freezing level. This means while there is likely less warm rain and stronger size sorting resulting in the higher Z_{DR} values above and below the freezing level for the high $PM_{2.5}$ DCCs, the precipitation is not enhanced compared to low $PM_{2.5}$ DCCs at the times of maximum ETH. These patterns are consistent with findings of Fan et al. (2009) who showed that high shear can lead to decreases in precipitation enhancement by causing increased evaporation and sublimation through entrainment effects on high $PM_{2.5}$ DCCs. Additionally, Altaratz et al. (2014) explained that environments of low CAPE can suppress the AIE and precipitation intensity due to the lack of vertical velocity available to loft the increased concentrations of hydrometeors further past the freezing level to allow for more efficient cold-phase precipitation production. Additional subset figures that are similar to these are shown in Appendix A.

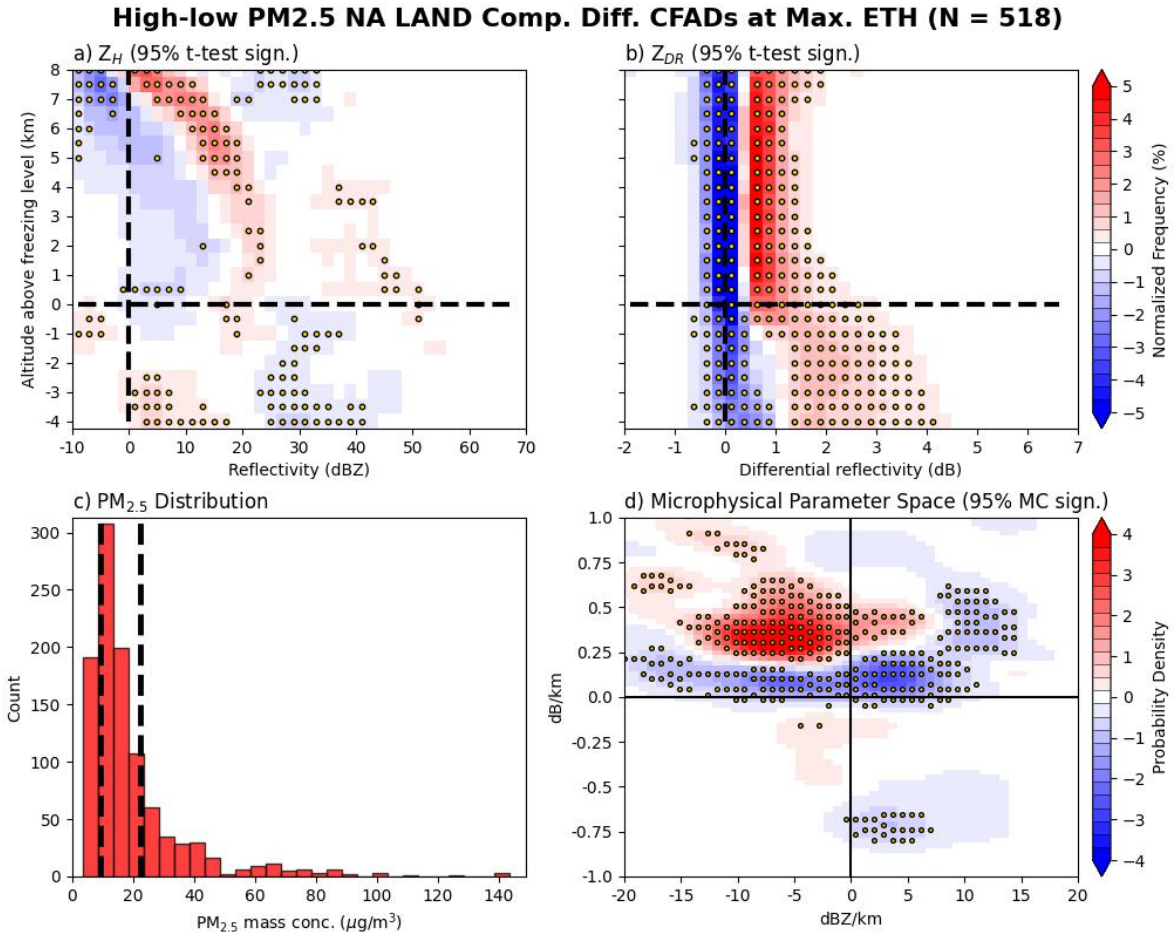

Figure 4.34: As in Figure 4.30 but for all *NA* LAND DCCs.

Subsets LAND-GULF, *NA* GULF LOW CAPE, and MED BLH, shown in Figures 4.39, 4.40, and 4.41, all show similar Z composite difference CFADs to subsets such as *NA* LAND HIGH CAPE, in which increased size sorting strength, increased precipitation intensity, and increased Z above the freezing level are more likely for high $PM_{2.5}$ or land DCCs. However, the Z_{DR} CFADs show that the dominance of higher Z_{DR} switches to favor low $PM_{2.5}$ or Gulf DCCs above the freezing level and that there is generally a lack of statistically significant differences in the Z_{DR}-column region. This is consistent with the high $PM_{2.5}$ or land DCCs having less efficient riming and accretion,

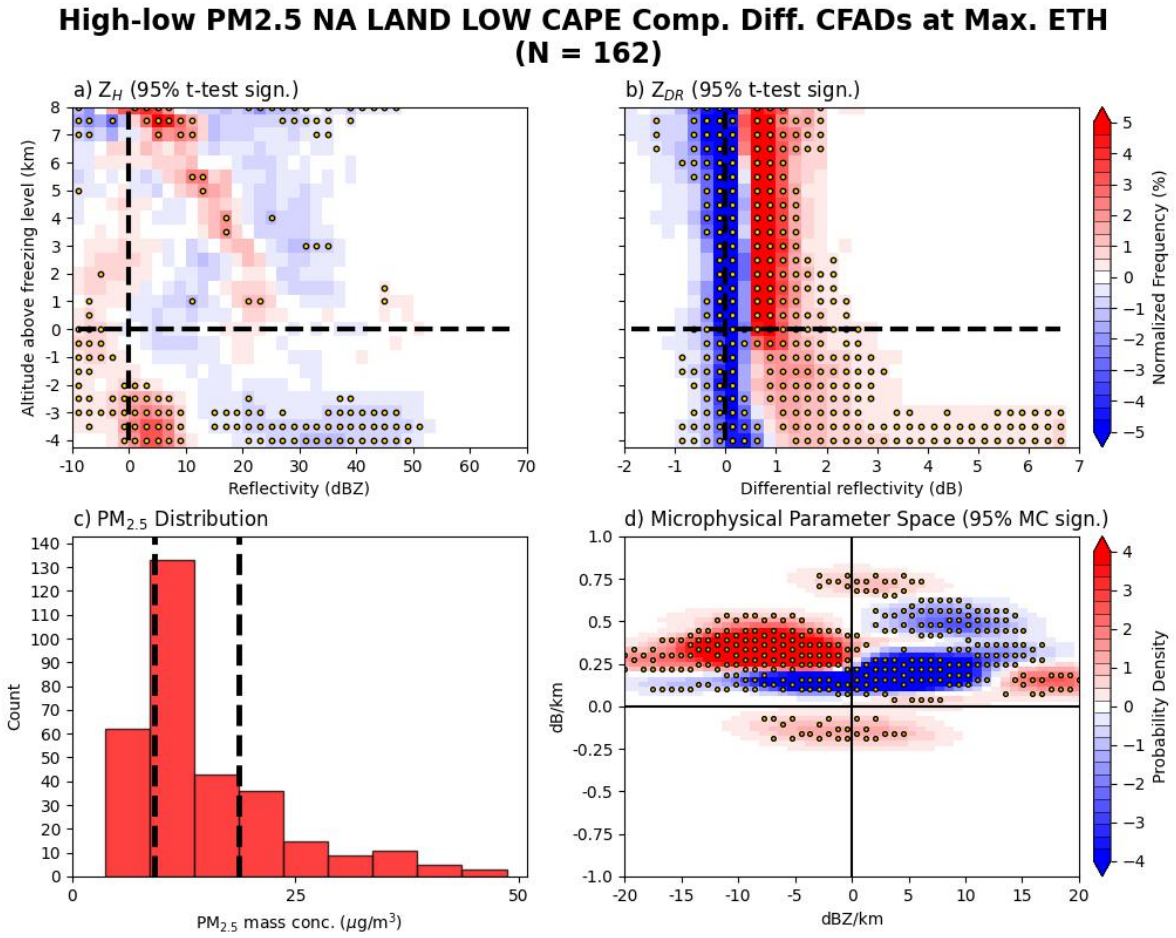

Figure 4.35: As in Figure 4.30 but for all *NA* LAND DCCs within the LOW CAPE tercile.

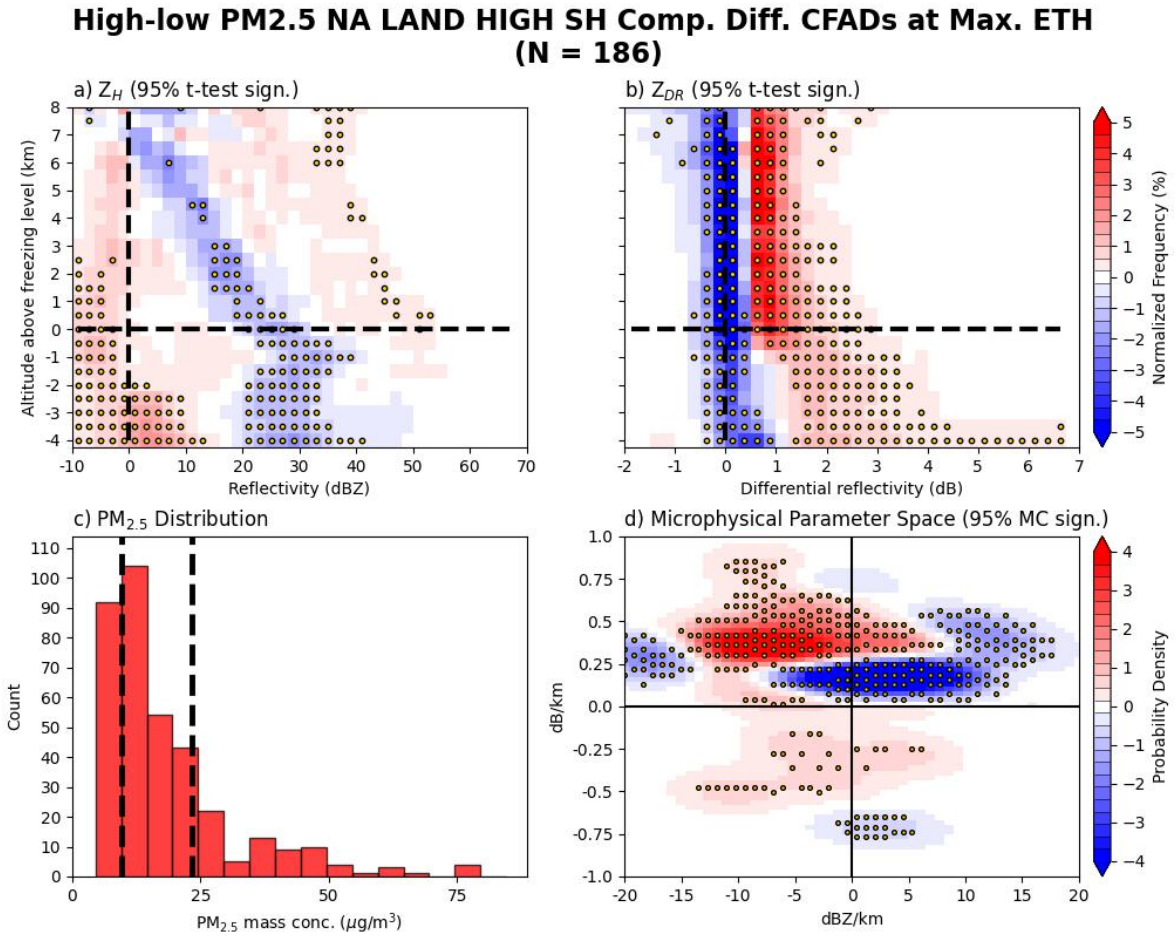

Figure 4.36: As in Figure 4.30 but for all *NA* LAND DCCs within the HIGH SH tercile.

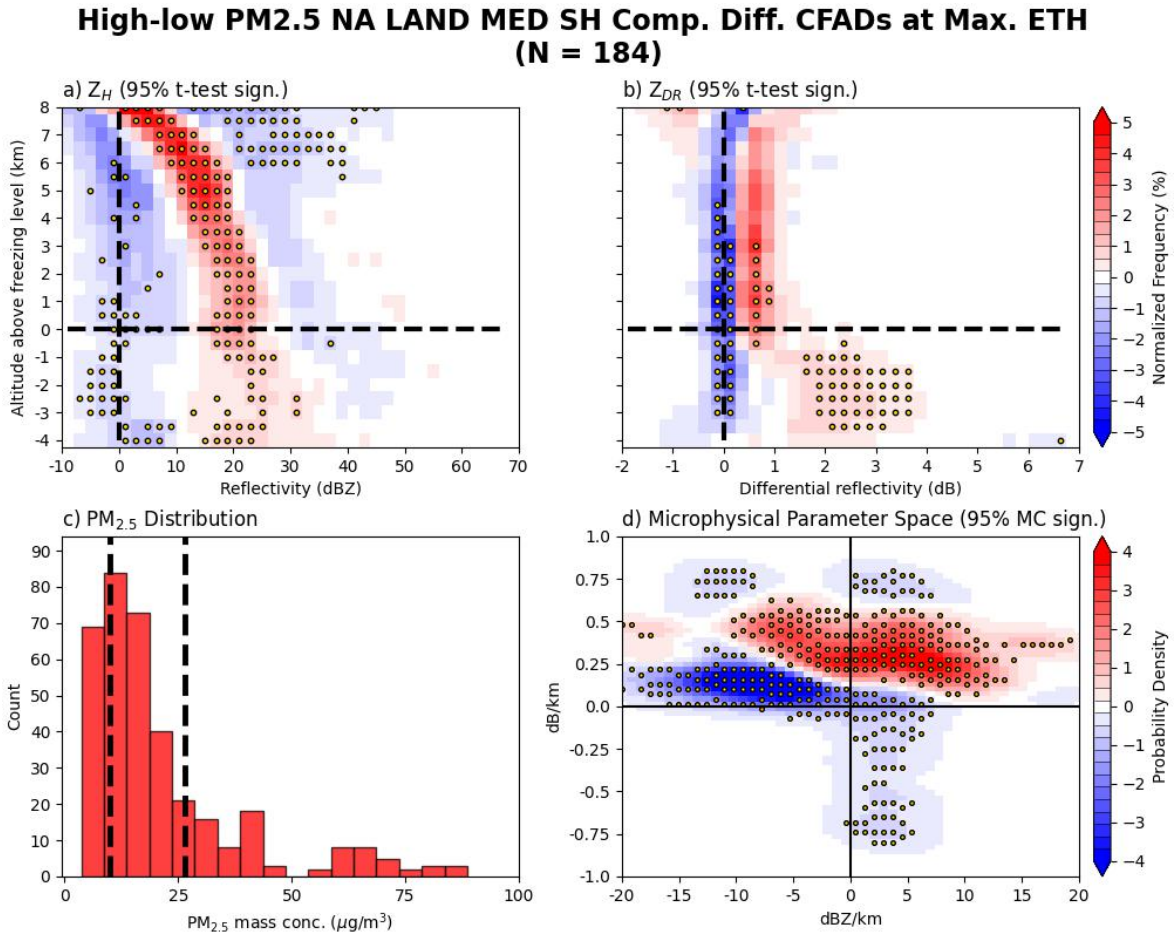

Figure 4.37: As in Figure 4.30 but for all *NA* LAND DCCs within the MED SH tercile.

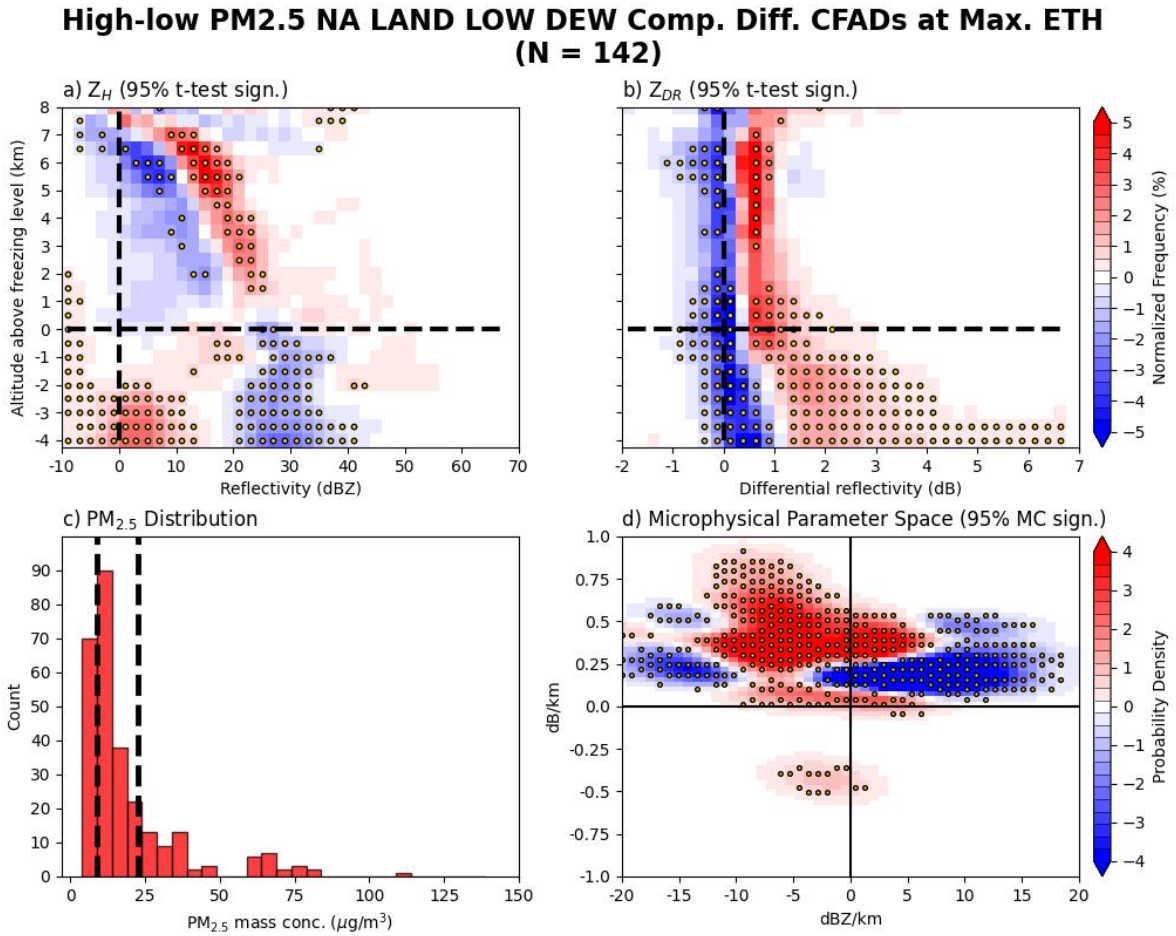

Figure 4.38: As in Figure 4.30 but for all *NA* LAND DCCs within the LOW DEW tercile.

even though the probability of increased transport of liquid mass past the freezing level via the inhibition of warm rain should be larger. The exact microphyiscal mechanisms behind why the high $PM_{2.5}$ or land DCCs in these subsets exhibit higher likelihoods of lower Z_{DR} above the freezing while still exhibiting higher likelihoods of stronger updrafts illustrated by the CFADs and MPS plots is not known. In-situ observations within DCCs at these altitudes above the freezing level along with measurements of background aerosol characteristics would be beneficial to conclude why riming and accretion are not as efficient for high $PM_{2.5}$ or land DCCs in these subsets.

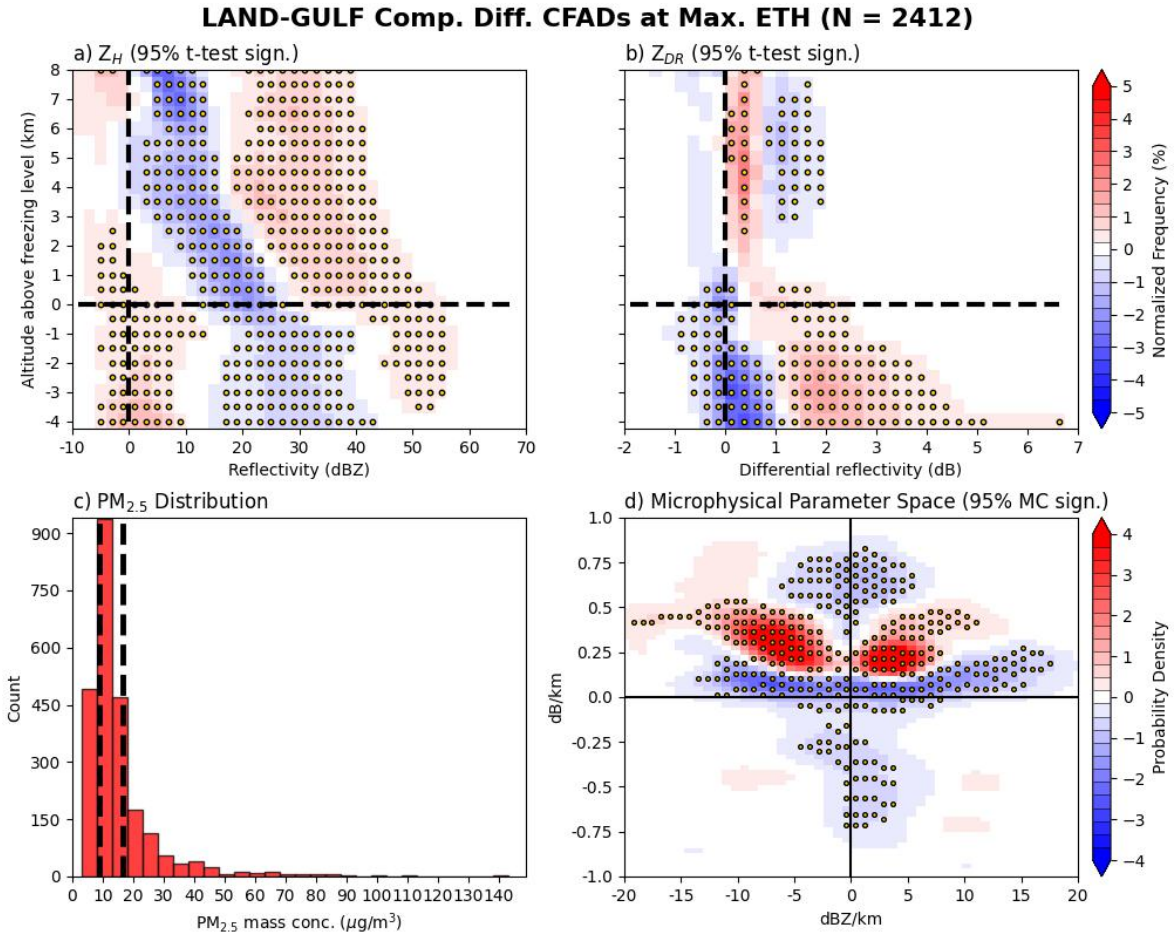

Figure 4.39: As in Figure 4.30 but for all DCCs. Distinction is made between LAND (red) and GULF (blue) DCCs.

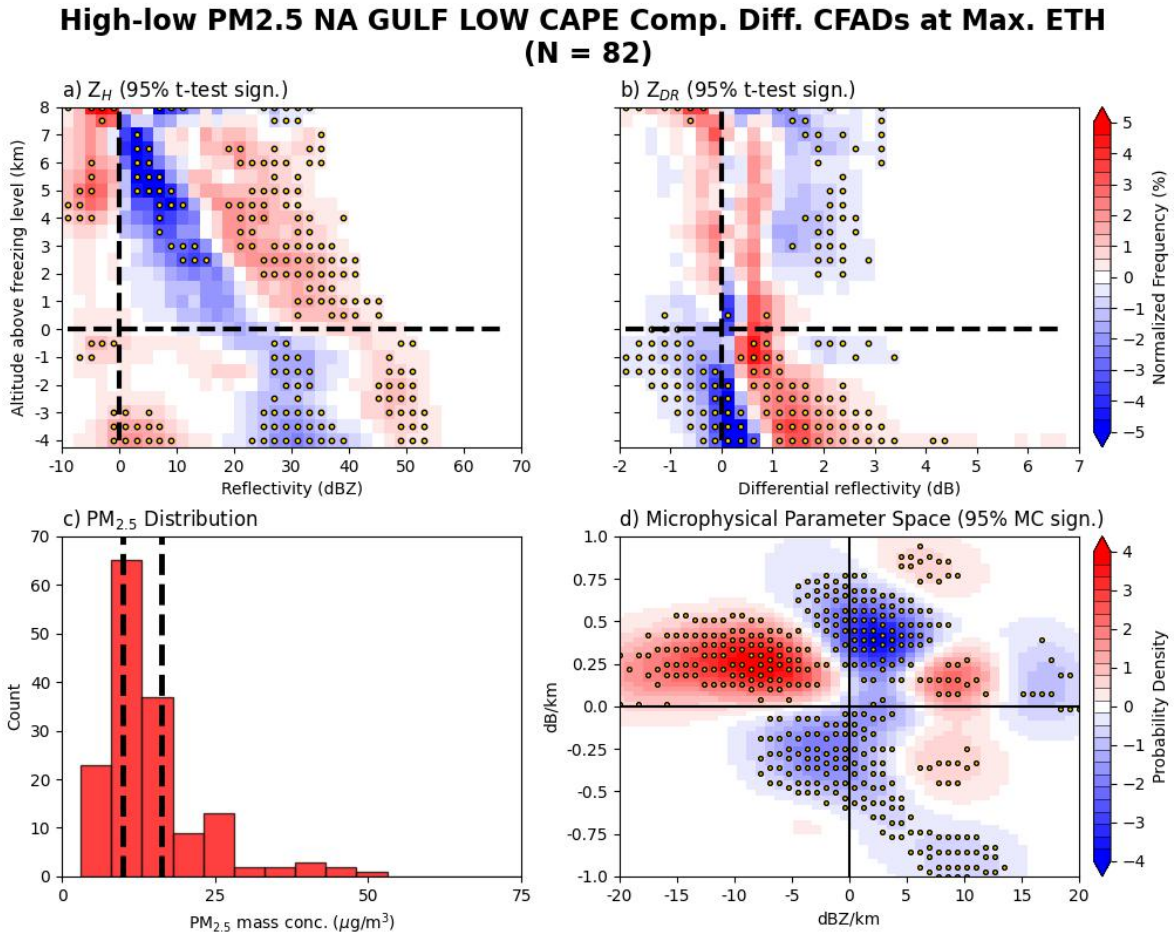

Figure 4.40: As in Figure 4.30 but for all *NA* GULF DCCs within the LOW CAPE tercile.

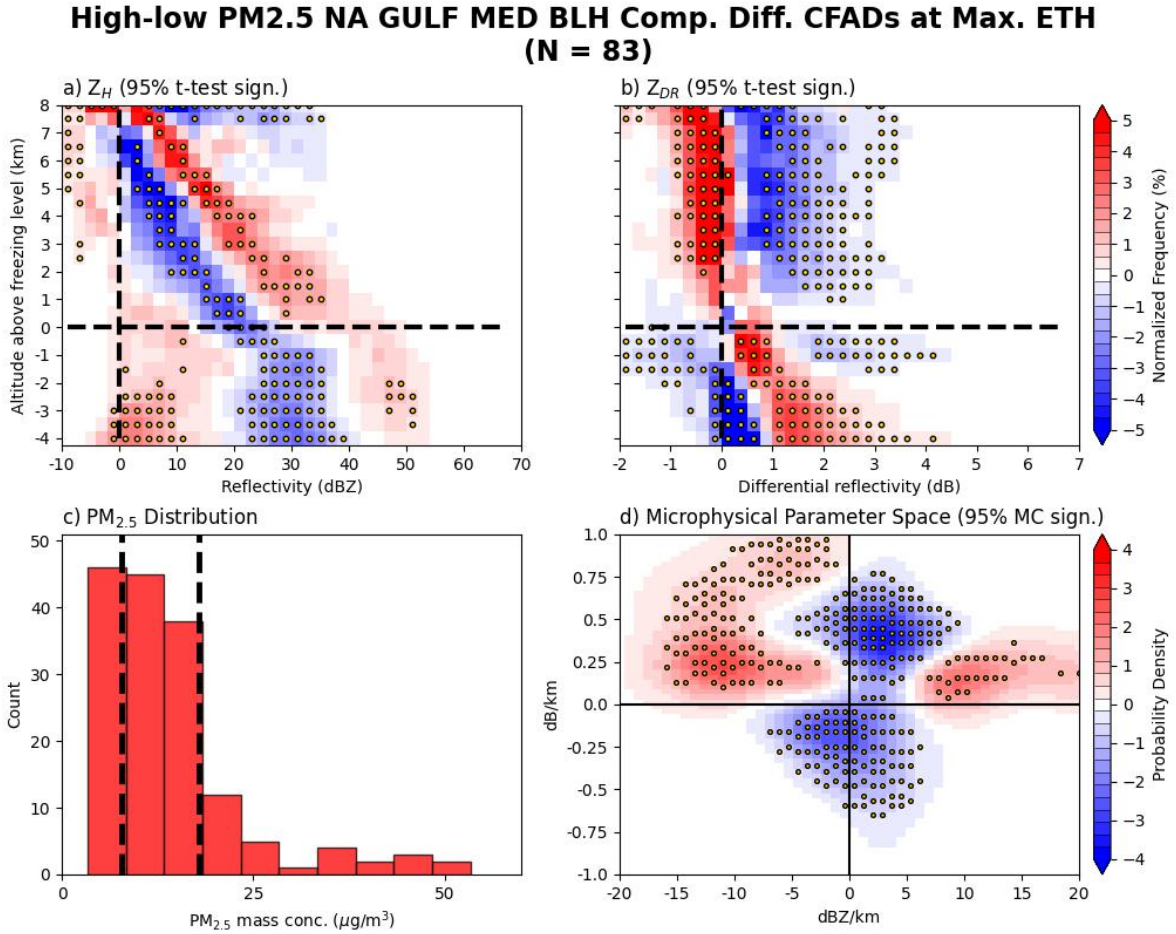

Figure 4.41: As in Figure 4.30 but for all *NA* GULF DCCs within the MED BLH tercile.

Figure 4.42b shows that there is a lack of a dominant DCC regime within the Z_{DR}-column region for the *NA* GULF HIGH RH subset. The Z_{DR}-column region is shown to have a relative difference no larger than 0.5% and thus is consistent with the high $PM_{2.5}$ DCCs not exhibiting more efficient riming and accretion processes, even if the updrafts are more likely stronger from the observed signature stronger of size sorting (Figure 4.42d). For the altitudes above the Z_{DR}-column region the likelihood of Z_{DR} > 1 dB switches toward the low $PM_{2.5}$ DCCs and is statistically significant all the way to near 3 dB, meaning that the low $PM_{2.5}$ DCCs are more likely to exhibit ice crystal habits such as needles and columns that are horizontally oriented, which produce high Z_{DR} high above the freezing level (Giangrande et al., 2016; Hogan et al., 2002; Sinclair et al., 2016). Meanwhile, $Z_{DR} < 1$ dB is more likely in the high $PM_{2.5}$ DCCs which indicates larger likelihood of aggregated ice crystal habits due to their more random aspect ratios and orientations. The mechanisms behind why these different ice crystal habits occur more frequently depending on the $PM_{2.5}$ mass concentration in this subset is not immediately clear. A plausible cause is that the high ambient relative humidity allows for more efficient columnar ice production at these altitudes for both DCC aerosol regimes. However, the high $PM_{2.5}$ DCCs are more likely to have ice crystals aggregate together because their concentrations are higher from the typical AIE mechanism of increased amount of droplets transported above the freezing level, which can lead to higher number concentrations of frozen hydrometeors (Rosenfeld et al., 2008). Once aggregates form, they can exhibit higher mean aspect-ratios and thus lower Z_{DR} measurements (e.g., Andrić et al., 2013; Kennedy and Rutledge, 2011; Schrom et al., 2015). It is important to note that this process may not be as frequent for the *NA* LAND HIGH RH subset because the riming and accretion processes may be more efficient for high $PM_{2.5}$ DCCs over land illustrated in Figure 4.43b. This figure shows higher Z_{DR} for high $PM_{2.5}$ DCCs above the freezing level and is consistent with more

efficient riming and accretion, causing a smaller number concentration of ice crystals further above the freezing level if they grow to larger sizes and precipitate out, which is likely given that high $PM_{2.5}$ DCCs exhibit higher Z above the freezing level. Interestingly, the *NA* GULF HIGH BLH subset also shows a similar pattern to the *NA* GULF HIGH RH subset, where low $PM_{2.5}$ DCCs dominate very large values of Z_{DR} far above the freezing level (Figure 4.41b). The mechanisms behind why moderate BLH would cause this is not known and would require further data from field campaigns. Other subsets that present unclear patterns when uncovering likely processes that lead to updraft invigoration through aerosol impacts are shown in Appendix B.

In summary, the subsets discussed here have all shown that high $PM_{2.5}$, LAND, and *A* DCCs exhibit patterns consistent with stronger size sorting than the low $PM_{2.5}$, GULF, or *NA* DCCs as noted in the Z and Z_{DR} CFADs and the MPS plots. This stronger size sorting is a signature of stronger vertical velocities in updrafts, and thus is consistent with the action of the AIE "invigorating" DCCs through the inhibition of warm rain. Consistent signatures are also noted in MPS plots throughout these subsets. However, differences have been seen and analyzed in both the intensity of the precipitation and the efficiency of cold-phase precipitation processes depending on meteorological conditions, with exact reasons and mechanisms for this not known.

4.2.2.1.2 Stronger size sorting for DCCs under low aerosol loading

A discussion regarding subsets of DCCs that exhibit lower precipitation intensity and updraft strength when loaded under high $PM_{2.5}$ mass concentration is presented next, with Table 4.1 listing them and their respective sample sizes. It should be noted that the sample sizes for these subsets can sometimes be quite low, with contributions of not more than 22 DCCs included in the calculation of the CFADs for all but one

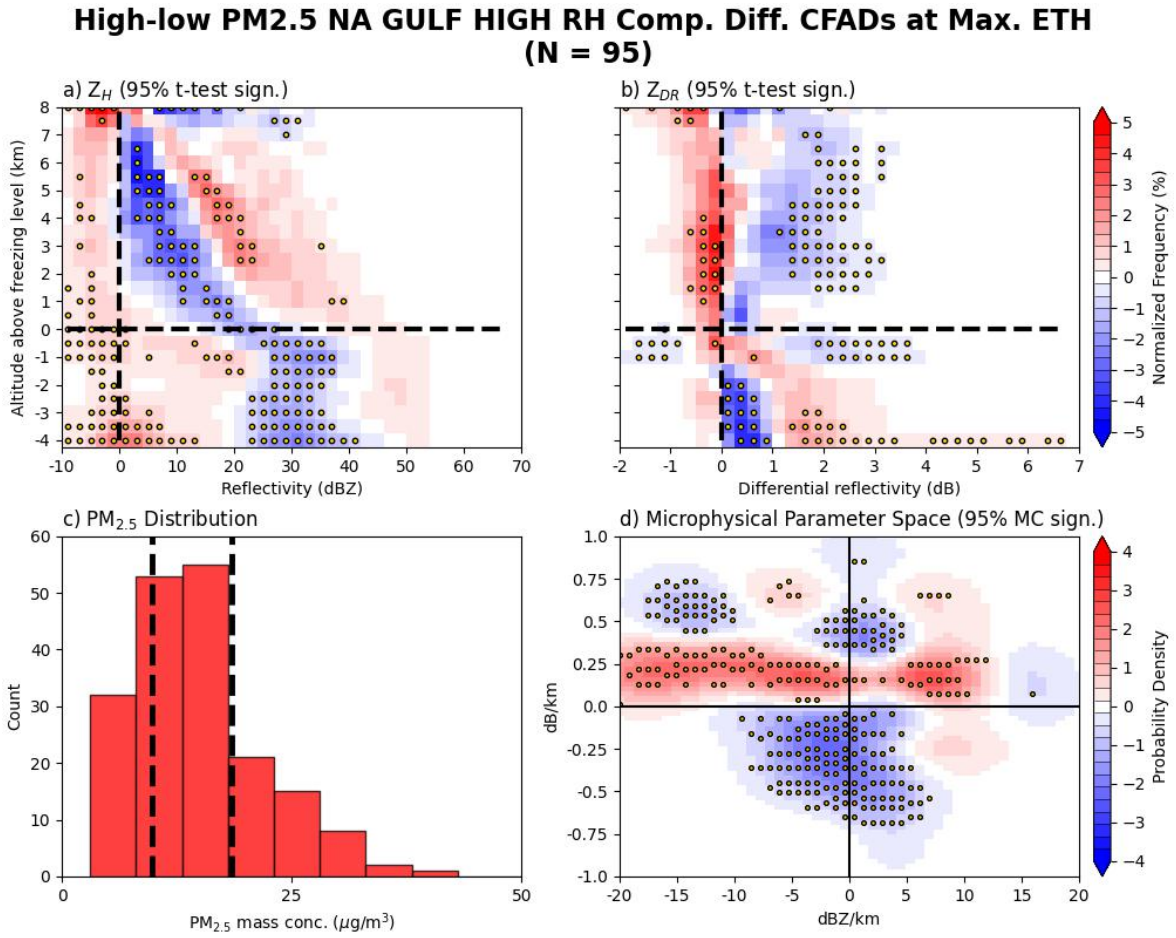

Figure 4.42: As in Figure 4.30 but for all *NA* GULF DCCs within the HIGH RH tercile.

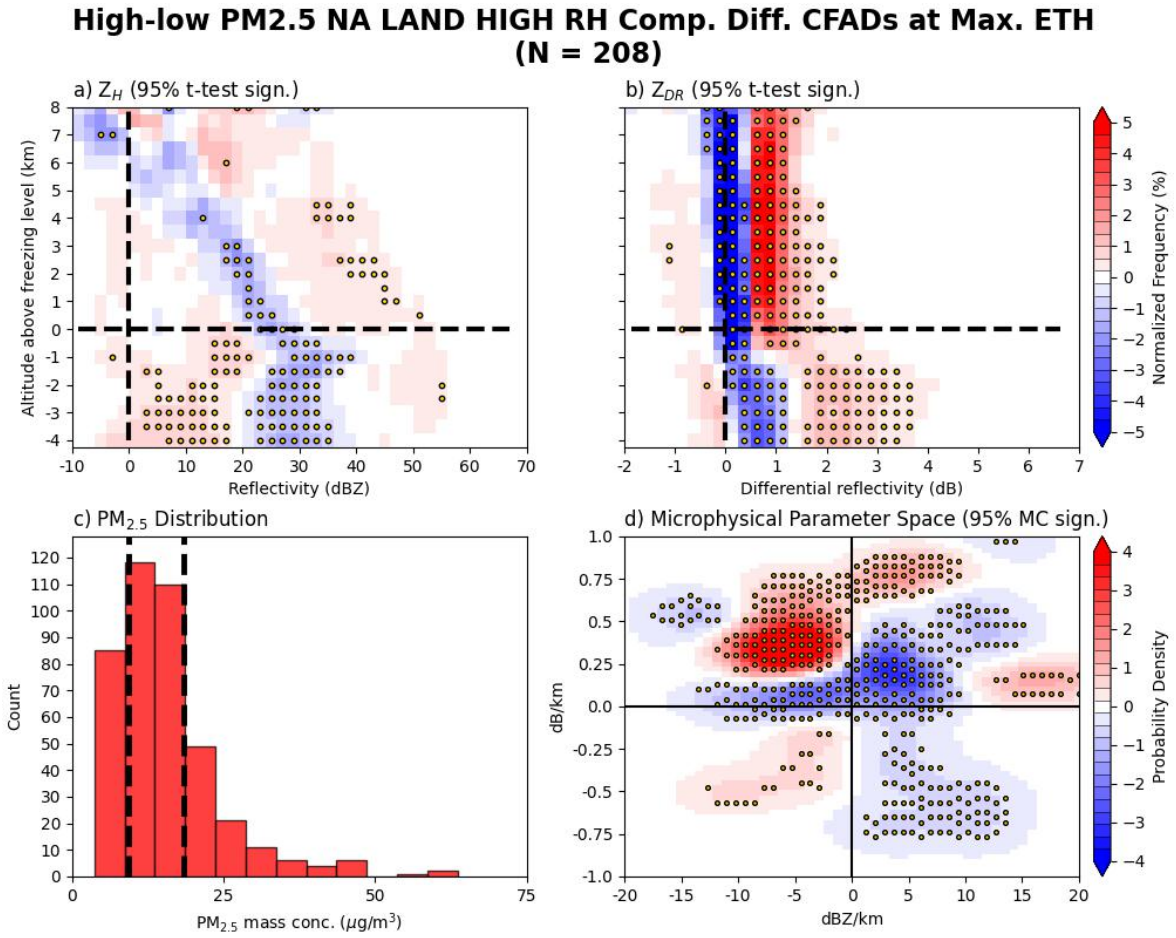

Figure 4.43: As in Figure 4.30 but for all *NA* LAND DCCs within the HIGH RH tercile.

subset. Therefore, results from this section should be interpreted with the caveat that minimal data were collected under these conditions. Nonetheless, the composite difference CFADs and MPS plots show a trend in that the high $PM_{2.5}$ or *A* DCCs can have signatures of weaker updraft strength and less precipitation compared to the low $PM_{2.5}$ or *NA* DCCs under certain meteorological conditions.

Figures 4.44 - 4.49 show the CFADs of Z and Z_{DR} along with the MPS plots for these subsets, which illustrate a decreased precipitation intensity for high $PM_{2.5}$ or *A* DCCs. All CFADs for these subsets show the opposite trend discussed in the section above, namely that the low $PM_{2.5}$ DCCs are more likely to have $Z_{DR} > 1$ dB and a Z distribution that is wider below the freezing level. This means that stronger size sorting and more intense precipitation are more likely present for the low $PM_{2.5}$ or *NA* DCCs. The MPS plots for these subsets also show that size sorting is likely stronger for the low $PM_{2.5}$ or *NA* DCCs as either blue pixels dominate the size sorting quadrant or they are distributed further away from the x-axis in the size sorting quadrant. The latter means a larger positive ΔZ_{DR} with a similar negative ΔZ and thus equates to only the very largest drops being able overcome the vertical velocity of the stronger updrafts in low $PM_{2.5}$ DCCs. For every subset in this category, the DCCs were under an anthropogenic aerosol regime and the meteorological variables for four of the subsets promoted low or moderate ETHs, namely low MUCAPE, low RH, low V, and moderate GH.

The larger probability of decreased precipitation intensity for the high $PM_{2.5}$ or *NA* DCCs is likely related to both the anthropogenic aerosol regimes and meteorological influences. An anthropogenic aerosol regime most likely consists of very high CCN

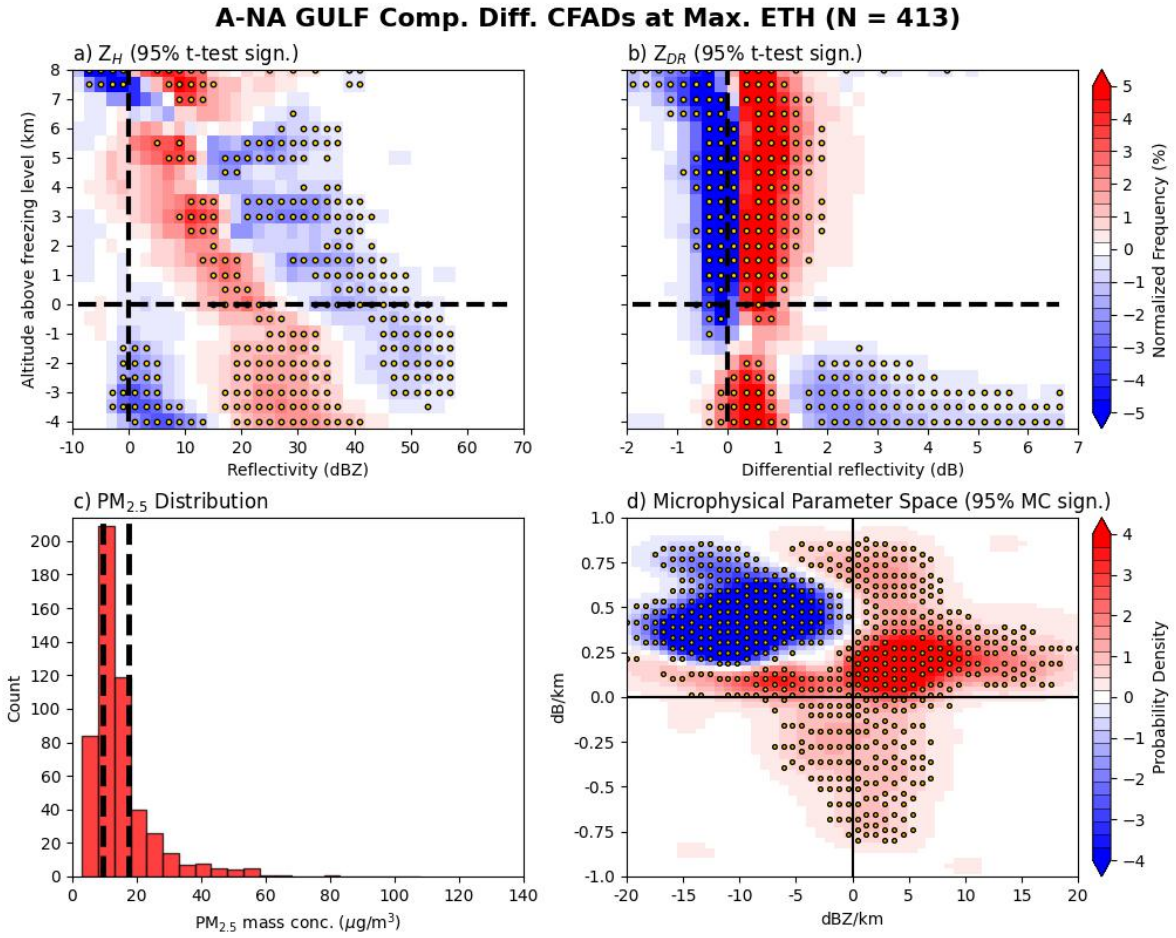

Figure 4.44: As in Figure 4.30 but for all GULF DCCs. Distinction is made between *A* (red) and *NA* (blue) DCCs.

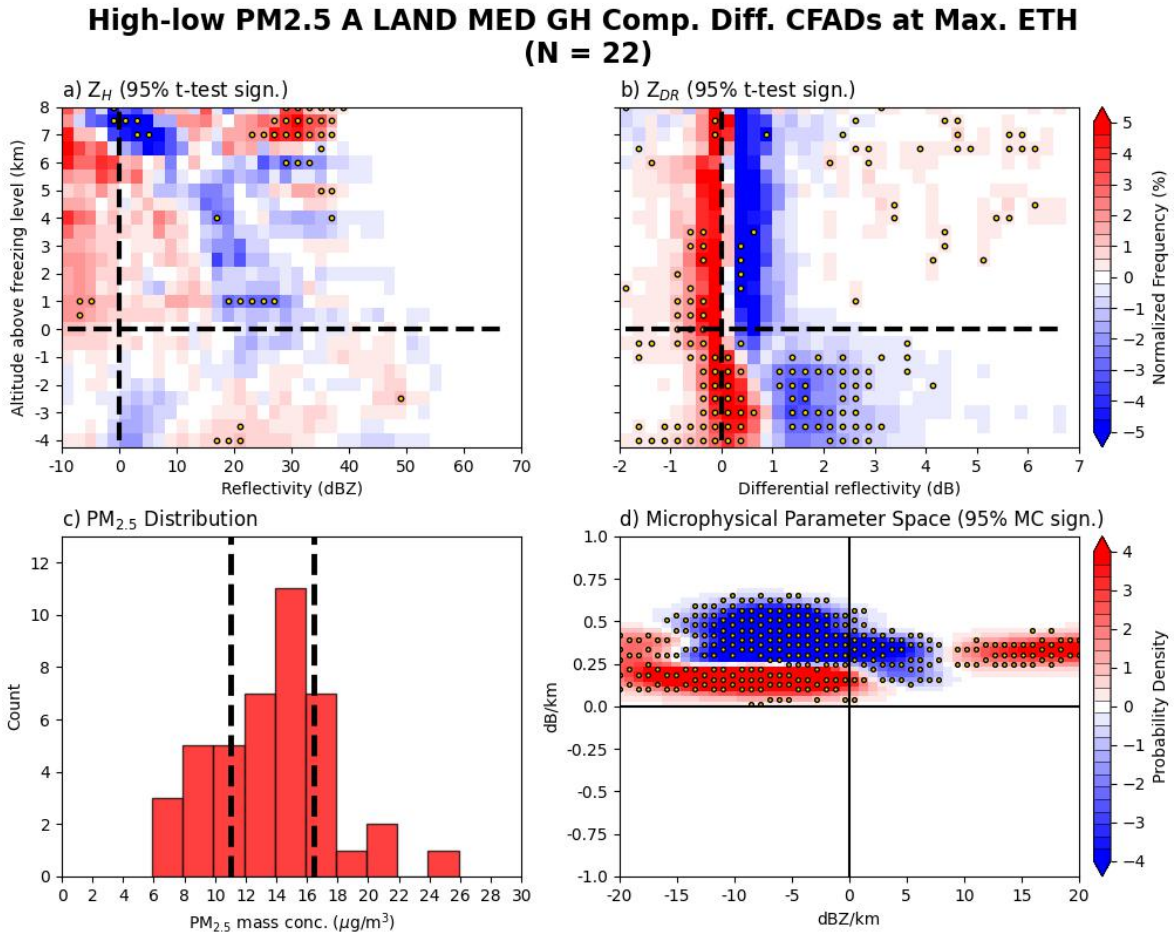

Figure 4.45: As in Figure 4.30 but for all *A* LAND DCCs within the MED GH tercile.

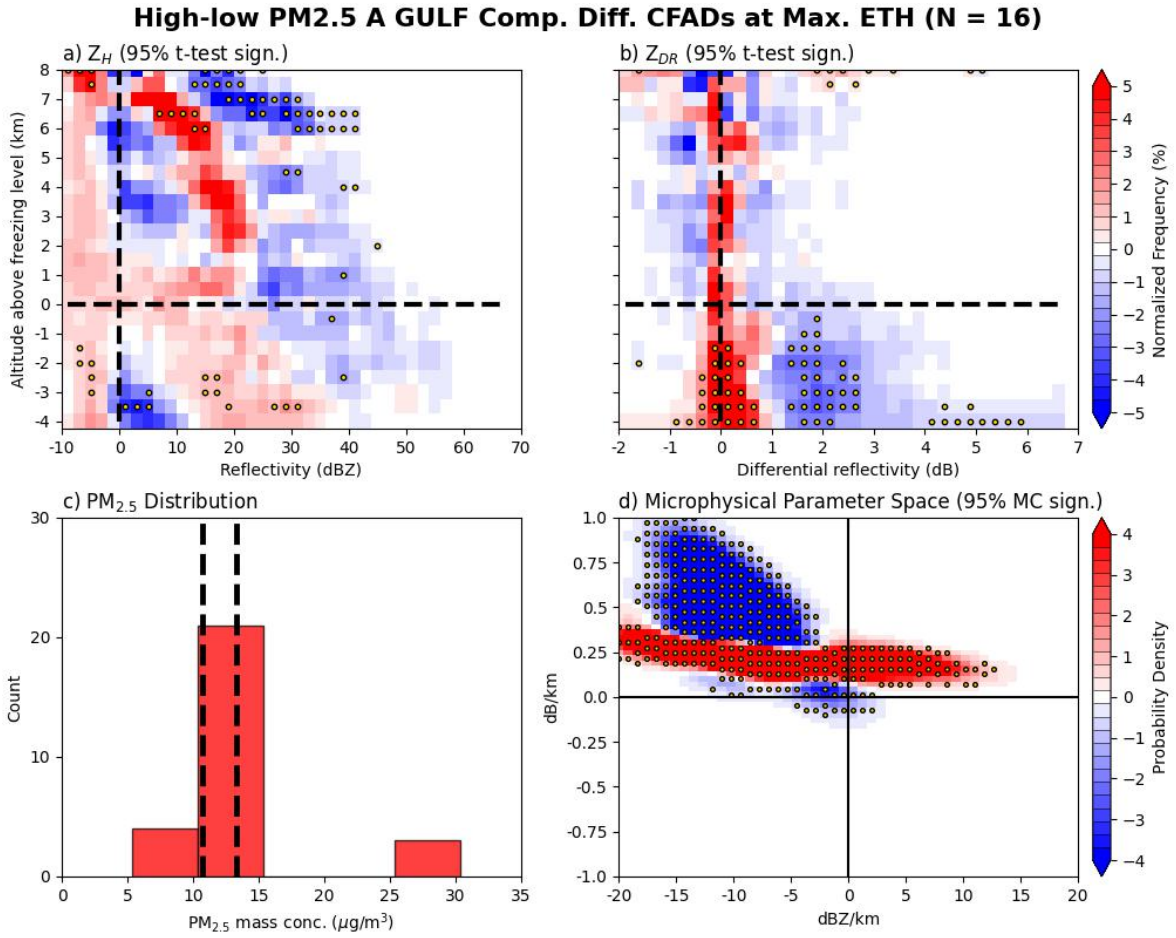

Figure 4.46: As in Figure 4.30 but for all *A* GULF DCCs.

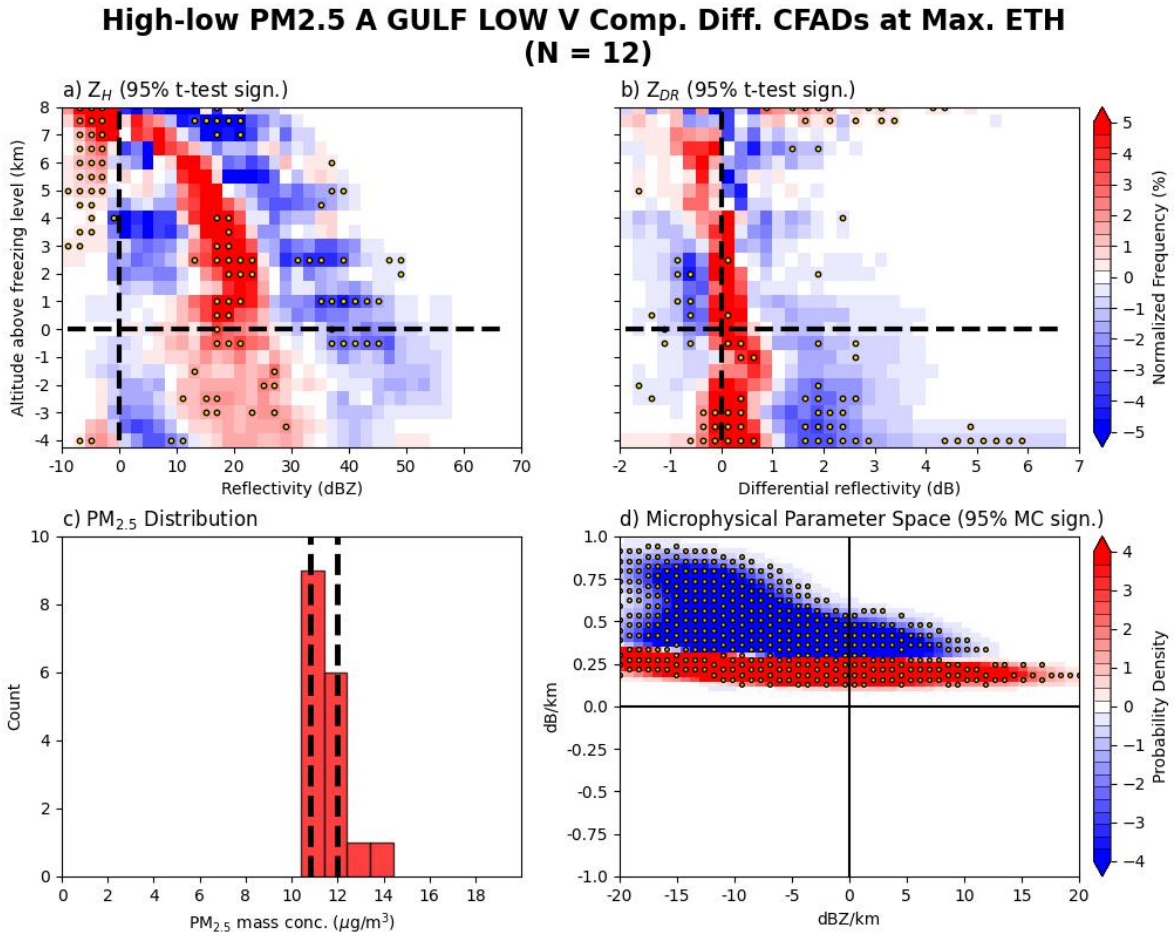

Figure 4.47: As in Figure 4.30 but for all *A* GULF DCCs within the LOW V tercile.

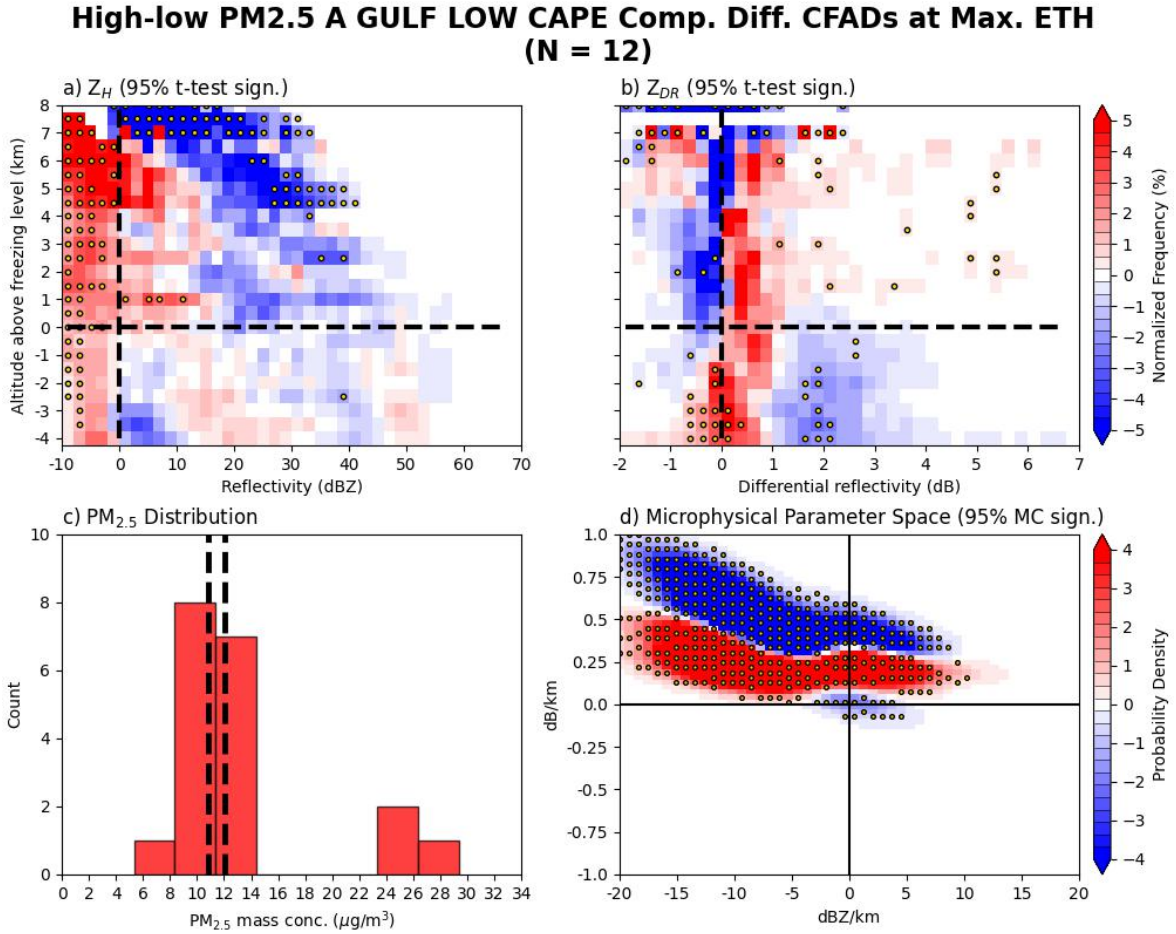

Figure 4.48: As in Figure 4.30 but for all *A* GULF DCCs within the LOW CAPE tercile.

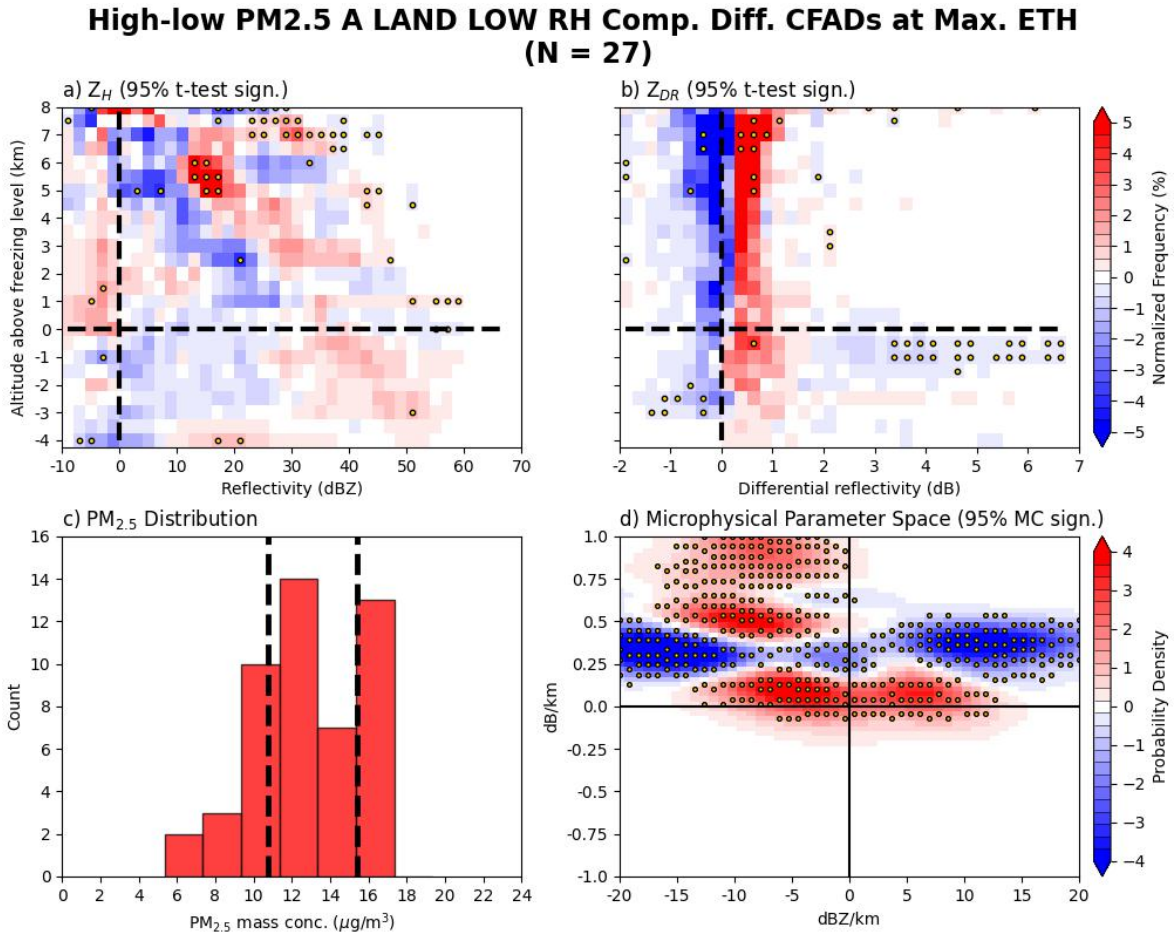

Figure 4.49: As in Figure 4.30 but for all *A* LAND DCCs within the LOW RH tercile.

number concentrations and thus the high $PM_{2.5}$ or A DCCs in these subsets are likely to exhibit warm rain inhibition. This is evident throughout six of the subsets in this section where almost all high $PM_{2.5}$ DCCs exist near the x-axis in both the size sorting and coalescence quadrants (Figures 4.45d, 4.46d, 4.47d, 4.48d, and 4.49d). This means that the observations in high $PM_{2.5}$ DCCs are consistent with more evaporation or weaker coalescence than for the low $PM_{2.5}$ DCCs within the warm region. This increased probability of evaporation is consistent with weaker precipitation efficiency from high CCN loading. Relatively weak updrafts that would occur in the meteorological conditions of low MUCAPE, low RH, low V, and moderate GH limit the impact of the increased CCN concentration, and instead precipitation intensity is weakened. This relationship has been found in previous studies (e.g., Fan et al., 2009; Ilotoviz et al., 2018; Khain et al., 2005) in which low free tropospheric relative humidity increases evaporation rates of the supercooled liquid transported above the freezing level, thus limiting the additional latent heat release typically caused by the AIE. These studies also found that lower instability leads to weaker transport of the supercooled liquid above the freezing level, decreasing riming efficiencies and subsequent precipitation enhancement and thus the results presented here may be caused by these mechanisms. All of these processes are consistent with trends seen throughout the CFADs as Z is more likely to be smaller above and below the freezing level for the high $PM_{2.5}$ DCCs (Figures 4.45a, 4.46a, 4.47a, 4.48a, and 4.49a). For the A GULF, A GULF LOW V, and A LAND MED GH subsets, Z_{DR} is also more likely to be smaller throughout the depth of the CFAD for the high $PM_{2.5}$ or A DCCs (Figures 4.46b, 4.47b, and 4.45b). These signatures point to the weaker updraft and precipitation intensity as discussed in section 4.2.2 with DCCs under high and low MUCAPE. However, the A-NA GULF and A LAND LOW RH Z_{DR} CFADs (Figures 4.44b and 4.49b) show that Z_{DR} is likely higher above the freezing level for the high $PM_{2.5}$ DCCs. This is consistent with more

frequent riming and accretion processes for the high $PM_{2.5}$ or A DCCs, but with the rates of these processes not being sufficient to invigorate the updrafts to overcome the combined effects of the meteorological environment of low free tropospheric relative humidity and high aerosol loading.

In summary, decreases in A DCC updraft strength and precipitation intensity are consistent with increases in $PM_{2.5}$ mass concentration when meteorological conditions do not favor stronger updrafts. The decreases in updraft strength and precipitation intensity may be caused by the combined effects of inefficient warm and cold rain processes and weak meteorological conditions in high $PM_{2.5}$ A DCCs.

4.2.2.2 Unclear microphysical impacts below the freezing level

4.2.2.2.1 A LAND DCCs

Table 4.1 lists the A LAND DCC subsets that do not show the expected below freezing level signature such as the reduction of warm rain and stronger size sorting in the CFADs. Typically, the figures for these subsets show that there are not statistically significant differences in Z or Z_{DR} below the freezing level, or MPS plots that do not show a coherent pattern of size sorting dominance as sample sizes in these subsets are low (< 23). Below is a discussion of subsets that have larger sample sizes than 23 DCCs and that show a trend within the warm region, even if statistical significance has not been achieved at the 95% confidence level.

The A LAND subset has the largest sample size but is also the one in which meteorological conditions are not accounted for. Above the freezing level, Figures 4.50a and b show that Z_{DR} is likely > 0 dB with Z either < 15 dBZ or 30 dBZ $< Z <$ 40 dBZ for high $PM_{2.5}$ DCCs, consistent with a larger likelihood of aggregated ice crystals, slightly wet hail, and graupel. Low $PM_{2.5}$ DCCs are more likely to have $Z_{DR} < 0$ and

20 dBZ $< Z <$ 30 dBZ, consistent with dry conical shaped graupel and dry aggregates in lower concentrations. However in-situ observations would be needed to definitively characterize hydrometeor shapes. At altitudes down to -3.5 km, the high $PM_{2.5}$ DCCs exhibit a narrower Z_{DR} distribution between 0 – 1 dB where the low $PM_{2.5}$ DCCs can exhibit greater likelihoods of negative Z_{DR} or $Z_{DR} > 1$ dB. This is coupled with a lack of dominant probabilities over any range of Z in this region and may be a result of a balance in returned signal power between the assumed higher concentrations of smaller drops in high $PM_{2.5}$ DCCs and assumed lower concentrations of larger drops in the low $PM_{2.5}$ DCCs. Below -3.5 km, both the Z and Z_{DR} patterns show that the high $PM_{2.5}$ DCCs are more likely to have $Z_{DR} > 3$ dB and $Z < 30$ dBZ. This suggests a larger likelihood of very large drops (D $>$ 3 mm) in sparse concentrations whereas the low $PM_{2.5}$ DCCs have a larger likelihood of slightly smaller drops, near 1 – 3 mm in diameter, in higher concentrations. However, these probabilities are small, no more than 1% and again are not statistically significant, and thus show that overall precipitation intensity is similar between the high and low $PM_{2.5}$ DCCs when not accounting for meteorological impacts.

The *A* LAND LOW DEW subset (Figure 4.51b) shows that Z_{DR} for high $PM_{2.5}$ DCCs are more likely to exhibit $Z_{DR} < 0$ dB above the freezing level. This is consistent with the low $PM_{2.5}$ DCCs exhibiting more efficient riming and accretion processes that create wet small hail, graupel, and ice crystals with updraft invigoration as discussed for the subsets in section 4.2.2.1.2. Below the freezing level, the high $PM_{2.5}$ DCCs are also more likely to have smaller Z_{DR} and 40 dBZ $< Z <$ 50 dBZ. The MPS plot (Figure 4.51d) is consistent with coalescence being more likely for the high $PM_{2.5}$ DCCs and size sorting more likely for low $PM_{2.5}$ DCCs but the pattern is not coherent. A similar pattern in the *A* LAND LOW CAPE subset can be seen in Figure 4.52, except that

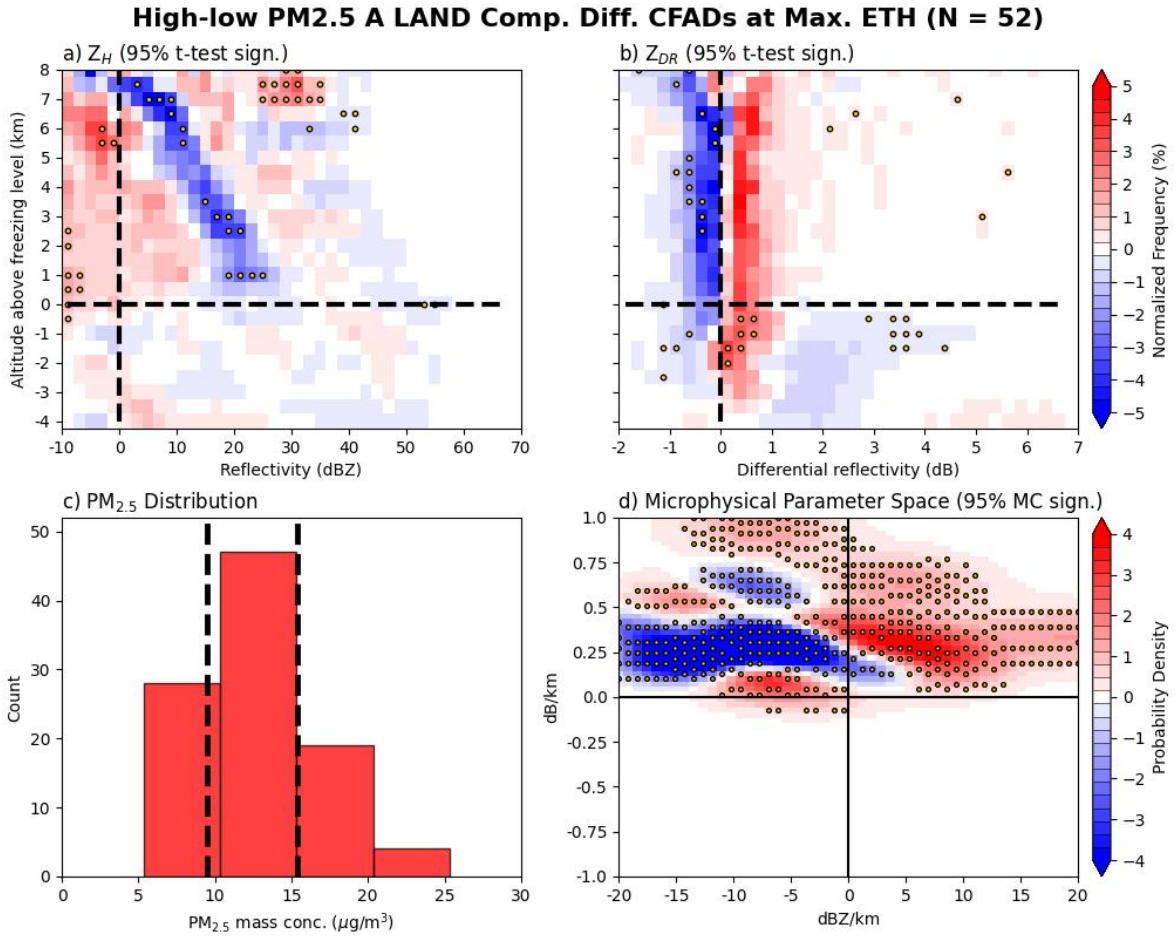

Figure 4.50: As in Figure 4.30 but for all *A* LAND DCCs.

there is no clear Z_{DR} dominance above the freezing level. It seems then that under low surface dew point or MUCAPE conditions, *A* DCCs over land exhibit slightly weaker updrafts and precipitation intensity when anthropogenic mass concentration is high. This is consistent with less efficient riming and accretion processes associated with the higher CCN number concentrations, similar to results discussed in section 4.2.2.1.2, but the differences are not robust.

4.2.2.2.2 NA GULF DCCs

Sample sizes are typically higher for *NA* GULF DCCs compared to those of the *A* LAND DCCs discussed above. This allows for more robust interpretations of patterns that are illustrated throughout the CFADs and MPS plots. However, many subsets within this category still show unclear differences because the differences in Z and Z_{DR} below the freezing level are not statistically significant. This means that conclusions like those reached for the subsets in sections 4.2.2.1.1 and 4.2.2.1.2 are not able to be reached here. Instead, only differences where significance is achieved are analyzed.

The MPS plots for *NA* GULF DCCs under high and low BLH conditions are presented in Figures 4.53d and 4.54d and show a similar pattern between high and low $PM_{2.5}$ DCCs. High $PM_{2.5}$ DCCs in the high and low BLH conditions exhibit a narrow distribution of ΔZ_{DR} with ΔZ being more variable. This means that the high $PM_{2.5}$ DCCs exhibit signatures of evaporation and weak coalescence since the distribution lies close to the x-axis. Low $PM_{2.5}$ DCCs for both subsets exhibit higher likelihoods of size sorting, meaning that their updrafts are likely stronger. While statistical significance is not achieved in much of the CFADs for HIGH BLH in Figure 4.53, it is achieved in the CFADs for the LOW BLH subset (Figures 4.54a and b). Interestingly, the CFADs do not completely agree with the MPS plot since Z_{DR} is likely larger for the high $PM_{2.5}$

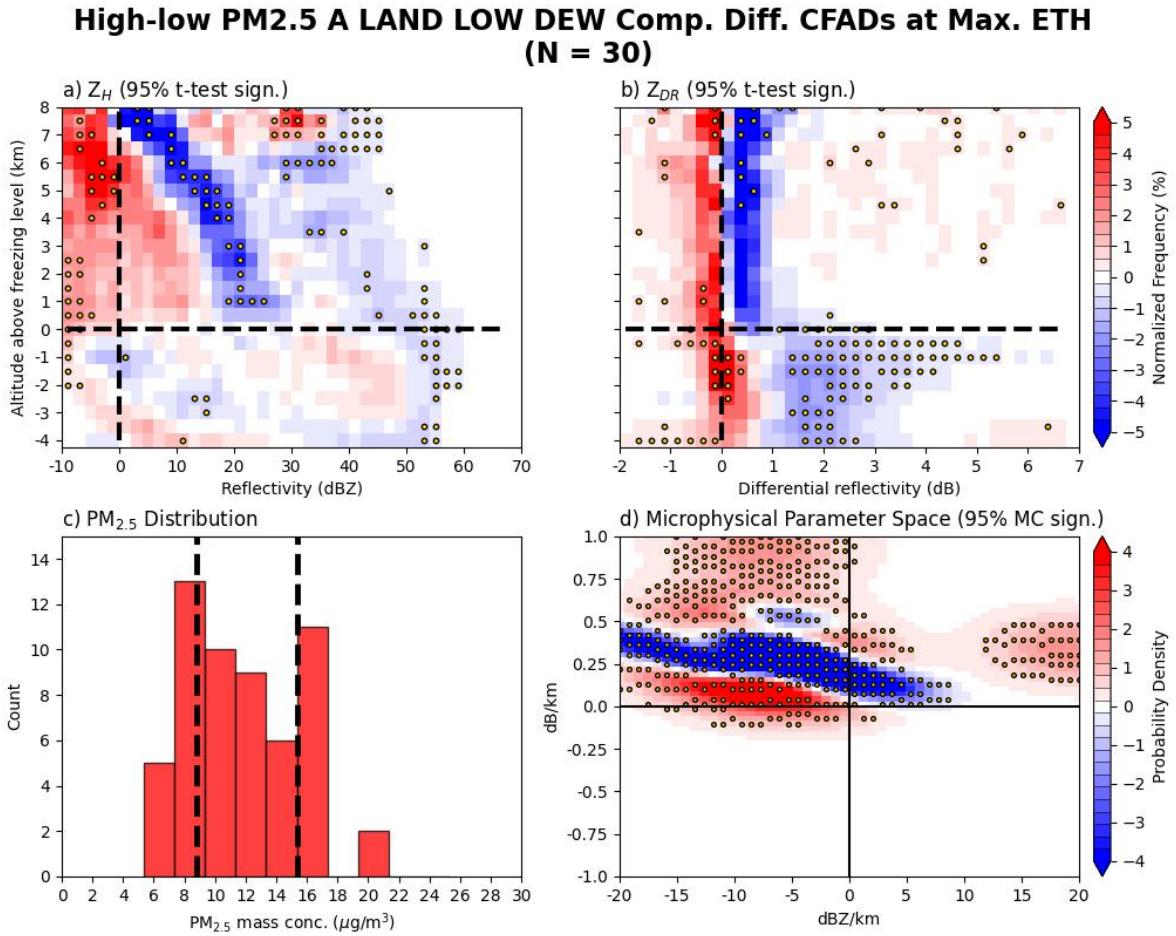

Figure 4.51: As in Figure 4.30 but for all A LAND DCCs within the LOW DEW tercile.

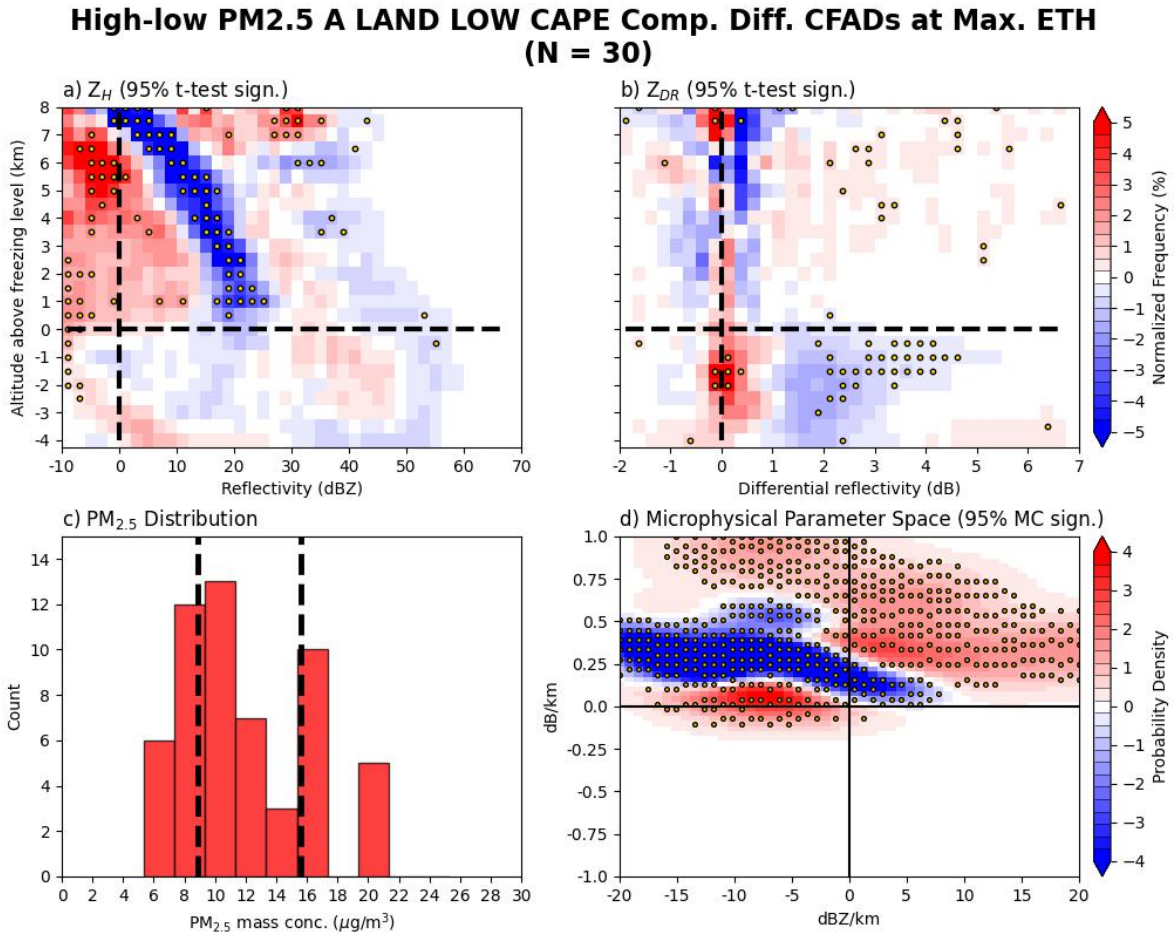

Figure 4.52: As in Figure 4.30 but for all *A* LAND DCCs within the LOW CAPE tercile.

DCCs in addition to larger Z, at least above the freezing level. The CFADs thus point to more efficient riming and accretion process for high $PM_{2.5}$ DCCs but these processes did not seem to invigorate the convection or change the precipitation intensity as Z is not statistically different below the freezing level.

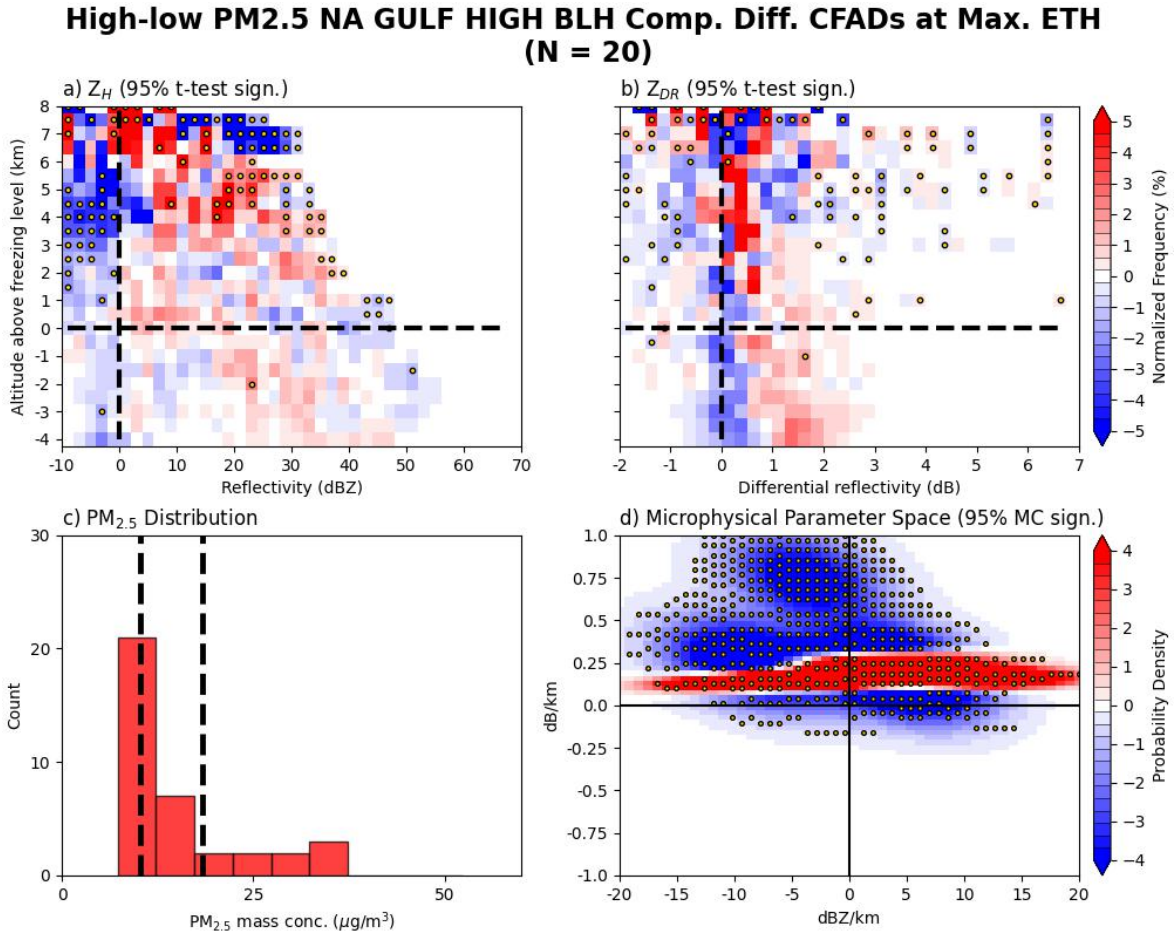

Figure 4.53: As in Figure 4.30 but for all *NA* GULF DCCs within the HIGH BLH tercile.

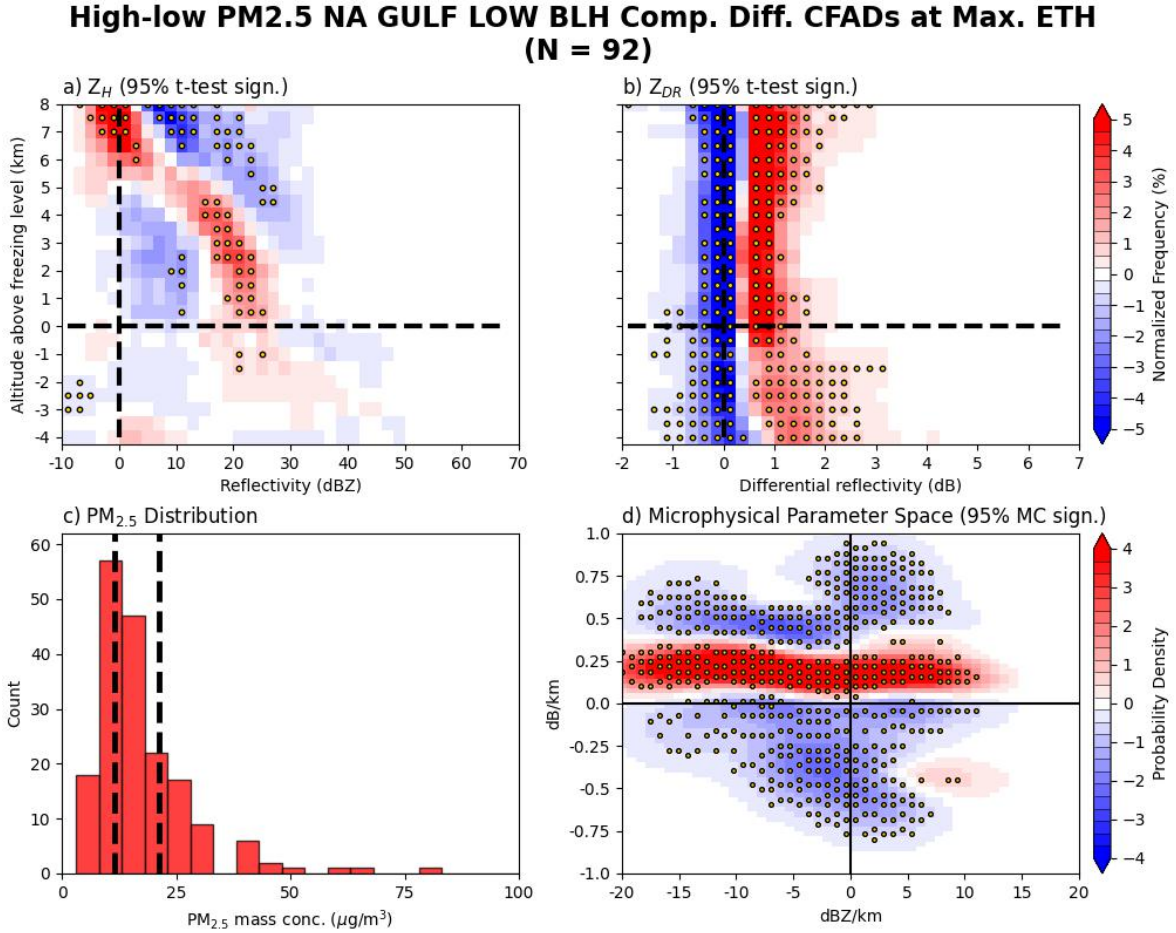

Figure 4.54: As in Figure 4.30 but for all *NA* GULF DCCs within the LOW BLH tercile.

When controlling for RH conditions, there is one subset within this section for *NA* GULF DCCs. Figure 4.55 shows the CFADs and MPS plot for the *NA* GULF LOW RH subset. Similar to the subsets discussed in the paragraph above, the Z CFAD lacks statistically different Z patterns below the freezing level but Z_{DR} is larger for all altitudes for high $PM_{2.5}$ DCCs. This is consistent with an invigoration of DCCs, but the MPS plot again disagrees as the high $PM_{2.5}$ DCCs are closer to the x-axis in both the size sorting and coalescence quadrants, meaning likely more evaporation and weaker coalescence for these cases. This suggests that even if warm rain was

inhibited from higher aerosol number concentration for high $PM_{2.5}$ DCCs leading to more efficient riming and accretion, it did not lead to stronger updrafts and more intense precipitation when RH $< 41\%$.

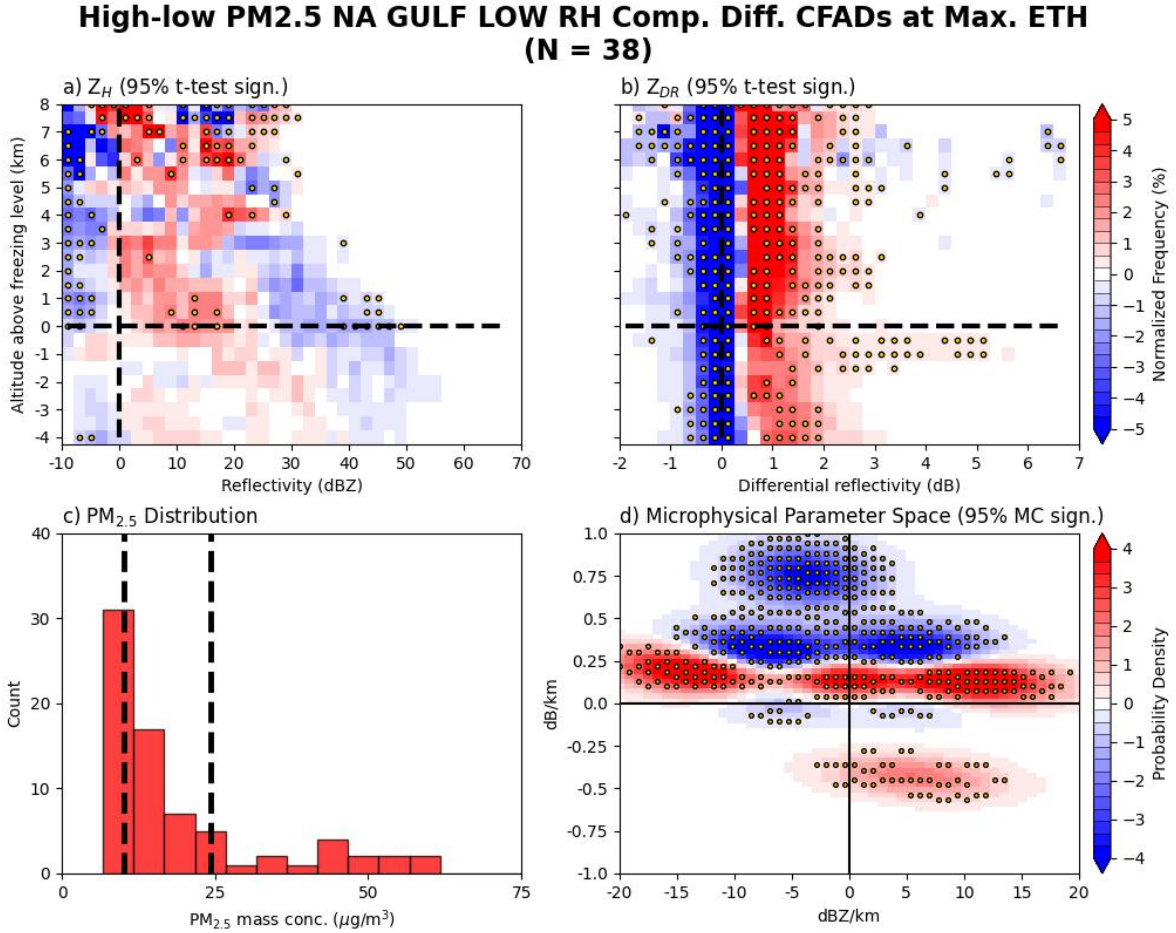

Figure 4.55: As in Figure 4.30 but for all *NA* GULF DCCs within the LOW RH tercile.

When controlling for D650, the MED D650 subset lacks statistically significant differences in Z and Z_{DR} above the freezing level (Figures 4.56a and b). Below the freezing level, high $PM_{2.5}$ DCCs typically exhibit $Z_{DR} > 1$ dB and a wider Z distribution at altitudes below -3.5 km. This is consistent with stronger updrafts with increased size sorting and more intense precipitation. While this is somewhat shown in the MPS plot, there are also indications of larger likelihoods of warm processes such as coalescence

and breakup evident in Figure 4.56d. Since differences above the freezing level are not clear in the CFADs, it is difficult to uncover why high $PM_{2.5}$ DCCs can exhibit more variable ΔZ and ΔZ_{DR}. The HIGH and LOW D650 subsets show similar patterns to each other in that both their CFADs and MPS plots show Z is less and Z_{DR} is greater for high $PM_{2.5}$ DCCs (Figures 4.57 and 4.58). This is consistent with the high $PM_{2.5}$ DCCs having higher likelihoods of evaporation since the MPS plots show most of the high $PM_{2.5}$ DCCs close to the x-axis in the size sorting quadrant. Therefore, the precipitation and updraft intensity do not seem to be enhanced for DCCs under high aerosol loading when D650 is high or low.

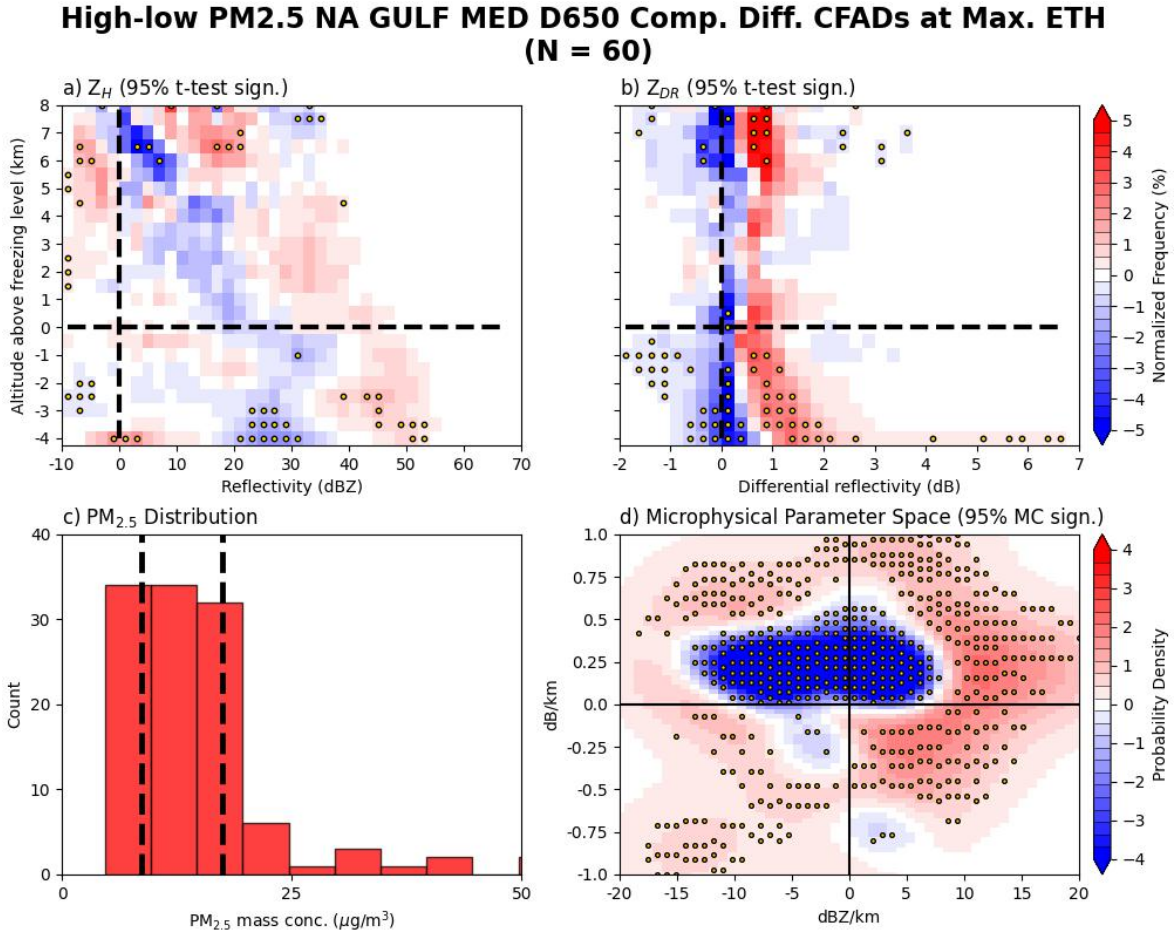

Figure 4.56: As in Figure 4.30 but for all *NA* GULF DCCs within the MED D650 tercile.

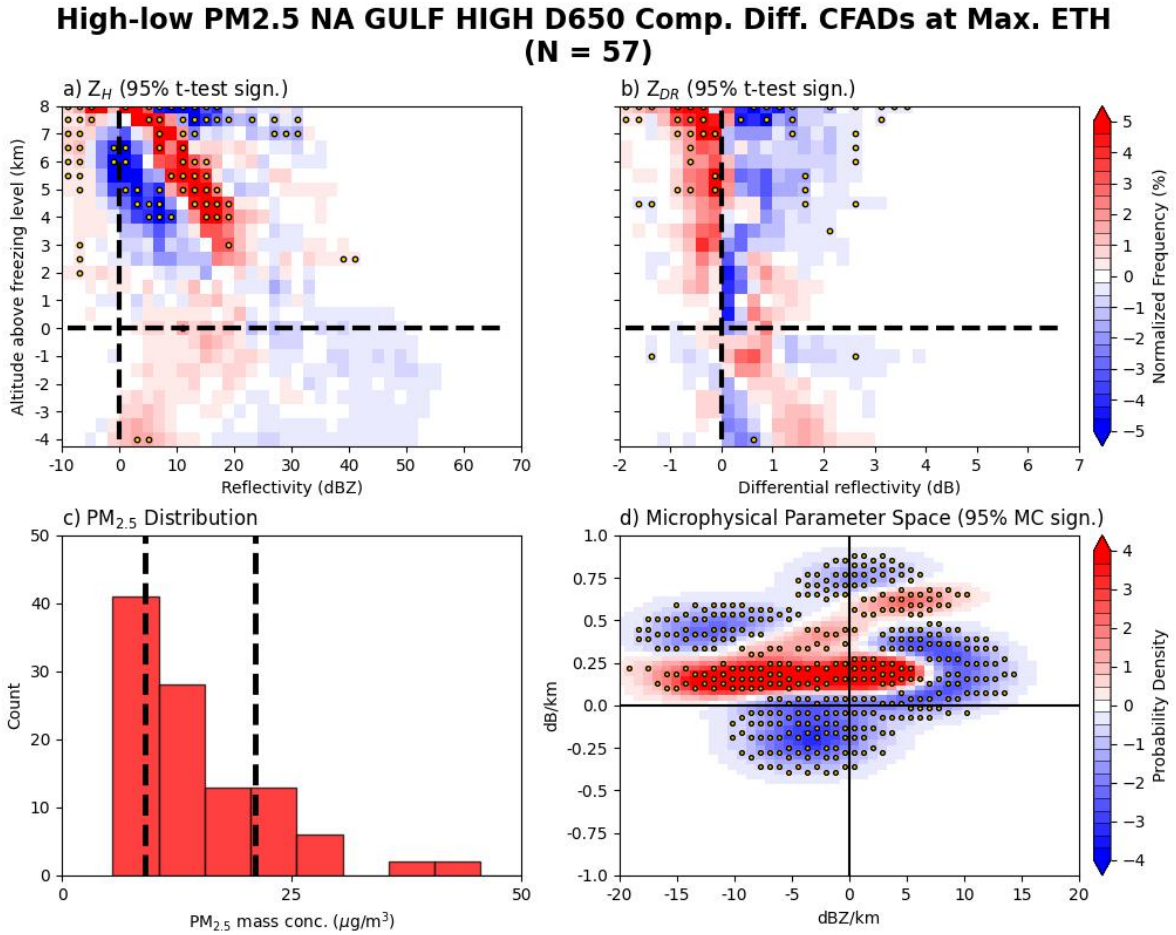

Figure 4.57: As in Figure 4.30 but for all *NA* GULF DCCs within the HIGH D650 tercile.

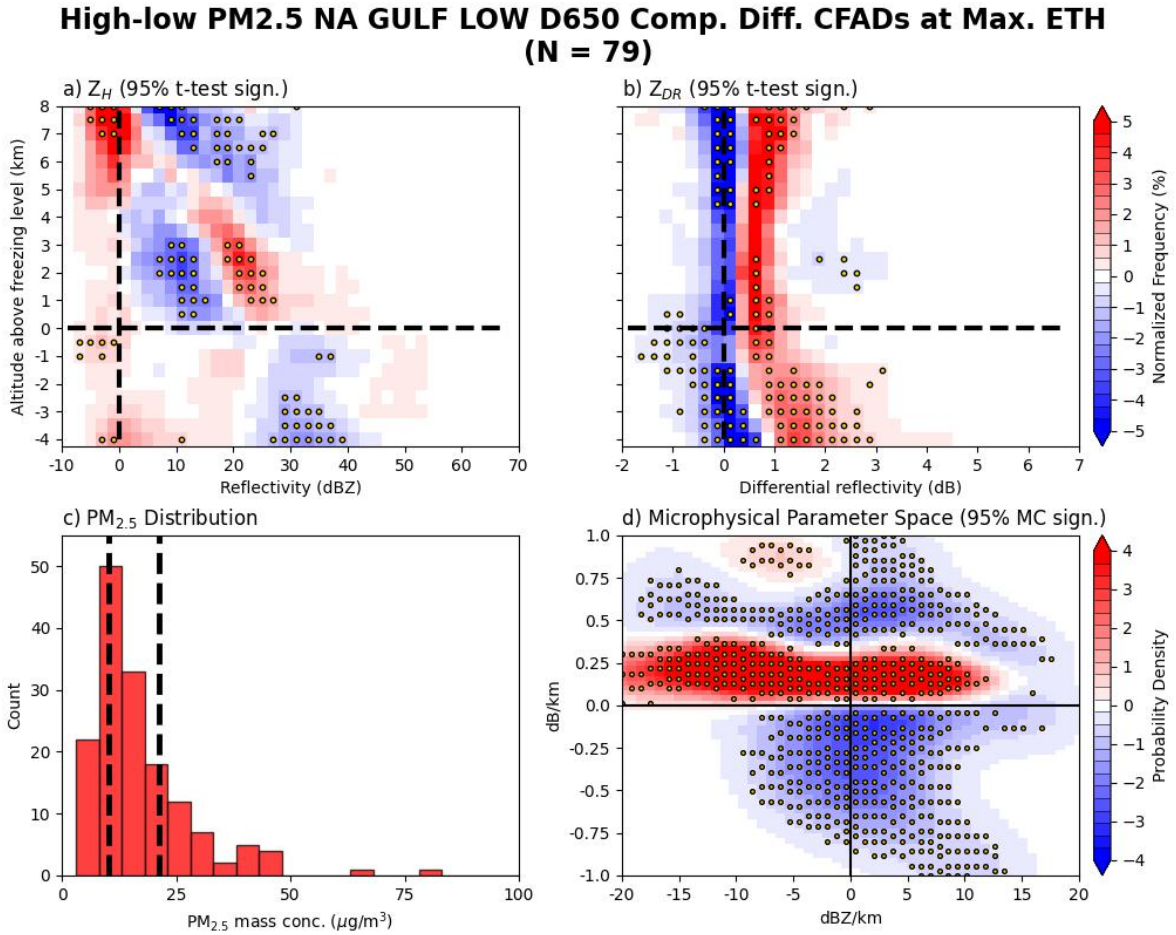

Figure 4.58: As in Figure 4.30 but for all *NA* GULF DCCs within the LOW D650 tercile.

High and moderate MUCAPE conditions for *NA* GULF DCCs both lead to similar Z CFAD differences evident in Figures 4.59 and 4.60a. These differences consist of Z being greater for the low $PM_{2.5}$ DCCs across all altitudes. Under high MUCAPE conditions, Figure 4.59d shows an interesting pattern in the warm region microphysics for the high and low $PM_{2.5}$ DCCs. High $PM_{2.5}$ DCCs exhibit a more variable ΔZ_{DR} in the size sorting quadrant, consistent with more drop evaporation for DCCs close to the x-axis or stronger size sorting when $\Delta Z_{DR} > 0.5$ dB/km. This large variability in the strength of the high $PM_{2.5}$ DCCs masks the expected trends of an inhibited warm rain

signature that are usually seen in the composite difference CFADs. Instead, weaker high $PM_{2.5}$ DCCs that are closer to the evaporation regime in Figure 4.59d shift the Z_{DR} distribution below the freezing level toward smaller values, leaving the low $PM_{2.5}$ DCCs to exhibit slightly higher probabilities of $Z_{DR} > 2$ dB, although not statistically significant. The same is seen in Figure 4.59a in which the weaker high $PM_{2.5}$ DCCs shift the distribution of Z towards smaller values, leaving $Z > 40$ dBZ to be more likely from low $PM_{2.5}$ DCCs. The shift in these distributions can be seen in Figure 4.61, which has the composite difference CFADs of the high and low $PM_{2.5}$ DCCs after removing high $PM_{2.5}$ DCCs that have $\Delta Z_{DR} < 0.5$ dB/km. Z below the freezing level is higher than 40 - 45 dBZ for the high $PM_{2.5}$ DCCs while the region of $Z_{DR} > 0.5$ dB lacks a dominant DCC regime that is significant, but shows that high $PM_{2.5}$ DCCs do have higher probabilities of larger Z_{DR}. This pattern begins to show a more typical invigoration by higher aerosol loading as seen in section 4.2.2.1.1. High $PM_{2.5}$ *NA* DCCs over the Gulf in environments with MUCAPE > 2500 J/kg can thus exhibit higher variability in their updraft strength and precipitation intensity whereas the low $PM_{2.5}$ DCCs are more consistent in their precipitation intensity and updraft strength. Under moderate MUCAPE conditions, higher $PM_{2.5}$ mass concentration seems to be a detriment to updraft strength and precipitation as Figures 4.60b and d both show that Z_{DR} is likely smaller and weaker size sorting/evaporation is more likely for high $PM_{2.5}$ DCCs.

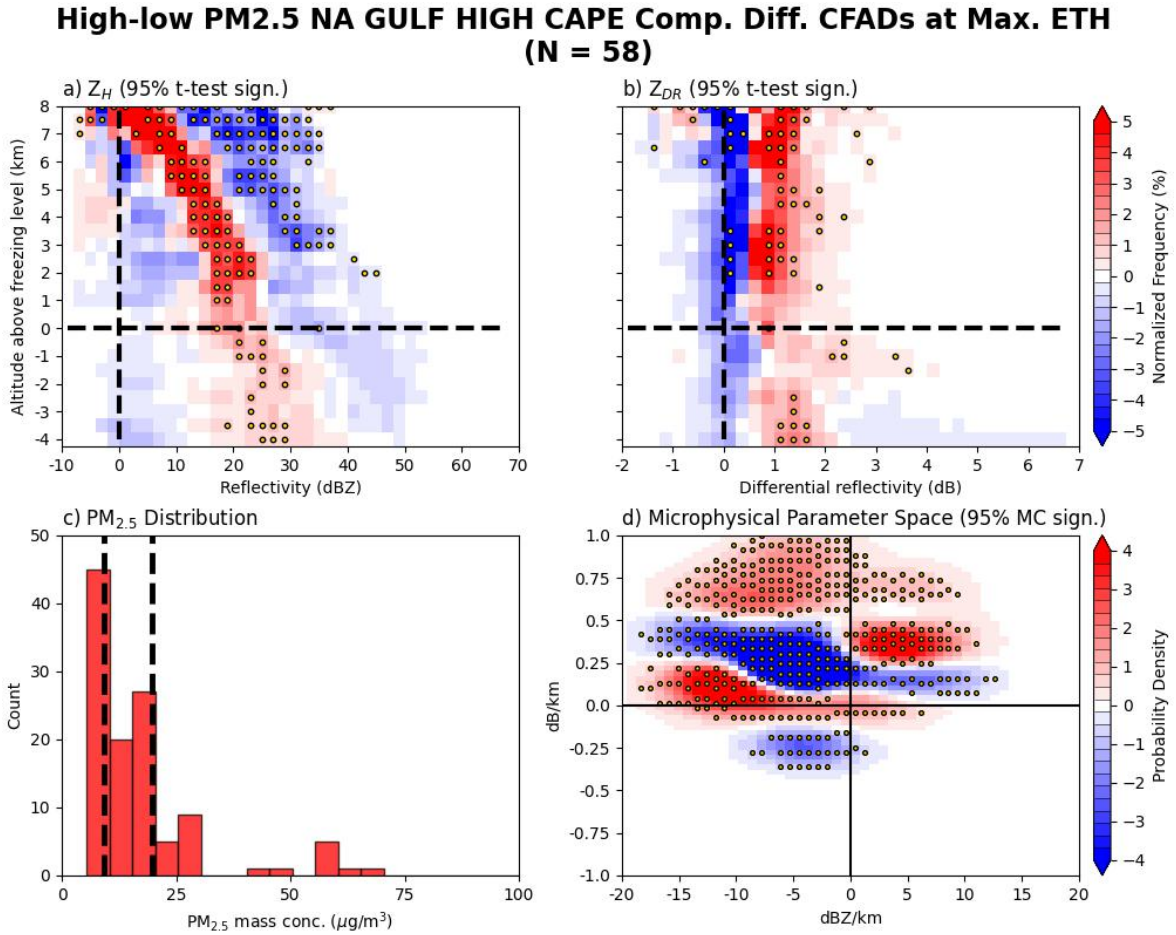

Figure 4.59: As in Figure 4.30 but for all *NA* GULF DCCs within the HIGH CAPE tercile.

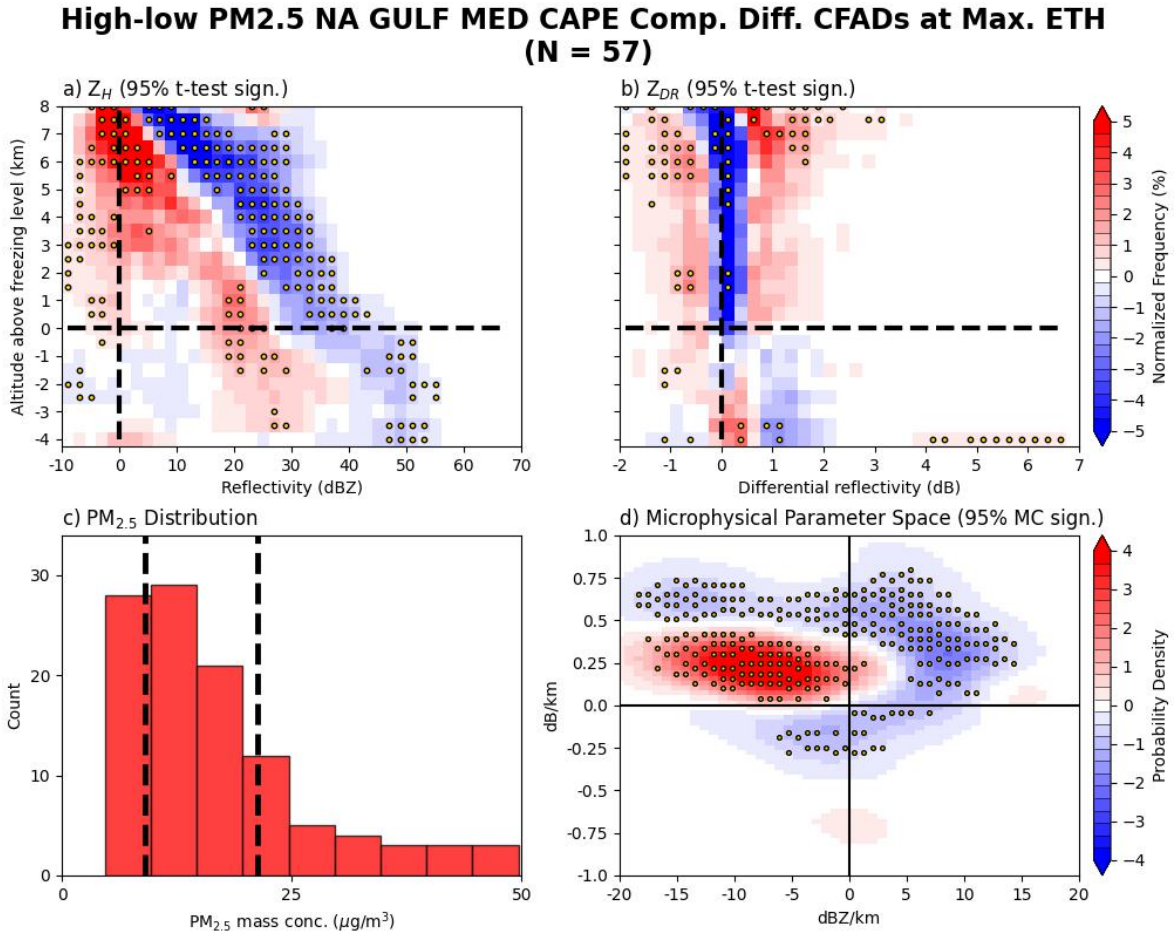

Figure 4.60: As in Figure 4.30 but for all *NA* GULF DCCs within the MED CAPE tercile.

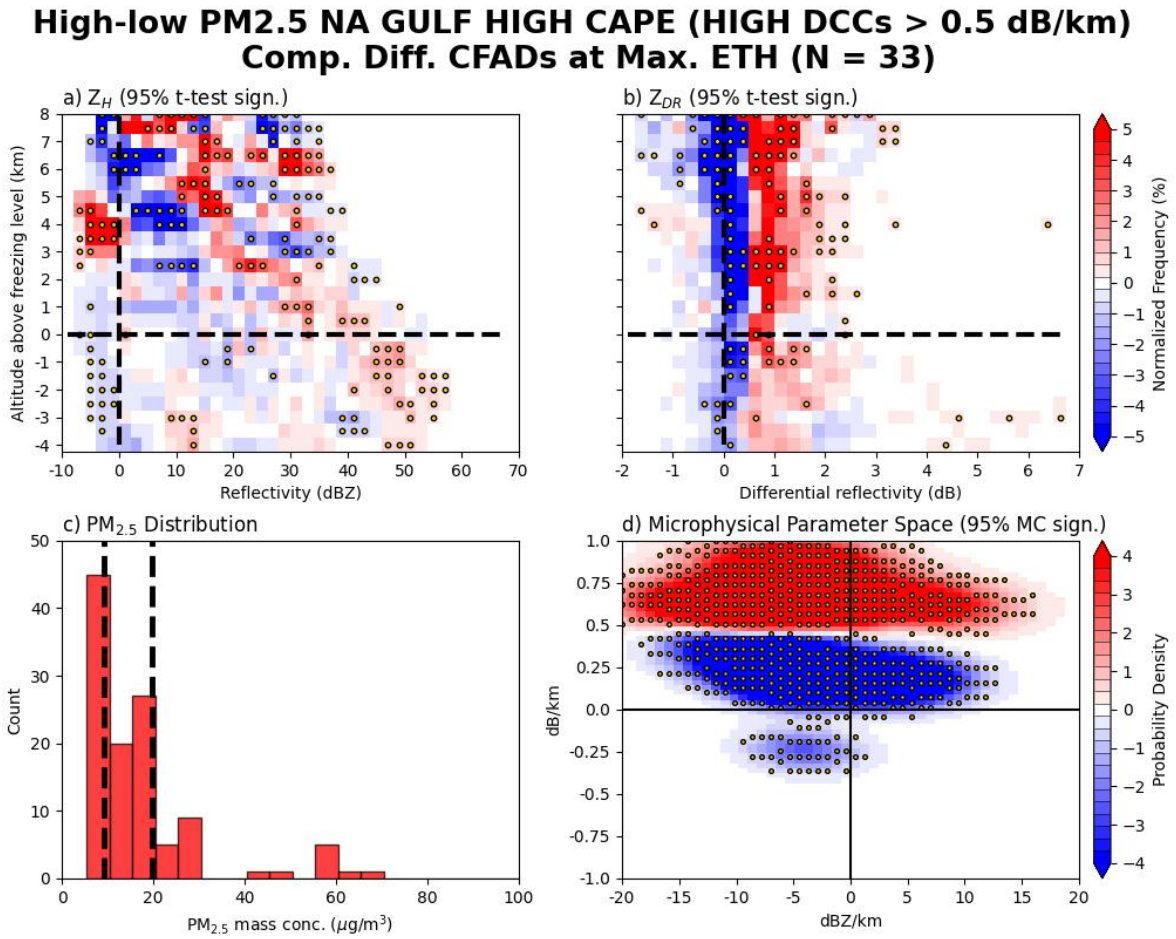

Figure 4.61: As in Figure 4.30 but for all *NA* GULF DCCs within the HIGH CAPE tercile and constraining high $PM_{2.5}$ DCCs to have $\Delta Z_{DR} > 0.5$ dB/km.

Lastly, when controlling for V all Z CFADs do not show large regions of statistically significant differences below the freezing level (Figures 4.62a, 4.63a, and 4.64a). Additionally, only the HIGH V subset shows significant differences in Z_{DR} below the freezing level and indicates that Z_{DR} is likely > 1 dB for high $PM_{2.5}$ DCCs (Figure 4.62b). Above the freezing level, Figure 4.62a does show that Z is also significantly higher for the high $PM_{2.5}$ DCCs in the HIGH V subset and that Z_{DR} is more likely to be $0 < Z_{DR} < 1$ dB whereas the low $PM_{2.5}$ DCCs are more likely to have $1 < Z_{DR} < 3.5$ dB above the Z_{DR}-column region. This is consistent with patterns discussed in

section 4.2.2.1.1 for the *NA* GULF HIGH RH subset in which ice crystal habits may be different between high and low $PM_{2.5}$ DCCs based upon riming and accretion efficiencies within the Z_{DR}-column region. The MED and LOW V subsets show an opposite trend in Z_{DR} above the freezing level compared to each other. Under moderate (low) V conditions, Z_{DR} is likely to be > 0.25 dB for the low (high) $PM_{2.5}$ DCCs. This is consistent with increased efficiency of riming and accretion processes occurring for low (high) $PM_{2.5}$ DCCs. Interestingly, these patterns are not what is typically expected for the low V conditions, as low V can mean higher shear magnitudes as discussed in section 4.2.1 and thus cause aerosol effects to typically hinder convective invigoration.

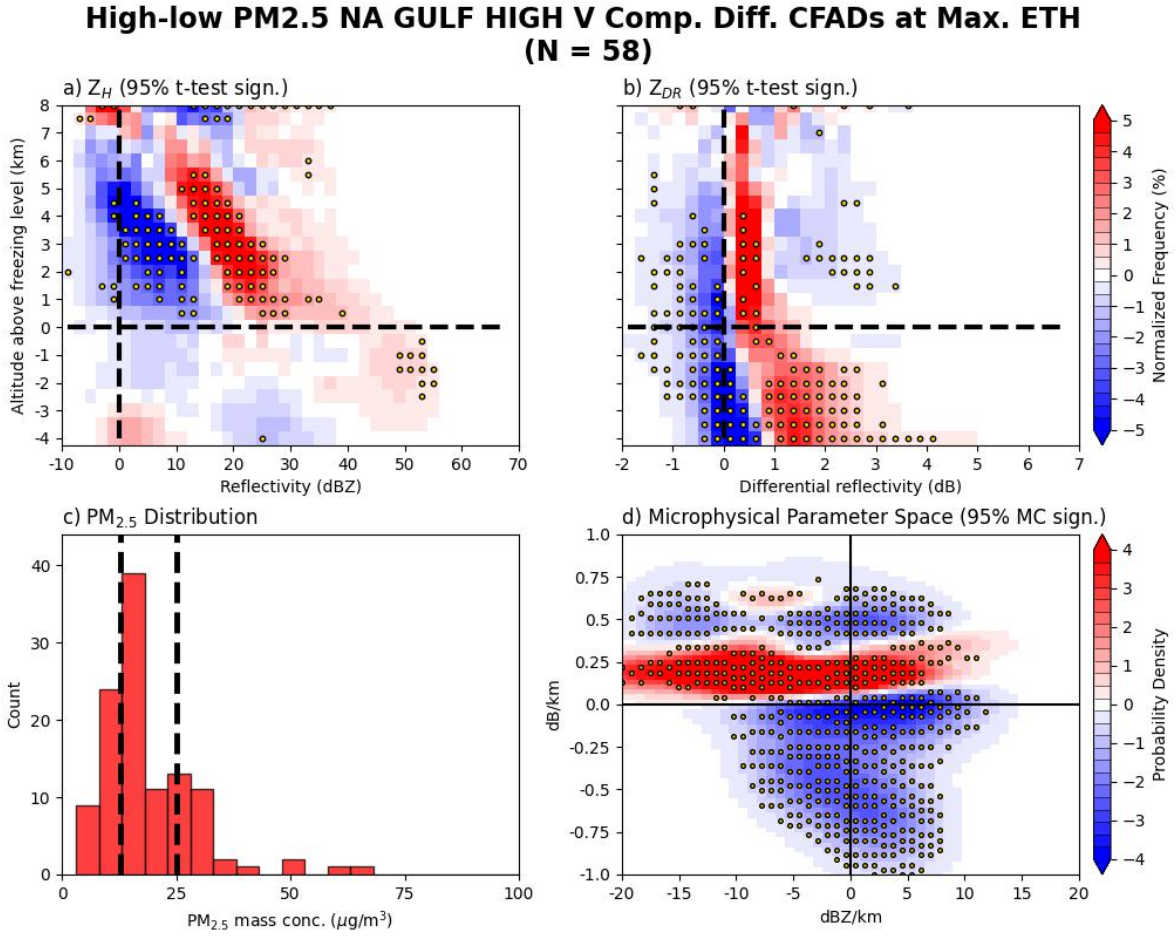

Figure 4.62: As in Figure 4.30 but for all *NA* GULF DCCs within the HIGH V tercile.

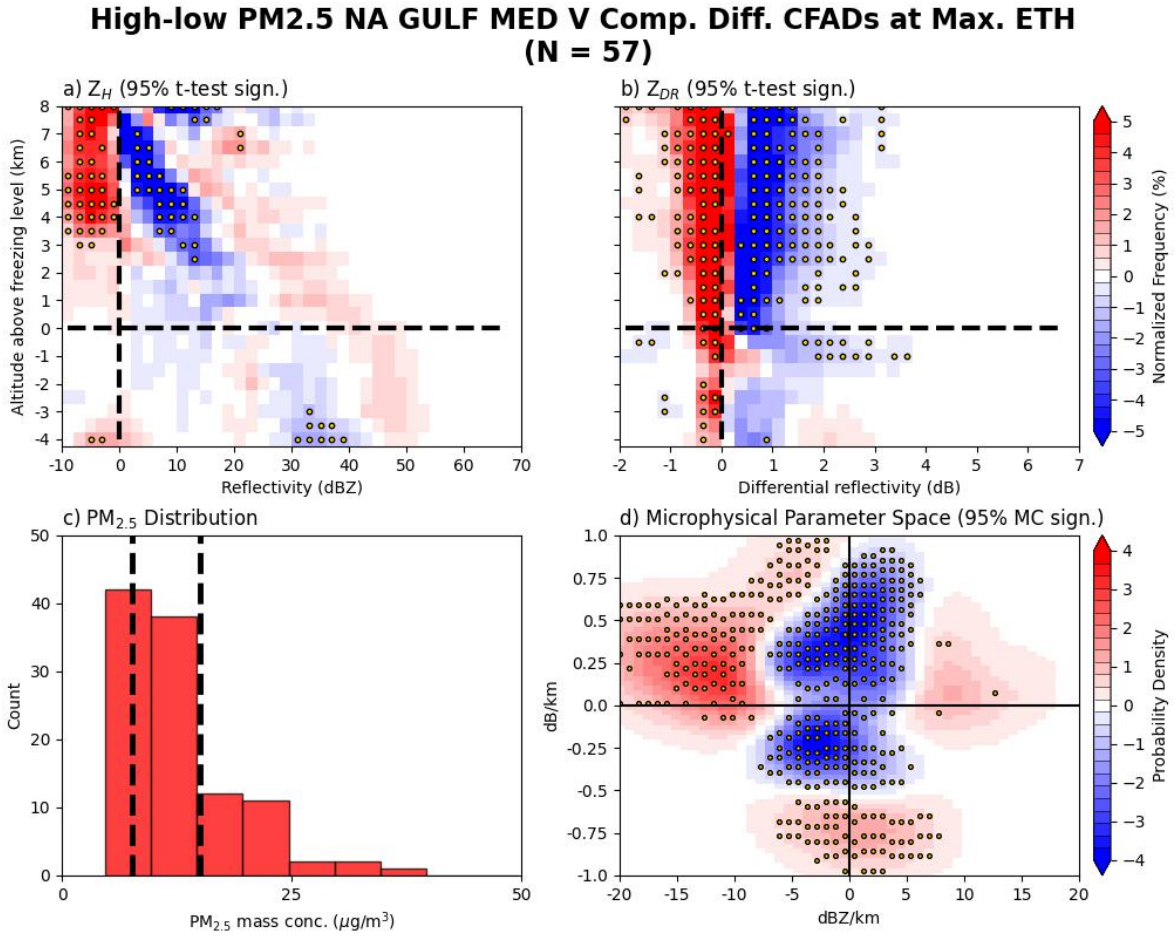

Figure 4.63: As in Figure 4.30 but for all *NA* GULF DCCs within the MED V tercile.

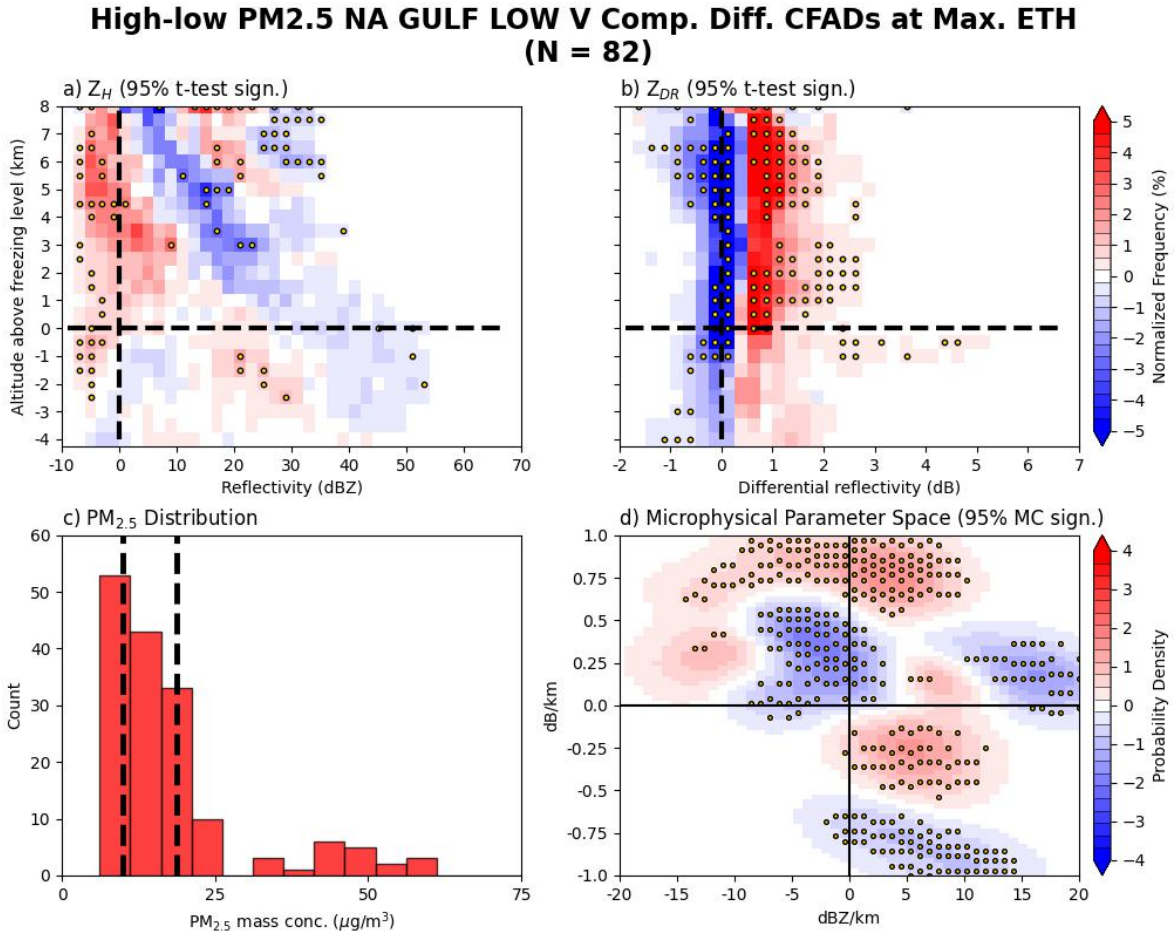

Figure 4.64: As in Figure 4.30 but for all *NA* GULF DCCs within the LOW V tercile.

4.2.2.2.3 NA LAND DCCs

The *NA* LAND MED GH and MED CAPE subsets exhibit similar patterns in their Z CFADs (Figures 4.65a and 4.66a), where Z for high $PM_{2.5}$ DCCs exhibits a narrower distribution compared to low $PM_{2.5}$ DCCs. However, the region marked by $Z > 35$ dBZ is statistically higher for low $PM_{2.5}$ DCCs only in the MED CAPE subset. Meanwhile, the Z_{DR} CFADs lack statistically significant differences above the freezing level for both subsets but exhibit significant differences below the freezing level (Figures 4.65b and 4.66b). In particular high (low) $PM_{2.5}$ DCCs are more likely to have $Z_{DR} > 1$ dB under

moderate GH (MUCAPE) conditions. Given the lack of statistical significance above the freezing level in Z_{DR}, it is difficult to asses the differences in the microphysical regimes that are consistent with the AIE theory.

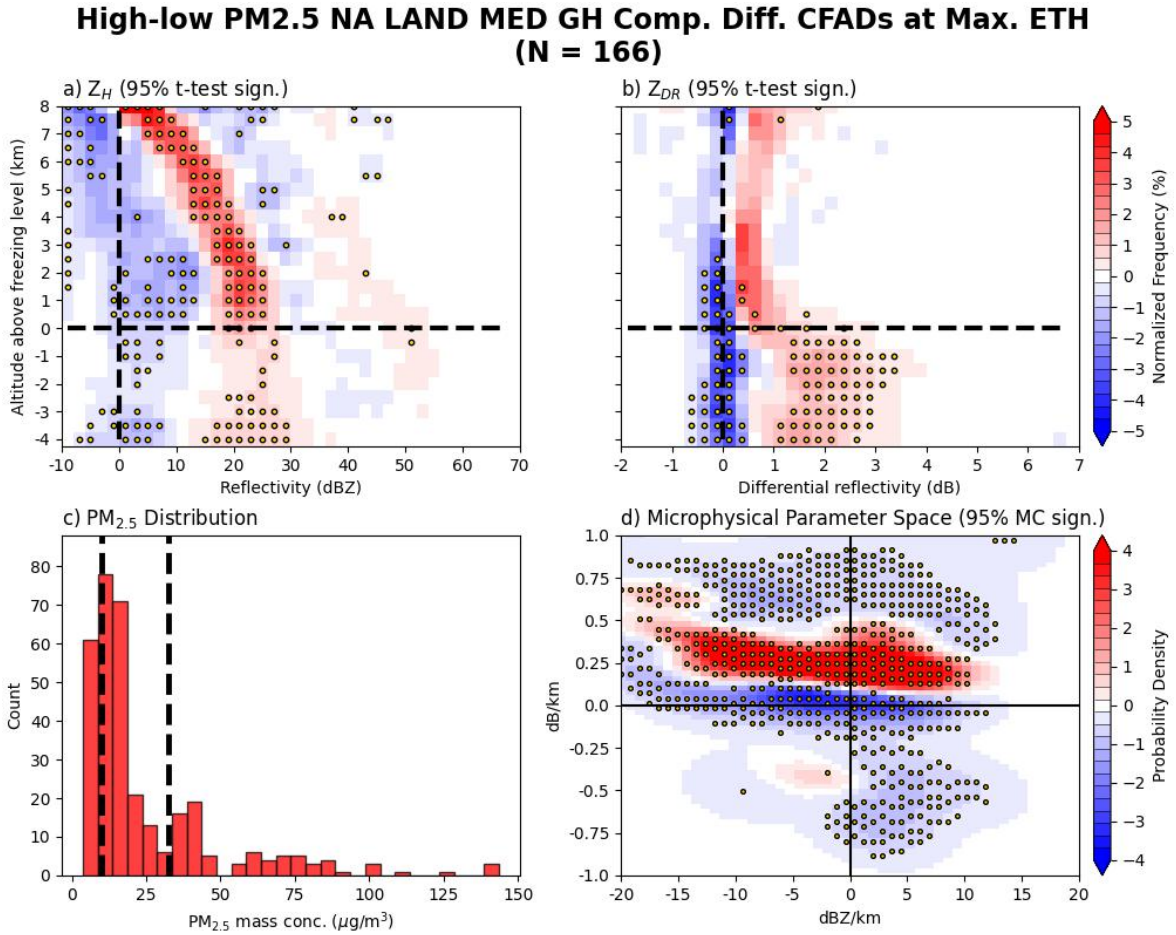

Figure 4.65: As in Figure 4.30 but for all *NA* LAND DCCs within the MED GH tercile.

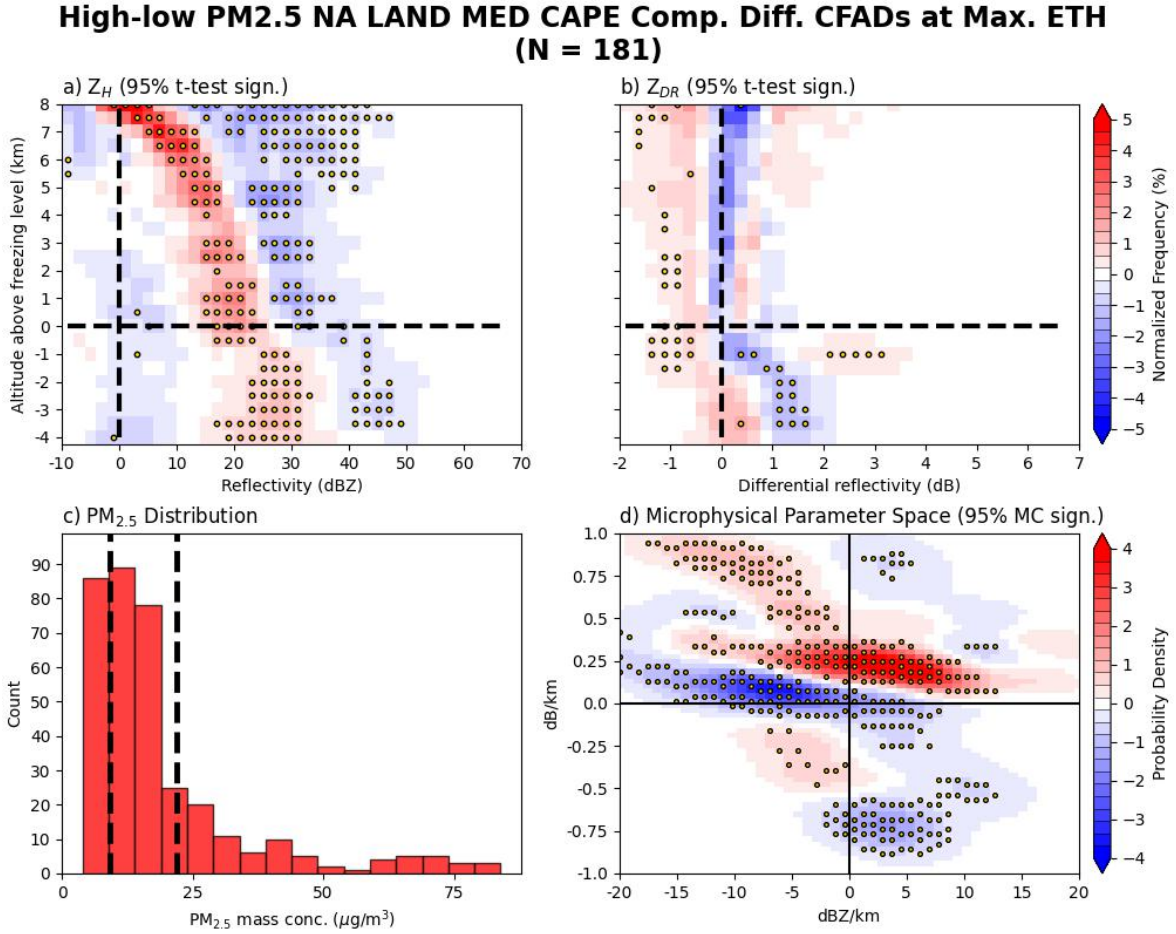

Figure 4.66: As in Figure 4.30 but for all *NA* LAND DCCs within the MED CAPE tercile.

Lastly, when controlling for DEW, the Z_{DR} CFADs show a similar pattern above the freezing level for high and moderate DEW (Figures 4.67b and 4.68b) where high $PM_{2.5}$ DCCs are more likely to have $Z_{DR} > 0.25$ dB, meaning that riming and accretion may be more prevalent. However, the HIGH DEW subset shows an overall lack of statistically significant differences of Z throughout most of the altitudes in the CFAD (Figure 4.67a) while the MED DEW shows significant likelihoods that Z is larger for high $PM_{2.5}$ DCCs (Figure 4.68a). In addition, significant differences in Z_{DR} below the freezing level only occur for the MED DEW subset and show that Z_{DR} is likely higher

for high $PM_{2.5}$ DCCs (Figure 4.68b). The lack of differences seen throughout most of the CFAD regions in the HIGH DEW subset suggests that the effects of high surface moisture over land dominate the impact on vertical radar data profiles rather than the $PM_{2.5}$ mass concentration. The only factor that does seem to be affected by the $PM_{2.5}$ mass concentration is Z_{DR} above the freezing level, which is consistent with the increased riming and accretion efficiencies that should occur from the AIE theory. The differences seen in the MED DEW subset CFADs and MPS plots are also consistent with slightly higher probabilities of invigoration of the high $PM_{2.5}$ DCCs' updrafts, but do not necessarily lead to an increase in the precipitation intensity since $Z > 35$ dBZ is not statistically different.

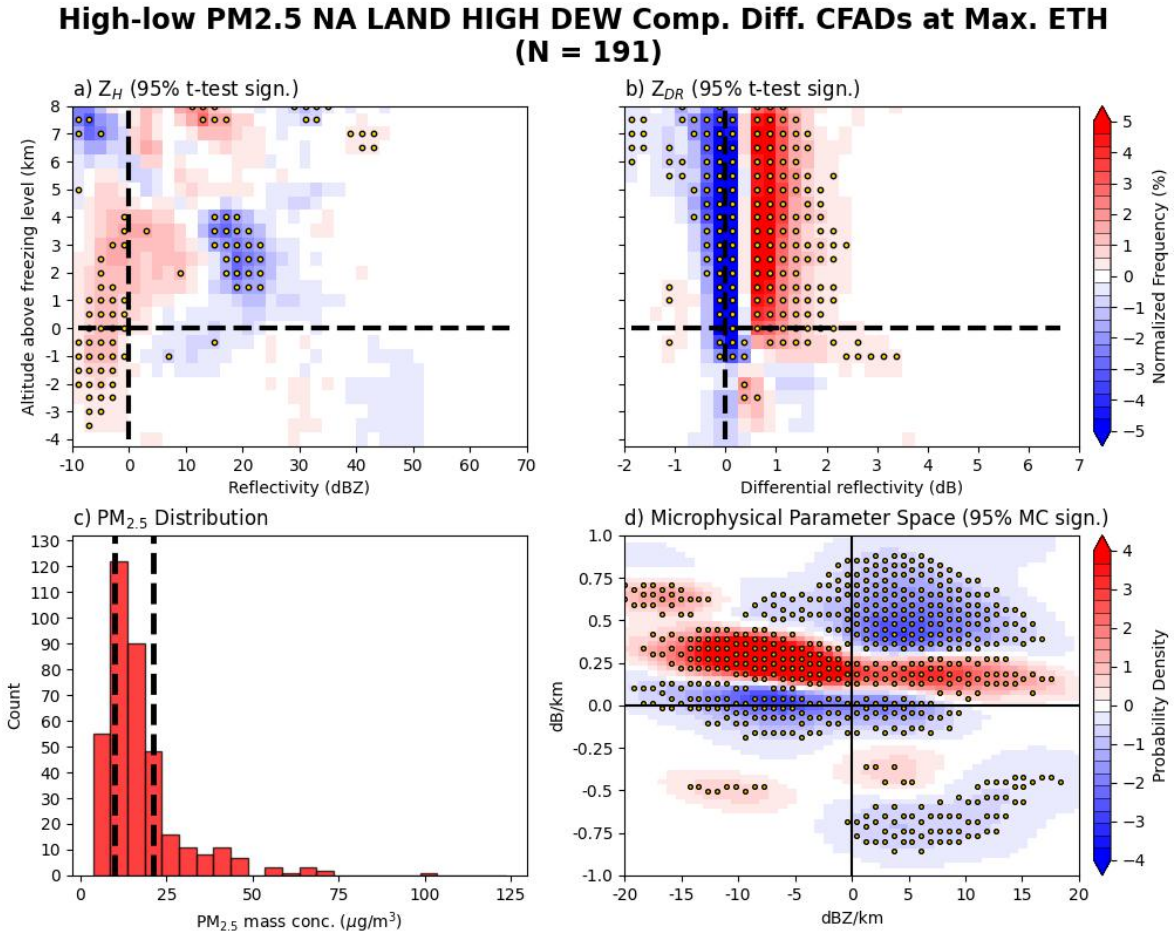

Figure 4.67: As in Figure 4.30 but for all *NA* LAND DCCs within the HIGH DEW tercile.

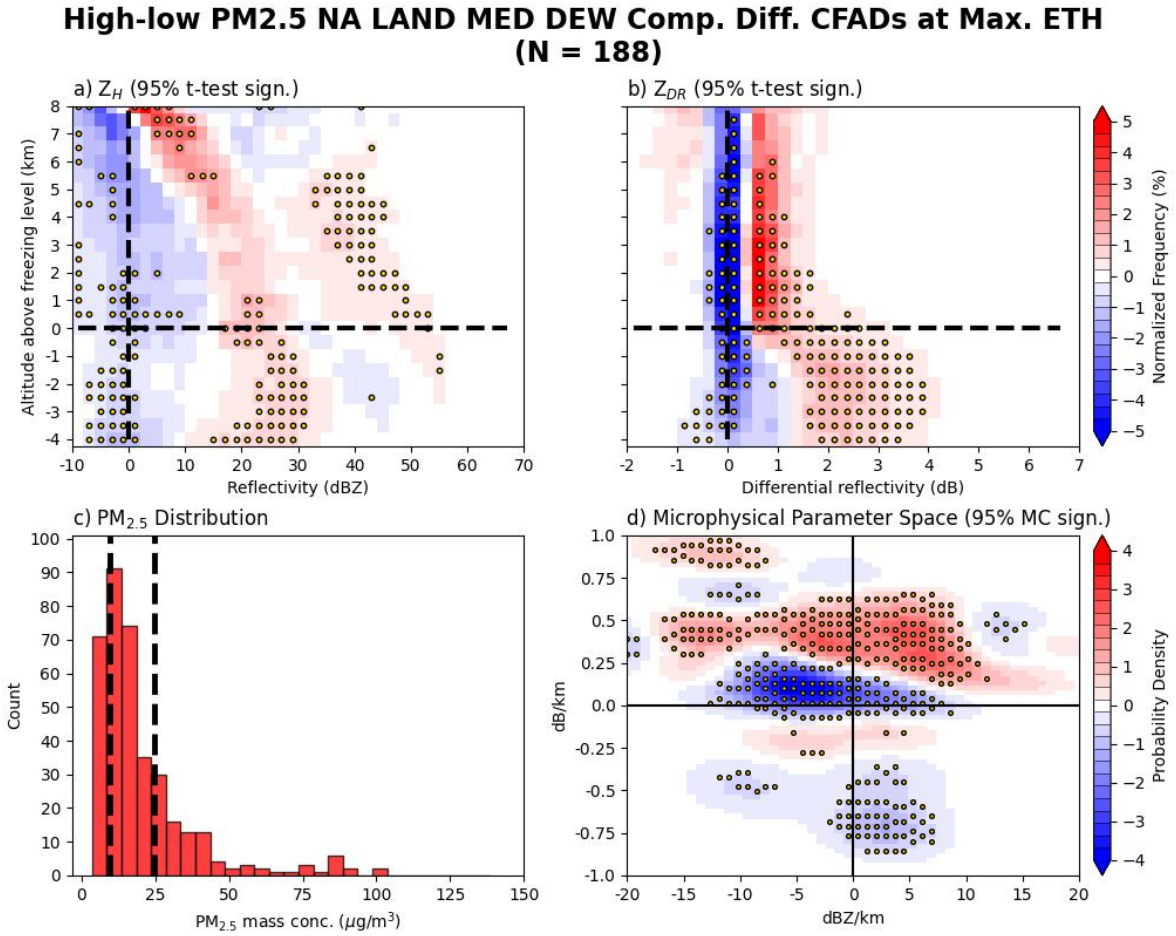

Figure 4.68: As in Figure 4.30 but for all *NA* LAND DCCs within the MED DEW tercile.

In summary, this section has explored differences in the vertical distributions of Z and Z_{DR} for subsets that do not show large statistically significant differences in their radar profiles and thus are difficult to classify when analyzing aerosol effects. In total, the subsets within this category can be under either of the the aerosol regimes, either of the geographic regimes, and many different meteorological conditions. Overall, they point to the need of more robust in-situ and remote sensing measurements of microphyiscal processes under differing meteorological conditions as well as model

simulations to understand different processes that need to be evaluated against observational data. Further, an even larger statistical study is needed to get more statistical significance in determining how the meteorological, geographic, and aerosol regimes influence the AIE.

Chapter 5

Summary, Conclusions, & Future Work

5.1 Summary

This study constructed a bulk statistical framework using dual-polarization radar data from KHGX, model reanalysis data from the ERA5, and aerosol data from the MERRA-2 to uncover effects of aerosol loading on DCCs within the Houston area. First, this study used the dataset to identify spatio-temporal locations of DCC occurrence around the Houston area, while characterizing DCCs based on a natural or anthropogenic regime. Important findings from the spatial analysis include a dependence of DCC aerosol regime based upon three main factors, surface sea-breeze flow characteristics, time of day, and location relative to large human populated areas such as Houston and Beaumont. Second, composite difference CFADs of Z and Z_{DR} were used to uncover mean differences in the vertical radar profiles of DCCs under differing aerosol loadings while constraining DCCs to similar meteorological conditions. For DCCs under similar MUCAPE, SH, or RH conditions, CFADs of Z and Z_{DR} show a wider distribution of Z and larger Z_{DR} below and above the freezing level for DCCs under high $PM_{2.5}$ conditions compared to low $PM_{2.5}$ DCCs. These differences are consistent with signatures of stronger size sorting and more intense precipitation for high $PM_{2.5}$ DCCs, leading to inferred aerosol induced invigoration which agree well with much of the previous work. Below, more detailed conclusions are drawn out for the vertical radar profile and spatial analyses.

5.2 Conclusions

5.2.1 Meteorological mediation of aerosol effects

5.2.1.1 Most-unstable CAPE

NA DCCs with high $PM_{2.5}$ mass concentration under low MUCAPE conditions over the Gulf exhibit differences in Z and Z_{DR} that are consistent with an invigoration of convection through the inhibition of warm rain. The updrafts and precipitation within these DCCs were shown to have higher probability of being more intense (Figure 4.40). However, as MUCAPE increases, the magnitude of the differences of radar data between high and low *NA* $PM_{2.5}$ DCCs over the Gulf wane, especially below the freezing level (Figures 4.59 and 4.60). Therefore, MUCAPE mediates the AIE for DCCs over the Gulf by decreasing the magnitude of aerosol effects with increasing MUCAPE.

Low and high MUCAPE regimes yield differences between high and low *NA* $PM_{2.5}$ DCCs over land in Z and Z_{DR} that are consistent with aerosol invigoration. Under both MUCAPE regimes, Figures 4.35 and 4.30 show that updrafts are more likely to be stronger for high $PM_{2.5}$ DCCs. However, only under high MUCAPE conditions do high $PM_{2.5}$ DCCs exhibit more intense precipitation than low $PM_{2.5}$ DCCs with this updraft invigoration, while under low MUCAPE conditions high $PM_{2.5}$ DCCs do not exhibit more intense precipitation than low $PM_{2.5}$ DCCs. Moderate MUCAPE leads to small differences in Z_{DR} and higher Z for low $PM_{2.5}$ DCCs compared to high $PM_{2.5}$ DCCs, consistent with the inhibition of updrafts and precipitation within high $PM_{2.5}$ DCCs (Figure 4.66).

The sample size is limited for *A* DCCs over the Gulf, and thus much of CFADs do not achieve statistical significance. The only region that does in the low MUCAPE subset is Z_{DR} below the freezing level and indicates that low $PM_{2.5}$ DCCs are more

likely to have larger drops than high $PM_{2.5}$ DCCs (Figure 4.48). For *A* DCCs over land, the low MUCAPE regime shows unclear differences between high and low $PM_{2.5}$ DCCs due to inconsistent patterns seen in the CFADs and MPS plot. Namely, that the MPS plot indicates stronger size sorting for high $PM_{2.5}$ DCCs even though they are more likely to have lower Z_{DR} than low $PM_{2.5}$ DCCs below the freezing level (Figure 4.52).

5.2.1.2 550 - 400 mb relative humidity

High and low *NA* $PM_{2.5}$ DCCs under low RH conditions over the Gulf exhibit differences in Z and Z_{DR} that result in unclear patterns of hydrometeor production, and thus aerosol effects cannot be quantified (Figure 4.55). Under moderate and high RH conditions, the statistically significant differences in Z and Z_{DR} between high and low $PM_{2.5}$ DCCs show a pattern that is consistent with aerosol invigoration (Figures A.7 and 4.42). However, the CFADs are consistent with different processes dominating hydrometeor production for high $PM_{2.5}$ DCCs, as the differences in Z everywhere and Z_{DR} above the freezing level show opposite patterns in the dominant $PM_{2.5}$ regime depending on moderate or high RH. In other words, moderate RH conditions promote higher Z_{DR} and narrower Z distributions for high $PM_{2.5}$ DCCs, where high RH conditions promote this pattern for low $PM_{2.5}$ DCCs. This points to the importance of RH when analyzing the AIE for Gulf DCCs.

Over land, high and low *NA* $PM_{2.5}$ DCCs across all three RH regimes have statistically significant differences in their Z and Z_{DR} profiles that exemplify patterns that are consistent with aerosol invigoration for high *NA* $PM_{2.5}$ DCCs. These patterns are consistent with a delaying of warm rain causing formation of rain at higher altitudes, stronger updrafts causing stronger size sorting, and increases in Z_{DR} above the freezing

level that are consistent with increased amounts of riming and accretion (Figures A.1, A.10, and 4.43). This supports aerosol invigoration of *NA* DCCs.

High and low *A* $PM_{2.5}$ DCCs over land under the low RH conditions exhibit insignificant differences in their Z and Z_{DR} CFADs due to the small number of DCCs in the subset. Thus, an incoherent pattern is also seen in the MPS plot (Figures 4.49) and aerosol impacts cannot be deduced.

5.2.1.3 400 mb shear magnitude

High and low *NA* $PM_{2.5}$ DCCs over land across all three SH regimes have statistically significant differences in their Z and Z_{DR} profiles that exemplify patterns that are consistent with updraft invigoration for high *NA* $PM_{2.5}$ DCCs (Figures 4.31, 4.37, and 4.36). Additionally, more intense precipitation is observed for the high $PM_{2.5}$ DCCs compared to low $PM_{2.5}$ DCCs for DCCs in the low and moderate SH regimes, but not the high SH regime, consistent with findings by Fan et al. (2009). Therefore, SH mainly moderates aerosol effects on DCCs by decreasing precipitation intensity for high $PM_{2.5}$ DCCs compared to low $PM_{2.5}$ DCCs with increasing SH.

5.2.1.4 650 mb divergence

NA DCCs under the moderate D650 regime over the Gulf show that there are only minimal areas of significant differences in the Z CFAD between high and low $PM_{2.5}$ DCCs (Figure 4.56a). Figure 4.56b also shows that there are larger likelihoods of higher Z_{DR} below the freezing level for high $PM_{2.5}$ DCCs compared to low $PM_{2.5}$ DCCs, but this does not equate to a clear pattern of stronger precipitation intensity as the MPS plot shows highly variable $\Delta Z/\Delta Z_{DR}$ pairs (Figure 4.56d). Thus, aerosol effects are difficult to quantify in this subset.

5.2.1.5 Boundary layer height

Low BLH conditions for *NA* DCCs over the Gulf do not promote differences in Z and Z_{DR} between high and low $PM_{2.5}$ DCCs that are consistent with updraft invigoration. While Figure 4.54b shows higher Z_{DR} for high $PM_{2.5}$ DCCs compared to low $PM_{2.5}$ DCCs, this does not mean stronger updrafts or precipitation intensity as noted in the MPS plot (Figure 4.54d). Instead, precipitation intensity is lower for high $PM_{2.5}$ DCCs compared to low $PM_{2.5}$ DCCs under low BLH conditions. Moderate BLH conditions promote differences in Z and Z_{DR} between high and low $PM_{2.5}$ DCCs that show a clearer pattern consistent with updraft invigoration and increases in precipitation intensity (Figure 4.41). However, there is still higher probability that low $PM_{2.5}$ DCCs exhibit high Z_{DR} above the freezing level compared to high $PM_{2.5}$ DCCs and may be a result of different ice crystal habits. High BLH conditions promote no coherent differences between high and low $PM_{2.5}$ DCCs which may be the result of a small number of DCCs sampled under such conditions (Figure 4.53). Therefore, only moderate BLH conditions promote aerosol invigoration, while low and high BLH conditions yield unclear aerosol impacts.

5.2.1.6 400 mb v-wind

High and low *NA* $PM_{2.5}$ DCCs over the Gulf exhibit differences in Z and Z_{DR} that do not show a clear pattern consistent with aerosol invigoration under all three of the V regimes. However, Figures 4.64b and 4.63b show significant differences in Z_{DR} between high and low $PM_{2.5}$ DCCs above the freezing level for the low and moderate V subsets. Low V promotes higher Z_{DR} above the freezing level for high $PM_{2.5}$ DCCs compared to low $PM_{2.5}$ DCCs while moderate V promotes higher Z_{DR} for low $PM_{2.5}$ DCCs compared to high $PM_{2.5}$ DCCs. This is somewhat consistent with Fan et al. (2009)'s findings of stronger shear (recall, V and SH are significantly correlated and discussed in section

4.2.1.1) decreasing aerosol invigoration due to entrainment effects which would lead to decreased riming and accretion efficiency and hence lower Z_{DR} values for high $PM_{2.5}$ DCCs compared to low $PM_{2.5}$ DCCs above the freezing level. This trend however is not seen clearly in the high V Z_{DR} CFAD (Figure 4.62b). Instead, the high V regime promotes higher Z_{DR} for high $PM_{2.5}$ DCCs compared to low $PM_{2.5}$ DCCs below the freezing level, but this does not mean stronger updrafts or larger precipitation intensity as seen in the MPS plot (Figure 4.62d).

5.2.1.7 650 - 550 mb geopotential height

High and low $PM_{2.5}$ *NA* DCCs over the land exhibit significant differences in Z and Z_{DR} that are consistent with updraft invigoration under low and high GH conditions (Figures 4.32 and A.5). However, high $PM_{2.5}$ DCCs only exhibit increases in precipitation intensity compared to low $PM_{2.5}$ DCCs under low GH conditions. Moderate GH conditions lead to small differences in Z_{DR} above the freezing level (Figure 4.65b) as well as unclear patterns the MPS plot (Figure 4.65d) between high and low $PM_{2.5}$ DCCs. These observations are consistent with low GH conditions promoting aerosol invigoration of updrafts and precipitation intensity, high GH conditions promoting only invigoration of updrafts at the time of maximum ETH, and unclear effects on the processes for moderate GH conditions.

High $PM_{2.5}$ *A* DCCs over the land exhibit a decrease in precipitation intensity compared to low $PM_{2.5}$ DCCs for moderate GH conditions. This is evident in Figure 4.45 where Z_{DR} is likely larger for low $PM_{2.5}$ DCCs below the freezing level and the MPS plot shows that the high $PM_{2.5}$ DCCs are likely to exhibit evaporation within the warm region.

5.2.1.8 Surface temperature

High and low $PM_{2.5}$ *NA* DCCs over the land exhibit significant differences in Z and Z_{DR} that are consistent with updraft invigoration for all three regimes of T (Figures A.4, A.3, and A.2). However, none of these subsets show a corresponding increase in precipitation intensity evident in the Z CFADs. This means that T does not strongly mediate aerosol effects on updraft and precipitation intensity for *NA* DCCs, since all subsets show similar results.

While the sample size is low, differences illustrated Z and Z_{DR} between high and low *A* $PM_{2.5}$ DCCs over land are consistent with updraft invigoration when T conditions are high, as noted by the Z_{DR} CFAD and MPS plot (Figures A.8b and A.8d).

5.2.1.9 500 mb divergence

Much like for T, high $PM_{2.5}$ *NA* DCCs over the land exhibit an increase in updraft strength compared to low $PM_{2.5}$ *NA* DCCs for all three regimes of D500 while precipitation intensity is not enhanced (Figures A.6, 4.33, and A.11). The magnitude of the differences in the Z and Z_{DR} CFADs for high and low $PM_{2.5}$ DCCs do wane with increasing D500, consistent with positive D500 generally minimizing aerosol effects on the vertical radar structure while stronger aerosol effects on the vertical radar profile, especially for Z_{DR}, are present for negative D500.

5.2.1.10 Surface dew point

A DCCs over land under low DEW conditions show differences in Z and Z_{DR} between high and low $PM_{2.5}$ DCCs that are consistent with an unclear pattern of aerosol effects, evident in the MPS plot (Figure 4.51d). However, the low $PM_{2.5}$ DCCs do exhibit higher Z_{DR} below the freezing level compared to high $PM_{2.5}$ DCCs, meaning that

precipitation intensity may be somewhat decreased for the high $PM_{2.5}$ DCCs under low DEW conditions.

5.2.2 Aerosol effects

Below, conclusions that can be drawn from the subsets that do not account for meteorological conditions are presented. Sample sizes are much larger for these subsets, but the important influences of meteorology are not accounted for, and the results should thus be interpreted with caution.

5.2.2.1 High vs. low $PM_{2.5}$

For *NA* DCCs over the Gulf and land, differences in Z and Z_{DR} between high and low $PM_{2.5}$ DCCs that are consistent with updraft invigoration are seen in Figures 4.34 and A.9. For both geographical regimes, the high $PM_{2.5}$ DCCs exhibit Z_{DR} that is higher throughout the vertical depth of the CFAD, dominance in the size sorting quadrant, and higher Z above the freezing level compared to low $PM_{2.5}$ DCCs. However, Figures 4.50 and 4.46 show that *A* DCCs have a nearly opposite pattern, where in general the low $PM_{2.5}$ DCCs exhibit higher or minimal differences in Z_{DR} throughout the vertical depth of the CFAD, dominance in the size sorting quadrant, and Z that is larger above the freezing level or a Z distribution that is wider below the freezing level compared high $PM_{2.5}$ DCCs. These results suggest that high *NA* $PM_{2.5}$ mass concentration can invigorate updrafts across both geographical regimes, while high *A* $PM_{2.5}$ mass concentration can inhibit updrafts and their precipitation.

5.2.2.2 *NA* vs. *A*

When comparing differences of the *NA* and *A* DCCs across the Gulf and land, the patterns in the CFADs and MPS plots shown in Figures A.12 and 4.44 are nearly

opposite based on aerosol regime (NA or A). This means that NA (A) DCCs over the Gulf (land) exhibit stronger updrafts consistent with higher Z and Z_{DR} below the freezing level and dominance in the size sorting quadrant of the MPS plot compared to A (NA) DCCs. However, the Z_{DR} CFADs show that Z_{DR} is higher for A (NA) DCCs over the Gulf (land) (Figures A.12b and 4.44b). This is consistent with condensational invigoration within the warm region being more prominent in NA (A) DCCs over the Gulf (land) than mixed-phase invigoration within the cold region, which was previously seen in the model simulations of Cotton and Walko (2021).

5.2.3 Spatio-temporal conclusions

The spatial analysis presented in section 4.1 showed that there are key factors that determine the likelihood of DCCs occurring in different areas, times, and aerosol regimes around Houston. The most important factor is the diurnal cycle, with increased probability of DCCs occurring within the early morning hours and peaking in occurrence near 18 – 20 UTC (1 – 3 PM local time) (Figure 4.3). The diurnal cycle dictates the onset and dissipation times of the sea breeze, which are noted in Figure 4.4a as approximately 12 -14 UTC (7 – 9 AM) and 1 UTC (8 PM) on average, respectively. Between the hours of 8 PM – 9 AM, DCCs were found to be under mostly southerly flow, with NA (A) DCCs more likely to exhibit flow $>$ ($<$) 7 m/s (Figure 4.5). This stronger flow should lead to stronger sea-salt aerosol advection from the Gulf, meaning the DCCs are more likely to be classified within an NA air mass. When flow is weak and thus sea-salt aerosols are not prominent, A DCCs may be more prevalent east of 95°W over the Gulf and land due to shipping emissions. After sea breeze onset, NA and A DCC occurrence is heavily dependent upon the strength and direction of the on-shore flow. It was found that if the flow is weak and/or easterly, then A DCCs were more likely to occur near heavily populated cities such as Houston and Beaumont. If the

flow is stronger and southerly, then *NA* DCCs were likely to form in all areas south of Houston (Figure 4.17). Finally, DCC lifetime exhibited no significant correlation with $PM_{2.5}$ mass concentration, no matter the type of aerosol (*NA* or *A*) or meteorological influence.

5.3 Limitations, recommendations, & future work

The differences and conclusions reached for DCC subsets presented in chapter 4 are only valid for comparing numerous DCCs. For example, differences in the vertical structure of Z and Z_{DR} that were uncovered under differing aerosol regimes most likely will not be found if comparing just two individual DCCs using an NEXRAD WSR-88D, due to both resolution of the 88D and subtle differences in meteorology that are impossible to completely account for. Thus the AIE influences on the radar structure are only valid in a mean sense when comparing numerous DCCs under similar meteorological environments. Further, only differences in cloud properties, and not processes, can be obtained from observations such as those within this study. Modeling studies that turn on and off various aerosol processes are needed to understand reasons for the observed differences.

There are some limitations for uncovering aerosol effects on DCCs in this study that lead to some uncertainties, namely the coarse resolution of data, parameterizations of MERRA-2, ERA5's inability to resolve interactions of DCCs with one another, and the dependency of the results on the sensitivity of MCIT. To mitigate these uncertainties, future work should compare use of a Z_{DR}-column algorithm with the current ETH method to gain further insights into how aerosol loading changes temporal evolution of Z_{DR}-column heights in DCCs. The coarse resolution of the meteorological and aerosol data could be dealt with by including further data, such as the use of the

North American Regional Reanalysis (NARR), which has data available similar to ERA5 to compare results, and the inclusion of a second aerosol dataset consisting of satellite-retrieved CCN number concentration estimates (e.g., Hu et al., 2019a). These estimates would also greatly improve the uncertainty caused by the parameterizations of MERRA-2's $PM_{2.5}$ representation. With the two aerosol datasets, much work could be done in validating MERRA-2's ability to estimate periods of high CCN loading and compare results of this study when using satellite-retrieved estimates. Finally, the dependency of the results to the MCIT algorithm parameters could be quantified by using sensitivity tests that change the MCIT thresholds such as minimum valley depth, minimum cell size, and minimum cell depth which would allow for easier temporal analysis of DCC evolution and the AIE.

The Experiment of Sea Breeze Convection, Aerosols, Precipitation, and Environment (ESCAPE) field campaign was conducted from May 30 to June 30, 2022 within the southeast Texas and southwestern Louisiana regions. The goals of this campaign consisted of characterizing DCC kinematic and microphysical vertical profiles using rapid-scan, dual-polarization weather radars, quantifying meteorological and aerosol impacts on DCCs, and modeling the roles of aerosols and meteorological environments on DCCs. An integral part of ESCAPE was to quantify aerosol effects on DCCs in Houston under similar meteorological conditions using in-situ and remote sensing measurements, which is precisely what this current study examined using a bulk statistical framework. In ESCAPE, utilization of the PX-1000, RaXPol, and SKYLER ground-based mobile radars along with numerous airborne radars allowed for high resolution dual-polarization radar data collection of DCCs in both the vertical and horizontal planes. Coincident in-situ measurements using cloud microphysical probes aboard the National Research Council Canada Convair-580 and the SPEC LearJet-35A were also taken within DCCs. The data obtained throughout this campaign could easily be

appended to a study such as this in which specific case studies from ESCAPE can be analyzed and compared with bulk statistical properties found within this study to verify or conflict with the conclusions reached.

Reference List

Adler, G., J. Flores, A. Abo Riziq, S. Borrmann, and Y. Rudich, 2011: Chemical, physical, and optical evolution of biomass burning aerosols: a case study. *Atmospheric Chemistry and Physics*, **11 (4)**, 1491–1503.

Al-Naiema, I. M., and Coauthors, 2018: Source apportionment of fine particulate matter in houston,¡? xmltex\break?¿ texas: insights to secondary organic aerosols. *Atmospheric chemistry and physics*, **18 (21)**, 15 601–15 622.

Albrecht, B. A., 1989: Aerosols, cloud microphysics, and fractional cloudiness. *Science*, **245 (4923)**, 1227–1230.

Allen, R. J., A. T. Evan, and B. B. Booth, 2015: Interhemispheric aerosol radiative forcing and tropical precipitation shifts during the late twentieth century. *Journal of Climate*, **28 (20)**, 8219–8246.

Altaratz, O., R. Bar-Or, U. Wollner, and I. Koren, 2013: Relative humidity and its effect on aerosol optical depth in the vicinity of convective clouds. *Environmental Research Letters*, **8 (3)**, 034 025.

Altaratz, O., I. Koren, L. Remer, and E. Hirsch, 2014: Cloud invigoration by aerosols—coupling between microphysics and dynamics. *Atmospheric Research*, **140**, 38–60.

Andreae, M., and D. Rosenfeld, 2008: Aerosol–cloud–precipitation interactions. part 1. the nature and sources of cloud-active aerosols. *Earth-Science Reviews*, **89 (1-2)**, 13–41.

Andreae, M. O., 2001: The dark side of aerosols. *Nature*, **409 (6821)**, 671–672.

Andreae, M. O., C. D. Jones, and P. M. Cox, 2005: Strong present-day aerosol cooling implies a hot future. *Nature*, **435 (7046)**, 1187–1190.

Andreae, M. O., D. Rosenfeld, P. Artaxo, A. Costa, G. Frank, K. Longo, and M. A. F. d. Silva-Dias, 2004: Smoking rain clouds over the amazon. *science*, **303 (5662)**, 1337–1342.

Andrić, J., M. R. Kumjian, D. S. Zrnić, J. M. Straka, and V. M. Melnikov, 2013: Polarimetric signatures above the melting layer in winter storms: An observational and modeling study. *Journal of Applied Meteorology and Climatology*, **52 (3)**, 682–700.

Arritt, R. W., 1993: Effects of the large-scale flow on characteristic features of the sea breeze. *Journal of Applied Meteorology and Climatology*, **32 (1)**, 116–125.

Balakrishnan, N., and D. Zrnic, 1990: Use of polarization to characterize precipitation and discriminate large hail. *Journal of Atmospheric sciences*, **47 (13)**, 1525–1540.

Bao, J.-W., S. Michelson, S. McKeen, and G. Grell, 2005: Meteorological evaluation of a weather-chemistry forecasting model using observations from the texas aqs 2000 field experiment. *Journal of Geophysical Research: Atmospheres*, **110 (D21)**.

Bauer, H., H. Giebl, R. Hitzenberger, A. Kasper-Giebl, G. Reischl, F. Zibuschka, and H. Puxbaum, 2003: Airborne bacteria as cloud condensation nuclei. *Journal of Geophysical Research: Atmospheres*, **108 (D21)**.

Bechtold, P., J.-P. Pinty, and F. Mascart, 1991: A numerical investigation of the influence of large-scale winds on sea-breeze-and inland-breeze-type circulations. *Journal of Applied Meteorology and Climatology*, **30 (9)**, 1268–1279.

Bell, T. L., D. Rosenfeld, K.-M. Kim, J.-M. Yoo, M.-I. Lee, and M. Hahnenberger, 2008: Midweek increase in us summer rain and storm heights suggests air pollution invigorates rainstorms. *Journal of Geophysical Research: Atmospheres*, **113 (D2)**.

Blair, W. F., 1950: Ecological factors in speciation of peromyscus. *Evolution*, 253–275.

Boer, G., G. Flato, and D. Ramsden, 2000: A transient climate change simulation with greenhouse gas and aerosol forcing: projected climate to the twenty-first century. *Climate dynamics*, **16 (6)**, 427–450.

Boucher, O., and J. Quaas, 2013: Water vapour affects both rain and aerosol optical depth. *Nature Geoscience*, **6 (1)**, 4–5.

Bozlaker, A., J. M. Prospero, M. P. Fraser, and S. Chellam, 2013: Quantifying the contribution of long-range saharan dust transport on particulate matter concentrations in houston, texas, using detailed elemental analysis. *Environmental science & technology*, **47 (18)**, 10 179–10 187.

Bringi, V., K. Knupp, A. Detwiler, L. Liu, I. Caylor, and R. Black, 1997: Evolution of a florida thunderstorm during the convection and precipitation/electrification experiment: The case of 9 august 1991. *Monthly weather review*, **125 (9)**, 2131–2160.

Byers, H. R., and H. R. Rodebush, 1948: Causes of thunderstorms of the florida peninsula. *Journal of Atmospheric Sciences*, **5 (6)**, 275–280.

Cao, Q., M. Knight, J. Hu, A. Ryzhkov, and P. Zhang, 2021: A novel multi-cell identification and tracking algorithm implemented on eec radars. *101st American Meteorological Society Annual Meeting*, AMS.

Carrió, G., , and W. Cotton, 2011: Urban growth and aerosol effects on convection over houston. part ii: Dependence of aerosol effects on instability. *Atmospheric research*, **102 (1-2)**, 167–174.

Carrió, G., W. Cotton, and W. Cheng, 2010: Urban growth and aerosol effects on convection over houston: Part i: The august 2000 case. *Atmospheric Research*, **96 (4)**, 560–574.

Cash, M., 2013: Houston market overview. *Major, Hagen, and Africa*.

Chand, D., and Coauthors, 2012: Aerosol optical depth increase in partly cloudy conditions. *Journal of Geophysical Research: Atmospheres*, **117 (D17)**.

Charlson, R. J., S. Schwartz, J. Hales, R. D. Cess, J. Coakley Jr, J. Hansen, and D. Hofmann, 1992: Climate forcing by anthropogenic aerosols. *Science*, **255 (5043)**, 423–430.

Chen, T., Z. Li, R. A. Kahn, C. Zhao, D. Rosenfeld, J. Guo, W. Han, and D. Chen, 2021: Potential impact of aerosols on convective clouds revealed by himawari-8 observations over different terrain types in eastern china. *Atmospheric Chemistry and Physics*, **21 (8)**, 6199–6220.

Chew, B. N., J. R. Campbell, J. S. Reid, D. M. Giles, E. J. Welton, S. V. Salinas, and S. C. Liew, 2011: Tropical cirrus cloud contamination in sun photometer data. *Atmospheric Environment*, **45 (37)**, 6724–6731.

Chin, M., and Coauthors, 2002: Tropospheric aerosol optical thickness from the gocart model and comparisons with satellite and sun photometer measurements. *Journal of the atmospheric sciences*, **59 (3)**, 461–483.

Conway, J. W., and D. S. Zrnić, 1993: A study of embryo production and hail growth using dual-doppler and multiparameter radars. *Monthly weather review*, **121 (9)**, 2511–2528.

Cotton, W. R., and R. Walko, 2021: Examination of aerosol-induced convective invigoration using idealized simulations. *Journal of the Atmospheric Sciences*, **78 (1)**, 287–298.

Council, N. R., and Coauthors, 2002: *Weather radar technology beyond NEXRAD*. National Academies Press.

Dagan, G., I. Koren, and O. Altaratz, 2015: Aerosol effects on the timing of warm rain processes. *Geophysical Research Letters*, **42 (11)**, 4590–4598.

Dai, Q., and Coauthors, 2019: Seasonal differences in formation processes of oxidized organic aerosol near houston, tx. *Atmospheric Chemistry and Physics*, **19 (14)**, 9641–9661.

Daum, P. H., L. I. Kleinman, S. R. Springston, L. Nunnermacker, Y.-N. Lee, J. Weinstein-Lloyd, J. Zheng, and C. M. Berkowitz, 2004: Origin and properties of plumes of high ozone observed during the texas 2000 air quality study (texaqs 2000). *Journal of Geophysical Research: Atmospheres*, **109 (D17)**.

Diehl, K., C. Quick, S. Matthias-Maser, S. Mitra, and R. Jaenicke, 2001: The ice nucleating ability of pollen: Part i: Laboratory studies in deposition and condensation freezing modes. *Atmospheric Research*, **58 (2)**, 75–87.

Diehl, T., A. Heil, M. Chin, X. Pan, D. Streets, M. Schultz, and S. Kinne, 2012: Anthropogenic, biomass burning, and volcanic emissions of black carbon, organic carbon, and so 2 from 1980 to 2010 for hindcast model experiments. *Atmospheric Chemistry and Physics Discussions*, **12 (9)**, 24 895–24 954.

Donaldson Jr, R. J., 1964: A demonstration of antenna beam errors in radar reflectivity patterns. *Journal of Applied Meteorology and Climatology*, **3 (5)**, 611–623.

Doviak, R. J., D. S. Zrnic, and R. M. Schotland, 1994: Doppler radar and weather observations. *Applied Optics*, **33 (21)**, 4531.

Duan, J., and Coauthors, 2018: Influence of pollutants on activity of aerosol cloud condensation nuclei (ccn) during pollution and post-rain periods in guangzhou, southern china. *Science of the total environment*, **642**, 1008–1019.

Dzubay, T. G., R. K. Stevens, C. W. Lewis, D. H. Hern, W. J. Courtney, J. W. Tesch, and M. A. Mason, 1982: Visibility and aerosol composition in houston, texas. *Environmental Science & Technology*, **16 (8)**, 514–525.

Estoque, M. A., 1962: The sea breeze as a function of the prevailing synoptic situation. *Journal of Atmospheric Sciences*, **19 (3)**, 244–250.

Evans, J., K. Carusone, M. Wolfson, M. Robinson, E. Ducot, and B. Crowe, 2004: P1. 5 improving convective weather operations in highly congested airspace with the corridor integrated weather system (ciws).

Fan, J., and Coauthors, 2009: Dominant role by vertical wind shear in regulating aerosol effects on deep convective clouds. *Journal of Geophysical Research: Atmospheres*, **114 (D22)**.

Fan, J., and Coauthors, 2018: Substantial convection and precipitation enhancements by ultrafine aerosol particles. *Science*, **359 (6374)**, 411–418.

Feingold, G., W. R. Cotton, S. M. Kreidenweis, and J. T. Davis, 1999: The impact of giant cloud condensation nuclei on drizzle formation in stratocumulus: Implications for cloud radiative properties. *Journal of the atmospheric sciences*, **56 (24)**, 4100–4117.

Franc, G. D., and P. J. DeMott, 1998: Cloud activation characteristics of airborne erwinia carotovora cells. *Journal of Applied Meteorology and Climatology*, **37 (10)**, 1293–1300.

Fuchs, B. R., and Coauthors, 2015: Environmental controls on storm intensity and charge structure in multiple regions of the continental united states. *Journal of Geophysical Research: Atmospheres*, **120 (13)**, 6575–6596.

Ghan, S. J., and S. E. Schwartz, 2007: Aerosol properties and processes: A path from field and laboratory measurements to global climate models. *Bulletin of the American Meteorological Society*, **88 (7)**, 1059–1084.

Giangrande, S. E., and Coauthors, 2016: Convective cloud vertical velocity and mass-flux characteristics from radar wind profiler observations during goamazon2014/5. *Journal of Geophysical Research: Atmospheres*, **121 (21)**, 12–891.

Givati, A., and D. Rosenfeld, 2004: Quantifying precipitation suppression due to air pollution. *Journal of Applied Meteorology and Climatology*, **43 (7)**, 1038–1056.

Gong, S., 2003: A parameterization of sea-salt aerosol source function for sub-and super-micron particles. *Global biogeochemical cycles*, **17 (4)**.

Grabowski, W. W., 2015: Untangling microphysical impacts on deep convection applying a novel modeling methodology. *Journal of the Atmospheric Sciences*, **72 (6)**, 2446–2464.

Grabowski, W. W., and H. Morrison, 2016: Untangling microphysical impacts on deep convection applying a novel modeling methodology. part ii: Double-moment microphysics. *Journal of the Atmospheric Sciences*, **73 (9)**, 3749–3770.

Gryspeerdt, E., P. Stier, and D. Partridge, 2014: Links between satellite-retrieved aerosol and precipitation. *Atmospheric Chemistry and Physics*, **14 (18)**, 9677–9694.

Guggenheim, E., 1937: The theoretical basis of raoult's law. *Transactions of the Faraday Society*, **33**, 151–156.

Gunn, R., and B. Phillips, 1957: An experimental investigation of the effect of air pollution on the initiation of rain. *Journal of the Atmospheric Sciences*, **14 (3)**, 272–280.

Guo, J., and Coauthors, 2016: Three-dimensional structure of aerosol in china: A perspective from multi-satellite observations. *Atmospheric Research*, **178**, 580–589.

Guo, J., and Coauthors, 2018: Aerosol-induced changes in the vertical structure of precipitation:¡? xmltex\break?¿ a perspective of trmm precipitation radar. *Atmospheric Chemistry and Physics*, **18 (18)**, 13 329–13 343.

Hall, M. P., J. W. Goddard, and S. M. Cherry, 1984: Identification of hydrometeors and other targets by dual-polarization radar. *Radio Science*, **19 (1)**, 132–140.

Hall, W. D., 1980: A detailed microphysical model within a two-dimensional dynamic framework: Model description and preliminary results. *Journal of Atmospheric Sciences*, **37 (11)**, 2486–2507.

Hansen, J., M. Sato, R. Ruedy, A. Lacis, and V. Oinas, 2000: Global warming in the twenty-first century: An alternative scenario. *Proceedings of the National Academy of Sciences*, **97 (18)**, 9875–9880.

Haurwitz, B., 1947: Comments on the sea-breeze circulation. *Journal of Atmospheric Sciences*, **4 (1)**, 1–8.

Held, G., 1978: The probability of hail in relation to radar echo heights on the south african highveld. *Journal of Applied Meteorology and Climatology*, **17 (6)**, 755–762.

Hersbach, H., and Coauthors, 2020: The era5 global reanalysis. *Quarterly Journal of the Royal Meteorological Society*, **146 (730)**, 1999–2049.

Hogan, R. J., P. Field, A. Illingworth, R. Cotton, and T. Choularton, 2002: Properties of embedded convection in warm-frontal mixed-phase cloud from aircraft and polarimetric radar. *Quarterly Journal of the Royal Meteorological Society: A journal of the atmospheric sciences, applied meteorology and physical oceanography*, **128 (580)**, 451–476.

Hu, J., and Coauthors, 2019a: Polarimetric radar convective cell tracking reveals large sensitivity of cloud precipitation and electrification properties to ccn. *Journal of Geophysical Research: Atmospheres*, **124 (22)**, 12 194–12 205.

Hu, J., and Coauthors, 2019b: Tracking and characterization of convective cells through their maturation into stratiform storm elements using polarimetric radar and lightning detection. *Atmospheric Research*, **226**, 192–207.

Huang, J., Q. Fu, J. Su, Q. Tang, P. Minnis, Y. Hu, Y. Yi, and Q. Zhao, 2009: Taklimakan dust aerosol radiative heating derived from calipso observations using the fu-liou radiation model with ceres constraints. *Atmospheric Chemistry and Physics*, **9 (12)**, 4011–4021.

Ilotoviz, E., A. Khain, A. V. Ryzhkov, and J. C. Snyder, 2018: Relationship between aerosols, hail microphysics, and zdr columns. *Journal of the Atmospheric Sciences*, **75 (6)**, 1755–1781.

IPCC, 2007: Ipcc fourth assessment report (ar4). *Climate change*, **374**.

Jin, M., J. M. Shepherd, and M. D. King, 2005: Urban aerosols and their variations with clouds and rainfall: A case study for new york and houston. *Journal of Geophysical Research: Atmospheres*, **110 (D10)**.

Jirak, I. L., and W. R. Cotton, 2006: Effect of air pollution on precipitation along the front range of the rocky mountains. *Journal of Applied Meteorology and Climatology*, **45 (1)**, 236–245.

Kanakidou, M., K. Tsigaridis, F. J. Dentener, and P. J. Crutzen, 2000: Human-activity-enhanced formation of organic aerosols by biogenic hydrocarbon oxidation. *Journal of Geophysical Research: Atmospheres*, **105 (D7)**, 9243–9354.

Kennedy, P. C., and S. A. Rutledge, 2011: S-band dual-polarization radar observations of winter storms. *Journal of Applied Meteorology and Climatology*, **50 (4)**, 844–858.

Khain, A., N. BenMoshe, and A. Pokrovsky, 2008: Factors determining the impact of aerosols on surface precipitation from clouds: An attempt at classification. *Journal of the Atmospheric Sciences*, **65 (6)**, 1721–1748.

Khain, A., D. Rosenfeld, and A. Pokrovsky, 2005: Aerosol impact on the dynamics and microphysics of deep convective clouds. *Quarterly Journal of the Royal Meteorological Society: A journal of the atmospheric sciences, applied meteorology and physical oceanography*, **131 (611)**, 2639–2663.

Köhler, H., 1921: *Zur Kondensation des Wasserdampfes in der Atmosphäre*. I kommission hos Cammermeyers boghandel Kristiania.

Kondratyev, K. Y., L. S. Ivlev, V. F. Krapivin, and C. A. Varotsos, 2006: Aerosol radiative forcing and climate. *Atmospheric Aerosol Properties: Formation, Processes and Impacts*, 507–566.

Koren, I., O. Altaratz, L. A. Remer, G. Feingold, J. V. Martins, and R. H. Heiblum, 2012: Aerosol-induced intensification of rain from the tropics to the mid-latitudes. *Nature Geoscience*, **5 (2)**, 118–122.

Koren, I., Y. J. Kaufman, D. Rosenfeld, L. A. Remer, and Y. Rudich, 2005: Aerosol invigoration and restructuring of atlantic convective clouds. *Geophysical Research Letters*, **32 (14)**.

Koren, I., L. Remer, O. Altaratz, J. Martins, and A. Davidi, 2010: Aerosol-induced changes of convective cloud anvils produce strong climate warming. *Atmospheric Chemistry and Physics*, **10 (10)**, 5001–5010.

Kuba, N., and M. Murakami, 2010: Effect of hygroscopic seeding on warm rain clouds – numerical study using a hybrid cloud microphysical model. *Atmospheric Chemistry and Physics*, **10 (7)**, 3335–3351, https://doi.org/10.5194/acp-10-3335-2010, URL https://acp.copernicus.org/articles/10/3335/2010/.

Kumjian, M. R., 2013: Principles and applications of dual-polarization weather radar. part i: Description of the polarimetric radar variables. *Journal of Operational Meteorology*, **1**.

Kumjian, M. R., A. P. Khain, N. Benmoshe, E. Ilotoviz, A. V. Ryzhkov, and V. T. Phillips, 2014: The anatomy and physics of z dr columns: Investigating a polarimetric radar signature with a spectral bin microphysical model. *Journal of Applied Meteorology and Climatology*, **53 (7)**, 1820–1843.

Kumjian, M. R., O. P. Prat, K. J. Reimel, M. van Lier-Walqui, and H. C. Morrison, 2022: Dual-polarization radar fingerprints of precipitation physics: A review. *Remote Sensing*, **14 (15)**, 3706.

Kumjian, M. R., and A. V. Ryzhkov, 2012: The impact of size sorting on the polarimetric radar variables. *Journal of the Atmospheric Sciences*, **69 (6)**, 2042–2060.

Lakshmanan, V., K. Hondl, C. K. Potvin, and D. Preignitz, 2013: An improved method for estimating radar echo-top height. *Weather and Forecasting*, **28 (2)**, 481–488.

Lance, S., and Coauthors, 2009: Cloud condensation nuclei activity, closure, and droplet growth kinetics of houston aerosol during the gulf of mexico atmospheric composition and climate study (gomaccs). *Journal of Geophysical Research: Atmospheres*, **114 (D7)**.

Lebo, Z., and J. Seinfeld, 2011: Theoretical basis for convective invigoration due to increased aerosol concentration. *Atmospheric Chemistry and Physics*, **11 (11)**, 5407–5429.

Lei, W., R. Zhang, X. Tie, and P. Hess, 2004: Chemical characterization of ozone formation in the houston-galveston area: A chemical transport model study. *Journal of Geophysical Research: Atmospheres*, **109 (D12)**.

Levin, Z., E. Ganor, and V. Gladstein, 1996: The effects of desert particles coated with sulfate on rain formation in the eastern mediterranean. *Journal of Applied Meteorology and Climatology*, **35 (9)**, 1511–1523.

Levin, Z., and S. A. Yankofsky, 1983: Contact versus immersion freezing of freely suspended droplets by bacterial ice nuclei. *Journal of climate and applied meteorology*, 1964–1966.

Levy, M. E., and Coauthors, 2013: Measurements of submicron aerosols in houston, texas during the 2009 sharp field campaign. *Journal of Geophysical Research: Atmospheres*, **118 (18)**, 10–518.

Lewis, A. C., 2018: The changing face of urban air pollution. *Science*, **359 (6377)**, 744–745.

Li, Z., F. Niu, J. Fan, Y. Liu, D. Rosenfeld, and Y. Ding, 2011: Long-term impacts of aerosols on the vertical development of clouds and precipitation. *Nature Geoscience*, **4 (12)**, 888–894.

Lin, J. C., T. Matsui, R. Pielke Sr, and C. Kummerow, 2006: Effects of biomass-burning-derived aerosols on precipitation and clouds in the amazon basin: A satellite-based empirical study. *Journal of Geophysical Research: Atmospheres*, **111 (D19)**.

Lindsey, D. T., and M. Fromm, 2008: Evidence of the cloud lifetime effect from wildfire-induced thunderstorms. *Geophysical Research Letters*, **35 (22)**.

Mansell, E. R., and C. L. Ziegler, 2013: Aerosol effects on simulated storm electrification and precipitation in a two-moment bulk microphysics model. *Journal of the Atmospheric Sciences*, **70 (7)**, 2032–2050.

Marticorena, B., and G. Bergametti, 1995: Modeling the atmospheric dust cycle: 1. design of a soil-derived dust emission scheme. *Journal of geophysical research: atmospheres*, **100 (D8)**, 16 415–16 430.

Martin, S. T., and Coauthors, 2017: The green ocean amazon experiment (goamazon2014/5) observes pollution affecting gases, aerosols, clouds, and rainfall over the rain forest. *Bulletin of the American Meteorological Society*, **98 (5)**, 981–997.

Matsui, T., H. Masunaga, R. A. Pielke Sr, and W.-K. Tao, 2004: Impact of aerosols and atmospheric thermodynamics on cloud properties within the climate system. *Geophysical Research Letters*, **31 (6)**.

Mauger, G. S., and J. R. Norris, 2007: Stratocumulus sensitivity to aerosols and dynamics. *Eos Trans. AGU*, **88**.

Mazzuca, G. M., K. E. Pickering, D. A. New, J. Dreessen, and R. R. Dickerson, 2019: Impact of bay breeze and thunderstorm circulations on surface ozone at a site along the chesapeake bay 2011–2016. *Atmospheric Environment*, **198**, 351–365.

McFarquhar, G. M., 2022: Rainfall microphysics. *Rainfall*, 1–26.

McFarquhar, G. M., and H. Wang, 2006: Effects of aerosols on trade wind cumuli over the indian ocean: Model simulations. *Quarterly Journal of the Royal Meteorological Society: A journal of the atmospheric sciences, applied meteorology and physical oceanography*, **132 (616)**, 821–843.

Menon, S., J. Hansen, L. Nazarenko, and Y. Luo, 2002: Climate effects of black carbon aerosols in china and india. *Science*, **297 (5590)**, 2250–2253.

Meyer, F., 1994: Topographic distance and watershed lines. *Signal processing*, **38 (1)**, 113–125.

Miskell, G., J. Salmond, and D. E. Williams, 2017: Low-cost sensors and crowd-sourced data: Observations of siting impacts on a network of air-quality instruments. *Science of the total Environment*, **575**, 1119–1129.

Möhler, O., P. DeMott, G. Vali, and Z. Levin, 2007: Microbiology and atmospheric processes: the role of biological particles in cloud physics. *Biogeosciences*, **4 (6)**, 1059–1071.

Moncrieff, M. W., and M. J. Miller, 1976: The dynamics and simulation of tropical cumulonimbus and squall lines. *Quarterly Journal of the Royal Meteorological Society*, **102 (432)**, 373–394.

Morawska, L., and Coauthors, 2018: Applications of low-cost sensing technologies for air quality monitoring and exposure assessment: How far have they gone? *Environment international*, **116**, 286–299.

Morrison, H., 2012: On the robustness of aerosol effects on an idealized supercell storm simulated with a cloud system-resolving model. *Atmospheric Chemistry and Physics*, **12 (16)**, 7689–7705.

Morrison, H., and W. Grabowski, 2011: Cloud-system resolving model simulations of aerosol indirect effects on tropical deep convection and its thermodynamic environment. *Atmospheric Chemistry and Physics*, **11 (20)**, 10 503–10 523.

Nel, A., 2005: Air pollution-related illness: effects of particles. *Science*, **308 (5723)**, 804–806.

Nishant, N., S. C. Sherwood, and O. Geoffroy, 2019: Aerosol-induced modification of organised convection and top-of-atmosphere radiation. *npj Climate and Atmospheric Science*, **2 (1)**, 33.

Noonan, J. A., and R. K. Smith, 1987: The generation of north australian cloud lines and the'morning glory'. *Aust. Meteor. Mag*, **35**, 31–45.

Olalekan, R. M., A. A. Timothy, E. Enabulele Chris, and A. S. Olalekan, 2018: Assessment of air quality indices and its health impacts in ilorin metropolis, kwara state, nigeria. *Science Park Journals of Scientific Research and Impact*, **4 (4)**, 060–074.

Omar, A., and Coauthors, 2013: Caliop and aeronet aerosol optical depth comparisons: One size fits none. *Journal of Geophysical Research: Atmospheres*, **118 (10)**, 4748–4766.

Oue, M., S. M. Saleeby, P. J. Marinescu, P. Kollias, and S. C. van den Heever, 2022: Optimizing radar scan strategies for tracking isolated deep convection using observing system simulation experiments. *Atmospheric Measurement Techniques*, **15 (16)**, 4931–4950.

Pielke, R. A., 1974: A comparison of three-dimensional and two-dimensional numerical predictions of sea breezes. *Journal of the Atmospheric Sciences*, **31 (6)**, 1577–1585.

Ramanathan, V., P. J. Crutzen, J. Kiehl, and D. Rosenfeld, 2001: Aerosols, climate, and the hydrological cycle. *science*, **294 (5549)**, 2119–2124.

Randles, C., and Coauthors, 2017: The merra-2 aerosol reanalysis, 1980 onward. part i: System description and data assimilation evaluation. *Journal of climate*, **30 (17)**, 6823–6850.

Rodríguez, O., and J. Bech, 2021: Tornadic environments in the iberian peninsula and the balearic islands based on era5 reanalysis. *International Journal of Climatology*, **41**, E1959–E1979.

Rogers, R., and M. Yau, 1989: A short course in cloud physics. *Bull. Amer. Meteor. Soc*, **45**, 619.

Rosenfeld, D., and I. M. Lensky, 1998: Satellite-based insights into precipitation formation processes in continental and maritime convective clouds. *Bulletin of the American Meteorological Society*, **79 (11)**, 2457–2476.

Rosenfeld, D., U. Lohmann, G. Raga, C. O'Dowd, M. Kulmala, S. Fuzzi, A. Reissell, and M. Andreae, 2008: Flood or drought: How do aerosols affect precipitation? *Science*, **321 (5894)**, 1309–1313.

Rosenfeld, D., S. Sherwood, R. Wood, and L. Donner, 2014: Climate effects of aerosol-cloud interactions. *Science*, **343 (6169)**, 379–380.

Rosenfeld, D., and W. L. Woodley, 2000: Deep convective clouds with sustained supercooled liquid water down to-37.5 c. *Nature*, **405 (6785)**, 440–442.

Rotstayn, L. D., and J. E. Penner, 2001: Indirect aerosol forcing, quasi forcing, and climate response. *Journal of climate*, **14 (13)**, 2960–2975.

Ryzhkov, A., V. Zhuravlyov, and N. Rybakova, 1994: Preliminary results of x-band polarization radar studies of clouds and precipitation. *Journal of Atmospheric and Oceanic Technology*, **11 (1)**, 132–139.

Saleeby, S. M., and W. R. Cotton, 2004: A large-droplet mode and prognostic number concentration of cloud droplets in the colorado state university regional atmospheric modeling system (rams). part i: Module descriptions and supercell test simulations. *Journal of Applied Meteorology and Climatology*, **43 (1)**, 182–195.

Sattler, B., H. Puxbaum, and R. Psenner, 2001: Bacterial growth in supercooled cloud droplets. *Geophysical Research Letters*, **28 (2)**, 239–242.

Saxena, P., and L. M. Hildemann, 1996: Water-soluble organics in atmospheric particles: A critical review of the literature and application of thermodynamics to identify candidate compounds. *Journal of atmospheric chemistry*, **24**, 57–109.

Schadewald, B., 1999: Houston: Fastest-growing city in the 20th century. *Houston Business Journal*.

Schnell, R., and G. Vali, 1976: Biogenic ice nuclei: Part i. terrestrial and marine sources. *Journal of Atmospheric Sciences*, **33 (8)**, 1554–1564.

Schrom, R. S., M. R. Kumjian, and Y. Lu, 2015: Polarimetric radar signatures of dendritic growth zones within colorado winter storms. *Journal of Applied Meteorology and Climatology*, **54 (12)**, 2365–2388.

Schulze, B. C., and Coauthors, 2018: The impacts of regional shipping emissions on the chemical characteristics of coastal submicron aerosols near houston, tx. *Atmospheric Chemistry and Physics*, **18 (19)**, 14 217–14 241.

Schwartz, S. E., 1996: The whitehouse effect—shortwave radiative forcing of climate by anthropogenic aerosols: An overview. *Journal of Aerosol Science*, **27 (3)**, 359–382.

Sectors, H. I., 2022: Houston industries.

Seinfeld, J. H., 1986: Es&t books: atmospheric chemistry and physics of air pollution. *Environmental science & technology*, **20 (9)**, 863–863.

Seliga, T. A., and V. Bringi, 1976: Potential use of radar differential reflectivity measurements at orthogonal polarizations for measuring precipitation. *Journal of Applied Meteorology and Climatology*, **15 (1)**, 69–76.

Shakya, K. M., P. Louchouarn, and R. J. Griffin, 2011: Lignin-derived phenols in houston aerosols: Implications for natural background sources. *Environmental science & technology*, **45 (19)**, 8268–8275.

Sharma, P., and K. H. Rao, 2002: Analysis of different approaches for evaluation of surface energy of microbial cells by contact angle goniometry. *Advances in Colloid and Interface Science*, **98 (3)**, 341–463.

Shepherd, J. M., and S. J. Burian, 2003: Detection of urban-induced rainfall anomalies in a major coastal city. *Earth Interactions*, **7 (4)**, 1–17.

Sherwood, S. C., 2002: Aerosols and ice particle size in tropical cumulonimbus. *Journal of Climate*, **15 (9)**, 1051–1063.

Sherwood, S. C., V. T. Phillips, and J. Wettlaufer, 2006: Small ice crystals and the climatology of lightning. *Geophysical Research Letters*, **33 (5)**.

Shupyatsky, A., L. Dinevitch, I. Kapitalchuk, and D. Shtivelman, 1990: Use of polarization measurements in cb for the analysis of their stage of development. *Meteor. Hydrol*, **12**, 57–66.

Sinclair, V. A., D. Moisseev, and A. von Lerber, 2016: How dual-polarization radar observations can be used to verify model representation of secondary ice. *Journal of Geophysical Research: Atmospheres*, **121 (18)**, 10–954.

Snyder, J. C., A. V. Ryzhkov, M. R. Kumjian, A. P. Khain, and J. Picca, 2015: A z dr column detection algorithm to examine convective storm updrafts. *Weather and Forecasting*, **30 (6)**, 1819–1844.

Song, S.-K., Y.-N. Choi, Y. Choi, J. Flynn, and B. Sadeghi, 2021: Characteristics of aerosol chemical components and their impacts on direct radiative forcing at urban and suburban locations in southeast texas. *Atmospheric Environment*, **246**, 118 151.

Squires, P., 1958: The microstructure and colloidal stability of warm clouds: Part i—the relation between structure and stability. *Tellus*, **10 (2)**, 256–261.

Storer, R. L., and S. C. Van den Heever, 2013: Microphysical processes evident in aerosol forcing of tropical deep convective clouds. *Journal of the Atmospheric Sciences*, **70 (2)**, 430–446.

Stull, R. B., 1988: *An introduction to boundary layer meteorology*, Vol. 13. Springer Science & Business Media.

Sullivan, D. W., J. H. Price, B. Lambeth, K. A. Sheedy, K. Savanich, and R. J. Tropp, 2013: Field study and source attribution for pm2. 5 and pm10 with resulting reduction in concentrations in the neighborhood north of the houston ship channel based on voluntary efforts. *Journal of the Air & Waste Management Association*, **63 (9)**, 1070–1082.

Tao, W.-K., J.-P. Chen, Z. Li, C. Wang, and C. Zhang, 2012: Impact of aerosols on convective clouds and precipitation. *Reviews of Geophysics*, **50 (2)**.

Tao, W.-K., X. Li, A. Khain, T. Matsui, S. Lang, and J. Simpson, 2007: Role of atmospheric aerosol concentration on deep convective precipitation: Cloud-resolving model simulations. *Journal of Geophysical Research: Atmospheres*, **112 (D24)**.

Tuttle, J. D., V. Bringi, H. Orville, and F. Kopp, 1989: Multiparameter radar study of a microburst: Comparison with model results. *Journal of Atmospheric Sciences*, **46 (5)**, 601–620.

Twomey, S., 1959: The nuclei of natural cloud formation part i: The chemical diffusion method and its application to atmospheric nuclei. *Geofisica pura e applicata*, **43**, 227–242.

Twomey, S., 1977: The influence of pollution on the shortwave albedo of clouds. *Journal of the atmospheric sciences*, **34 (7)**, 1149–1152.

van den Heever, S. C., G. G. Carrió, W. R. Cotton, P. J. DeMott, and A. J. Prenni, 2006: Impacts of nucleating aerosol on florida storms. part i: Mesoscale simulations. *Journal of the atmospheric sciences*, **63 (7)**, 1752–1775.

van den Heever, S. C., G. L. Stephens, and N. B. Wood, 2011: Aerosol indirect effects on tropical convection characteristics under conditions of radiative–convective equilibrium. *Journal of the Atmospheric Sciences*, **68 (4)**, 699–718.

Varble, A., 2018: Erroneous attribution of deep convective invigoration to aerosol concentration. *Journal of the Atmospheric Sciences*, **75 (4)**, 1351–1368.

Veals, P. G., A. C. Varble, J. O. Russell, J. C. Hardin, and E. J. Zipser, 2022: Indications of a decrease in the depth of deep convective cores with increasing aerosol concentration during the cacti campaign. *Journal of the Atmospheric Sciences*, **79 (3)**, 705–722.

Virtanen, P., and Coauthors, 2020: SciPy 1.0: Fundamental Algorithms for Scientific Computing in Python. *Nature Methods*, **17**, 261–272, https://doi.org/10.1038/s41592-019-0686-2.

Wall, C., E. Zipser, and C. Liu, 2014: An investigation of the aerosol indirect effect on convective intensity using satellite observations. *Journal of the Atmospheric Sciences*, **71 (1)**, 430–447.

Wang, C., J. J. Corbett, and J. Firestone, 2007: Modeling energy use and emissions from north american shipping: application of the ship traffic, energy, and environment model. *Environmental science & technology*, **41 (9)**, 3226–3232.

Wang, Y., Q. Wan, W. Meng, F. Liao, H. Tan, and R. Zhang, 2011: Long-term impacts of aerosols on precipitation and lightning over the pearl river delta megacity area in china. *Atmospheric Chemistry and Physics*, **11 (23)**, 12 421–12 436.

White, A. B., J. R. Jordan, B. E. Martner, F. Martin Ralph, and B. W. Bartram, 2000: Extending the dynamic range of an s-band radar for cloud and precipitation studies. *Journal of Atmospheric and Oceanic Technology*, **17 (9)**, 1226–1234.

White, B., E. Gryspeerdt, P. Stier, H. Morrison, G. Thompson, and Z. Kipling, 2017: Uncertainty from the choice of microphysics scheme in convection-permitting models significantly exceeds aerosol effects. *Atmospheric Chemistry and Physics*, **17 (19)**, 12 145–12 175.

Williams, E., D. Rosenfeld, N. Madden, C. Labrada, J. Gerlach, and L. Atkinson, 1999: The role of boundary layer aerosol in the vertical development of precipitation and electrification: another look at the contrast between lightning over land and over ocean. *11th International Conference on Atmospheric Electricity*.

Wurzler, S., T. G. Reisin, and Z. Levin, 2000: Modification of mineral dust particles by cloud processing and subsequent effects on drop size distributions. *Journal of Geophysical Research: Atmospheres*, **105 (D4)**, 4501–4512.

Yang, D., H. Zhang, Z. Wang, S. Zhao, and J. Li, 2022: Changes in anthropogenic particulate matters and resulting global climate effects since the industrial revolution. *International Journal of Climatology*, **42 (1)**, 315–330.

Yoon, S., S. Usenko, and R. J. Sheesley, 2020: Fine and coarse carbonaceous aerosol in houston, tx, during discover-aq. *Atmosphere*, **11 (5)**, 482.

Yuan, T., L. A. Remer, K. E. Pickering, and H. Yu, 2011: Observational evidence of aerosol enhancement of lightning activity and convective invigoration. *Geophysical Research Letters*, **38 (4)**.

Yuter, S. E., and R. A. Houze Jr, 1995: Three-dimensional kinematic and microphysical evolution of florida cumulonimbus. part ii: Frequency distributions of vertical velocity, reflectivity, and differential reflectivity. *Monthly weather review*, **123 (7)**, 1941–1963.

Yuter, S. E., M. A. Miller, M. D. Parker, P. M. Markowski, Y. Richardson, H. Brooks, and J. M. Straka, 2013: Comment on "why do tornados and hailstorms rest on weekends?" by d. rosenfeld and t. bell. *J. Geophys. Res. Atmos*, **118**, 7332–7338.

Zhang, J., J. S. Reid, and B. N. Holben, 2005: An analysis of potential cloud artifacts in modis over ocean aerosol optical thickness products. *Geophysical Research Letters*, **32 (15)**.

1 Appendix A

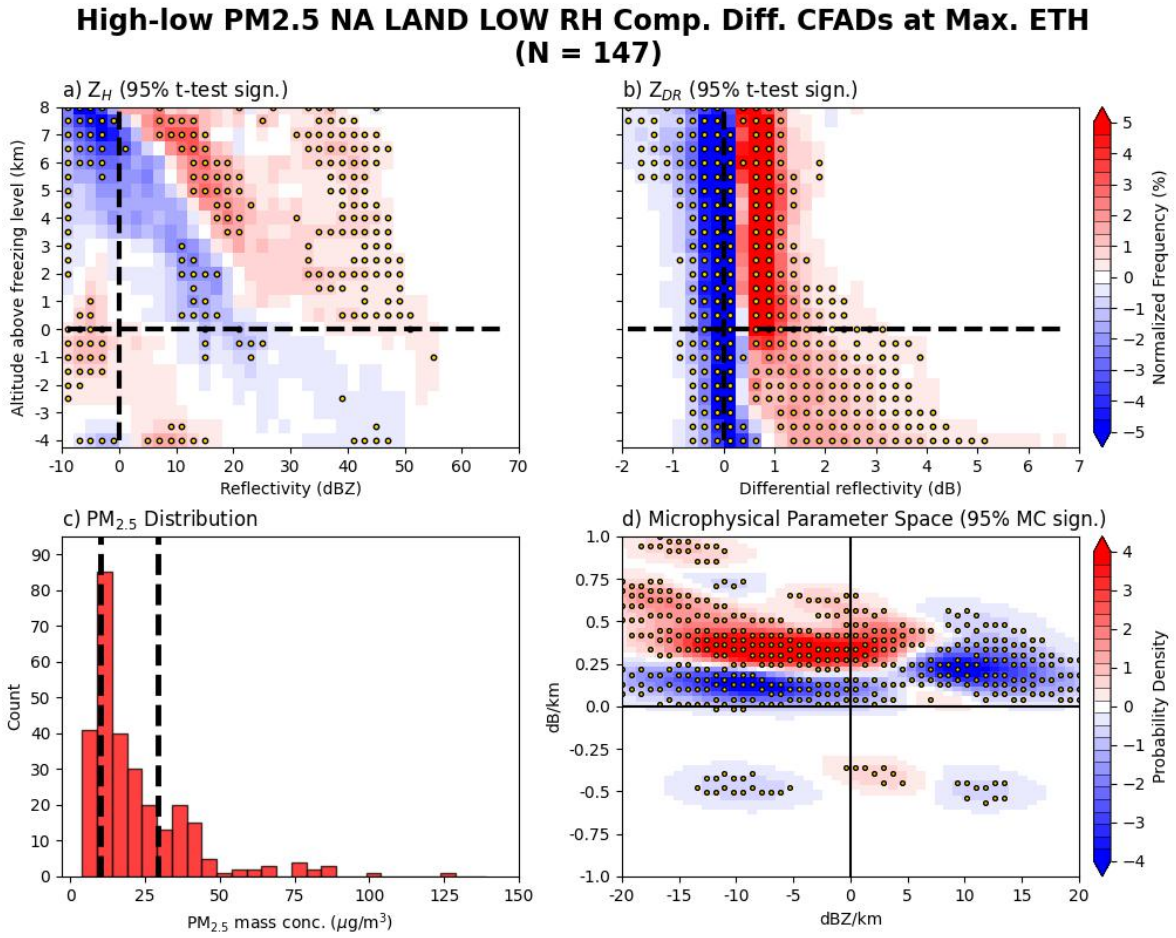

Figure A.1: As in Figure 4.30 but for all *NA* LAND DCCs within the LOW RH tercile.

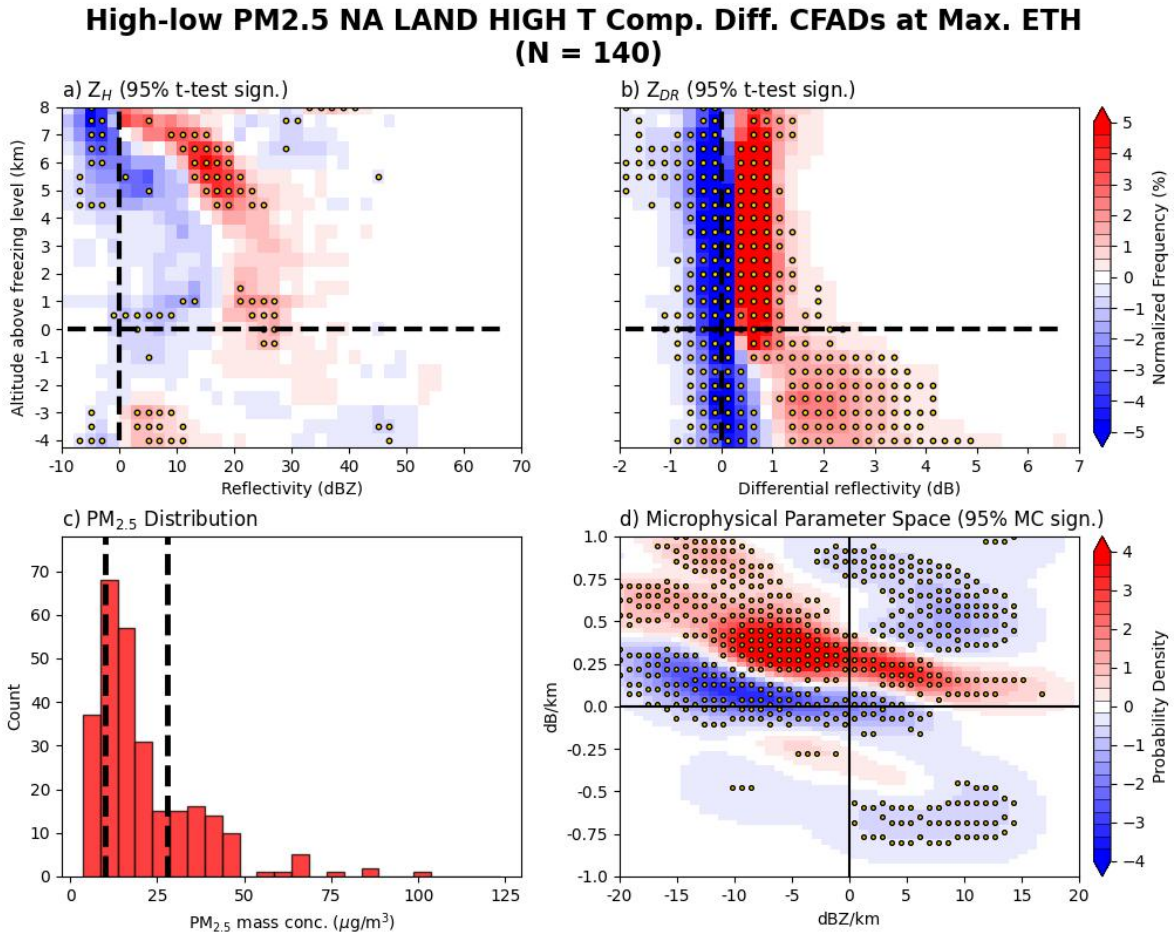

Figure A.2: As in Figure 4.30 but for all *NA* LAND DCCs within the HIGH T tercile.

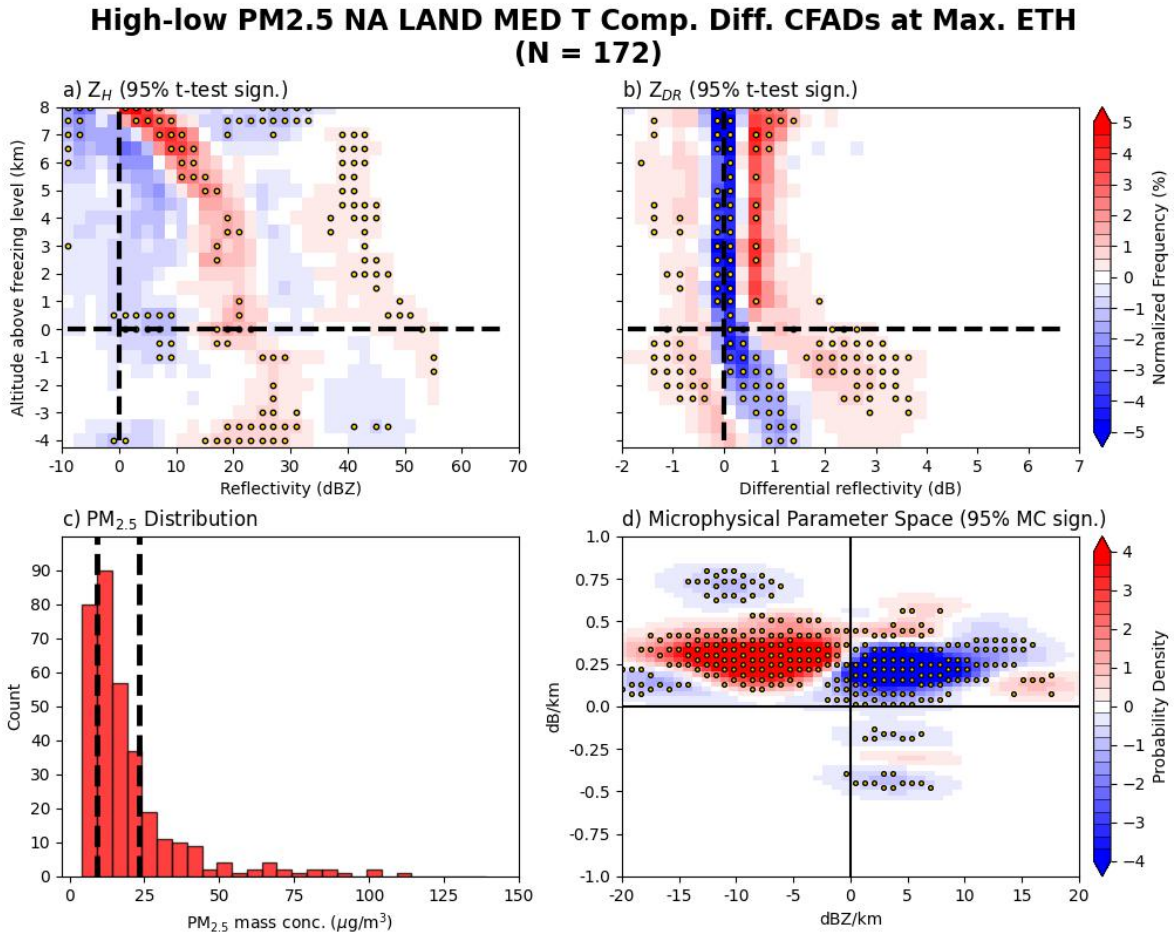

Figure A.3: As in Figure 4.30 but for all *NA* LAND DCCs within the MED T tercile.

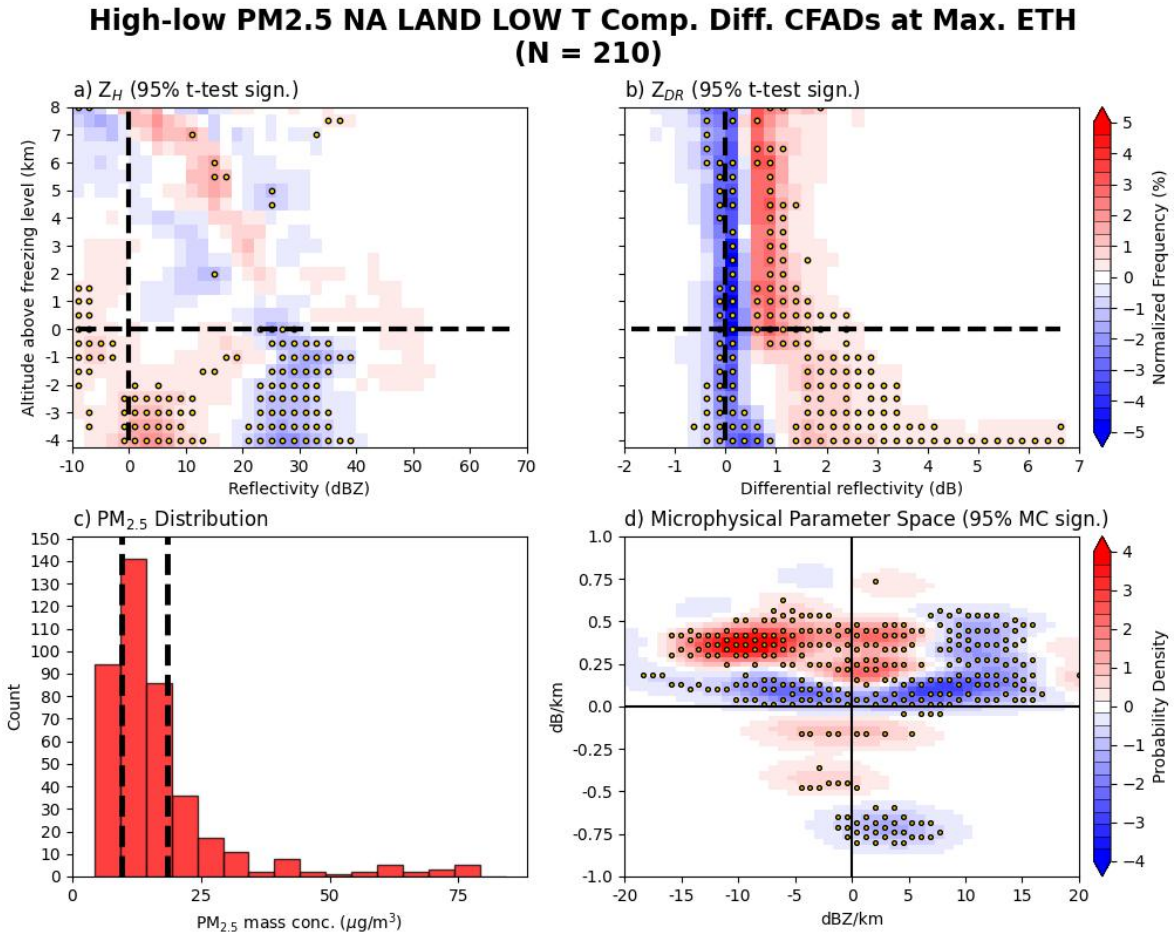

Figure A.4: As in Figure 4.30 but for all *NA* LAND DCCs within the LOW T tercile.

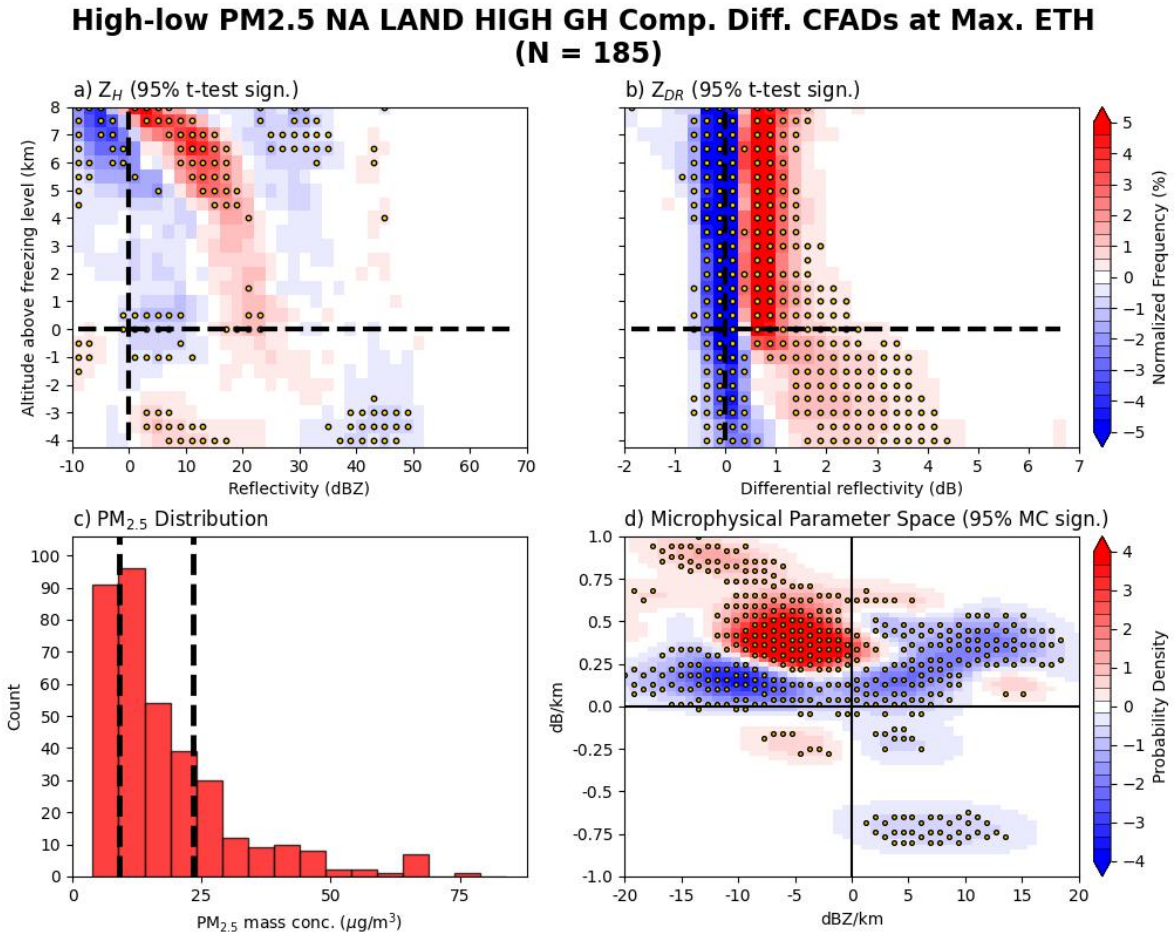

Figure A.5: As in Figure 4.30 but for all *NA* LAND DCCs within the HIGH GH tercile.

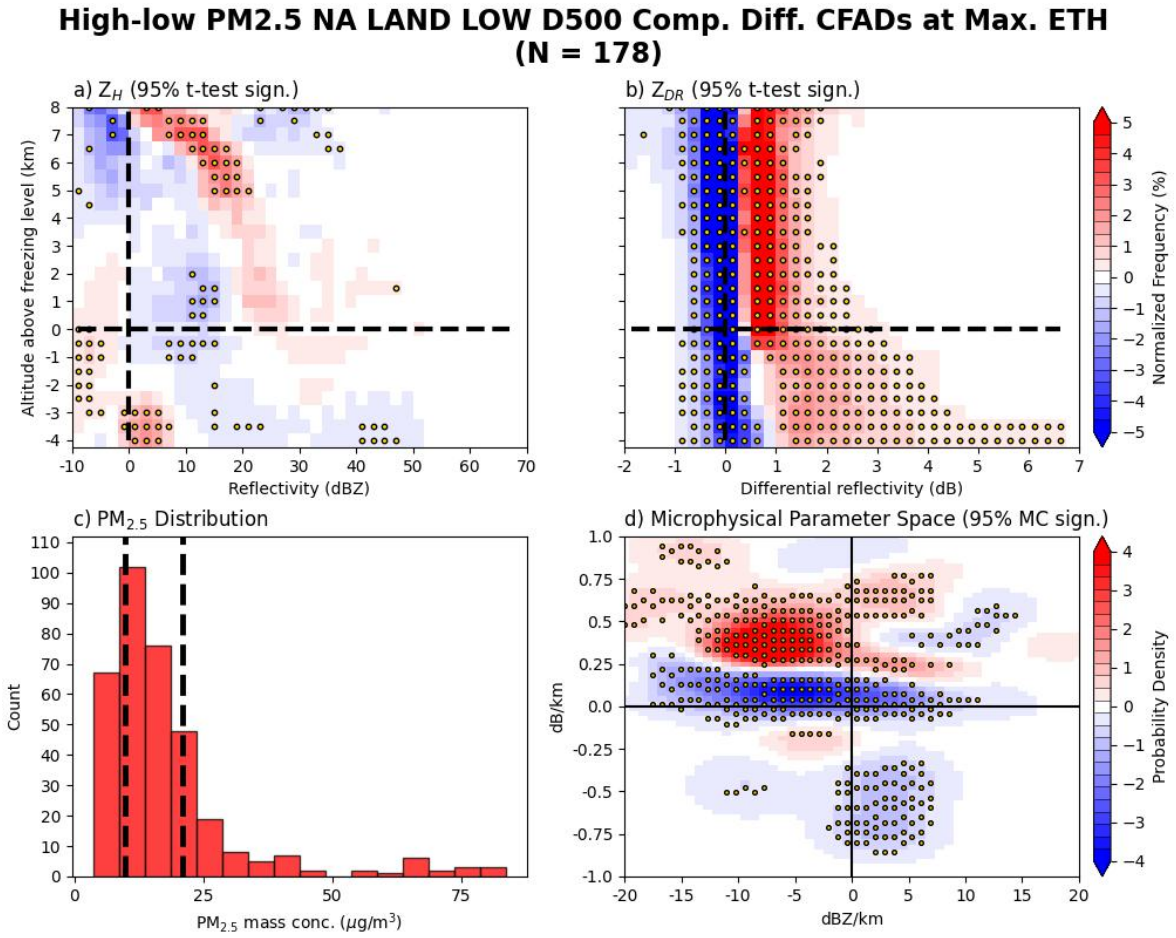

Figure A.6: As in Figure 4.30 but for all *NA* LAND DCCs within the LOW D500 tercile.

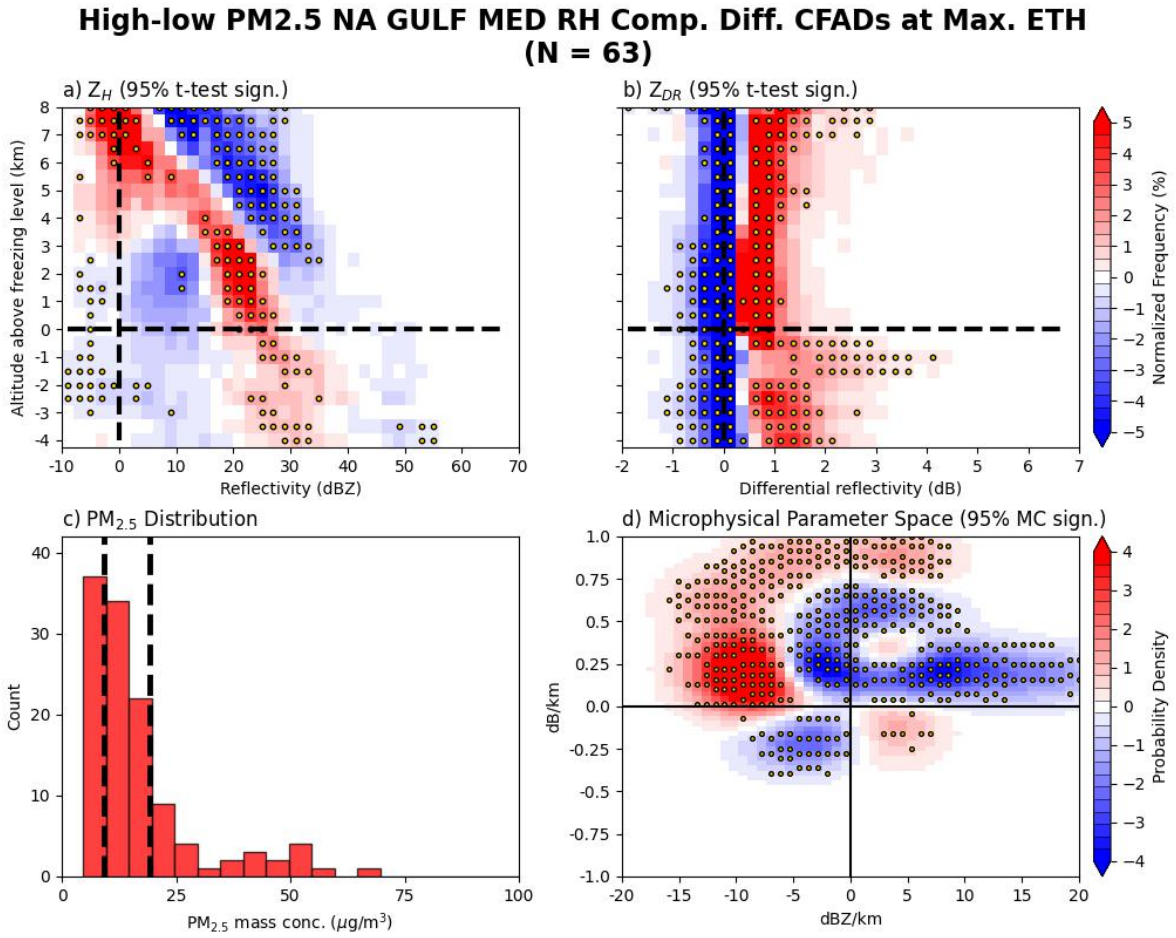

Figure A.7: As in Figure 4.30 but for all *NA* GULF DCCs within the MED RH tercile.

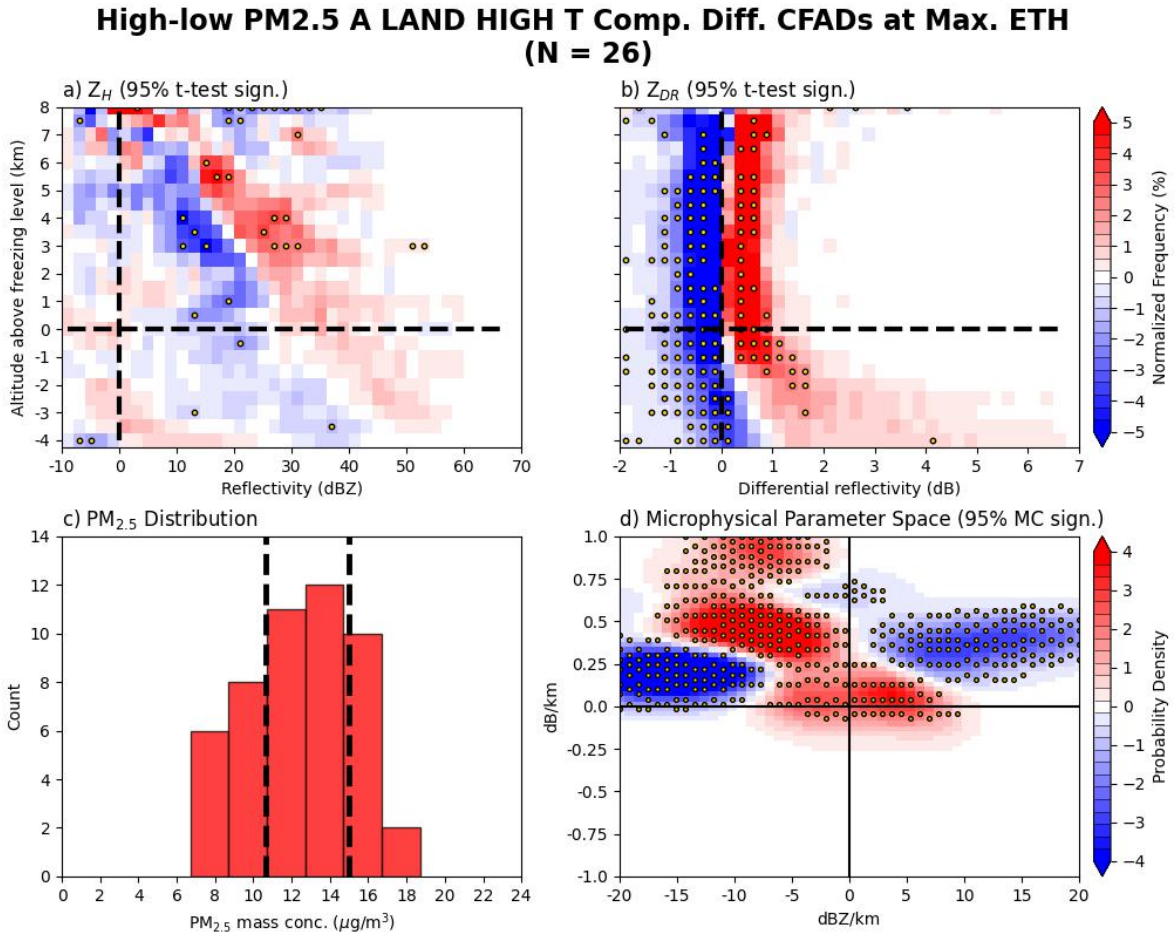

Figure A.8: As in Figure 4.30 but for all A LAND DCCs within the HIGH T tercile.

2 Appendix B

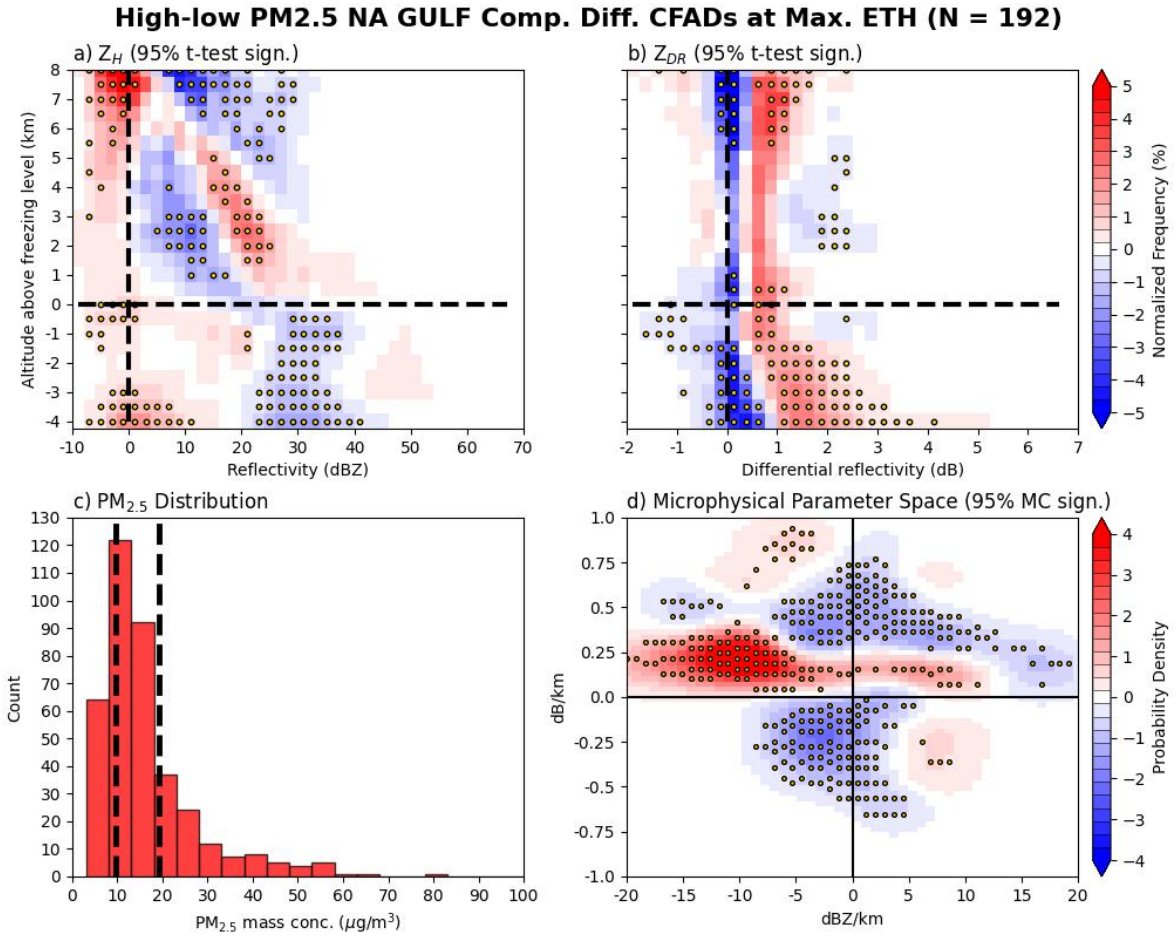

Figure A.9: As in Figure 4.30 but for all *NA* GULF DCCs.

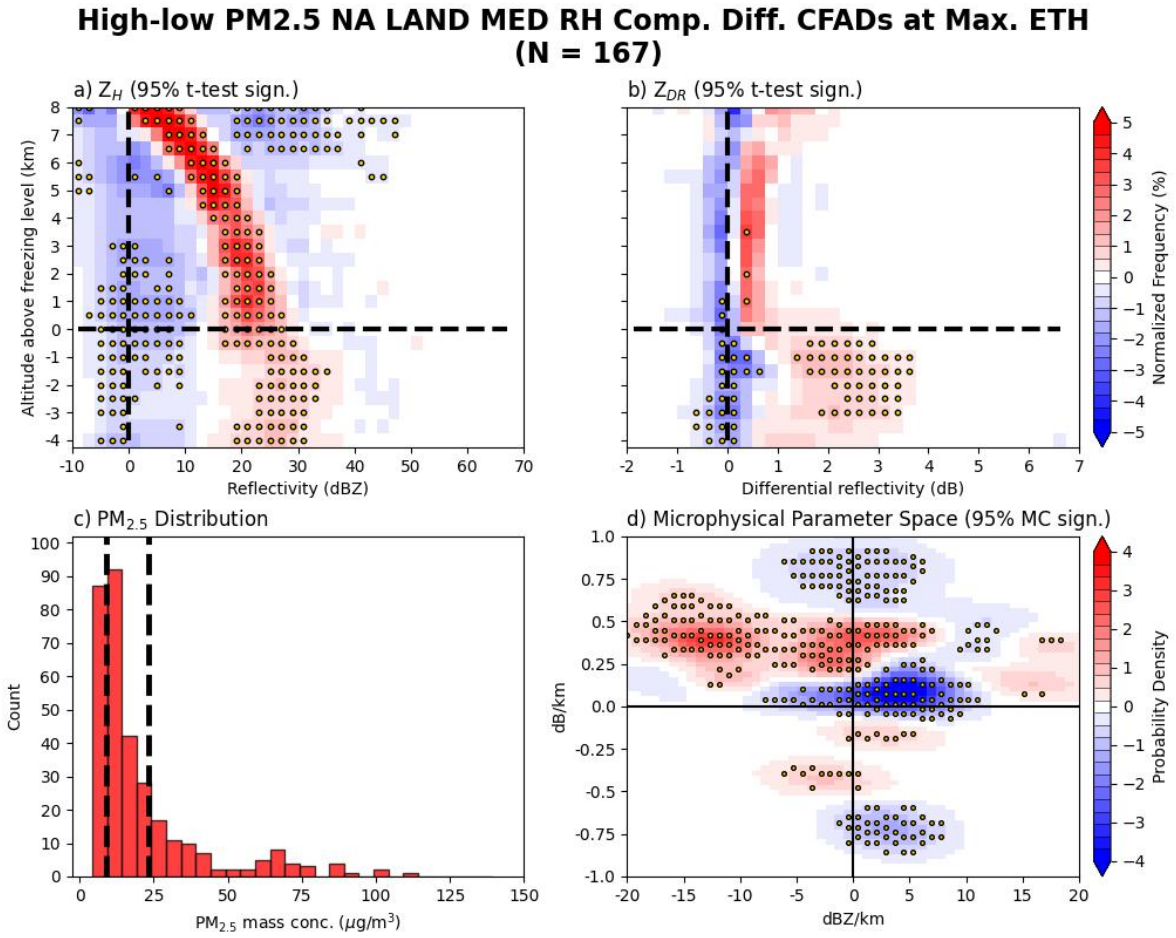

Figure A.10: As in Figure 4.30 but for all *NA* LAND DCCs within the MED RH tercile.

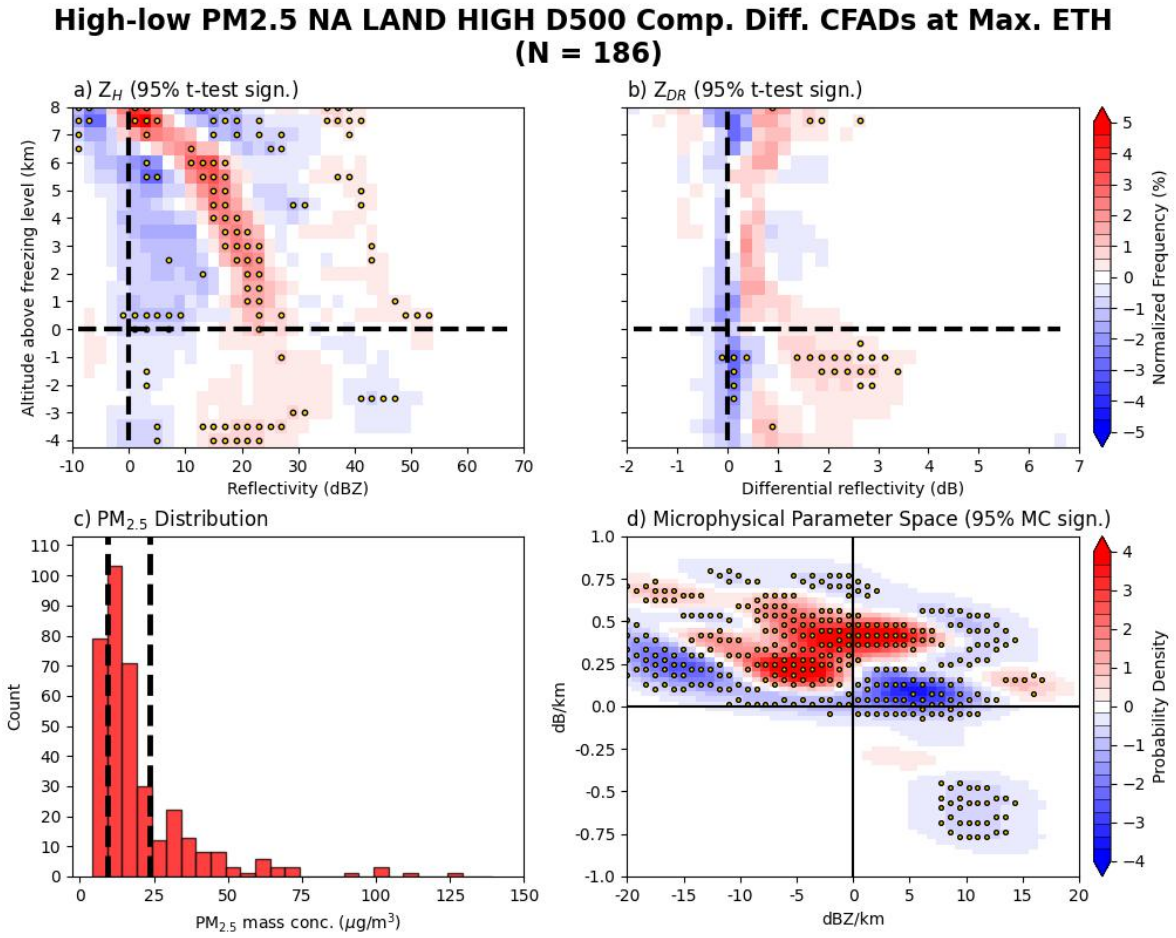

Figure A.11: As in Figure 4.30 but for all *NA* LAND DCCs within the HIGH D500 tercile.

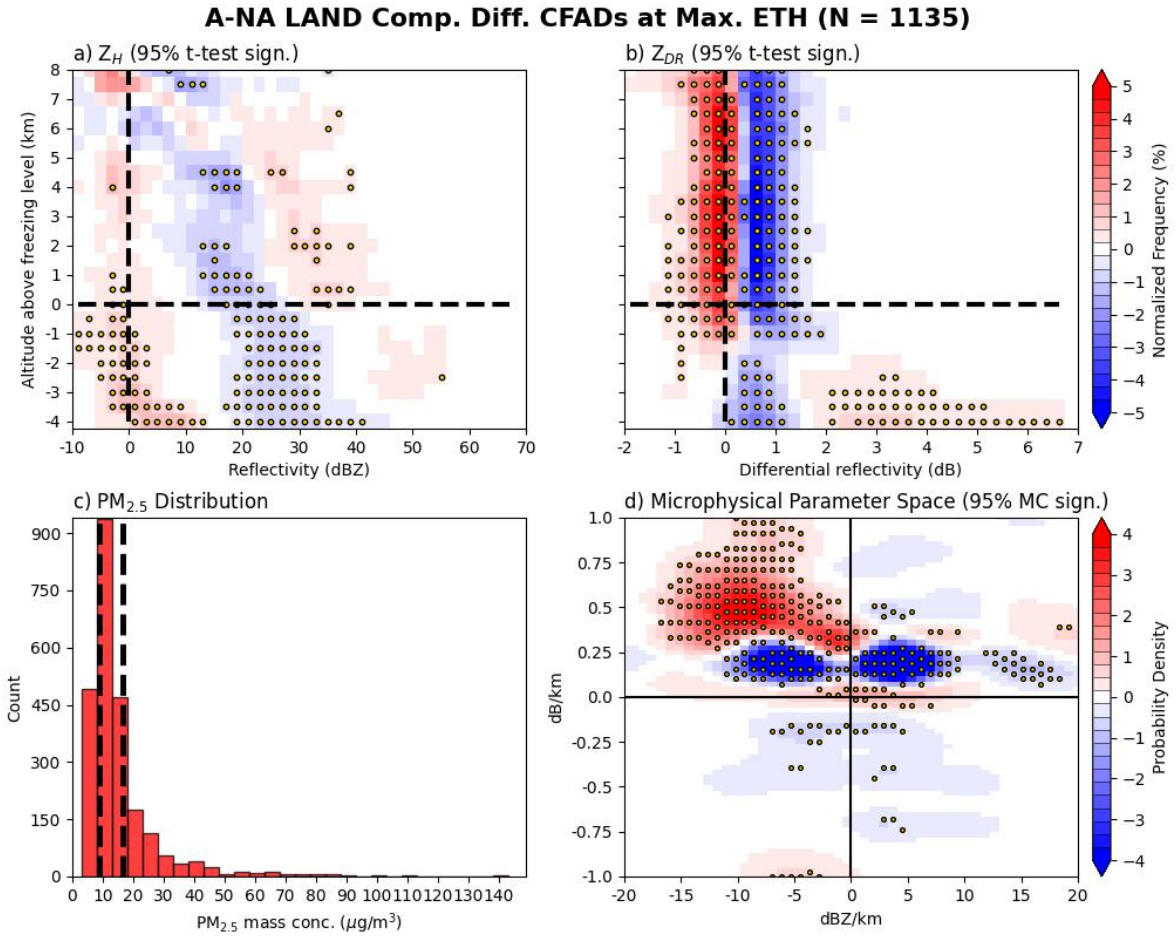

Figure A.12: As in Figure 4.30 but for all LAND DCCs. Distinction is made between *A* (red) and *NA* (blue) DCCs.